MEASUREMENT OF PROTON-PROTON BREMSSTRAHLUNG CROSS SECTIONS AT 42 MeV

by Leslie Gordon Greeniaus

March, 1972

A Thesis Submitted to
the Faculty of Graduate Studies
University of Manitoba

In Partial Fulfillment
of the Requirements for the Degree
Doctor of Philosophy

ABSTRACT

Proton-proton bremsstrahlung ($pp\gamma$) cross sections have been measured at 42 MeV incident beam energy, using a wire chamber spectrometer developed for the study of three-body final states. $PP\gamma$ events from a 22 cm long gaseous target were detected simultaneously over a large kinematic region. Polar angle ranges were from 14° to 42° and the maximum allowed event non-coplanarity could be detected for all observed proton polar angles. Resolutions were typically $\pm 0.75^\circ$ for the proton polar angles and $\pm$ 25% of the maximum allowed non-coplanarity. The spectrometer was able to reject most random events by testing for an event vertex in the long gas target, resulting in significantly lower random background than for most previous $pp\gamma$ experiments.

The data have been analyzed by separating them into 18 independent polar angle regions and extracting the $d\sigma/d\Omega_1 d\Omega_2 d\Psi_\gamma$, $d\sigma/d\Omega_1 d\Omega_2$ and $d\sigma/d\theta_1 d\theta_2$ cross sections. These results have been compared to Liou's predictions for the Hamada-Johnston potential. The weighted mean ratio of Expt/Theory for the $d\sigma/d\theta_1 d\theta_2$ cross sections was $0.967 \pm 4.6\%$. The data indicate that predictions of the Hamada-Johnston potential, with Coulomb corrections included, would be in good agreement with the measured cross sections.

The data have also been analyzed by integrating over the observed proton polar angle ranges. The distribution of events as a function of the measured non-coplanarity is in excellent agreement with predictions of the Hamada-Johnston potential. Distributions of events versus Ψ_γ and the proton polar angle asymmetry are also in good agreement with the theoretical predictions.

ACKNOWLEDGEMENTS

Successful completion of the research presented in this thesis would not have been possible without the support of many people. I owe a special debt of gratitude to my advisor, Dr. J. V. Jovanovich, whose encouragement, enthusiasm, guidance and sound advice were especially welcomed. His dedication and active participation in all aspects of the experiment have been major factors in its success.

The development of the spectrometer hardware and large portions of the software used in the two-computer system, were mainly the responsibility of other people. Dr. K. G. Standing participated in the initial design of the spectrometer, while major hardware components were designed and constructed by Dr. J. McKeown, Dr. J. C. Thompson, Mr. T. Millar and Mr. D. Peterson. The monitor program used at the PDP-15 was written by Mr. D. Reimer, and Dr. E. Lipson wrote the preliminary version of the VRTX program. Dr. J. C. Thompson, Mr. D. Peterson, Mr. R. Kawchuk, Mr. R. King and Mr. P. O'Connor wrote most of the remaining PDP-15 software.

Large portions of the IBM 360/65 on-line kinematic analysis program were written by Dr. J. McKeown. The spectrometer and two-computer system were brought to fully-

operational status and a firm foundation for the analysis procedures was developed during his participation in the experiment. The initial versions of the COMBINE Monte Carlo program were written by Dr. W. F. Prickett and Dr. K. F. Suen, who also implemented useful improvements in several parts of the spectrometer hardware. Dr. Suen also developed the spline fitting procedures which were included in COMBINE. Mr. P. O'Connor provided programming assistance for both the PDP-15 and 360/65 analyses. Dr. M. K. Liou graciously offered the use of his computer code for calculation of the required $pp\gamma$ cross sections.

The arduous burden of data collection was shared by Dr. W. F. Prickett, Dr. K. F. Suen, Mr. T. Millar, Mr. D. G. Peterson and Mr. P. O'Connor. The technical support of the cyclotron staff, the able assistance from personnel of the electronics laboratory, particularly Mr. A. Neufeld, and the willing cooperation of the University of Manitoba Computer Department were essential during the running of the experiment.

Dr. K. G. Standing kindly consented to read the final draft of this thesis during the absence of my advisor. Dr. R. Kerchner also provided several valuable comments and criticisms.

The patient support and assistance of my wife, Carolyn, especially during the latter stages of this work, have not gone unnoticed and cannot be sufficiently rewarded. A note of appreciation must be given to Mrs. J. Peets, who did an expert job of typing the thesis.

I wish to gratefully acknowledge the National Research Council of Canada for a Graduate Scholarship, held during the period 1967 - 1971, and support by the Atomic Energy Control Board of Canada since October 1971.

TABLE OF CONTENTS

CHAPTER

CHAPTER

APPENDIX

LIST OF TABLES

LIST OF FIGURES

CHAPTER I

INTRODUCTION

The nucleon-nucleon interaction has long been an interesting, albeit frustrating problem. Its importance derives from application in divers areas of nuclear physics. Nuclear matter and nuclear structure calculations, many-body theory and particle production processes depend on the understanding of both elastic and inelastic nucleon-nucleon scattering.

At low energies, a number of phenomenological and semi-phenomenological potential models have been developed which describe the existing elastic nucleon-nucleon scattering data with varying degrees of success. The potential models have taken a wide variety of forms. They include the hard core Hamada-Johnston (HJ)[1)] and Yale[2)] potentials, the Reid potential[3)], the finite-core potential of Bressel and Kerman (BK)[4)], the boundary condition model (BCM) of Feshbach and Lomon[5)], the non-local separable Tabakin potential[6)], momentum dependent potentials[7)] and a number of one-boson exchange models[8)]. In most of these models there are sets of free parameters that are adjusted to give the best possible agreement with phase shifts and coupling parameters obtained from nucleon-nucleon scattering experiments.

Until recently, all the data available for determination of the potential parameters consisted of p-p and n-p elastic scattering experiments. Of necessity then, only information on the elastic (on-energy shell) nature of the NN interaction has been built into the detailed specification of these models. In an effort to describe the inelastic or off-energy shell (OES) portions of the interaction and perhaps choose the potential that gives the best fit to all possible data, interest has been aroused in inelastic processes. At energies below the π-production threshold, the only possible inelastic scattering process between two nucleons is nucleon-nucleon bremsstrahlung (NNγ). The nuclear potential and the NNγ process are discussed in a recent review article by P. Signell[9].

All nuclear processes except N-N elastic scattering depend on inelastic portions of the N-N interaction to some degree, but NNγ is by far the simplest. The electromagnetic interaction is well understood and since it represents a minor perturbation to a strongly interacting system, its effects only need be calculated to first order. In a DWBA analysis, this results in a truncation of the multiple-scattering series at the second order terms in the NN scattering amplitude. The identity of the nucleons and the small contributions of the double scattering terms make the ppγ reaction the easiest to investigate theoretically. This is also true experimentally since detection of neutrons is more difficult than detection of protons. Nucleon-nucleon bremsstrahlung is easier to handle theoretically than even the simplest inelastic nucleon-nucleus scattering (e.g. $p + d \rightarrow p + p + n$) processes where rescattering effects are large and the many-body problem must be solved.

* * * * *

Historical Review

The first attempt to evaluate ppγ cross sections was made by Ashkin and Marshak[10] in 1949. They showed that the ppγ cross section was identically zero for a central potential in Born approximation. Interest in ppγ waned until 1963 when Sobel and Cromer (SC)[11] obtained a finite value for the cross section in a DWBA calculation using the Hamada-Johnston potential. The subsequent experiments at Harvard[51-53], Manitoba[57] and UCLA[60] measured cross sections significantly lower than those predicted. Shortly thereafter, Duck and Pearce[12] presented theoretical results for the Tabakin potential. In both of these calculations, the approximations used were identical in nature, the most important being to neglect the contributions of the internal scattering (re-scattering) terms. This was justified on the basis of a calculation by Sobel[13-14]. The two independent calculations did not agree with each other or with the experimental results. The Duck and Pearce calculations, however, showed a less violent disagreement with the measured cross sections.

Signell and Marker[15], after a detailed examination, discovered a number of errors in both formulations of the theory. This had the effect of bringing the subsequent results of Pearce, Gale and Duck (PGD)[16] into fair agreement with experiment. (The first predictions of the non-coplanar dependence also appeared in this paper by PGD.) The revised SC results[17] were still too high, particularly at lower energies. At 48 MeV there was a factor of 6 disagreement between the two predictions. It appeared that this discrepancy could not be explained by the fact that different potential models had been used.

In 1967 the difference between the two theoretical calculations was explained by Signell[18]. It had been shown much earlier by Low[19] that a gauge-invariant theory requires inclusion of both pole and internal radiation contributions. As it turns out, the difficult internal scattering terms are very small in the center of mass of the two protons. In the laboratory system, this is not the case, especially at lower energies where the internal and pole radiation terms tend toward complete cancellation. PGD had performed their calculations in the center of mass system before transforming the cross sections to the laboratory. SC had evaluated the cross sections in the lab and simply chosen the wrong frame in which to ignore the difficult rescattering terms.

Since that time a number of authors have done $pp\gamma$ calculations in one form or another. Nyman[20)] and Felsner[21)] have calculated model-independent predictions which do not agree very well with the experimental results. McGuire and Pearce[22-24)] have investigated off-shell effects, as have Signell and Marker[25)]. Signell and Marker[26)] have also included Coulomb effects for the HJ potential, and Brown[27)] has calculated the rescattering terms directly. Baier, Kuhnelt and Urban[28)] have presented results for a one-boson exchange model. The non-coplanar dependence for the HJ and Reid potentials was predicted by Drechsel and Maximon[29)] by evaluation of the scattering matrix in the center of mass. Heller[30)], Liou[31)] and Cromer[32)] have shown how to include corrections for the internal scattering terms in the lab $pp\gamma$ calculations. Liou and Cho[33)] and Liou and Sobel[34)] have also included the relativistic spin correction (RSC) for cross sections evaluated in the lab system as was first suggested by McGuire[23)].

Calculations for the HJ potential by different authors now agree within a few percent.

In the seven years since the publication of the first experimental ppγ results, there have been about twenty different experiments* at incident proton energies ranging from 3 to 204 MeV[51-71]. Except for the first Rochester experiment[54-56], all have used the so-called "Harvard geometry" where only the two inelastic protons are detected and the energy and direction of the gamma ray are inferred from measurements of the proton energies and directions. In most experiments the polar angles of the detected protons were equal and the detector heights were comparable to the maximum non-coplanarity of the protons, the latter condition being necessary to obtain reasonable event rates.

In all Harvard geometry experiments it has been standard procedure to extract the coplanar $d\sigma/d\Omega_1 d\Omega_2$ cross section, and in some cases the average polar angle distribution of the photon as well. Three measurements of the Φ_r dependence of the cross sections have been made - at 157 MeV[53], 64.4 MeV[69] and 20 MeV[63]. Experiments with good azimuthal resolution (which have negligible error due to uncertainty

---

* Preliminary measurements of ppγ cross sections using our wire chamber spectrometer have been published (Ref. 70). They are not discussed here as these results will be included in this thesis.

in the Φ_r distribution) have been done at 157 MeV[53], 99 MeV[66], 64.4 MeV[69], 61.7 MeV[61] and 46 MeV[62] but only the 99 MeV McGill and 157 MeV Harvard results have good enough statistics to be really useful.

The photon polar angle distributions that have been extracted suffer from a number of difficulties. Finite energy and angular resolutions compound into relatively large uncertainties in the photon direction and most results are integrated over the full non-coplanar range. The results also suffer from poor statistical accuracy and therefore are difficult to compare to theoretical predictions. At present only the McGill and Harvard distributions can be considered sufficiently precise to warrant detailed comparison to theoretical predictions.

The ppγ experiment[54-56] performed by the Rochester I group used spark chambers to determine proton directions and also detected the gamma ray at symmetric angles in the lab system. In this experiment a polarized proton beam was used. Distributions of the two-nucleon center of mass scattering angles, the γ-ray energy spectra and the γ-ray and p-p asymmetries due to the initially polarized beam were measured. In some respects, the equipment used in the Rochester experiment is most similar to that described in this thesis.

The results of all NNγ experiments to date are summarized in the excellent review article by M. L. Halbert[72). The range of measurements is now fairly extensive. The energy dependence of the measured coplanar cross sections is in moderately good agreement with theory, although there are some apparent differences. In the energy range from 30 to 65 MeV there are also some discrepancies between the various experimental results. The theoretical predictions are in better agreement with the Oak Ridge data[61,62,67,69). The relatively precise data at 99 MeV[66) have mixed agreement with theory. In particular, the 35° point differs by 3 standard deviations from the theoretical predictions. The shapes of the photon angular distributions, at all energies where they have been measured, agree qualitatively with theoretical predictions. Most of the experimental results are limited by statistics in the number of detected ppγ events because of the very low event rates (typically 1 - 2 per hour) and only small ranges of the available phase space have been observed.

* * * * *

No comprehensive, quantitative theoretical predictions on the effects of different potential models have been made, but the limited number and type of ppγ cross section calculations that have been attempted[10-38] indicate that the difference between potential models is not very large. It now appears that to select between the various potential models, ppγ measurements must either be very precise or correspond to conditions that are further off the energy shell than most experiments to date (i.e. higher incident energies and/or smaller polar angles). However, it has yet to be shown that the theoretical predictions agree with precise experimental results even in a relatively model-independent region. The agreement between the theoretical predictions and existing experimental results is only moderately good in spite of the large experimental uncertainties.

The concept of the experiment described here evolved in 1966 after R. Warner had completed his first ppγ experiment[57] at the University of Manitoba. This was during the period of large disagreement between experiment and theory and between different theorists. While such a situation could hardly be expected to continue to the present (and indeed has not), it was hoped that a sufficiently precise experiment might be able to distinguish between potential models. A need for accurate experiments with which to test theoretical predictions certainly existed. The present experiment makes use of a wire chamber spectrometer designed for the observation of reactions with three-body final states[39-50]. The trajectories of the two final state protons are detected in wire chambers and the proton energies are measured in large area scintillation counters. Data is processed on an event by event basis on-line to a two-computer system which forms an integral part of the spectrometer.

This work represents a major departure from the methods of previous experiments which have been characterized by small solid angles, low event rates and measurements over small phase space ranges. In the experiment described in this thesis, $pp\gamma$ events have been detected over a large kinematic range. At the same time, angular and energy resolutions comparable to or better than previous experiments have been retained. The large solid angles and long gaseous target result in overall event rates that are as much as a factor of 100 greater than in previous experiments, and regions of phase space that are relatively far off the energy-shell are observed. The ability of the spectrometer to reject random events because they lack an event vertex has resulted in reduced random backgrounds.

The data collected have good statistics and relatively accurate overall normalization. The large volume of phase space observed makes it possible to test theoretical predictions in ways that have not been attempted before. This can be done by grouping all the data together and looking at cross sections and distributions of specific interesting variables. Alternatively, it is possible to separate the data and analyze them in a conventional manner over an extended range with generally better statistics than previously available.

CHAPTER II

EXPERIMENTAL METHOD

II.1 PRELIMINARY DISCUSSION

Proton-proton bremsstrahlung measurements have proved to be very difficult because the measured cross sections are small while the competing natural processes, as well as those introduced by the experimental apparatus, create a sea of background. The customary procedure has been to detect the final state protons in coincidence using scintillation detectors* placed at symmetric polar angles (typically $\sim 30^{\circ}$) on opposite sides of the beam. Small solid angles have been used to define the polar angles of each particle with reasonable accuracy. Generally, azimuthal ranges just large enough to permit observation of events having the maximum kinematically allowed non-coplanarity were used.

In the measurement of $pp\gamma$ cross sections, background problems are unusually severe. Random coincidences are the worst source of background and have limited data rates in previous experiments. Prompt backgrounds have

---

* Several experiments at incident energies below 30 MeV have used solid state detectors (Ref. 63-65, 68).

resulted from impurities in the target gas, reactions in beam and solid angle defining slits, walls of the target container and from p-p elastic events multiple-scattered into the detectors. The magnitude of the difficulties (and the patience required to perform ppγ experiments) becomes apparent if an estimate of the various counting rates is made.

II.1.1 PPγ Event Rates in Previous Experiments

The event rates calculated below are based on the experimental arrangement used by R. Warner in the first ppγ measurement made at the University of Manitoba[57]. All symbols used are defined in Appendix A.

In the experiment six final state parameters were measured - the energy, polar angle and azimuthal angle of each proton. A gas target 3 cm long was used and the solid angle of each detector was 0.0063 sr ($\pm$ 1.8^o in the polar angle and $\pm$ 5.8^o in the azimuthal angle at a polar angle of 30^o). The ppγ cross section measured was $\sim 2\ \mu b/sr^2$. At 1 na the following ppγ event rate is obtained

$$N_{pp\gamma} = \frac{d\sigma}{d\Omega_L d\Omega_R} 2A_o I_o L \Delta\Omega_L \Delta\Omega_R \qquad \text{II-1}$$

$$= 0.28/hr$$

The p-p elastic cross section at 48 MeV is 32 mb/sr[74)] yielding a proton singles event rate in each detector of

$$N_{el} = \left.\frac{d\sigma}{d\Omega}\right)_{el} 2A_o I_o L_{el} \Delta\Omega \qquad \text{II-2}$$

$$= 7.28 \times 10^5/\text{hr}$$

In these two equations $L = L_{el}$. Thus $\sim 3 \times 10^6$ p-p elastic events occurred for every ppγ event. In the experiment the beam intensity was limited to 4 na because of random events, and the ppγ event rate was about 1/hr. This is typical of almost all ppγ experiments performed to date. Geometrical factors of order unity have been neglected in these order of magnitude calculations.

II.1.2 Background Problems

The random coincidence rates are determined by the single particle fluxes in the counters and coincidence resolving time.

$$R = 2\tau n_L n_R \qquad \text{II-3}$$

The coincidence resolving time used in the Warner experiment was 35 ns.* The random rate then becomes R = 165/hr at 4 na or about 160 times that for ppγ events. All random coincidences between elastically scattered protons can, in principle, be distinguished from ppγ events on the basis of the

* Determined by the separation between cyclotron beam bursts. Resolution times smaller than the pulse width (~1 ns) were not attainable.

proton energies. However, not all the protons are detected with pulse heights corresponding to their incident energy. Some of them undergo nuclear reactions while stopping and have abnormally small pulse heights. Coincidences between two such protons yield random background in the ppγ region. Presence of slits near the beam can also result in significant numbers of low energy protons entering the detectors. It would not be surprising to find that the total low energy proton flux due to slit-scattering, was 10% or more of the p-p elastic singles flux - depending on the material from which the slits were made and how close they were to the beam. Some early experiments were probably very seriously limited by random coincidences from this extra source of low energy protons. A true to random ratio of 2 : 1 was observed in the Warner experiment and 10 - 15% of the protons detected had pulse heights in the scintillation counters corresponding to the ppγ energy range.

In order to increase the ppγ data rate it is not sufficient to raise the beam intensity or increase the target size. Rejection of protons which cause random coincidences must be correspondingly improved if the true to random ratio is not to become intolerably small. A number of techniques have been used to reduce random backgrounds in the ppγ region. Elastic protons have been rejected in most of the experiments by using dE/dx counters*. This also prevents neutron-proton coincidences from contributing to the background (neutrons can come from the beam dump for example). Conjugate veto counters[63,66], time of flight[51-53,66,68], veto of long range protons[51-53,71] and "live" slit edges[69] have also been used to reduce random background. Only the latter technique can be used to reduce coincidences between actual low energy protons.

Most types of prompt background have been reduced by careful design of the experimental arrangement. All ppγ experiments make use of the fact that the opening angle between the two protons is $\lesssim 90^{\circ}$ to eliminate most prompt p-p elastic events. Events in which both elastic protons are multiple-scattered into the detectors are eliminated by judicious placement of baffles, and foils are not placed where they can be seen by the detectors. Deuterium is a natural contaminant of H_2 gas ($\sim$150 ppm), but the D(p,2p)n reaction is not a very serious problem. Its low Q-value effectively removes it from the kinematic regions allowed for ppγ except for polar angles near 45°. Other

---

* Ref. 51-53, 61, 62, 66, 67, 69, 71.

contaminants in the target which are a problem (i.e. H_2O, O_2, CO_2 or N_2), can be reduced by using high purity hydrogen. The impurity levels must be kept quite low since (p,2p) reactions may have cross sections as much as 10^3 times larger than ppγ. Cross sections for the reactions $O^{16}(p,2p)N^{15}$ and $N^{14}(p,2p)C^{13}$ have been measured near 45 MeV[78-80] and are $\sim 100\ \mu b/sr^2$. Thus impurities of a few hundred parts per million can prove to be significant. Background from (p,2p) and other reactions on contaminants can easily be 10% or more.

II.2 DESCRIPTION OF THE PRESENT EXPERIMENT

II.2.1 Experimental Apparatus

A two-arm wire chamber spectrometer[47], designed for observation of reactions with three-body final states, was used in the experiment (See Fig. 2 in Sec. III.1.2). The trajectories and energies of the two final state protons were determined in a pair of hodoscopes, each consisting of two wire chambers with magnetic core read-out and a large area scintillation counter. For each event the proton trajectories were projected back to the beam plane in a long gaseous H_2 target and tested for an event vertex. Initial data read-in and reduction, track reconstruction and vertex determination were performed by a PDP-15 computer. Wire chamber coordinates and energy information for "good vertex" events were sent via a high speed data-link to a 360/65 computer, recorded on magnetic tape, and a more complete kinematic and statistical analysis performed.

Use of two computers allowed the reliability of the system to be continuously monitored and on-line feedback from the 360/65 enabled an assessment of the quality of fully analyzed data to be made as it was collected. As a result, saving of all unprocessed data was not necessary and the volume of information that had to be recorded was reduced by a factor of almost 100 during the on-line analysis. However, the volume of data handled was much larger than for conventional experiments and made analysis cumbersome. The chances that there are significant uncorrected systematics are probably reduced.

II.2.2 PPγ Cross Section Normalization

In the experiment, the problem of cross section normalization was not a trivial one. The spark detection efficiency of the wire chambers is a function of their operating conditions and the particle fluxes (i.e. beam intensity) passing through them. Drifts in efficiency might be as large as 5 to 10% during the course of a run. The dead-time of the system is very large because of the time ($\sim$ 20 msec) required to process each event. Again this dead-time correction is dependent on beam intensity and very uncertain. To eliminate these problems, the experimental geometry was designed to observe a small fraction of the p-p elastic events occurring at polar angles of $44.7^\circ \pm 1.0^\circ$ on each side of the beam. The p-p elastic events detected were used to calculate the beam charge that had passed through the scattering chamber, corrected for wire chamber detection inefficiencies and dead-time. Equations II-1 and II-2 are used to eliminate the beam charge. If the photon angular variable, Ψ_γ, is not integrated over, the measured $pp\gamma$ cross sections can be written

$$\frac{d\sigma}{d\Omega_L d\Omega_R d\Psi_\gamma} = C_\epsilon \left.\frac{d\sigma}{d\Omega}\right)_{el} \circ \frac{N_{pp\gamma}}{N_{el}} \circ \frac{L_{el}}{L} \circ \frac{\Delta\Omega}{\Delta\Omega_L \Delta\Omega_R \Delta\Psi_\gamma} \qquad \text{II-4}$$

An additional factor C_ϵ is added to include the effects of geometrical and kinematic biases introduced by the spectrometer. The quantity $d\sigma/d\Omega)_{el}$ has been measured in an auxiliary experiment (See Chapter V).

II.2.3 Comparison to Previous Experiments

The use of wire chambers in this experiment made large solid angles available while retaining good geometric and angular resolution. In addition, the length of gas target was increased by a factor of 5 to 10 over other experiments. Normally this would have resulted in an increase in randoms relative to $pp\gamma$. However, use of wire chambers allowed a large fraction of random events to be rejected because the protons lacked a sufficiently accurate event vertex. This "vertex criterion" for rejection of random events resulted in significant improvement in the prompt to random ratio and was effective for both low energy protons and p-p elastic protons with degraded pulse heights. Overall data rates were as much as a factor of 100 greater than previous experiments, and $pp\gamma$ event rates of 100/hour were routinely achieved.

Unlike any other experiment to date, the limiting factor in the data-taking rates was not determined by the number of random events. In our case, the front wire chambers could not operate properly when charged particle fluxes through them became greater than $\sim 10^5$/sec and the computer analysis time limited the trigger rate to ≤ 100/sec. These considerations limited the maximum beam intensity to about 5 na.

The fundamental differences between this experiment and all others using the Harvard geometry manifest themselves in the required data analysis procedures. A completely new set of problems and systematic errors had to be handled properly. The open geometry and long gaseous target presented problems in the calculation of solid angles, effective target lengths and geometrical corrections. Uncertainties in wire chamber efficiency, beam charge measurement and correction for the large system dead-time during computer analysis necessitated development of a completely different method for cross section normalization. Extraction of the $pp\gamma$ events, which amount to $\sim 0.5\%$ of all data recorded, required careful procedures that are not necessary when most background is rejected by the experimental hardware.

II.3 CROSS SECTIONS AND DETECTION EFFICIENCIES

The equations relating cross sections, detection efficiencies and the number of observed events are developed here for use in the general analysis of the experiment. The reader is referred to Appendix A for definitions of all symbols used.

The observed cross sections must be corrected for the detection efficiency ϵ of the spectrometer. The energy losses in the hodoscopes result in a finite energy cut-off and therefore not all of the Ψ_γ* distributions can be seen in some cases. In addition, the finite size of the wire chambers and vertical distribution of the beam result in a dependence of detection efficiency on the polar and azimuthal angles and on the vertex origin.

The number of $pp\gamma$ events detected by the spectrometer in infinitesimal solid angles ($dN_{pp\gamma}$) is first considered.

$$dN_{pp\gamma} = \frac{d\sigma}{d\Omega_L d\Omega_R d\Psi_\gamma} 2QA_o I_o d\Omega_L d\Omega_R d\Psi_\gamma \; U_1(E_L, E_R) \times$$

$$\int_{Z_o}^{Z_o+L} \int_{Y_{min}}^{Y_{max}} U_o(Z_{min}, Z_{max}) \, F(Y) dY dZ \qquad \text{II-5}$$

---

* See Appendix B for a definition of Ψ_γ.

Where

$$U_1 = \begin{cases} 0 & E_L \leq E_{Lmin} \text{ or } E_R \leq E_{Rmin} \\ 1 & \text{otherwise} \end{cases} \qquad \text{II-6}$$

$$U_o = \begin{cases} 1 & Z_{min}(Y,\Omega_L,\Omega_R) \leq Z \leq Z_{max}(Y,\Omega_L,\Omega_R) \\ 0 & \text{otherwise} \end{cases} \qquad \text{II-7}$$

F(Y) represents the vertical beam profile such that

$$\int_{Y_{min}}^{Y_{max}} F(Y)dY = 1 \qquad \text{II-8}$$

The limits Z_{min} and Z_{max} are determined by the wire chambers or baffles along the beam direction. U_1 gives the effect of the finite energy cut-offs in the spectrometer. When the integrations over Y and Z are performed

$$dN_{pp\gamma} = \frac{d\sigma}{d\Omega_L d\Omega_R d\psi_\gamma} 2QA_oI_o d\Omega_L d\Omega_R d\psi_\gamma U_1 \ \delta Z \qquad \text{II-9}$$

where δZ is the value of $Z_{max}-Z_{min}$ averaged over the vertical beam distribution. Depending on the values of Ω_L and Ω_R this may or may not be zero.

Assuming that the cross section varies slowly, then for finite, but small solid angles

$$N_{pp\gamma} = \frac{d\sigma}{d\Omega_L d\Omega_R d\Psi_\gamma} 2QA_o I_o \Delta\Omega_L \Delta\Omega_R \left(\int U_1 d\Psi_\gamma \right) \langle \delta z \rangle \qquad \text{II-10}$$

Letting $\int U_1 d\Psi_\gamma = \epsilon_1 \Delta\Psi_\gamma$ and $\langle \delta z \rangle = \epsilon_o L$, then

$$N_{pp\gamma} = \frac{d\sigma}{d\Omega_L d\Omega_R d\Psi_\gamma} 2QA_o I_o \, L \, \epsilon_o \, \epsilon_1 \Delta\Omega_L \Delta\Omega_R \, \Delta\Psi_\gamma \qquad \text{II-11}$$

The detection efficiency may be considered as the product of two independent terms - one due only to geometrical effects (ϵ_o) and another (ϵ_1) dependent on the kinematic parameters of the particular event. The quantity ϵ_o is essentially the probability of the particle trajectories being detected in the wire chambers, while ϵ_1 is to a first approximation, the probability of the event having the correct energies to cause a wire chamber trigger. The latter also contains the effects of angular and energy resolutions. The magnitude of the correction ϵ_1 is most significant when some of the events for a given pair of polar angles lie below the spectrometer energy thresholds. Corrections for ϵ_1 depend on the ppγ cross sections themselves and for our purposes must be evaluated using theoretical predictions. On the other hand, the correction for ϵ_o can be calculated to any required degree of precision from geometrical considerations only. In practice both ϵ_1 and ϵ_o are evaluated using Monte Carlo techniques because of the great difficulty in obtaining analytic solutions. This is discussed in detail in Chapter IV.

In $pp\gamma$, it is the event non-coplanarity that has physical significance and not the azimuthal angles themselves. Therefore, instead of the variables ϕ_L and ϕ_R we use ϕ_L and $\Delta\phi$* and express all quantities as functions of the relative non-coplanarity $\Phi_r = |\Delta\phi/\Delta\phi_m|$. Rearranging equation II-11, the cross section is obtained.

$$\frac{d\sigma}{d\Omega_L d\Omega_R d\psi_\gamma} = \frac{N_{pp\gamma}(\theta_L \theta_R \Phi_r \psi_\gamma)}{2QA_o I_o L \epsilon_o \epsilon_1 \Delta\Omega_L \Delta\Omega_R \Delta\psi_\gamma} \qquad \text{II-12}$$

The non-coplanarity distribution is obtained by integration over ψ_γ from 0 to 2π.

$$\frac{d\sigma}{d\Omega_L d\Omega_R} = \frac{1}{2QA_o I_o L \Delta\Omega_L \Delta\Omega_R} \int_0^{2\pi} \frac{N_{pp\gamma} d\psi_\gamma}{\epsilon_o \epsilon_1 \Delta\psi_\gamma} \qquad \text{II-13}$$

The integrated cross section is obtained by further integration over the left azimuthal angle and the non-coplanarity.

$$\frac{d\sigma}{d\theta_L d\theta_R} = \frac{\Delta\phi_m \sin\theta_L \sin\theta_R}{QA_o I_o L \Delta\cos\theta_L \Delta\cos\theta_R} \int_0^{\pi} \int_0^{1} \int_0^{2\pi} \frac{N_{pp\gamma} d\phi_L d\Phi_r d\psi_\gamma}{\epsilon_o \epsilon_1 \Delta\phi_L \Delta\Phi_r \Delta\psi_\gamma} \qquad \text{II-14}$$

In performing what shall be referred to as a

---

* $\Delta\phi = \phi_R - \phi_L - \pi$. The maximum value of $\Delta\phi$ allowed by kinematics for $pp\gamma$ events is called $\Delta\phi_m$.

"global" analysis, we make use of ppγ Monte Carlo events generated to conform to the predictions of the Hamada-Johnston potential. All undesired variables are integrated over and distributions and cross sections of certain specific interesting variables observed. No efficiency corrections are required when comparing the generated and measured distributions because all experimental inefficiencies and biases are contained in the generated events by demanding they be detected in both hodoscopes and have the proper energies. This also is discussed in detail in Chapter IV.

CHAPTER III

EXPERIMENTAL DETAILS

III.1 EXPERIMENTAL APPARATUS

III.1.1 Beam Transport System

A variable energy (21 - 45 MeV) proton beam is obtained from the University of Manitoba sector-focused cyclotron. The beam transport system has been carefully designed to eliminate all beam-defining slits from inside the experimental area. This reduces the neutron and gamma background in the experimental environs. A diagram of the system is shown in Fig. 1. A horizontal waist in the beam is produced at the first beam-defining slits S1, using quadrupoles Q1 and Q2. These also produce a vertical waist inside quadrupole Q4. Using quadrupole Q4 and the switching magnet (SW) a horizontal focus is produced at the second pair of slits S2, which define the beam energy. Q3 is not used in this application. Normally each pair of slits is 2 mm wide and 12.5 mm high. Quadrupoles Q5 and Q6 are used to produce a beam profile 40 mm high and 2 mm wide inside the scattering chamber. Steering magnet SM3 is used to keep the beam direction parallel to the symmetry plane of the scattering chamber while SM4 is controlled dynamically by a beam positioning device to prevent lateral beam

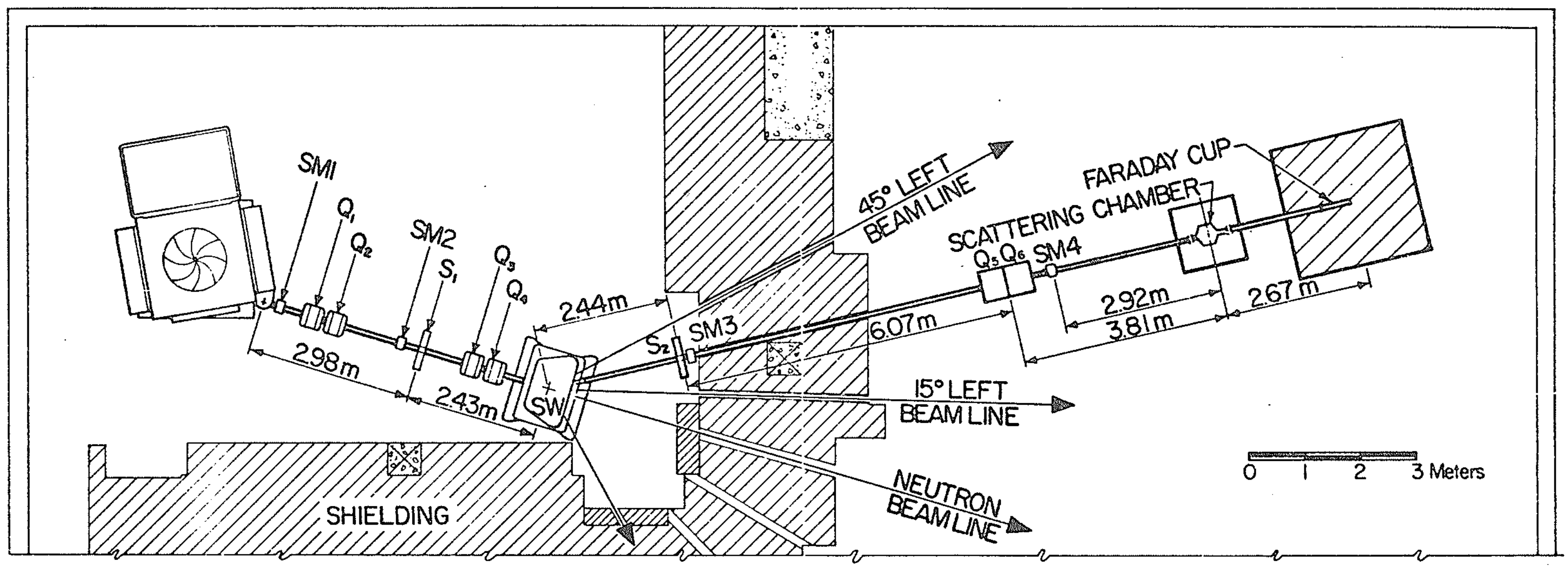

Figure 1

Diagram of the beam transport system as used in the ppγ experiment.

drifts[48]. The proton beam is dumped into a heavily shielded Faraday cup situated 3 metres downstream from the scattering chamber. The relevant beam properties are given in Table 1.

III.1.2 Scattering Chamber and Hodoscopes

A diagram of the hodoscopes and the scattering chamber is shown in Fig. 2. A summary of the important dimensions and properties of the scattering chamber and hodoscopes is contained in Table 2. A more detailed description of the spectrometer is found in J. McKeown's Ph.D. thesis[47]. In each hodoscope there are two wire chambers. Each wire chamber consists of three wire planes. The two outside planes have wires oriented in horizontal and vertical directions and are pulsed to a negative high voltage. The third central plane has wires oriented along a 45^{o} diagonal and serves as a common ground electrode. Use of three planes allows double tracks in each chamber to be resolved and provides some redundancy for the detection of single tracks. Each wire chamber has very thin entrance and exit windows of Mylar foil and is filled with a Ne-He gas mixture. The two chambers in each hodoscope are separated by He gas to reduce multiple-scattering and energy losses of the detected particles. The front chamber is

Table 1

Beam Characteristics in Scattering Chamber

(Double Focus at Center of Scattering Chamber)

Energy	21 - 45 MeV
Energy resolution	$\pm$ 200 keV HWHM
Intensities used	0.01 - 10 na
Multiple scattering in entrance foils and air gap at 42 MeV	$\pm$ 0.25° (r.m.s. projected angle)
Energy loss in entrance foils and air gap at 42 MeV	200 keV
Horizontal waist	$\pm$ 1.0 mm (HWHM)
Horizontal divergence*	$\pm$ 0.3° maximum ($\pm$ 0.1° avg)
Vertical waist	$\pm$ 2 mm (HWHM)
Vertical divergence*	$\pm$ 0.15° maximum
Typical beam profile used for ppγ data	40 mm high by 2 mm wide
Typical ppγ beam intensities	1.0 - 3 na

* Excludes effects of multiple scattering in the Havar foils and air gaps.

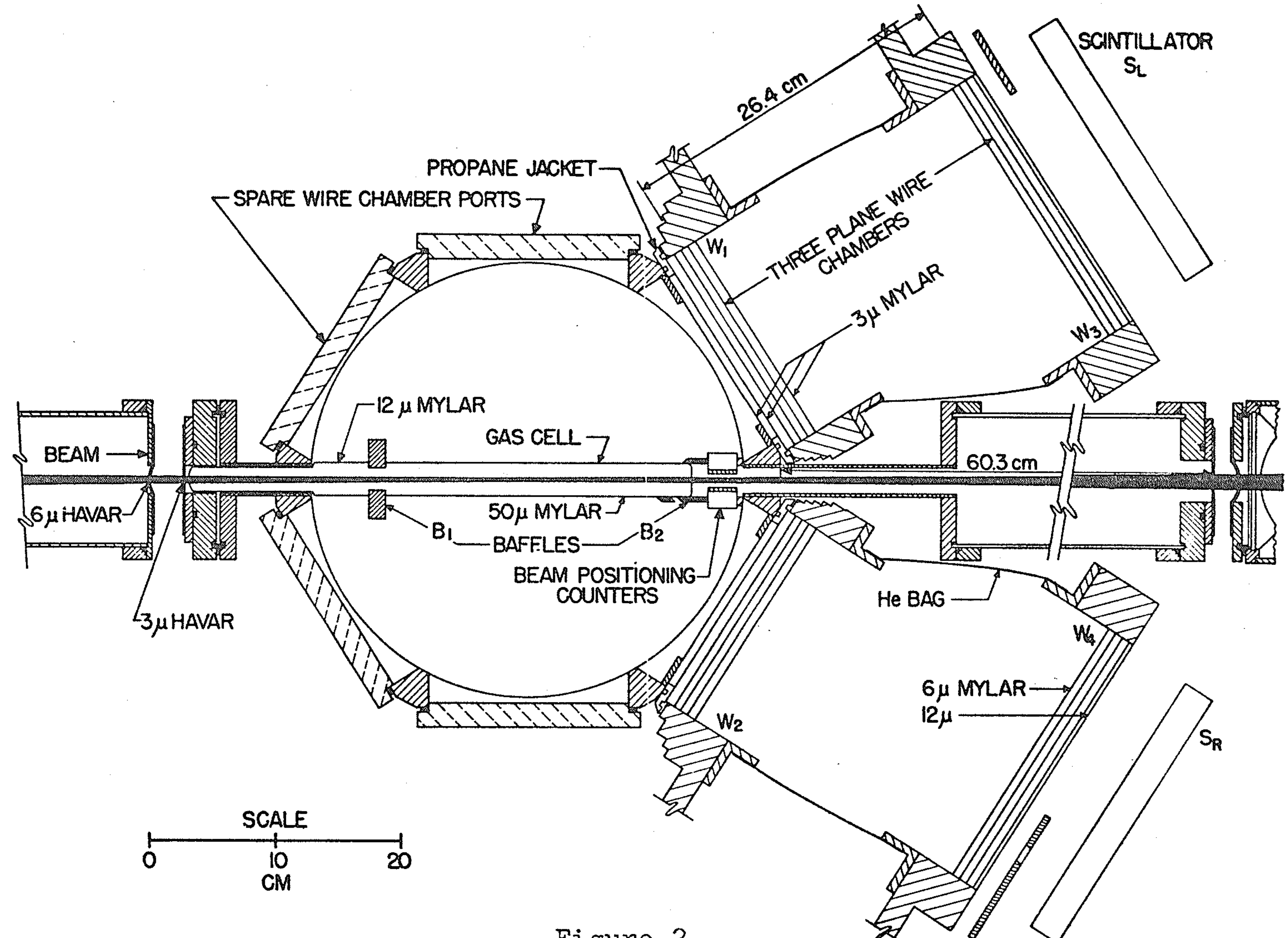

Figure 2

Scale drawing of the spectrometer showing the scattering chamber, wire chambers and scintillation counters. The slit in the baffles at B2 allows p-p elastic events with polar angles of 44.7° to be detected. The baffles at B1 prevent protons, multiple-scattered in the entrance Havar foils, from entering the wire chambers. The scattering chamber can be used with or without the gas cell shown.

Table 2

Dimensions of Scattering Chamber and Hodoscopes

Inside diameter of scattering chamber	-	34.3 cm
Size of entrance port	-	1.75 cm x 9 cm
Size of exit port	-	3.3 cm x 9 cm
Thickness of Havar foils on scattering chamber	-	2.5 µm
Thickness of Havar foils on vacuum lines	-	6 µm
Maximum observed length of gas reaction volume	-	22 cm
Maximum height of beam	-	5 cm
Thickness of Mylar foil parallel to the beam	-	50 µm
Separation of Aluminum baffles (B1)	-	1.8 cm
Separation of BPD counters	-	1.0 - 1.4 cm
Separation of adjacent wires in all wire planes	-	.12 cm
Gap between wire planes	-	0.63 cm
Sensitive area of front wire chambers	-	13.7 cm x 16 cm
Sensitive area of rear wire chambers	-	20.6 cm x 20.6 cm
Solid angle subtended by Hodoscopes Left	-	0.22 sr
at center of scattering chamber Right	-	0.16 sr
Thickness of Mylar windows on front chambers	-	3 µm
Thickness of Mylar windows on rear chambers	-	(6 µm entrance (12 µm exit
Separation between front and rear wire chambers	-	25.1 cm
Maximum polar angle range for geometry shown	-	$14^\circ - 48^\circ$
Maximum azimuthal range	-	$\pm 38^\circ$
Size of large scintillation counters	-	22.5 cm x 22.5 cm x 2.5 cm
Separation between rear chambers and counters	-	7 cm
Separation between B2 baffles (Hevimet baffles)	-	2.5 cm
Size of slit in B2 baffles	-	.285 cm x 5 cm
Size of p-p elastic calibration slit	-	Table 4) Collimator II
Solid angle of p-p elastic calibration slit	-	Table 4)

isolated from the scattering chamber by a partition filled with propane gas. This prevents contamination of the target gas by He and keeps the target gas out of the wire chambers. Large area scintillation counters[49] are placed behind the rear wire chambers and are used to determine particle energies. Each counter is made from a rectangular piece of plastic scintillator* and viewed by two XP1040 phototubes, through lucite light pipes at the top and bottom edges.

The scattering chamber is isolated from the vacuum in the cyclotron and Faraday cup beam lines by 2 cm air gaps. Havar foil is used on the beam entrance and exit ports because it provides the least multiple-scattering for the thickness needed to sustain a one-atmosphere pressure differential. The scattering chamber is normally filled with commercial grade H_2 gas at atmospheric pressure.

The scattering chamber can be used with or without the gas cell shown in Fig. 3. The gas cell has been used with He, N_2, D_2, ultra-high purity ($\lesssim 5$ ppm impurity) H_2 and commercial grade H_2 gases for data-taking and various calibration purposes. The cell contains two moveable target holders and a moveable screen that is used to observe the

---

* NE110 plastic scintillator was used for one detector, and NE102 scintillator for the other.

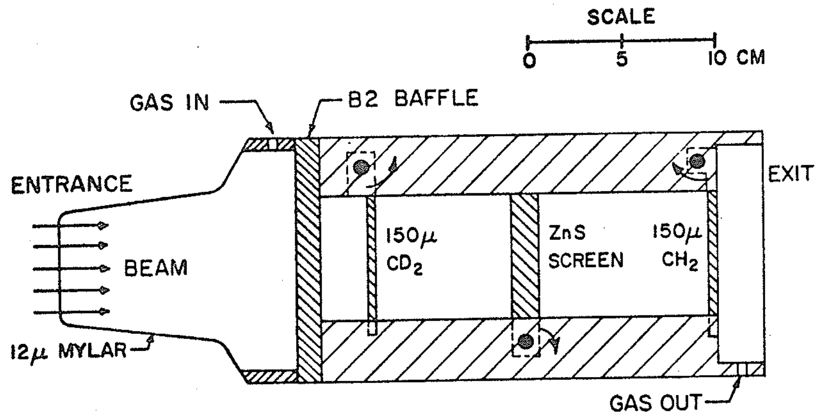

(a) GAS CELL

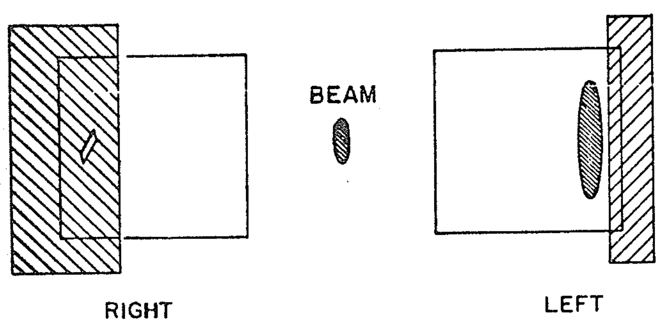

(b) REAR CHAMBERS AND BAFFLES

Figure 3

(a) Diagram of the gas cell used in the experiment. The beam passes from left to right. Two solid targets and a ZnS screen can be moved in and out of the beam as desired. A Ta target was sometimes used in place of the CD_2 target for calibration purposes. The beam enters the gas cell immediately after entering the scattering chamber.

(b) Diagram of the baffles placed behind the rear wire chambers to limit detection of p-p elastic events. The shaded area on the LEFT side shows the usual distribution of 45° p-p elastic events that pass through the small diagonal slit on the RIGHT.

beam profile. The Mylar walls of the gas cell have the auxiliary purpose of preventing δ-rays, created by the proton beam, from entering the front wire chambers. This is discussed in detail in Ref. 47.

The baffles B1 in Fig. 2 do not limit the beam and are used only to prevent protons scattered at the entrance port from entering the front wire chambers. These baffles also provide mechanical support for the gas cell. The downstream baffles B2 are specially designed to allow detection of p-p elastic events with 44.7° angles from a well-defined region of the gas target. The collimators behind the rear chambers (See Fig. 3(b)) are used to reduce the p-p elastic coincidence rates to desired levels. If one proton from a p-p elastic event originating between the baffles B2 passes into the open slit behind the right chamber, then the conjugate proton will be detected in the left hodoscope. If a p-p elastic proton enters the major open area behind the right chamber ($\theta_R \lesssim 40^{\circ}$), then its conjugate particle cannot be detected.

A pair of detectors which monitor the intensity of the proton beam tails and control the position of the beam centroid[48)] are situated between baffles B2 a little further downstream from the p-p elastic region.

III.1.3 Fast Electronics

A schematic of the electronics used in the experiment is shown in Fig. 4. The modules required to trigger the chambers are kept in the experimental area a few feet from the spectrometer to reduce the time delay between event occurrence and the triggering of the wire chambers. Most of the electronics for the slow pulse height digitization is kept in the cyclotron control room.

Information on the particle energies required to trigger the wire chambers is provided by the anode pulses of the phototubes. The two pulses for each counter are added in fast linear mixers (MIXER) and fed into differential discriminators (DIFF DISC) set to accept protons with detected energies in the range

$$7 \text{ MeV} \lesssim E \lesssim 26 \text{ MeV}$$

Logic outputs from the differential discriminators are used as inputs to prompt and random coincidence units (COINC C_P and C_R). The right input into C_R is delayed by the time separation between cyclotron beam bursts.* The 35 ns delay after C_P minimizes the effects of timing differences in the wire chamber triggers on the relative detection efficiency for prompt and random events. Outputs from the coincidence circuits are used to trigger the wire chambers, disable the electronics, initiate the data read-in from the wire chamber

* See footnotes on pages 61 and 63.

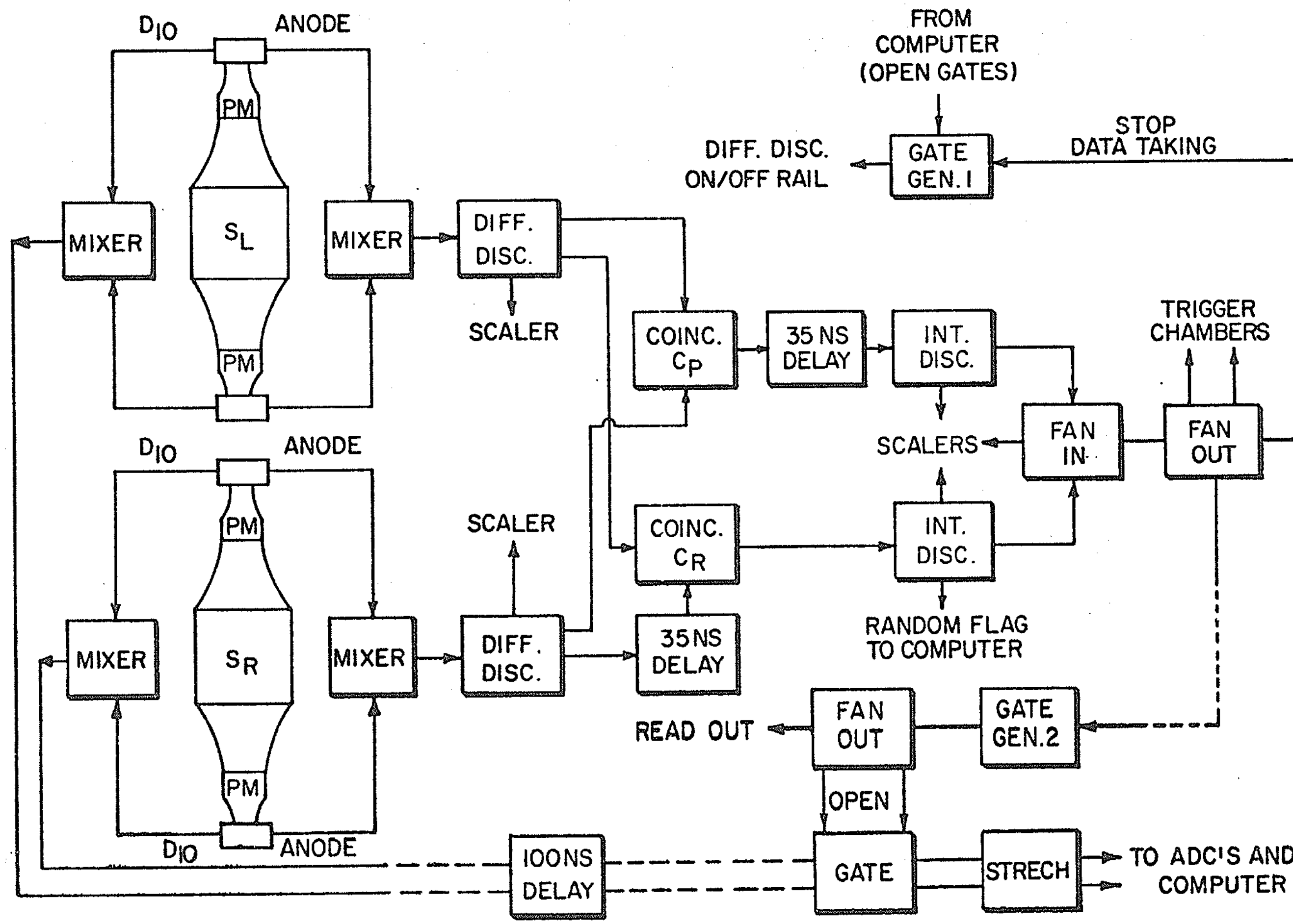

Figure 4

Schematic diagram of the fast electronics used in the ppγ experiment. "L" denotes the LEFT hodoscope and "R" the RIGHT hodoscope. The dashed lines indicate the distance between the experimental area and the cyclotron control room.

memory to the computer, and assist in the slow pulse height analysis in the control room. Outputs for the C_R coincidence unit are also used to label random events (RANFLG).

Analogue information for the accurate energy determination is obtained from dynode 10 of each phototube*. The pulses from each detector are mixed and sent via 80 metres long double-shielded cable to the control room where they are amplified and stretched. The analogue energy information is isolated from the noise generated during the sparking of the wire chambers, using a gate (GATE GEN.2) started by the pulse that triggers the wire chambers. Outputs from the stretchers are digitized by Northern Scientific ADC's and read in by the PDP-15 computer.

III.1.4 Computer Hardware

The two-computer system as used on-line to the wire chamber spectrometer[41,45] is shown in Fig. 5. A PDP-15/20 manufactured by the Digital Equipment Corporation (DEC) with some additional peripheral equipment is dedicated to the experiment. The PDP-15 is an 18 bit computer with 0.8 μsec. cycle time. The model 20 has the following configuration: 8K words of core memory, heavy duty KSR-35 console Teletype, 300 cps paper tape reader, 50 cps paper tape punch, extended arithmetic element (EAE) and dual small

* Dynode 11 was used in the latter stages of the experiment.

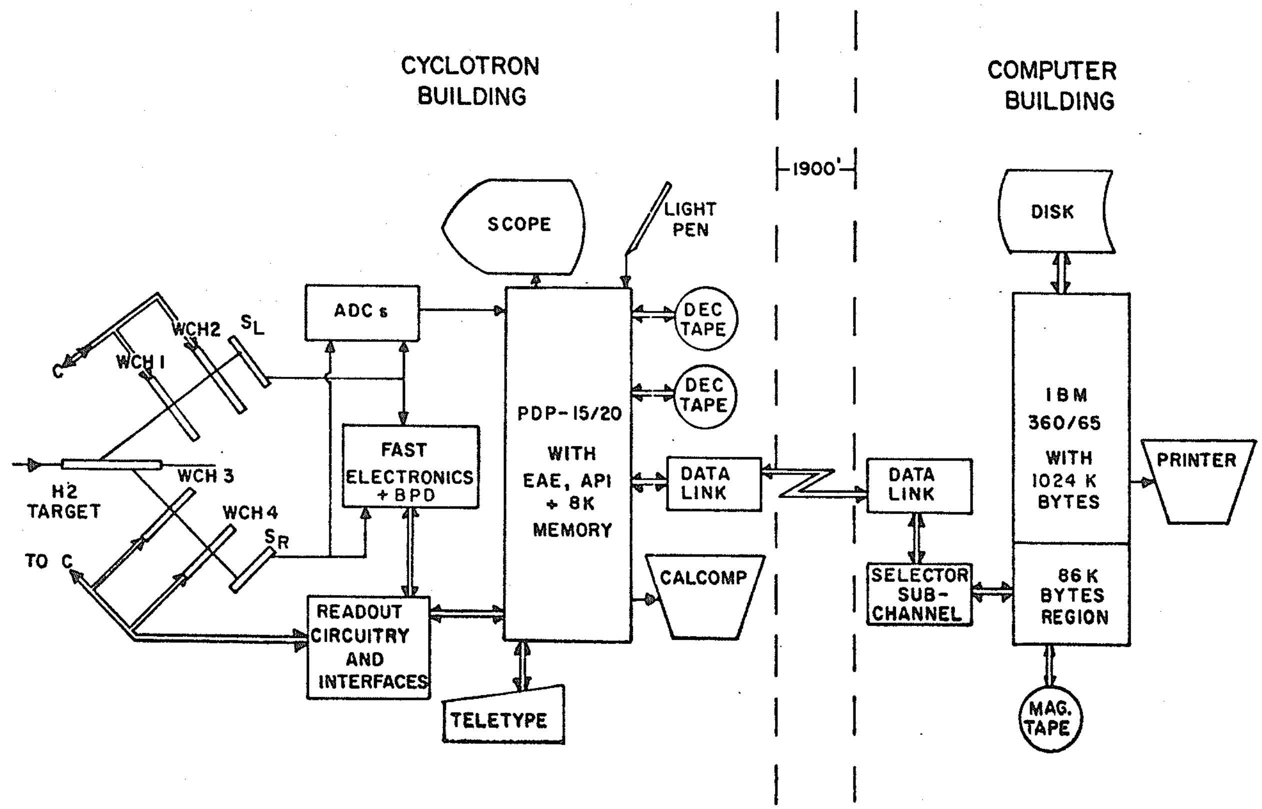

Figure 5

The two-computer system as used on-line to the wire chamber spectrometer during the ppγ experiment.

magnetic tape transports and controllers. The additional peripheral equipment used by the PDP-15 are a high speed data link to an IBM 360/65 computer, real time (60 cycle) clock, automatic priority interrupt (API), X-Y oscilloscope display and control with light pen, interface to a pair of analog to digital converters and an incremental plotter. Two sets of equipment used with the wire chamber spectrometer, which have been built at the Cyclotron laboratory, are a wire chamber (i.e. ferrite core read-out) interface[50] and three 10 MHz scalers and power supply control for the beam positioning device[48].

The second computer is an IBM System 360 Model 65 used as a general purpose batch processing facility. Features and peripherals that are of interest to the wire chamber spectrometer include 1M bytes of memory, 9-track and 7-track magnetic tape drives, line printers, card reader, 2311 and 2314 random access disc units and a selector sub-channel attached to the data link. On-line programs generally use about 80K - 90K bytes of 360/65 memory.

III.2 SPECTROMETER PROPERTIES

III.2.1 Geometrical Alignment

The scattering chamber and wire chambers rest on a 122 cm square Al plate 2.5 cm thick. The center line and lines making angles of $44.7^\circ \pm 0.1^\circ$ with it, have been scored on the plate to serve as references. The symmetry plane of the scattering chamber coincides with the center line of the support plate within $\pm$ 0.2 mm and the scattering chamber has been rigidly attached to the plate. Standard optical surveying instruments have been used to position the symmetry plane of the scattering chamber parallel to the desired beam path to an accuracy better than $\pm 0.05^\circ$. The reproducibility of positioning the transit over the permanent reference point on the beam line is estimated to be 0.5 mm. After the initial placement of the scattering chamber no systematic displacement in its symmetry plane has been observed.

The second reference point on the beam line is at the center of the switching magnet and is accurate to $\pm$ 0.05 mm. Using the transit, the center of the beam defining slits has been made collinear with the center of the switching magnet and the symmetry axis of the chamber to $\pm$ 0.25 mm. The error in the beam direction due to misalignment of the slits is less than $\pm 0.1^\circ$.

The front wire chambers are rigidly attached to two of the six faces of the scattering chamber. The angles that the normals to these faces (and thus the wire chambers) make with the beam direction, have been measured to be $32.25^{o} \pm 0.10^{o}$.

The wire chamber positions have been calibrated by detection of p-p elastic events at 44.7^{o} in the laboratory using the reference lines on the supporting plate. A 3 mm diameter collimator was positioned above this line at a height corresponding to the expected center of the beam. A 2 mm by 2 mm spot beam, tuned to the desired horizontal and vertical position to better than $\pm$ 0.5 mm in each direction by visual observation on a screen, was used. The analysis procedures for calculation of the required coordinate constants are described in Ref. 47. The maximum errors introduced in the polar and azimuthal angles were estimated to be $\pm 0.13^{o}$ and $\pm 0.19^{o}$ respectively.

III.2.2 Beam Position

The effect that lateral beam displacements has on the horizontal vertex errors is discussed in Sec. III.2.9.

In order to ensure that the beam did not wander from its desired position in the scattering chamber, a beam positioning device[48)] was constructed. The ratios of the proton fluxes in the beam tails were monitored and the beam steered to the left or right by modifying the current in a steering magnet upstream of the scattering chamber. Lateral drifts in the beam centroid were reduced to less than $\pm$ 0.1 mm when the beam positioning device (BPD) was used[48].

For technical reasons the BPD was not always available. In this case extra care was taken with regard to beam handling. The beam direction and position were checked frequently during the course of a data run, by visual observation. The uncertainty in the beam position under these conditions was estimated to be $\pm$ 0.5 mm.

III.2.3 Geometrical Ranges

The hodoscopes subtend large solid angles and can see up to 22 cm of the gas target. The actual angular ranges observed depend on the origin of the particles in the reaction volume. In addition, the polar (θ) and azimuthal (ϕ) ranges are not independent. In Fig. 6 the polar angle ranges are presented as a function of the particle origin for particles that lie in the horizontal plane of symmetry of the hodoscopes ($\phi_L = 0^o$ and $\phi_R = 180^o$). The upper limit seen in the right hodoscope is smaller than for the left because of the baffles and collimators needed for the detection of the p-p elastic events (See Fig. 2 and Fig. 3(b)).

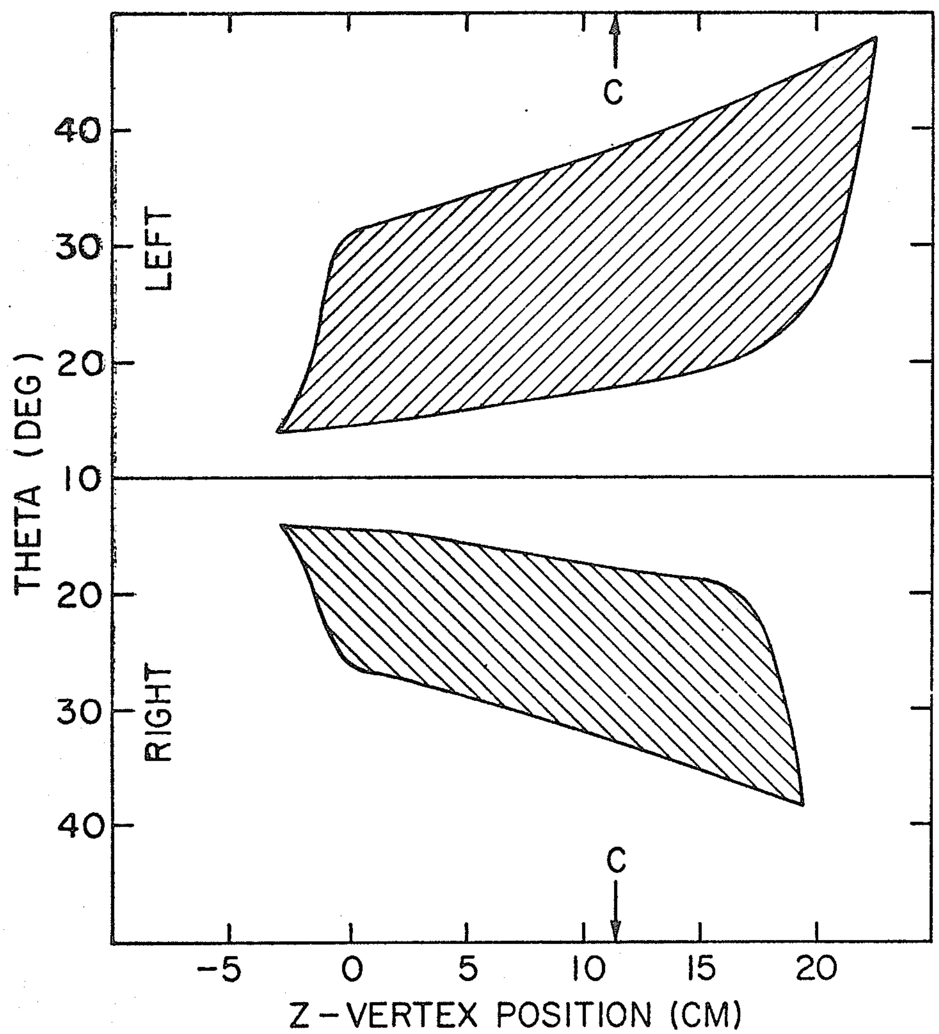

Figure 6

Diagram showing the polar angle acceptance (shaded area) of the hodoscopes as a function of the vertex position along the beam direction. The particles are assumed to lie in the median plane of the spectrometer. The point C corresponds to the geometrical center of the scattering chamber. Note the polar angle scale does not go to zero.

The azimuthal angle ranges and the distribution of detected events along the beam direction have been investigated using a Monte Carlo procedure. Simulated particle trajectories, with uncorrelated directions but a common vertex origin, were generated with random vertex position and uniform density per solid angle. These trajectories were then tested to see if they were detected in the hodoscopes. Histograms of the azimuthal angles and vertex positions of detected events were made. A typical ϕ distribution for $20^\circ \leqslant \theta \leqslant 24^\circ$ is shown in Fig. 7(a). The distribution is not uniform because of the integration over the target length. The slight enhancement at $\phi \approx 15^\circ$ and the depression near $\phi \approx 0^\circ$ occur because of the rectangular shape of the wire chambers. The corresponding distribution of events along the beam direction is shown in Fig. 7(b). The nearly linear rise in the central region is due to the increase in azimuthal range as the event origin gets closer to the wire chambers.

The non-uniform distributions make it very difficult to calculate solid angles and target lengths. In addition, the polar (θ), azimuthal (ϕ) and target (Z) ranges are not independent. Thus these distributions give only semi-quantitative information about the spectrometer

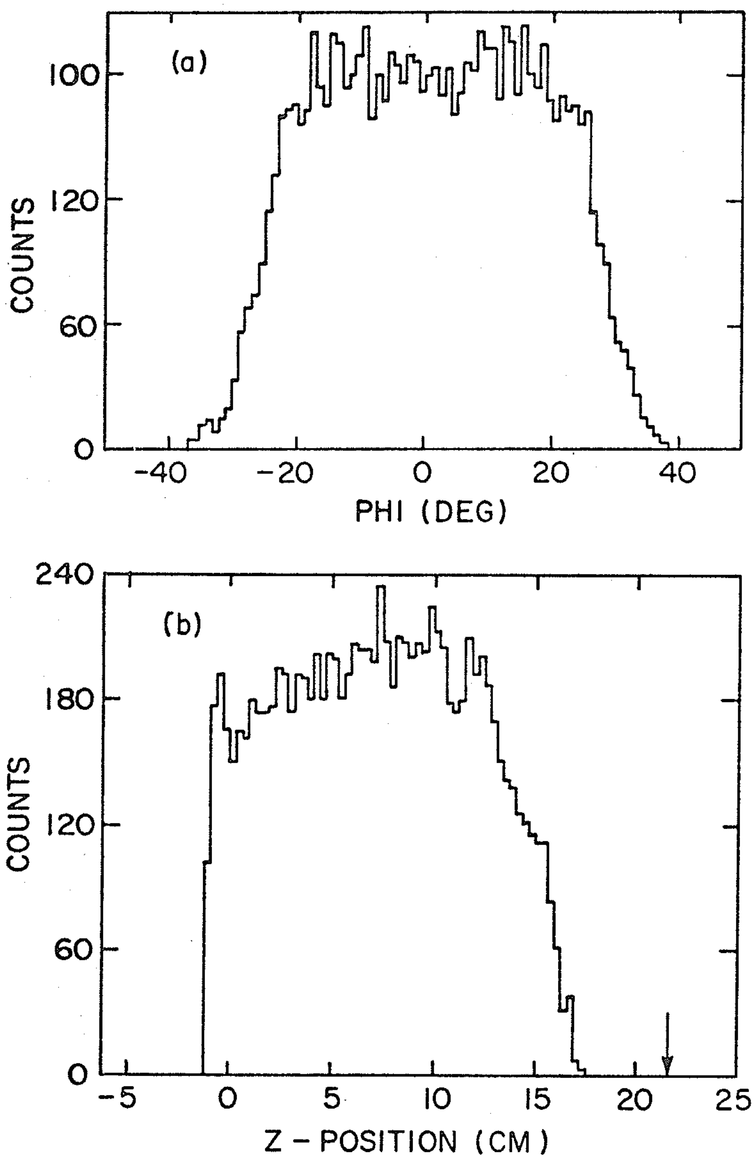

Figure 7

(a) Typical azimuthal angle distribution in one of the hodoscopes showing a relatively flat central region and a steep fall-off.

(b) Typical distribution of events along the beam direction. The cut-off at a Z-position of ~-1 cm is due to the B1 baffles. The arrow indicates the region between the B2 baffles where the calibration p-p elastic events originate.

ranges. If the effective azimuthal angle (Φ_{eff}) is defined as the HWHM of the Φ distributions generated by detected trajectories, then the dependence of Φ_{eff} on the polar angles as shown in Fig. 8 is obtained. The points are evaluated for detected trajectories with polar angles equal within $\pm$ 4^{o} and are integrated over vertex positions along the beam. The error bars in Fig. 8 correspond only to statistical uncertainties in determining the maximum of the distributions and the angles at half the maximum value.

III.2.4 Angular Resolutions

The azimuthal and polar angle resolutions have been measured by observing p-p elastic scattering events at 42 and 24 MeV incident beam energies. Measurements of the sum of the polar angles and the event non-coplanarity yield the desired resolutions under the assumption that the effects of each hodoscope are the same and add in quadrature. The histograms obtained are shown in Fig. 9(a & b). The measurements of the sum of the polar angles and the non-coplanarity do not include the effects of small misalignments of the scattering chamber or beam divergence. These errors are summarized in Table 3 along with the measured resolutions.

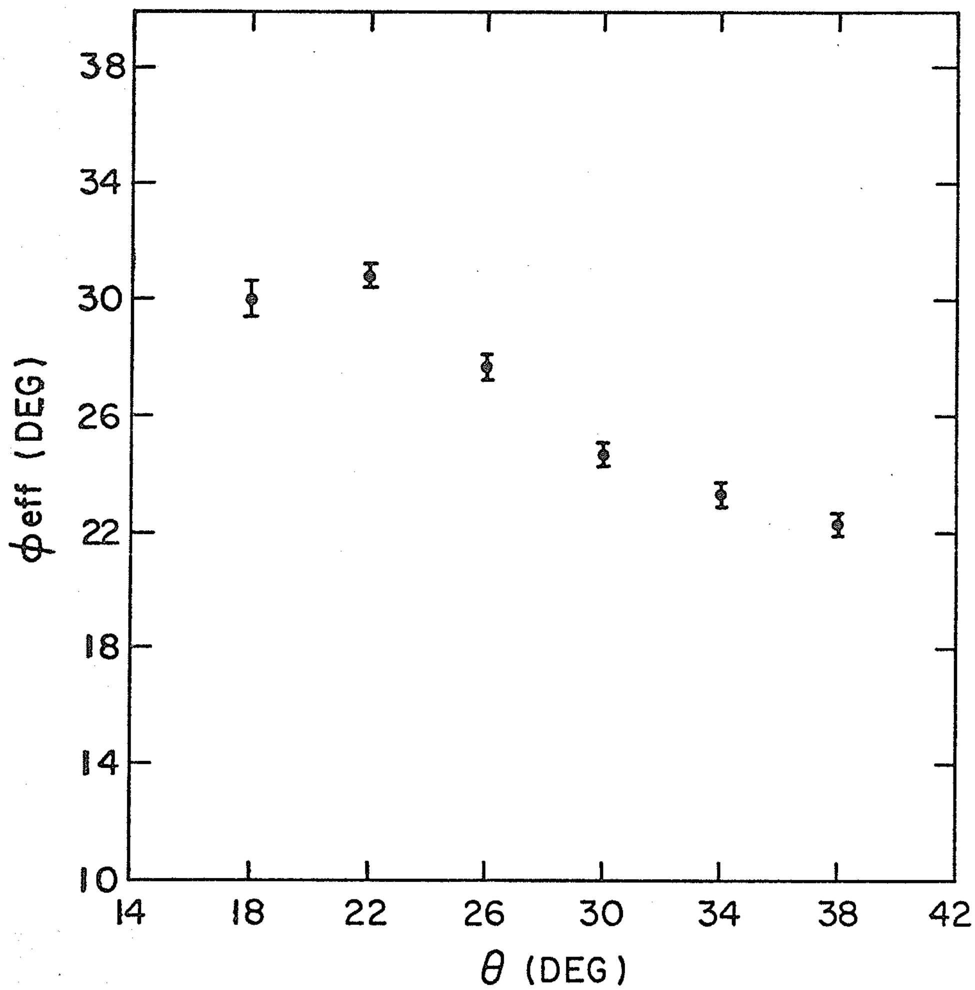

Figure 8

Variation of the effective azimuthal angle, ϕ_{eff}, as a function of the polar angle. ϕ_{eff} is defined as the HWHM of distributions similar to Fig. 7(a). The error bars represent statistical uncertainties only.

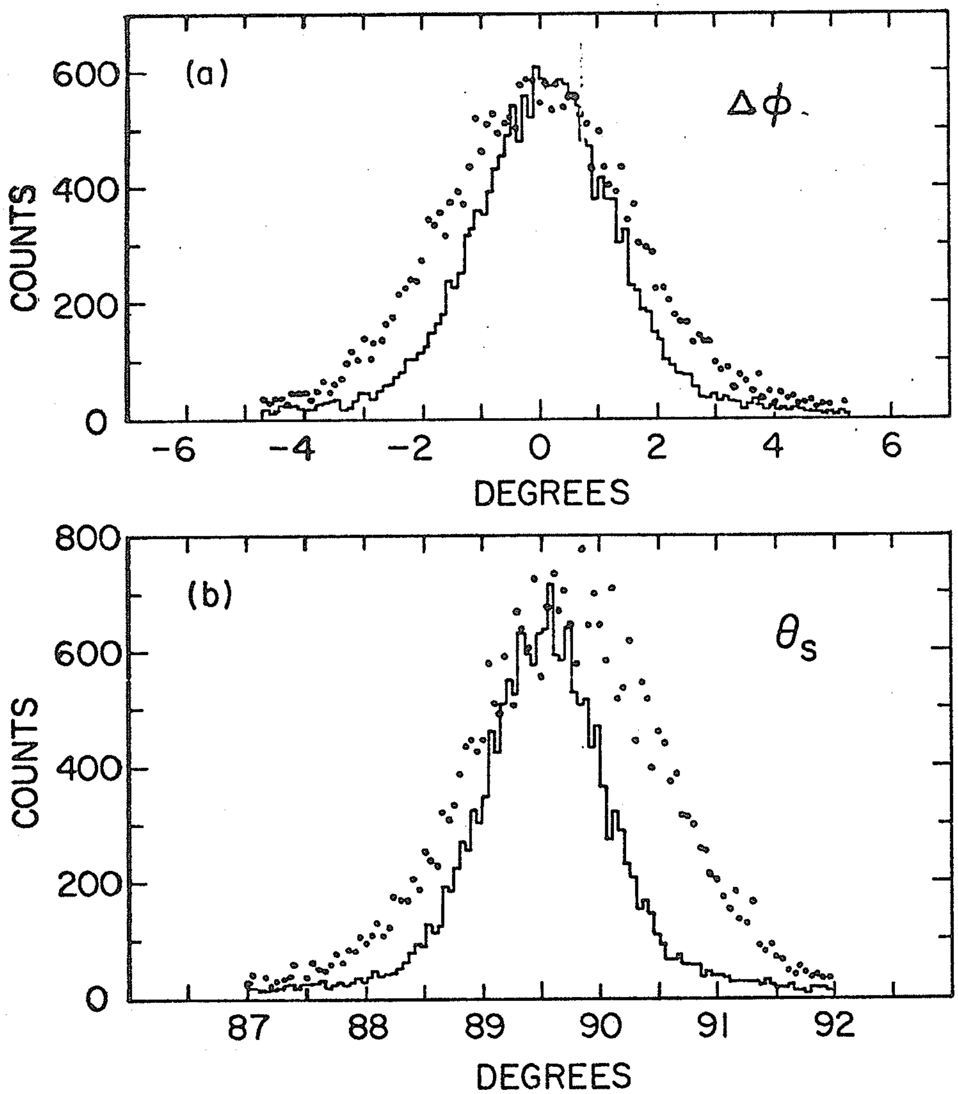

Figure 9

(a) Distribution of p-p elastic events as a function of the measured non-coplanarity $\Delta\phi = \phi_R - \phi_L - \pi$. The bar histogram is for 42 MeV incident beam energy and the dots for 24 MeV incident beam energy. The measured HWHM's were 1.25° and 1.90° respectively.

(b) Distribution of p-p elastic events as a function of the sum of the polar angles. The measured values for 42 MeV (bar histogram) and 24 MeV (dotted histogram) incident beam energies were 89.50°±0.64° HWHM and 89.75°±0.96° HWHM respectively.

Table 3

Summary of Angular Resolutions

Errors Quoted Are Standard Deviations

Estimated θ resolution at 42 MeV	-	$\pm 0.44^\circ$
Estimated θ resolution at 24 MeV	-	$\pm 0.68^\circ$
Horizontal beam divergence (estimated r.m.s.)	-	$\pm 0.1^\circ$
R.M.S. multiple scattering of beam at 42 MeV	-	$\pm 0.25^\circ$
Measured $\theta_s/\sqrt{2}$ resolution at 42 MeV*	-	$\pm 0.39^\circ$
Measured $\theta_s/\sqrt{2}$ resolution at 24 MeV*	-	$\pm 0.58^\circ$
Vertical beam divergence	-	$\pm 0.15^\circ$
Measured $\Delta\phi/\sqrt{2}$ resolution at 42 MeV*	-	$\pm 0.75^\circ$
Measured $\Delta\phi/\sqrt{2}$ resolution at 24 MeV*	-	$\pm 1.15^\circ$
Angle of wire chambers with the beam direction	-	$57.75^\circ \pm 0.10^\circ$
Absolute error in scattering chamber alignment	-	$\pm 0.05^\circ$
Absolute error in orientation of wire chambers	-	$\pm 0.05^\circ$
Maximum ϕ error due to errors in program constants**	-	$\pm 0.19^\circ$
Maximum θ error due to errors in program constants**	-	$\pm 0.13^\circ$

* Measured for p-p elastic protons at 44.7° polar angles in the laboratory.

** For $\phi = 0^\circ$ or 180° and $\theta = 32.25^\circ$. The errors decrease for angles different from these (See Ref. 47).

The angular resolutions are dominated by the 50 μm Mylar foils parallel to the beam. With the foils in position, the polar angle resolution for 21 MeV protons with polar angles of 45° deteriorates to $\pm 0.39^{\circ}$ from $\pm 0.30^{\circ}$.* The effect of the Mylar foils is even more dominant for polar angles smaller than 45°. The following functional dependences for the polar and azimuthal angular resolutions have been derived in Appendix C.

$$(\delta\theta)^2 = p(\theta,E)\, q(\theta,E) \qquad \text{III-1}$$

$$(\delta\phi)^2 = k^2 q(\theta,E)\, \csc^2\theta \qquad \text{III-2}$$

$$p(\theta) = \frac{4}{3}\cos^2\theta\,(1 + \sin^2\theta\,\tan^2\theta) \qquad \text{III-3}$$

$$q(\theta,E) = 0.23^{\circ 2} + \frac{0.19^{\circ 2}}{E_r^2} + \frac{0.25^{\circ 2}}{E_r^2}\,\frac{1}{\sqrt{2}\,\sin\theta} \qquad \text{III-4}$$

E_r is the proton energy relative to 21 MeV (i.e. $E_r = E(\text{MeV})/21$). The constant k is obtained from the ratio of the observed $\Delta\phi$ and θ_s resolutions and is equal to $\sim\sqrt{2}$ (See Table 3).

Using the functional dependence stated in equations III-1 to III-4, the angular resolutions for various ppγ cases have been calculated. The kinematics of

---

* All resolutions are standard deviations unless otherwise stated.

$pp\gamma$ events are discussed in Appendix B. It suffices here to note that for every pair of proton polar angles there is a maximum value for the non-coplanarity of the protons (defined by $\Delta\phi = \phi_R - \phi_L - \pi$). This maximum non-coplanarity is labelled $\Delta\phi_m$. This limiting kinematic condition also has a unique pair of proton energies associated with it. The relative non-coplanarity Φ_r is defined as the ratio of the observed $\Delta\phi$ to the maximum allowed by kinematics (i.e. $\Phi_r = |\Delta\phi/\Delta\phi_m|$).

Fig. 10 shows the polar angle resolution ($\delta\theta$), $\Delta\phi$ non-coplanarity resolution ($\delta\phi_D$) and the relative non-coplanarity resolution ($\delta\phi_D/\Delta\phi_m = \delta\Phi_r$) for $pp\gamma$ events where $\theta_L = \theta_R$. The proton energies used were those for the limiting kinematic point as this corresponds approximately to the average case.

III.2.5 Pulse Height Calibration

The photomultiplier voltages on the scintillation detectors were set with the aim of providing the lowest possible energy thresholds consistent with reasonably good linearity over the energy region of interest. The photomultiplier voltages used during $pp\gamma$ data-taking resulted in a linear pulse-height-energy response up to 37-38 MeV. This response was calibrated by observation of

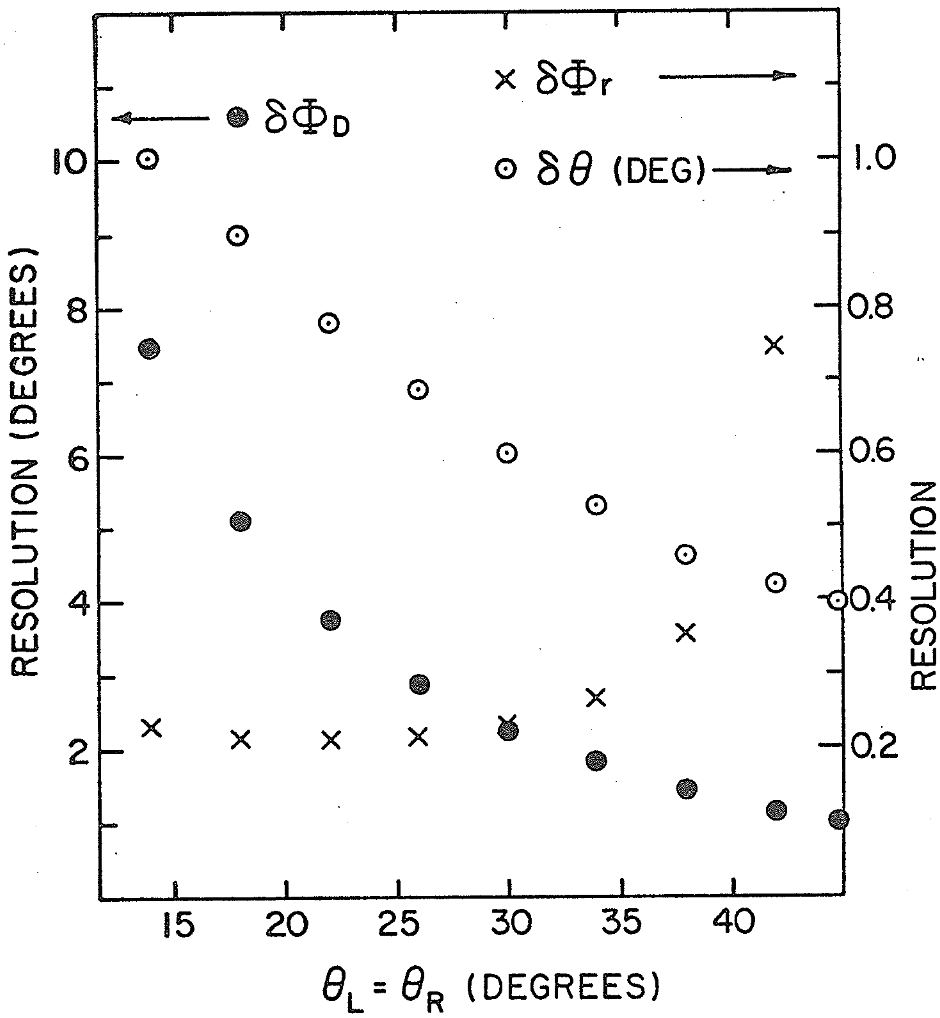

Figure 10

Angular resolutions in the polar angles ($\delta\theta$), azimuthal event non-coplanarity ($\Delta\Phi_D$) and relative non-coplanarity ($\delta\Phi_r = \delta\Phi_D/\Delta\Phi_m$) for symmetric pp$\gamma$ events at 42 MeV incident beam energy. $\delta\Phi_r$ diverges as $\theta_L=\theta_R \rightarrow 44.7°$ (p-p elastic case). The points all represent standard deviations.

45° p-p elastic events at a number of incident beam energies ranging from 42 MeV down to 23 MeV.

At the time that the prompt background measurements were made, the photomultiplier voltages were raised somewhat. As a result some non-linearity of the pulse heights appeared at about 20 MeV. The maximum deviation from linearity at the calibration p-p elastic energy of 21 MeV was about 2%. To investigate this non-linearity, p-p elastic scattering over the range of polar angles from 16° to 45° has been observed at three different incident beam energies--42, 31 and 23 MeV. Because of the dependence of the scattered energy on polar angle, this yields a curve of energy versus pulse height that is continuous between detected energies of 7 MeV to 38 MeV.* One of these curves is shown in Fig. 11.

During actual data-taking, p-p elastic events at 45° were monitored for the purpose of cross section normalization. They also provided a set of events with a well defined pulse height value. These events were used to monitor drifts in the photomultiplier gains during data runs and the energy calibration constants were updated about every five minutes.

---

* The curve in Fig. 11 is obtained using a program written by T. Millar. This program is also used to calibrate the dependence of pulse heights on the position where particles hit the large area detectors. (See Sec. III.2.6)

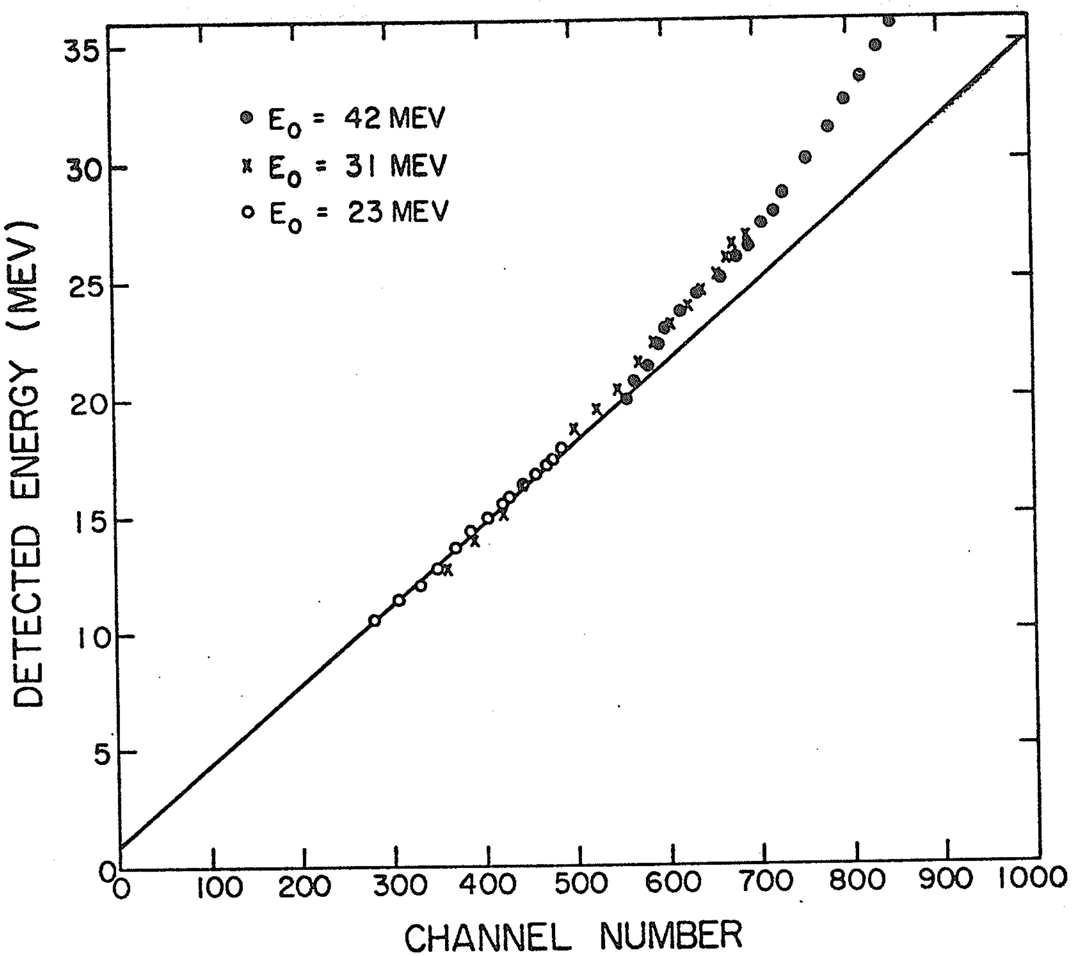

Figure 11

PHT-energy response curve for one of the scintillation counters as used during ppγ background investigations. The non-linearity becomes evident near 18 MeV detected energy. The PHT-energy response during ppγ data collection was linear up to ~37 MeV detected energy. The curve is obtained from p-p elastic scattering by using the correlation between angles and energies.

III.2.6 Energy Losses and Resolutions

The energy losses of particles in the hodoscopes are not negligible. In fact, protons with energies less than 5.8 MeV cannot be detected. The particle energies are therefore corrected for these losses before any kinematic and statistical analyses are made. Fig. 12(a) shows the energy loss for protons, calculated using the Bethe-Bloch formula.

The additional energy loss for particles hitting the tungsten wires in the front chambers is significant. However, there is no completely reliable way to isolate these events and treat them differently in the data analysis.

In the spectrometer, large area plastic scintillation detectors are used. The inherent resolution of these detectors is poor since the pulse height response is dependent on the position where the particle enters the scintillator. The energy resolution obtained is improved in the data analysis by compensating for the non-uniformity of the pulse heights on an event by event basis. This procedure is described in detail in references 43, 49 and 50.

The energy resolution of the hodoscopes has been determined by observation of p-p elastic events at 42 and 24 MeV incident beam energy and by observation of the $N^{14}(p,2p)C^{13}$ and $He^{4}(p,2p)T^{3}$ reactions at 42 MeV. For the

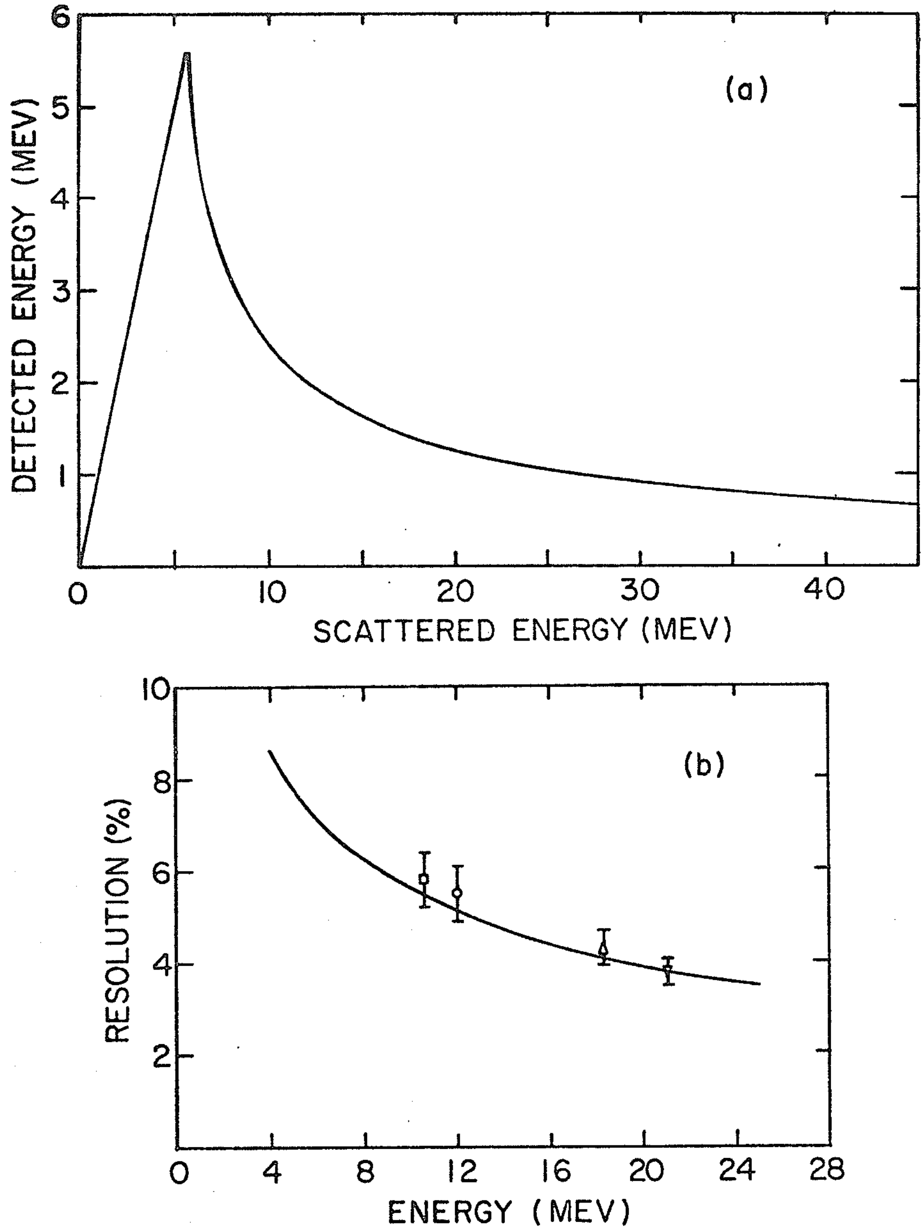

Figure 12

(a) Energy lost by protons in the hodoscopes as a function of the initial energy. Protons with energies less than 5.8 MeV are stopped in the hodoscope.

(b) Energy resolution of the detected protons as a function of the detected energy. The points were determined by observation of the missing energy for 42 MeV p-p elastic events (▽), 24 MeV p-p elastic events (○), $N^{14}(p,2p)C^{13}$ with Q=-7.54 MeV (△) and $He^{4}(p,2p)T^{3}$ with Q=-19.86 MeV (□).

(p,2p) reactions the energy carried away by the residual nucleus is negligible compared to the proton energies. The sum of the proton energies has a well-defined value depending on the Q-value for the reaction. Events with proton energies equal within $\pm$ 3 MeV have been selected and histograms of the missing energy obtained. Assuming that the two proton resolutions add in quadrature, the single particle resolutions can be estimated from the resolution in the missing energy and are shown in Fig. 12(b). Agreement with the expected $1/\sqrt{E}$ ($\Delta E/E = 0.17/\sqrt{E}$) dependence is fair.

III.2.7 <u>Energy Thresholds</u>

The discriminator thresholds used for the fast pulse height analysis do not translate into well-defined energy cut-offs, and care must be taken not to bias events of interest. If we wish to detect all events with energies between certain values, the $\pm$ 10% variation due to pulse height response must be allowed for.

The low energy thresholds were relatively high because of the voltages chosen for the photomultipliers. The differential discriminators used in the trigger electronics required minimum pulse heights in the range 60 - 80 mv (depending on the adjustments of the particular module). This corresponded to 6 - 7 MeV of energy (E_D)

deposited in the counter. When consideration of pulse height non-uniformities and energy resolution ($\Delta E = 0.17\sqrt{E_D}$) were taken into account, protons with scattered energies $\geq$9.5 MeV were detected with full efficiency.

In later measurements of the prompt backgrounds, the low energy thresholds were reduced. The lower levels of the triggering discriminators passed events which deposited $\geq$3 MeV of energy in each of the detectors. This corresponded to scattered energies of about 6.6 MeV, implying that the system detected 7.5 MeV particles with full efficiency.

The upper energy cut-offs were determined by the ΔE settings of the trigger discriminators. Calibration of these cut-offs was done by comparing singles spectra from the detectors taken with no upper cut-offs and with the cut-offs applied. An example is given in Fig. 13. The effect of the upper cut-off is very clear. The upper energy thresholds chosen corresponded to detected particle energies of 24 MeV. Thus, after including the effects of PHT non-uniformities, particle energies $\leq$ 21 MeV were detected with 100% efficiency and energies up to 22-23 MeV with close to 100% efficiency. The detection efficiency decreased smoothly to 0 over the range from 21 MeV to 27 MeV. Occasionally, due to photomultiplier drifts, some calibration

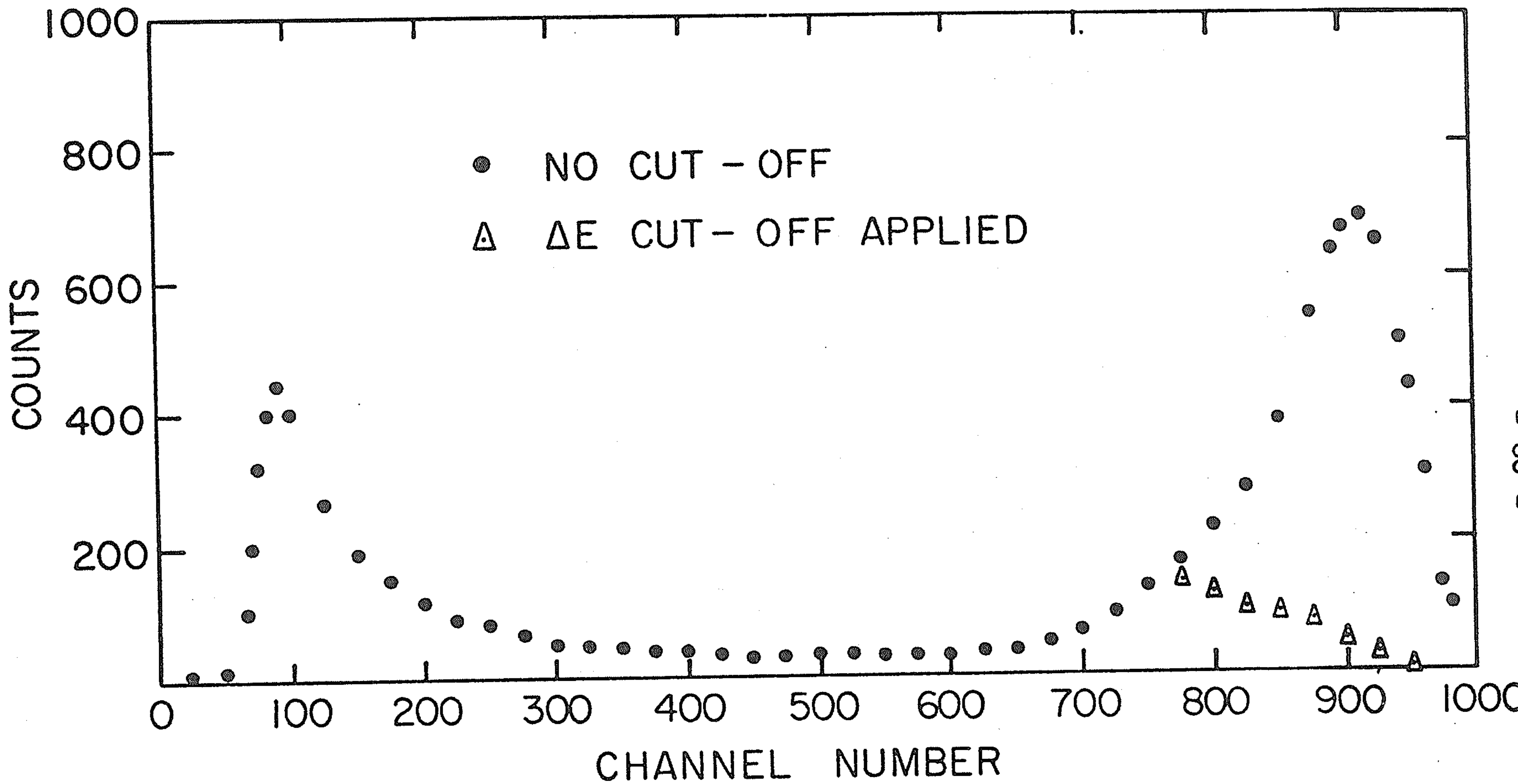

Figure 13

Typical pulse height spectrum of particles detected in the scintillators with and without the upper level ΔE cut-offs applied. The slow cut-off arises from pulse-height non-uniformity in the scintillation counters, time jitter in summing the photomultiplier outputs and heavy saturation of the anode pulses.

elastic protons with 21 MeV energies were rejected. This amounted to ~4% of these events in all ppγ data runs.

The value of the upper threshold is critically dependent on the calibration of the scintillation counters and the proper matching of the two photomultipliers for each detector. Only drifts in the photomultiplier gains $\lesssim$ 10% were tolerated and data-taking was halted by the 360 computer if drifts greater than this occurred. While taking data, the E and ΔE levels were routinely checked for drifts at least once every 24 hours.

III.2.8 Coincidence Circuit Efficiency

To ensure that all ppγ events between the energy thresholds were detected, it was necessary to obtain a delay curve for coincidence circuits C_P and C_R in Fig. 4.* This was done using a 42 MeV beam and a CD_2 target and observing protons separated by as much as two beam bursts. The prompt D(p,2p)n events had an asymmetry of energies (and therefore transit times in the hodoscopes) that corresponded to the worst cases for ppγ. The results of the delay curve measurements are shown in Fig. 14.

To obtain this curve, delays were added between the MIXER's and DIFF DISC's in Fig. 4. Negative delays on the right corresponded to a delay added on the left. The

* The right input to C_R has an intrinsic delay of 35 ns. Thus C_P and C_R never observe protons from the same pair of beam pulses.

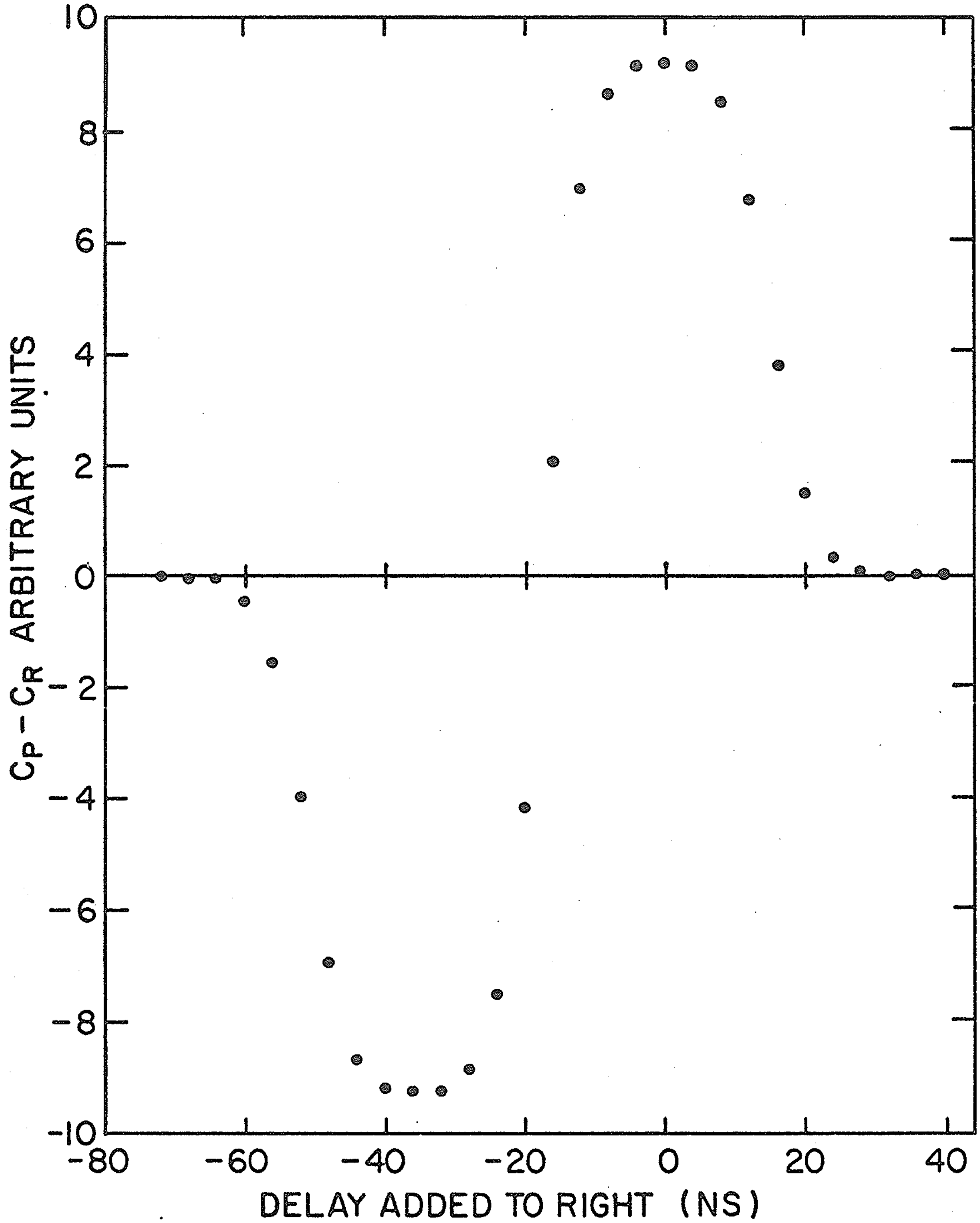

Figure 14

Curve showing C_P-C_R counts as a function of the relative delay (see text) between the coincidence circuit inputs. Prompt coincidences were between D(p,2p)n events. The error bars are smaller than the size of the points.

range of delays used resulted in the following sequence

(a) both C_P and C_R observed random coincidences only (delay $\approx$ -70 ns)

(b) C_R observed prompt D(p,2p)n coincidences while C_P observed random coincidences (delay $\approx$ -35 ns)

(c) C_P observed prompt D(p,2p)n coincidences while C_R observed random coincidences (delay $\approx$ 0 ns)

(d) both C_P and C_R observe random coincidences (delay $\approx$ 35 ns)

The peaks at -35 ns and 0 ns were not quite the same height and there was a small net count at delays of -70 ns and 35 ns, indicating that there were electronic inefficiencies in C_P which were beam intensity dependent.* This was approximately represented by

$$\frac{C_R - C_P}{C_R} \times 100 = (0.25\%) \times I(na) \qquad \text{III-5}$$

The widths of the discriminator pulses used for the inputs to the coincidence units were set for a 5 ns flat top on the delay curve.

III.2.9 Vertex Resolution

The trajectories of the protons are reconstructed by computer and projected back into the symmetry plane of the scattering chamber for each event. Normally,

* The cancellation of random counts for delays of -70 ns and 35 ns indicates there is no significant intensity modulation between consecutive beam pulses.

the tracks do not appear to have a common origin because of multiple-scattering effects and the finite spacing of the wire coordinates. Two coordinate axes are defined in the beam plane, one parallel to the beam (Z) and one perpendicular (Y) to it in the vertical direction (See Fig. C-1 in Appendix C). The differences (vertex errors) of the positions of the two track intersections with the beam plane are determined in these directions.

The Z-vertex error is sensitive to the lateral position of the beam. If the beam centroid does not coincide with the symmetry plane of the spectrometer, an asymmetry is introduced in the Z-vertex error distribution. For particles with polar angles θ_L and θ_R, the position of the Z-vertex error centroid ($\langle \Delta V_Z \rangle$) depends on the position of the lateral beam centroid ($\langle X_B \rangle$)

$$\langle \Delta V_Z \rangle = \langle X_B \rangle \cdot (\cot\theta_L + \cot\theta_R) \qquad \text{III-6}$$

At small angles this shift can become quite serious and cause events to be lost because of an apparent lack of vertex. The solution to this problem was discussed in Sec. III.2.2. For the rest of this discussion it is assumed that $\langle X_B \rangle = 0$.

Let $\langle \Delta Y_o \rangle$ and $\langle \Delta Z_o \rangle$ be standard deviations of the vertex errors as measured for 45^o p-p elastic events at 42 MeV incident beam energy. Simple geometric considerations show that $\langle \Delta Y \rangle$ and $\langle \Delta Z \rangle$, the vertex errors for sets of prompt events, are geometrically related under ideal conditions of zero beam width. The following approximate dependence on the geometric and kinematic parameters of the event is obtained. (See Appendix D for details.)

$$\langle \Delta Y \rangle = \langle \Delta Y_o \rangle \cdot \left(1.7 - \frac{0.7Z}{Z_{el}}\right) \left(0.36\,\rho^2 + 0.64\right)^{\frac{1}{2}} \qquad \text{III-7}$$

$$\langle \Delta Z_o \rangle = \langle \Delta Y_o \rangle \cdot \sqrt{2} \qquad \text{III-8}$$

$$\langle \Delta Z \rangle = \frac{\langle \Delta Y \rangle}{\sqrt{2}} \left(\csc^2\theta_L + \csc^2\theta_R\right)^{\frac{1}{2}} \qquad \text{III-9}$$

where

$$\rho^2 = \frac{21^2}{2} \frac{(E_L^{\,2} + E_R^{\,2})}{E_L^{\,2}\, E_R^{\,2}} \qquad \text{III-10}$$

In the above discussion the effect of the wires in the front chambers is not considered. These wires are 5 μm thick tungsten, 120 μm apart. Twelve percent of the particles hit these wires on each side and have different vertex error distributions because of the larger multiple-scattering in the tungsten. This is shown in a plot of the adjusted Y-vertex error* for 42 MeV D(p,2p)n events, in Fig. 15. The presence of two Gaussian distributions is clear. A large number of the events that hit the tungsten

---

* The meaning of the term "adjusted vertex error" is given in Sec. VII.1.1

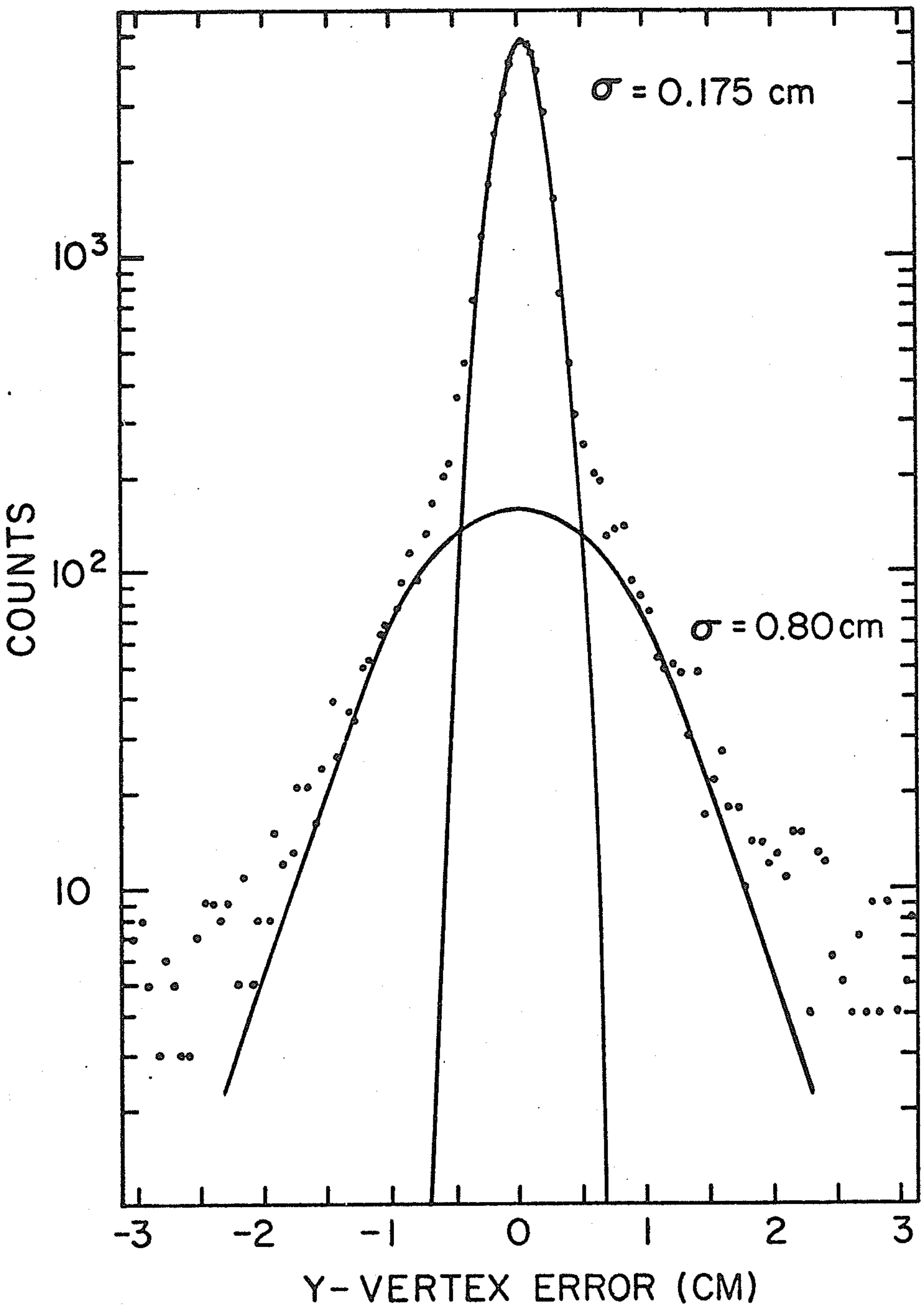

Figure 15

Log plot of the adjusted Y-vertex error for 42 MeV D(p,2p)n events, showing the effect of protons passing through a tungsten wire in the front chamber. The smooth curves represent Gaussian distributions with standard deviations of 0.175 cm and 0.80 cm. These values gave the best visual fit to the data in the central region.

wires are rejected because they do not make a sufficiently accurate vertex. Further discussion of the effect this has on the ppγ data analysis is given in Sec. VII.1.3.

III.2.10 Wire Chamber Efficiency

The fraction of true events that make an acceptable vertex is one of the most important properties to consider when discussing the spectrometer. This number is dependent on beam intensity because δ-rays and extra proton tracks may result in sparking inefficiencies for the track of interest or make the event too complex for analysis. The vertex efficiency has been measured using 42 MeV p-p elastic events at various beam intensities between 0.1 and 5 na. The results are shown in Fig. 16. Corrections for triggers on random events that do not make a vertex have been made. The vertex error limits were wide enough to accept almost all events that hit the tungsten wires. The upper curve shows the highest overall efficiency obtained to date while the lower curve represents a relatively poor but acceptable dependence on beam intensity. Almost all ppγ data runs were taken with vertex efficiencies between these two curves.

The range of vertex efficiency at a beam intensity of 3 na indicates the size of possible uncertainties

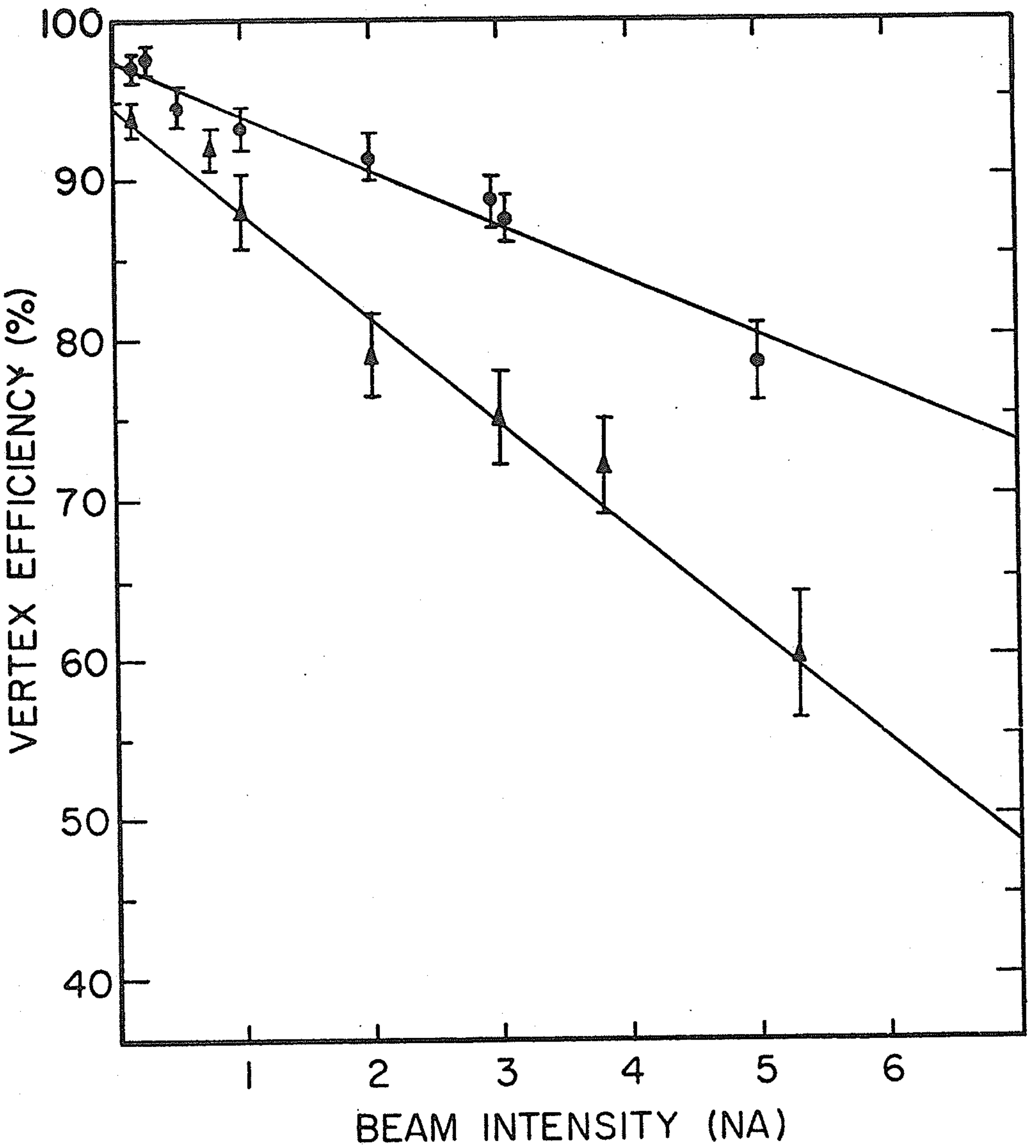

Figure 16

Plot of the spectrometer vertex efficiency as a function of the incident beam intensity. The upper curve (●) shows the best overall efficiency obtained in one test. The lower curve (▲) indicates a relatively poor but acceptable vertex efficiency. The error bars are statistical uncertainties in the number of undetected events and in corrections for random coincidences. Note that the vertical scale does not extend to zero.

during ppγ runs. The importance of having some method to eliminate this possible systematic error is clear. By detecting p-p elastic events at the same time as ppγ events, the effects of wire chamber inefficiencies are cancelled (See Sec. II.2.2). The reliability of this procedure depends only on the detection efficiency being uniform over the full surface of the wire chambers. This is discussed in the next section.

III.2.11 Wire Chamber Uniformity

The wire chambers observe a wide range of polar angles and it is necessary to determine if there are any systematic errors introduced by dependence of the track detection efficiency on polar angle or on the positions where the particles pass through the wire chambers. This has been checked in two ways. The p-p elastic distributions for polar angles in the range $20^\circ \leqslant \theta \leqslant 35^\circ$ have been observed and compared to expected distributions. The results are shown in Fig. 17(a). The R/L asymmetry in the polar angles has also been checked using the $He^4(p,2p)T^3$ reaction. This is shown in Fig. 17(b). The variation from uniformity for angles $\geqslant 37^\circ$ is due to the effect of the B2 baffles (See Fig. 2). From these results it is concluded that the systematic errors introduced by wire chamber non-uniformity are small and are therefore neglected.

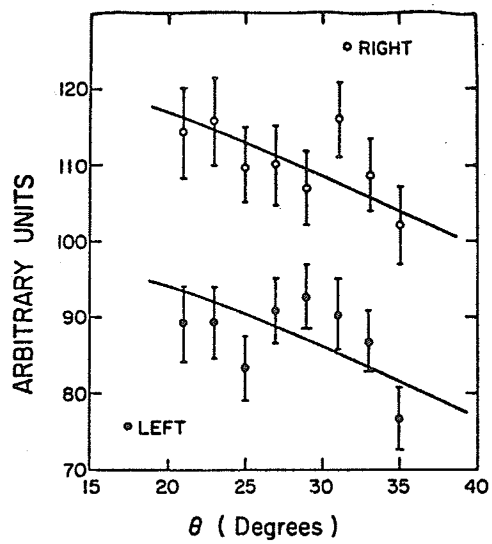

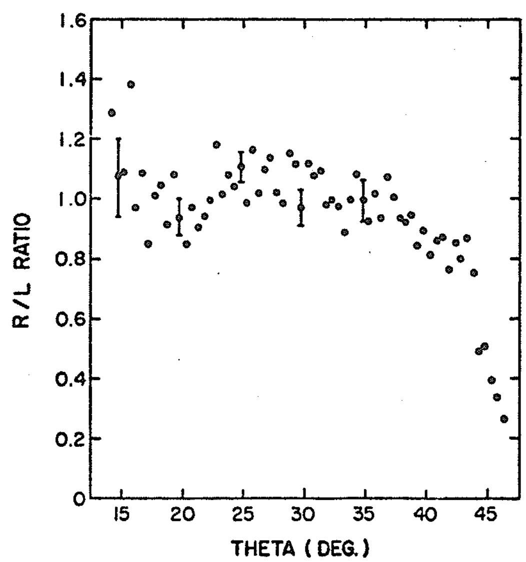

Figure 17

(a) Distribution of p-p elastic single particles as a function of the polar angles for the LEFT (●) and RIGHT (○) hodoscopes. The smooth curve is the expected distribution proportional to the p-p elastic cross section.

(b) Ratio of the number of $He^4(p,2p)T^3$ events in the RIGHT hodoscope to the number in the LEFT hodoscope as a function of the polar angles. The average value of the ratio is 1.0. The drop at angles $\gtrsim 37°$ is due to the B2 baffles.

CHAPTER IV

MONTE CARLO CALCULATIONS

In calculating ppγ cross sections, effects of the spectrometer detection efficiencies must be considered. Geometrical restrictions imposed by the baffles, hodoscopes and low energy cut-offs were considered in Sec. II.3, and the detection efficiencies ϵ_0 and ϵ_1 discussed. Analytical solutions for these quantities are very difficult to find and they have therefore been evaluated using Monte Carlo techniques.

In analyzing the ppγ data, all events were separated into bins depending on the variables θ_L, θ_R, Φ_r and Ψ_γ. The description of the subdivision is as follows:

(a) θ_L : the range from 16° to 40° is subdivided into 6 sub-ranges, each 4° wide.

(b) θ_R : the range from 16° to 36° is subdivided into 5 sub-ranges, each 4° wide.

(c) Φ_r : the range from 0 to 2.0 is subdivided into 20 sub-ranges, each 0.1 wide. The range extends to 2.0 because of multiple-scattering effects on the Φ_r distribution.

(d) Ψ_γ : the range from 0° to 360° is subdivided into 18 sub-ranges, each 20° wide.

The detection efficiency ϵ_1 has been evaluated for each bin (a total of 6 x 5 x 20 x 18 = 5400 bins). ϵ_o is independent of ψ_γ so it need only be determined for 600 individual cases. Calculations of ϵ_1 and ϵ_o were done independently. For the former, a simulated set of ppγ events, weighted according to the theoretical predictions of the Hamada-Johnston potential, was used. Calculations for ϵ_o required the generation of simulated proton trajectories (not necessarily corresponding to trajectories allowed for actual ppγ events) and tests to determine if these trajectories would be detected in the hodoscopes.

IV.1 PPγ EVENT SIMULATION

It was necessary to have a set of data with simulated ppγ events (similar to the data actually observed in the experiment) for a number of reasons associated with the design of the experiment and the data analysis.

(a) The acceptance of the spectrometer could be investigated and quantitative information about effects of low energy cut-offs and wire chamber positions could be obtained.

(b) In cross section calculations, corrections due to energy cut-offs in the spectrometer had to be made. These corrections depended on ppγ cross sections since the Ψ_γ distributions change rapidly and non-uniformly. Estimating the correction required a set of data that matched as closely as possible the measured distributions.

(c) Comparison of the experimental results to theoretical predictions could only be accomplished by including effects of all experimental biases in the theoretical predictions. In only a few simple cases could this be done analytically. When integrations over large ranges of the polar angles were performed, no theoretical predictions for the resulting cross sections were available. Theory and experiment could only be compared by analyzing sets of real and simulated events in the same manner and comparing the resulting distributions.

IV.1.1 The PPγ Event Generator

The Monte Carlo program (called COMBINE) used to generate the "fake" set of ppγ data, was a modified version of the random star generator contained in the program "OWL".* Each ppγ event was generated by a succession of two-body decays from a single particle with total energy equal to the C.M. energy of the two colliding protons. For example, the sequence could be represented by

$$p + p \rightarrow A \rightarrow p_1 + B \rightarrow p_1 + p_2 + \gamma$$

The principle of this particular type of event generator is described in detail by F. James[82]).

COMBINE generated ppγ events assuming that there were no interactions between the three outgoing particles. That is, the matrix element describing the interactions between the particles was unity. In this case all spectra were given by phase space alone, that is, by statistical (density of states) and kinematic factors. In COMBINE the following sequence of calculations was made:

---

* The original version of the OWL program was written by G. R. Lynch (Berkeley) and modified by J. P. Chandler (Florida State University).

(a) The momentum components for the ppγ event were generated and some simple variables calculated (i.e. θ_L, θ_R, ϕ_L, ϕ_R). A test was made to see if these variables were within ranges that could be observed in the spectrometer. If they were not, the event was rejected.

(b) A vertex origin in the allowed target volume was chosen, the position along the beam direction being picked at random. The vertical position was chosen so that the full set of simulated events had a distribution similar to that observed in the ppγ experiment. A test was then made to see if the particles missed the baffles along the beam (baffles B1 and B2 in Fig. 2). Particles hitting the baffles were rejected.

(c) Since real ppγ events undergo multiple-scattering in traversing the hodoscopes, and the detectors have finite energy resolutions, these effects are also included in the simulated ppγ events. The expected proton angular and energy resolutions were calculated for each event and the generated values of E, θ and ϕ altered. Adjustments between $\pm$ 3σ in each variable were chosen at random from Gaussian distributions. The energy and angle resolutions had the functional dependence described earlier in Chapter II.

(d) The proton trajectories were then tested to determine if they were detected in the hodoscopes. Events were rejected if both protons were not detected. Limits on the wire chamber coordinates corresponded to regions that were not blocked by baffles (See Fig. 3(b)).

(e) For detected events all required kinematic variables were calculated from the adjusted proton energies and angles in a similar manner as for the actual ppγ data. In this way effects of the resolutions were included in the photon kinematic variables.

(f) Since phase space spectra are not a good representation of the actual spectra measured, it was necessary to include results of theoretical calculations. The probability for a particular event to occur is given by

$$d\sigma = C R_3 \times |M.E.|^2 \qquad \text{IV-1}$$

where R_3 is the Lorentz-invariant phase space factor and M.E. is the matrix element for the interaction. In order to obtain spectra similar to the measured ppγ data, a weight was assigned to each generated event proportional to $|M.E.|^2$. How this weight was obtained is described in Sec. IV.1.2 and IV.1.3.

IV.1.2 Event Weighting Factor

In this thesis M. K. Liou's theoretical predictions for the Hamada-Johnston potential have been used. A basic theoretical outline is given in Appendix F. The cross section as calculated by Liou[36] is given by

$$d\sigma = \frac{\alpha}{\pi^2 m^3 P_1 K} \left\langle \tfrac{1}{4} \mathrm{tr}\, \mathcal{M}^\dagger \mathcal{M} \right\rangle F\, d\Omega_1 d\Omega_2 d\Psi_\gamma \qquad \text{IV-2}$$

where $\sqrt{\alpha}$ is the proton charge, m the proton mass, P_1 the incident proton laboratory momentum, K the photon energy, $\mathcal{M}$ the matrix element and $F\, d\Omega_1 d\Omega_2 d\Psi_\gamma$ a phase space (not Lorentz-invariant) function. This form is not appropriate for use in the Monte Carlo program. Equation IV-2 must be modified so that the Lorentz-invariant phase space factor can be separated out and the weighting factor derived. The cross section can be written

$$d\sigma = Wt \times R_3 \qquad \text{IV-3}$$

R_3 is the invariant phase space factor and Wt is a Lorentz-invariant function that contains all of the physics of the problem and in this case is also the correct weighting factor. The expression $F\, d\Omega_1 d\Omega_2 d\Psi_\gamma$ can also be written

$$F' = F d\Omega_1 d\Omega_2 d\Psi_\gamma = \delta^4(P_f - P_i) d^3p_1' \, d^3p_2' \, d^3K \qquad \text{IV-4}$$

The 3-body Lorentz-invariant phase space is given by

$$R_3 = \delta^4(P_f - P_i) \prod_{i=1}^{3} \delta(p_i'^2 - m_i^2) d^4 p_i' \qquad \text{IV-5}$$

Comparing IV-4 and IV-5, the following result is easily obtained

$$R_3 = \frac{F'}{E_1' E_2' K} \qquad \text{IV-6}$$

E_1' and E_2' are the proton energies in the final state. Substituting for F' in IV-2

$$d\sigma = \frac{\alpha E_1' E_2' R_3}{\pi^2 m^3 P_1} \langle \tfrac{1}{4} \mathrm{tr}\, \mathcal{M}^\dagger \mathcal{M} \rangle \qquad \text{IV-7}$$

The weighting function is then

$$Wt = \frac{d\sigma}{R_3} = \frac{\alpha E_1' E_2'}{\pi^2 m^3 P_1} \langle \tfrac{1}{4} \mathrm{tr}\, \mathcal{M}^\dagger \mathcal{M} \rangle \qquad \text{IV-8}$$

A large number of theoretical cross sections have been calculated and matrix elements obtained. Since kinematic parameters for the simulated ppγ events are chosen at random, they seldom coincide with points for which these matrix elements were evaluated. As a result it is necessary to interpolate between different matrix elements to obtain proper weights for each event. The procedure used is described in the next section.

IV.1.3 Evaluation of Individual Event Weights

The weights (proportional to $|M.E.|^2$) have been evaluated at regular intervals in θ_1, θ_2, Φ_r and Ψ_γ. The points at which they were calculated are summarized as follows.

(a) θ_1 from 14° to 42° in 4° steps.

(b) θ_2 from 14° to 38° in 4° steps.

(c) Ψ_γ from 0° to 360° in 10° steps.

(d) Φ_r at approximate values of 0.05, 0.25, 0.50, 0.75 and 0.95.

Using a spline fitting procedure* a two-dimensional fit to the weighting factor as a function of Φ_r and Ψ_γ has been made for each pair of polar angles described above. Evaluation of the weight for a particular event is a two-step process.

(a) The four polar angle pairs nearest the polar angles of the protons were determined (e.g. for $\theta_1 = 25^\circ$ and $\theta_2 = 19^\circ$ the four pairs would be $\theta_1 - \theta_2$** $= 22^\circ - 18^\circ$, $22^\circ - 22^\circ$, $26^\circ - 18^\circ$ and $26^\circ - 22^\circ$). The Ψ_γ and Φ_r values

---

* A package of programs for using spline functions in curve-fitting applications was obtained from the University of Maryland. Most of the modifications required for use in COMBINE were made by Dr. K. F. Suen.

** The values stated for $\theta_L - \theta_R$ are the centers of the polar angle bins (i.e. $22^\circ - 22^\circ$ means $20^\circ \leqslant \theta_L \leqslant 24^\circ$ and $20^\circ \leqslant \theta_R \leqslant 24^\circ$).

for the event (calculated using unadjusted proton angles and energies - see Sec. IV.1.1 (c)) were used to obtain weights corresponding to each of the four polar angle pairs previously mentioned.

(b) A two-way linear interpolation using the polar angles as variables was made from the 4 weights obtained in (a). This final result was used as the weight for the event.

Tests of the spline fit to the $\Phi_r - \Psi_\gamma$ distributions indicate the weights obtained are accurate to better than $\pm$ 2%.

IV.2 EVALUATION OF DETECTION EFFICIENCIES

IV.2.1 Geometrical Detection Efficiency

In equation II-11, the number of detected ppγ events is proportional to the proton solid angles and the effective target size. Thus

$$N_{pp\gamma} \propto \epsilon_o L \Delta\Omega_L \Delta\Omega_R \qquad \text{IV-9}$$

For sufficiently small solid angles, the cross section $d\sigma/d\Omega_L d\Omega_R d\psi_\gamma$ may be considered as constant. Changing the azimuthal angle variables in accordance with the discussion in Sec. II.3, and introducing a constant of proportionality C, equation IV-9 becomes

$$N_{pp\gamma} = C\epsilon_o L\Delta\Omega_L \; \Delta\cos\theta_R \; \Delta\phi_m \; \Delta\Phi_r \qquad \text{IV-10}$$

ϵ_o is a function of θ_L, θ_R and Φ_r, and is averaged over the proton solid angles $\Delta\Omega_L$ and $\Delta\Omega_R$. If ϵ_o were unity, this would correspond to all proton trajectories being detected by the hodoscopes. Evaluation of ϵ_o is achieved by simply finding the fraction of proton trajectories that are detected in the spectrometer for given values of θ_L, θ_R and Φ_r.

Consider pairs of uncorrelated trajectories, with common vertex origins, generated uniformly along the beam direction in the allowed target volume (L=23.0 cm, from near the B1 baffles to the B2 baffles in Fig. 2) and having uniform density per unit solid angle. If the number of such pairs is N_{go}, then

$$N_{go} = C' \Delta\phi_L \, L \, \Delta\cos\theta_L \, \Delta\cos\theta_R \, \Delta\Phi_m \, \Delta\Phi_r \qquad \text{IV-11}$$

The range of ϕ_L chosen ($\pm 40^o$) is just sufficiently large that the left hodoscope does not subtend angles outside this range. The ranges of θ_L and θ_R correspond to pairs of the polar angle bins described earlier. The vertical distribution of the origins of the particle trajectories was given a shape approximating that observed in the ppγ experiment. Following an argument similar to that in Sec. II.3, the number of pairs of trajectories detected (N_{do}) is

$$N_{do} = \epsilon_o N_{go} \qquad \text{IV-12}$$

Since the uncertainty in ϵ_o is statistical in nature, the precision to which it is calculated can be improved simply by increasing the number of randomly generated trajectories. Letting $N_{go} = N_{do} + N_{uo}$, then, since the expectation value of N_{do} is given by the binomial distribution, the fractional uncertainty $\delta\epsilon_o/\epsilon_o$ is

$$\frac{\delta\epsilon_o}{\epsilon_o} = \frac{N_{go}}{N_{do}} \, \delta\!\left(\frac{N_{do}}{N_{go}}\right) = \frac{1}{N_{do}}\sqrt{N_{go}\epsilon_o(1-\epsilon_o)} = \sqrt{\frac{N_{uo}}{N_{do}N_{go}}} \qquad \text{IV-13}$$

Replacing ϵ_o in equation II-12, the cross section becomes

$$\frac{d\sigma}{d\Omega_L d\Omega_R d\Psi_\gamma} = \frac{N_{pp\gamma}}{2QA_o I_o \epsilon_1} \cdot \frac{N_{go}}{N_{do}} \cdot \frac{1}{L\Delta\Omega_L \Delta\Omega_R \Delta\Psi_\gamma} \qquad \text{IV-14}$$

where $\Delta\Phi_L$, $\Delta\cos\theta_L$, $\Delta\cos\theta_R$ and $\Delta\Phi_r$ have the same values as in equation IV-11. Use of ϵ_o in equation IV-14 (in the form N_{do}/N_{go}) assumes that variation in the measured cross section can be neglected. In actual fact the cross section does change by as much as $\pm$ 10%. Since ϵ_o is also dependent on the polar angles, there is a small error introduced into calculation of the cross sections. The maximum value of this error has been estimated to be $\pm$ 2% and is much smaller than this in most cases. The error is small because the cross sections and ϵ_o vary smoothly and nearly linearly as a function of the polar angles.

The correction factors $(1/\epsilon_o)$ for coplanar trajectories range from a minimum of 1.95 for 22^o-22^o polar angle pairs to a maximum of 11.06 for 38^o-34^o. These factors increase with increasing Φ_r. The values of ϵ_o were calculated with statistical precision of about $\pm$ 5% for a given Φ_r value and about $\pm$ 1 to 2% when integrated over Φ_r.

IV.2.2 Energy Detection Efficiency

The quantity $N_{pp\gamma}/\epsilon_0\epsilon_1$ gives the number of $pp\gamma$ events that would be detected if all spectrometer efficiencies were unity. ϵ_0 has been evaluated in Sec. IV.2.1 and compensates for geometrical efficiencies provided that the proton solid angles are small. Events generated according to the procedure described in Sec. IV.1.1 have been used to evaluate ϵ_1, which is due to proton energy losses in the hodoscopes and the differential discriminator cut-offs.

Correction for ϵ_1 is translated directly into the Ψ_γ distributions. An example of ϵ_1 for coplanar events with polar angles of 22^o - 22^o would be similar to Fig. 18 when plotted as a function of Ψ_γ

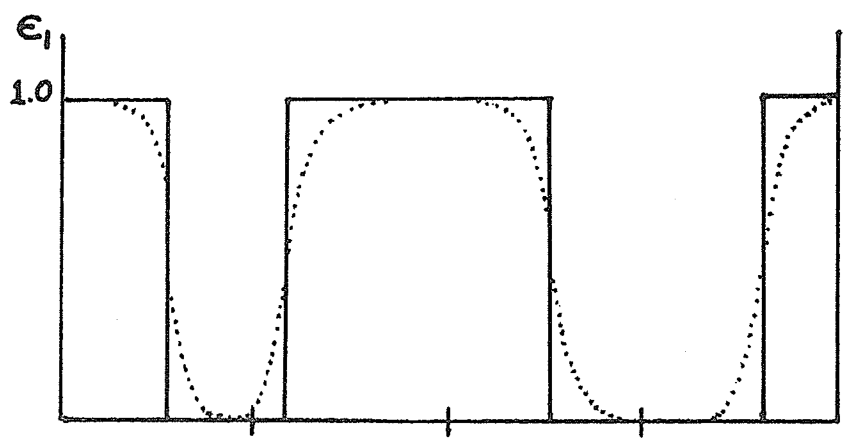

Figure 18

ϵ_1 as a function of Ψ_γ. The dotted curve shows how ϵ_1 is affected by finite angular and energy resolutions.

Let N_{gl} and N_{dl} be the number of generated and detected Monte Carlo ppγ events weighted according to theoretical predictions. Since all generated events have proton trajectories detected in the spectrometer (See Sec. IV.1.1-(d)), then

$$N_{dl}(\theta_L,\theta_R,\Phi_r,\psi_\gamma) = \epsilon_1 N_{gl}(\theta_L,\theta_R,\Phi_r,\psi_\gamma) \qquad \text{IV-15}$$

The statistical uncertainty in ϵ_1 is given by an expression similar to IV-13.

IV.2.3 Evaluation of Measured Cross Sections

The ppγ cross sections obtained from the actual data are calculated from equation IV-14 after substitution for ϵ_1

$$\frac{d\sigma}{d\Omega_L d\Omega_R d\psi_\gamma} = \frac{N_{pp\gamma}}{2QA_oI_o} \cdot \frac{N_{go}}{N_{do}} \cdot \frac{N_{gl}}{N_{dl}} \cdot \frac{1}{L\Delta\Omega_L\Delta\Omega_R\,\Delta\psi_\gamma} \qquad \text{IV-16}$$

To obtain the non-coplanarity distributions, an integration (summation) over ψ_γ is performed.

$$\frac{d\sigma}{d\Omega_L d\Omega_R} = \sum_{\psi_\gamma} \frac{d\sigma}{d\Omega_L d\Omega_R d\psi_\gamma}\,\Delta\psi_\gamma \qquad \text{IV-17}$$

A problem is immediately apparent. If $\epsilon_1 = 0$ for some range of ψ_γ then $N_{pp\gamma}$ for that range in IV-16 will also be zero. A computer cannot evaluate $N_{pp\gamma} \cdot \frac{N_{gl}}{N_{dl}} = 0 \cdot \infty$

and obtain a non-zero finite number (i.e. the number of $pp\gamma$ events created). Thus the summation in IV-17 cannot be performed numerically as shown if ϵ_1 is 0 anywhere in the ψ_γ range.

To overcome this problem, the non-coplanarity distribution is written in a different form. Remembering that N_{go}/N_{do} is independent of ψ_γ, then

$$\frac{d\sigma}{d\Omega_L d\Omega_R} = \frac{1}{2QA_oI_o} \cdot \frac{N_{go}}{N_{do}} \cdot \frac{1}{L\Delta\Omega_L\Delta\Omega_R} \cdot \frac{\sum N_{g1}}{\sum N_{d1}} \cdot \sum N_{pp\gamma} \qquad \text{IV-18}$$

where the summations are over ψ_γ. This yields the same result as equation IV-17 provided that N_{g1} and N_{d1} are derived from the same ψ_γ distributions as the experimental results (i.e. $N_{pp\gamma}/N_{d1}$ = constant for each ψ_γ value).

The integrated cross section as a function of the polar angles is obtained by summing over Φ_r. Letting $M_o = N_{go}/N_{do}$ and $M_1 = \sum N_{g1}/\sum N_{d1}$, then

$$\frac{d\sigma}{d\theta_L d\theta_R} = 2\pi\Delta\phi_m \sin\theta_L \sin\theta_R \sum_{\Phi_r} \frac{d\sigma}{d\Omega_L d\Omega_R} \Delta\Phi_r \qquad \text{IV-19}$$

An integration from $\phi_L = 0^o$ to $\phi_L = \pi$ has been performed.

In some cases the correction M_1 becomes very large. In these cases, the experimentally derived cross sections have additional error due to uncertainty in the proton energy cut-off (due to errors in the PHT-energy calibration). The maximum estimated error is $\pm$ 400 keV. Corrections for this have not been evaluated in detail, or included in the analysis. Estimated errors are given later in Table 16.

IV.3 RESULTS OF MONTE CARLO ANALYSES

IV.3.1 Spectrometer Acceptance

The spectrometer acceptance has been investigated using unweighted (i.e. phase space distributions) Monte Carlo $pp\gamma$ events. Approximately 1% of all events generated in the allowed target region are detected by the spectrometer. An indication of the effects of an individual hodoscope on the polar angle acceptance is shown in Fig. 19(a). The two $\theta_L+\theta_R$ distributions correspond to (1) all generated events and (2) all events detected in both hodoscopes. Fig. 19(b) shows the distribution in gamma ray energies with and without the energy cut-offs applied for events in curve (2) above. The relatively high energy cut-offs result in a significant reduction in the number of detected events.

IV.3.2 Generated Theoretical Distributions

The distributions of $pp\gamma$ events weighted according to the HJ potential predictions, have been checked by observation of the Ψ_γ and Φ_r distributions. Fig. 20(a) shows a typical generated Ψ_γ distribution (for 22^o-26^o $pp\gamma$ events) integrated over $\Phi_r \leqslant 0.4$. The solid curve is the expected shape. The agreement is excellent. The statistical errors for a particular value are about $\pm$ 10% as there are only $\sim$100 events per bin. Fig. 20(b) shows the Φ_r generated and expected distributions. Again agreement is seen to be good.

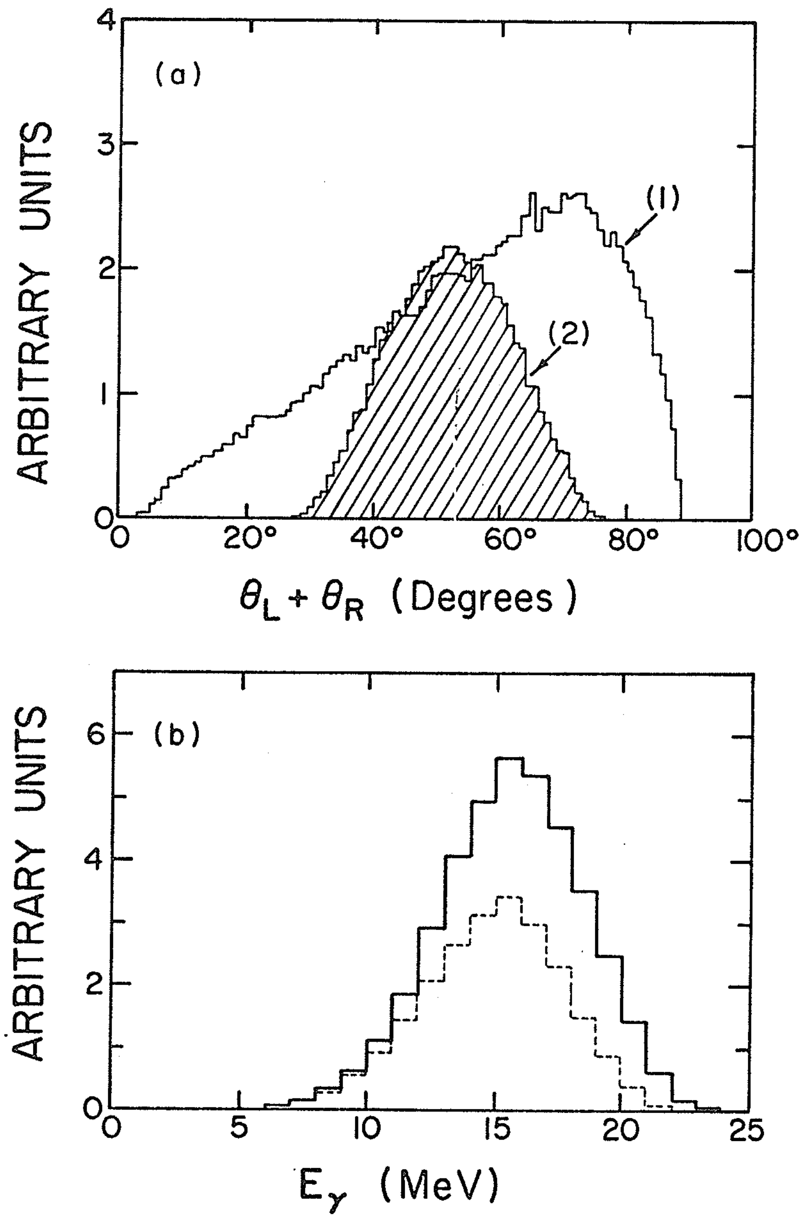

Figure 19

(a) Distribution of events as a function of the sum of the proton polar angles for all ppγ events (curve 1) and for those detected in the spectrometer (curve 2).

(b) Distribution of the photon laboratory energy with and without the energy cut-offs of the spectrometer applied. These cut-offs corresponded to $E_L \geqslant 9.25$ MeV and $E_R \geqslant 10.25$ MeV.

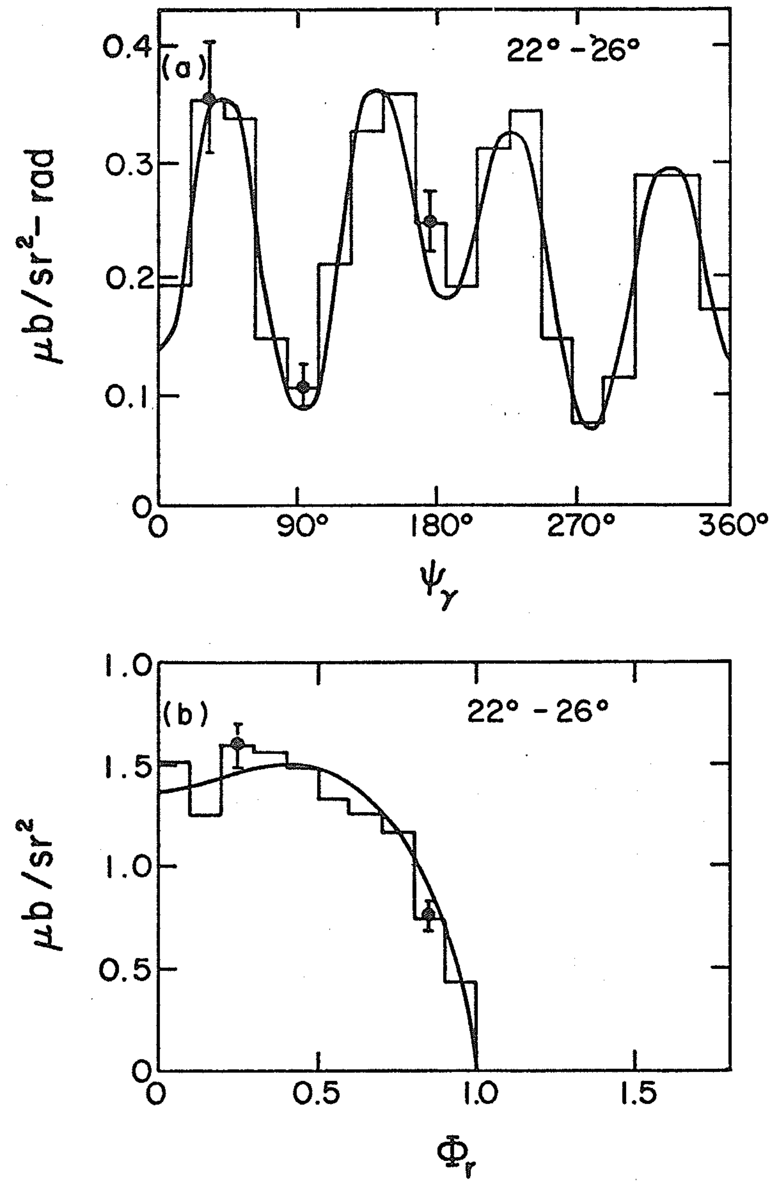

Figure 20

(a) Monte Carlo Ψ_γ distribution for events in the 22°-26° polar angle bin for relative non-coplanarities $\Phi_r \leq 0.4$. The smooth solid curve is the theoretical prediction as calculated by Liou for the Hamada-Johnston potential.

(b) Monte Carlo Φ_r distribution for the 22°-26° polar angle bin. The smooth curve is the HJ theoretical prediction.

IV.3.3 Effects of Spectrometer Resolutions

The effects of the finite energy and angular resolutions are shown in Fig. 21(a & b). The bar histograms for $22^o - 26^o$ ppγ events are the same as in Fig. 20. The dots show the same distributions with the resolutions folded in. In this particular case the Ψ_γ resolution is about $\pm 15^o$ and the Φ_r resolution is ± 0.216 (standard deviation).

The effects of the energy cut-offs are shown in Fig. 22. The bar histogram shows the events integrated over the observed proton polar angles and over Φ_r. The dots indicate the same set of events with the cut-offs applied. The effect is quite large for $220^o \leq \Psi_\gamma \leq 360^o$.

IV.3.4 Use of Monte Carlo Data in a Global Analysis

The set of weighted Monte Carlo ppγ events should, in principle, be identical to the measured ppγ data. Cross sections and distributions of specific variables for the two sets of data can be compared and any differences observed could be due to deviations of the actual nuclear potential from the HJ model, provided all experimental biases and background corrections have been properly considered. By integrating over large phase space ranges, particularly the proton polar angles, the

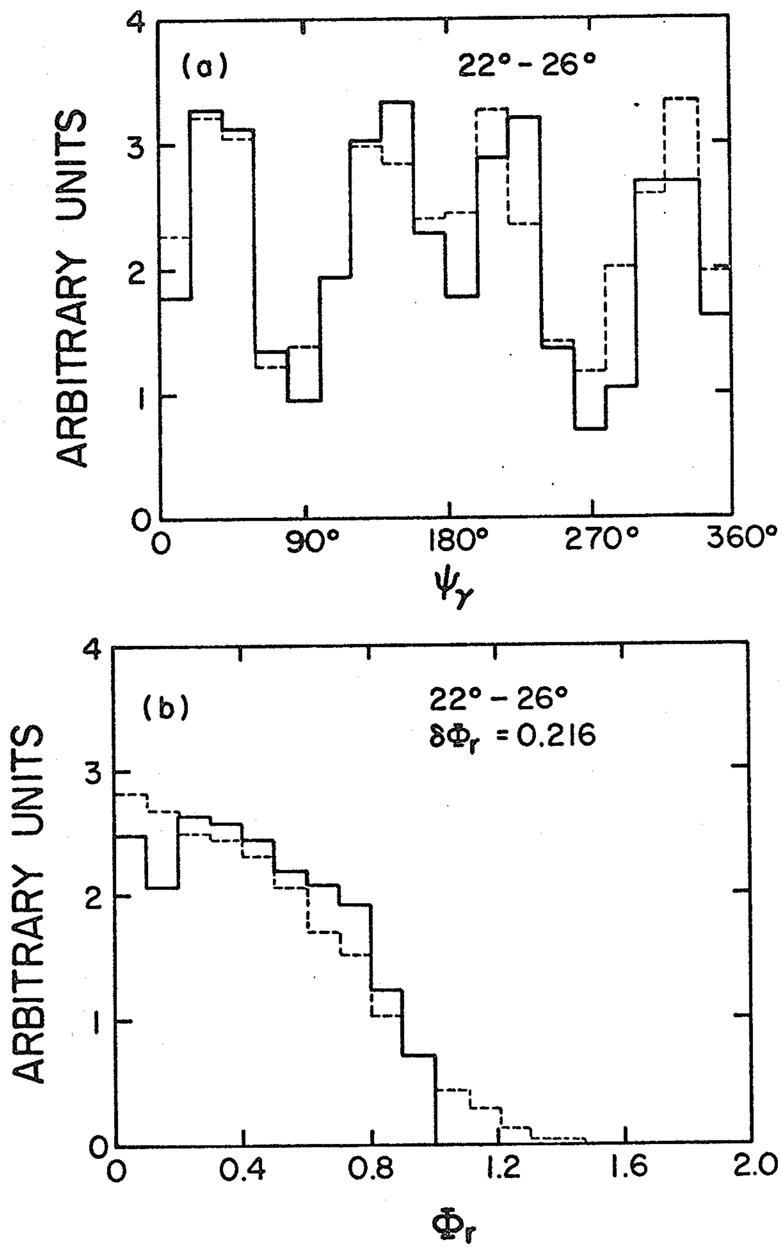

Figure 21

(a) Ψ_γ distribution of the Monte Carlo ppγ events for 22^o-26^o polar angle bin for $\Phi_r \leq 0.4$. The dotted histogram shows the effects of the finite angular and energy resolutions of the spectrometer.

(b) Φ_r distribution for the 22^o-26^o polar angle bin showing the effects of the resolution in Φ_r. For this case $\delta\Phi_r$=0.216.

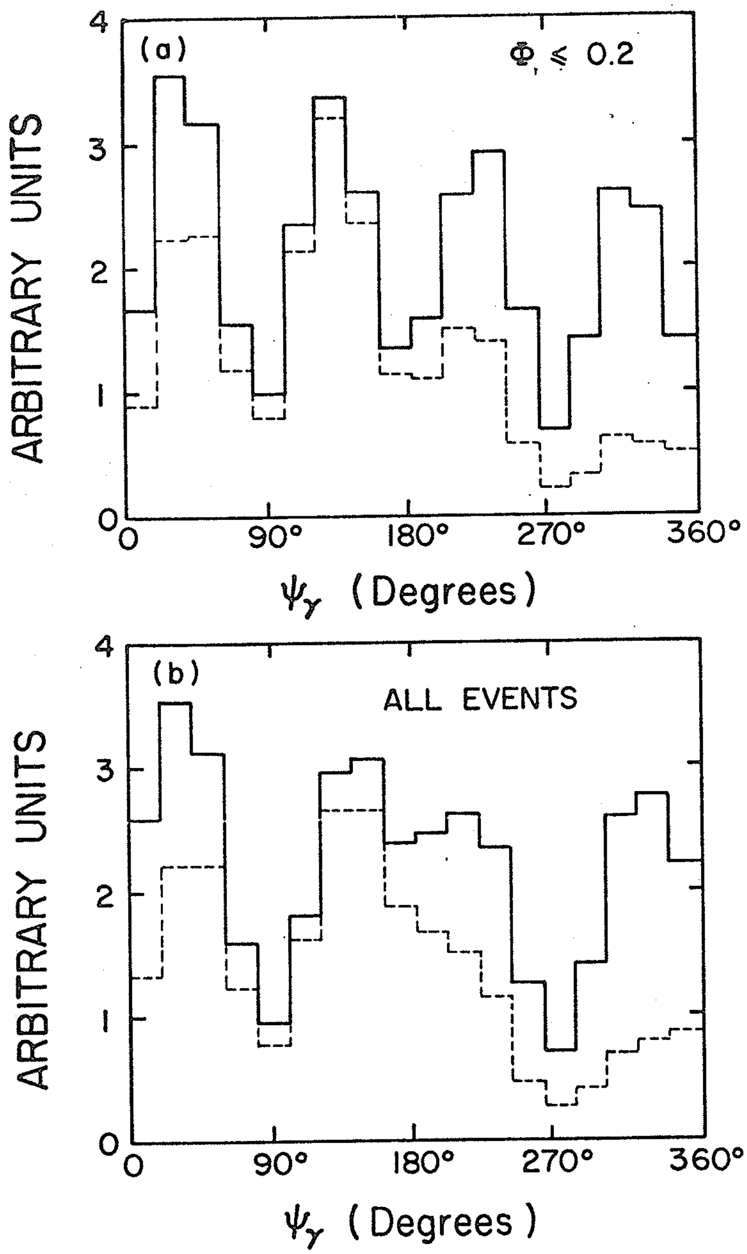

Figure 22

(a) Ψ_γ distribution for Monte Carlo ppγ events integrated over the proton polar angles and Φ_r up to 0.2. The effects of the energy cut-offs are shown in the dotted histogram.

(b) Similar to (a) except the events have been integrated over all possible non-coplanarities.

statistical accuracy in the measured distributions is improved, allowing more reliable comparisons to theoretical predictions. This procedure is referred to as a Global Analysis, and is used later to test the theoretical dependence of the cross sections on the sum and difference of the proton polar angles, and on the event non-coplanarity.

CHAPTER V

P-P ELASTIC CROSS SECTION MEASUREMENTS

The problems inherent in proper $pp\gamma$ cross section normalization and the solution adopted were outlined in Sec. II.2.2. The question is now treated in more detail and a description of the actual measurements performed is presented.

V.1 PRINCIPLE OF THE NORMALIZATION PROCEDURE

The crux of the problem was to normalize the charge that passed through the spectrometer for effects due to temperature, pressure, electronic and computer deadtime and wire chamber efficiency. The dependence of the measured cross sections on charge is given by equations II-12, 13, 14. It is possible to substitute for the charge Q in these equations by using equation II-2. Then

$$\frac{d\sigma}{d\Omega_L d\Omega_R d\Psi_\gamma} = \frac{\left.\frac{d\sigma}{d\Omega}\right)_{el}}{\epsilon_o \epsilon_1} \frac{N_{pp\gamma}}{\beta N_{el}} \frac{\epsilon_{we}}{\epsilon_{w\gamma}} \frac{\Delta\Omega}{\Delta\Omega_L \Delta\Omega_R \Delta\Psi_\gamma} \frac{L_{el}}{L} \qquad \text{V-1}$$

N_{el} and $N_{pp\gamma}$ are the number of p-p elastic and $pp\gamma$ events detected in the $pp\gamma$ data runs and $\left.\frac{d\sigma}{d\Omega}\right)_{el}$ is the elastic cross section measured in a separate experiment using conventional techniques. ϵ_{we} and $\epsilon_{w\gamma}$ are the wire chamber vertex efficiencies for p-p elastic and ppγ events respectively. These were nearly equal and are discussed later in Chapter VI. There were several systematic errors that had to be accounted for in determining N_{el}. These errors are also discussed in Chapter VI. The correction for them is given by β.

The normalization constant is given by the expression

$$C_N = \left.\frac{d\sigma}{d\Omega}\right)_{el} \cdot \frac{L_{el}\,\Delta\Omega}{\beta N_{el}} \frac{\epsilon_{we}}{\epsilon_{w\gamma}} \qquad \text{V-2}$$

Since the ppγ cross sections depend on the ratio $N_{pp\gamma}/N_{el}$, they are determined relative to the p-p elastic cross section. The terms in C_N that are independent of the ppγ runs $\left(\left.\frac{d\sigma}{d\Omega}\right)_{el},\ L_{el}\text{ and }\Delta\Omega\right)$ are now considered.

V.2 MEASUREMENT OF $\frac{d\sigma}{d\Omega})_{el}$

V.2.1 Procedure

Measurement of $\frac{d\sigma}{d\Omega})_{el}$ has been performed by detecting p-p elastic events in coincidence, using a geometrical arrangement similar to that used in ppγ data runs. The geometry of baffles B2 in Fig. 2 is such that if a proton from a p-p elastic event passes through the slit placed at 44.7^{o} to the beam behind the rear wire chamber (See Fig. 3(b)), then it must also be detected in the left hodoscope and counter. In the $\frac{d\sigma}{d\Omega}\}_{el}$ measurement the right detector was completely covered with brass, sufficiently thick to stop 50 MeV protons, except for the diagonal slit. In addition, a baffle was placed inside the scattering chamber in such a manner as to allow only protons passing through the slit in the B2 baffles to enter the right detector. Thus, only neutrons and p-p elastic protons passing through the diagonal collimator were detected in the scintillation counter on the right. On the left side, baffles were placed in front of the detector at small angles to reduce random rates. The discriminators were set to eliminate almost all low energy neutrons without eliminating any p-p elastic events in order to keep both prompt and random backgrounds low.

Measurements were performed using three different collimators--

(a) a circular 1.91 cm diameter collimator;

(b) a collimator nominally 2 mm wide and 27.4 mm long as used during ppγ data collection;

(c) a similar collimator to the one in (b).

The total measured charge ($\sim$12000 nc for (b) and (c)) resulted in $\gtrsim 10^4$ net p-p elastic events in each of the three measurements. Backgrounds due to true nn, np and pn coincidences were determined by blocking off the left and right detectors in turn and finally both together, and repeating the measurements.

The cross section was calculated using the following formula.

$$\left.\frac{d\sigma}{d\Omega}\right)_{el} = \frac{N'_{el}}{2QA_oI_oL_{el}\Delta\Omega} \frac{C_I\ C_{DT}\ C_C}{C_{TP}\ C_{FC}\ C_{MS}} \qquad \text{V-3}$$

C_I is a correction for the current integrator; C_{DT} is a correction due to electronic dead-time; C_C is a correction for coincidence circuit inefficiencies; C_{TP} is a correction to the number of hydrogen atoms per cm^3 due to effects of temperature and pressure; C_{FC} is a correction for the charge collection efficiency of the Faraday cup; and C_{MS} is a correction for events lost due to multiple-scattering in the tungsten wires of the front wire chambers. A summary of all results is contained in Table 4.

V.2.2 Electrometer and Faraday Cup Calibration

Charge measurement was made with a BIC Model 1000 electrometer.* It was calibrated using a very accurate voltage source and resistor to supply a known current. The average beam current was recorded during the $\frac{d\sigma}{d\Omega})_{el.}$ measurement and the correction C_I obtained from Table 5, which gives the results of the calibration measurements.

The charge collection efficiency has not been measured and only an estimate of the loss due to multiple-scattering (in the entrance and exit foils and H_2 gas) and divergence of the incident beam has been made. The beam shape used was typically 2 mm wide by 20 mm high. The beam properties are summarized in Table 1 in Sec. III.1.1. The Faraday Cup used had a diameter of 10 cm, a depth of 40 cm and its entrance was located 216 cm from the center of the scattering chamber. The r.m.s. projected width at the Faraday Cup entrance of an initial spot beam at the center of the scattering chamber has been estimated as $\pm$ 1.50 cm when the above effects are considered. This results in a total charge loss of 0.65%.

---

* Brookhaven Instruments Corporation, Brookhaven, New York.

Table 4

Auxiliary Calculations and Measurements for the p-p elastic cross section

Quantity	Units	Collimator I	Collimator II	Collimator III
Width of slit in B2 baffles	mm	2.85 ± 0.75%	2.85 ± 0.75%	2.85 ± 0.75%
Distance - beam to B2 baffle slit	mm	18.0 ± 0.75%	18.0 ± 0.75%	18.0 ± 0.75%
Distance - beam to collimator	mm	441.0 ± 0.5%	427.5 ± 0.5%	427.5 ± 0.5%
Length of gas target (L_{el})	mm	4.201 ± 1.5%	4.206 ± 1.5%	4.206 ± 1.5%
Length of collimator	mm	19.05 ± 0.5%	27.41 ± 0.7%	27.41 ± 0.7%
Width of collimator	mm	(diameter)	2.021 ± 1.3%	2.217 ± 1.5%
Area of collimator	mm^2	285.0 ± 0.8%	55.37 ± 1.5%	60.73 ± 1.7%
Angle Correction		1.00 ± 0.0%	0.976 ± 0.1%	0.976 ± 0.1%
Solid Angle ($\Delta\Omega$)	msr	1.466 ± 1.1%	0.296 ± 1.7%	0.324 ± 1.8%
Temperature	^oK	298.2 ± 0.2%	298.3 ± 0.2%	298.2 ± 0.2%
Pressure	mm	744 ± 0.2%	744 ± 0.2%	744 ± 0.2%
STP Correction (C_{TP})		0.897 ± 0.3%	0.897 ± 0.3%	0.897 ± 0.3%
Measured beam intensity	na	1.805 ± 0.5%	2.84 ± 0.5%	2.78 ± 0.5%
Actual beam intensity (Table 6)	na	1.931	2.983	2.923
Integrator correction (C_I)		0.935 ± 0.5%	0.953 ± 0.5%	0.951 ± 0.5%
Charge Collection Losses (C_{FC})	%	0.650 ± 0.25	0.650 ± 0.25	0.650 ± 0.25
Discriminator dead-time	μsec	1.2 ± 10%	1.2 ± 10%	1.2 ± 10%
Total time of run	sec	500 ± 0.4%	4180 ± 0.4%	4326 ± 0.4%
Sum of disc. rates	10^4/sec	2.704 ± 0.5%	4.503 ± 1.5%	4.300 ± 1%
Dead-time correction (C_{DT})		1.039 ± 0.4%	1.054 ± 0.6%	1.052 ± 0.6%

Table 4 (continued)

Quantity	Units	Collimator I	Collimator II	Collimator III
Net counts/unit charge (corrected for randoms)				
(pp + pn + np + nn)	counts/nc	5.300 ± 0.6%	1.137 ± 0.9%	1.227 ± 0.8%
(pn + np + nn)	counts/nc	0.015 ± 104%	0.047 ± 27%	0.043 ± 17%
Net p-p elastics (C_Q)	counts/nc	5.285 ± 0.8%	1.091 ± 1.5%	1.184 ± 1.1%
Effects of lateral beam instability				
(a) on target length		0.0 ± 0.25%	0.0 ± 0.25%	0.0 ± 0.25%
(b) on solid angle		0.0 ± 0.5%	0.0 ± 0.5%	0.0 ± 0.5%
Correction for coincidence inefficiencies (C_C)		1.005 ± 0.25%	1.008 ± 0.25%	1.008 ± 0.25%
Multiple-scattering correction (C_{MS})		0.97 ± 1%	0.97 ± 1%	0.97 ± 1%
Uncertainty if Faraday Cup efficiency		2%	2%	2%
$\frac{d\sigma}{d\Omega})_{el}$	mb/sr	28.48 ± 3.2%	30.15 ± 3.6%	29.77 ± 3.6%
Average measured $\frac{d\sigma}{d\Omega})_{el}$ at 42 MeV	mb/sr	29.39 ± 2.6%		
Extrapolated $\frac{d\sigma}{d\Omega})_{el}$ at 42 MeV from published values	mb/sr	29.83 ± 1.0%		

Table 5

Summary of Electrometer Calibration

Error in applied voltage	10 μV
Resistance used*	391.4 MΩ ± 0.5%
Time for all trials**	10.00 sec

* Error includes estimated uncertainties due to humidity and other effects that can affect high impedances values.

** All values below are averages for 10 trials.

Nominal Beam Intensity	Measured Current na	Actual Current na	Absolute Deviation na	Correction Factor
0.5	0.4692 ± 0.0025	0.5895	0.1203 ± 0.0025	0.797
1.0	0.9636 ± 0.0025	1.0870	0.1238 ± 0.0025	0.887
2.0	1.8966 ± 0.0025	2.0288	0.1322 ± 0.0025	0.934
3.0	2.8434 ± 0.0032	2.9831	0.1397 ± 0.0032	0.953
4.0	3.7704 ± 0.0032	3.9172	0.1468 ± 0.0032	0.963
5.0	4.7844 ± 0.0032	4.9384	0.1540 ± 0.0032	0.969
6.0	5.8092 ± 0.0050	5.9711	0.1619 ± 0.0050	0.973

Error in charge measurement due to loss of secondary electrons also has not been measured. Some measurements made at the University of Manitoba[77] indicate that this effect is small. A 2% error for this effect is added in quadrature to the uncertainty in the measured cross section.

V.2.3 Solid Angle Calculations

The p-p elastic solid angle depends on the area of the collimators used in the experiment, and the distance from the beam to the collimators. Three collimator sizes were used during the elastic cross section measurements. Their areas were measured using a vernier caliper accurate to 10 μ. The distances from the beam to the exits of the collimators have been measured from a scale drawing of the spectrometer. Collimators II and III made an angle of 12.5^{o} to the proton directions. The effective areas are therefore reduced by 2.4%. The measured values of all pertinent quantities and their uncertainties are given in Table 4.

V.2.4 Reaction Length Determination

The observed length of hydrogen gas depends on three quantities: The width (W) of the slit in the baffles at B2 (See Fig. 2); the distance from the beam to the collimator behind the right wire chamber (d_1); and the distance from the beam to the slit in the baffles at B2 (d_2). Distances d_1 and d_2 are measured along the proton paths. From a simple geometrical argument, the observed length of target is

$$L_{el} = W \cdot \frac{d_1}{(d_1 - d_2)} \qquad \text{V-4}$$

The denominator is independent of beam position. The results are shown in Table 4.

V.2.5 Dead-Time Correction

Dead-time effects in the fast electronics were dominated by the discriminators used in the measurement. The dead-time associated with each pulse was 1.2 μsec. Corrections were made for this by counting the number of output pulses from each of the two discriminators. Typical corrections (C_{DT}) were ~5%.

V.2.6 Correction for H_2 Gas Density

The $\left.\frac{d\sigma}{d\Omega}\right)_{el}$ measurements are corrected (C_{TP}) for the deviation of the H_2 gas density in the scattering chamber from STP conditions. The temperature was measured to $\pm$ 0.2°C using a mercury thermometer mounted inside the scattering chamber. The H_2 gas was at atmospheric pressure, which was determined three times (at intervals of 8 hours) using a mercury barometer. The three measurements were nearly the same (within 0.7 mm), but uncertainty in the gas pressure is estimated as $\pm$ 1.5 mm because of the long time span between measurements.

V.2.7 Multiple-Scattering Corrections

Corrections due to multiple-scattering (C_{MS}) are small in spite of the fact that one proton in ~24% of the events hits a tungsten wire in the front wire chambers. The polar angle resolution for protons hitting wires is 2.4°. The upper cut-off in the polar angle for the left hodoscope was 47.5°. For Collimator I the polar angle range was 44.7° $\pm$ 1.24°. As a result, 3 $\pm$ 1% of the p-p elastic events were lost because the left proton hit the baffle behind the left wire chamber (See Fig. 3(b)). The polar angle ranges for Collimators II and III were both 44.7° $\pm$ 1.09°. The lost events again amount to 3 $\pm$ 1% of the p-p elastic events.

V.2.8 Uncertainty in $\left.\frac{d\sigma}{d\Omega}\right)_{el}$

The uncertainties of all the quantities in equation V-3 have been estimated. The total uncertainty in $\left.\frac{d\sigma}{d\Omega}\right)_{el}$ is obtained by compounding the individual errors in quadrature. A 2% error for possible losses of secondary electrons from the Faraday Cup is also added in quadrature. The results are summarized in Table 4.

These uncertainties overestimate the error in the product $\frac{d\sigma}{d\Omega}\}_{el}$ L_{el} $\Delta\Omega$ in C_N (Equation V-2). If equation V-3 is substituted into V-2, the effects of L_{el} and $\Delta\Omega$ are cancelled. In addition, the correction C_{MS} is common to N_{el} (from the ppγ data runs) and is also cancelled. The uncertainty in the product $\frac{d\sigma}{d\Omega}\}_{el}$ L_{el} $\Delta\Omega$ for ppγ cross section normalization purposes (Collimator II) is 2.7%.

V.2.9 <u>Results</u>

A summary of the $\frac{d\sigma}{d\Omega}\}_{el}$ measurement is contained in Table 4. The mean measured cross section was 29.39 ± 2.6% mb/sr. A value for 42 MeV, extrapolated from the results contained in References 74 and 75, is 29.83 ± 1.0% mb/sr. The agreement is good.

CHAPTER VI

DATA COLLECTION

The ppγ data were collected in the summer of 1970. During much of the next year the analysis procedures were carefully optimized, systematic errors identified and eliminated if possible, and improvements in the experimental procedures investigated.* A total of 950,000 events was recorded on magnetic tape during ppγ data runs and was collected under a variety of experimental conditions. Analysis to identify the 5000 ppγ events was a lengthy process, since each individual run was examined in detail for systematic errors and anomalies. In addition, several other sets of data were collected and used to make various calibrations, to test analysis procedures, and to estimate prompt backgrounds in the ppγ data. A summary of all data collected is given in Table 6. The data-collection procedures and a description of the on-line data analyses are presented in this chapter.

---

* In October 1971, a sequel to this experiment was performed, also at 42 MeV incident beam energy. Analysis of this new data is not completed at present.

Table 6

Summary of Data

	Reaction	Beam Energy	Target Gas	Purpose
1.	p-p elastic scattering	42 MeV	H_2	Determination of angular resolutions, energy resolutions and vertex error distributions; test of X^2 analysis procedure
2.	p-p elastic scattering	24 MeV	H_2	Determination of angular resolutions, energy resolutions and vertex error distributions; test of X^2 analysis procedure
3.	$He^4(p,2p)T^3$	42 MeV	He	Determination of energy resolutions and wire chamber uniformity; tests of X^2 analysis procedure and procedure for adjustment of vertex errors; investigation of prompt background in $pp\gamma$ data
4.	Various (p,2p) and other reactions on N^{14} and O^{16}	42 MeV	Air	Investigation of prompt background in $pp\gamma$ data
5.	$N^{14}(p,2p)C^{13}$	42 MeV	N_2	Same purpose as in 3. above
6.	$D(p,2p)n$	42 MeV	D_2	Same purpose as in 3. above
7.	$p(p,2p)\gamma$	42 MeV	H_2	$pp\gamma$ data for cross section measurements

VI.1 ORIGIN OF WIRE CHAMBER TRIGGERS

The wire chambers were triggered whenever the scintillation counters detected two particles within 28 ns of each other (prompt trigger) or when the particle in the left counter was detected 35 ± 14 ns after the one in the right (random trigger). Since the plastic scintillators used were also good detectors of neutrons, these coincidences could be between two protons, two neutrons or one proton and one neutron.

The relative frequency of the possible types of coincidence was investigated at various incident beam intensities. Some results are shown in Table 7 for proton beam intensities of 1 and 3 na. The uncertainties in comparing to the number of ppγ events, are due only to statistical errors in the number of counts of each type.

At 1 na beam intensity, the coincidence rate is about 20/sec which yields ~120 ppγ events/hour. At 3 na beam intensity, the coincidence rate is ~110/sec, yielding ~350 ppγ events/hour. The observed rates are reduced by the computer dead-time and wire chamber inefficiencies. The random trigger rate was ~4 times the prompt rate at the average beam current ($\lesssim 3$ na) used in the experiment and ~1200 wire chamber triggers were needed to detect 1 ppγ event.

Table 7

Classification of Coincidences in PPγ Runs

The numbers of coincidences caused by the various combinations of triggering particles are summarized and compared to the number of ppγ events.

Note: Particles are specified for the left and right hodoscopes in the order left-right.
p = proton, n = neutron

(a) 1 na Beam Intensity

Type	Prompt #/nc	Random #/nc	Net	Net:Ratio to ppγ	Total:Ratio to ppγ
pp	5.39	2.38	3.01 ± 0.41	100 ± 14	259 ± 14
pn	2.26	1.84	0.42 ± 0.23	14 ± 8	137 ± 8
np	1.57	0.59	0.98 ± 0.20	33 ± 4	72 ± 7
nn	2.22	0.42	1.80 ± 0.12	60 ± 4	88 ± 4
p-p elastics	1.09		1.09	36 ± 1	36 ± 1
ppγ	0.03		0.03	1	1
Total	12.56	5.23	7.33 ± 0.53	244 ± 18	593 ± 18

(b) 3 na Beam Intensity

Type	Prompt #/nc	Random #/nc	Net	Net:Ratio to ppγ	Total:Ratio to ppγ
pp	9.50	6.28	3.22 ± 0.60	107 ± 20	526 ± 20
pn	5.66	4.94	0.72 ± 0.33	24 ± 11	353 ± 11
np	2.31	1.77	0.54 ± 0.27	18 ± 9	136 ± 9
nn	3.74	1.73	2.01 ± 0.17	67 ± 6	182 ± 6
p-p elastics	1.09		1.09	36 ± 1	36 ± 1
ppγ	0.03		0.03	1	1
Total	22.33	14.72	7.61 ± 0.79	253 ± 26	1234 ± 26

VI.2 DATA-TAKING PROCEDURES

To ensure reliability of all data runs, a standard set of data-taking procedures was followed to provide checks for possible errors, equipment malfunctions and changes in any of the important equipment calibrations. In the set-up stages of the experiment, before any ppγ data accumulation was attempted, all equipment was checked and calibrated. This included tuning of the fast electronics, testing the reliability of the wire chamber readout electronics, determination of the proper sparking conditions for the wire chambers, calibration of the beam positioning device and setting approximate photomultiplier voltages for the scintillation counters.

A number of programs were used on the PDP-15 to check equipment and perform calibrations. The reader is referred to References 39, 41 and 47-49 for more details on their use and on the software system developed for use on the PDP-15. The data-taking procedures before, during and after data runs are described below.

VI.2.1 Pre-Run Checks

(a) The pulse heights for p-p elastic events were set to their desired values. Special care was taken to ensure that the pulse heights from the top and bottom photomultipliers of each counter were equalized, since this affected the upper energy cut-offs. This check was repeated about every 24 hours or when unacceptable photomultiplier drifts occurred.

(b) The chamber and vertex efficiencies were checked and minor adjustments made in the sparking voltages to maximize the vertex efficiency. The pulse height spectra were also checked to ensure that the sparking noise was properly gated out. P-P elastic events and low beam intensity were used.

(c) The beam profile in the chamber was observed and beam tuning parameters were adjusted if necessary.

VI.2.2 Mid-Run Checks

(a) Measured parameters were continuously observed to monitor electronic drifts, the lateral position of the beam and the vertical beam profile. Histograms produced by the on-line 360/65 program were used to check the quality of fully processed data.

(b) During actual data-taking there was no means of monitoring the wire chamber efficiency in detail due to limitations in the memory and basic speed of the PDP-15. Accordingly, only a coarse estimate of the overall vertex efficiency was provided by printing the number of events processed for every n buffers of events sent to the 360 computer. Whenever this number became too large, data-taking was halted and the causes of the observed inefficiency investigated. It was possible to interrupt a run, load different PDP-15 programs, check chambers and resume the run where it left off.

VI.2.3 Post-Run Checks

Wire chamber efficiencies and the overall vertex efficiencies were routinely checked at the completion of each run, scalers recorded, beam tuning checked and the PDP-15 and 360 run summaries checked for any anomalies. Examples of these summaries are given in Sec. VI.3.

VI.3 ON-LINE COMPUTER ANALYSIS

VI.3.1 Description of PDP-15 Analysis

The PDP-15 computer was used to start and stop data-taking, pre-process events and provide feedback to the experimenter. The most important on-line program used on the PDP-15 was the VRTX program, which is described in Ref. 47. The function of the VRTX program was to record the 111 words of wire chamber and ADC information for each event, decode the sparks to obtain their track coordinates and reject undesired events in order to condense the volume of data. Events rejected included

(a) events where the particle tracks were uncorrelated and did not make an acceptable vertex in the 22 cm long reaction volume;

(b) events produced by neutral particles; and

(c) events where there was insufficient or ambiguous information about the particle tracks.

No information for rejected events was saved for further processing. For each event accepted at the PDP-15, only 11 words of information were required for the subsequent 360 analysis. These were the real-random flag (identifying the coincidence unit, C_P or C_R, causing the trigger), two coordinates for each of the four wire chambers and the two ADC values for the particle energies.

The PDP-15 made histograms of the vertical vertex position and the vertex error along the beam direction and displayed them on the oscilloscope. A set of six histograms returned from the 360 computer, after every buffer of 45 vertex events was collected and transferred from the PDP-15 to the 360, could be displayed on the oscilloscope if desired. The VRTX program created a table, for each data run, summarizing the PDP-15 analysis. This indicated how events were rejected in each wire chamber and gave information on the track combinations and chamber efficiencies. Examples of these run summaries are given in Sec. VI.3.3.

VI.3.2 On-Line Analysis at the 360/65

The 360/65 computer was used to perform a complete statistical and kinematical analysis of each event accepted by the PDP-15. The usual on-line program used was the KIN program which is described in References 47 and 81.

The Kin program produced six 50-channel histograms that could be displayed at the PDP-15 (in place of the two previously mentioned histograms). These histograms and their constraints were specified at the PDP-15 at the start of each run and could be changed as desired. They were very useful while debugging and running the experiment and often identified hardware faults or setup errors. During the ppγ experiment, some of the histograms observed included the X^2 distributions (explained later) for prompt and random ppγ events, the lateral beam position for p-p elastic events, the distribution of events along the beam direction and the missing energy (E_o-E_L-E_R) for random events.

The KIN program also used the p-p elastic calibration events to update the detector PHT-energy calibration constants every few minutes.

All pre-processed data was recorded on magnetic tape for future analysis and processing. A run summary containing the numbers and types of events collected (ppγ, D(p,2p)n, calibration elastics) was produced and sent to the PDP-15 computer after each data run. An example is given in Table 8. All important steps in the run were also recorded on the 360/65 line printer--the time data-taking commenced, what histograms were specified, changes in the energy calibration constants, run constants, the times at which interruptions in the run occurred and the time that data-taking was stopped. The KIN program could process 80 events/sec and record ~80000 fully-processed events on a 2400 ft magnetic tape.

Table 8

Summary of a PPγ Data Run Returned from the 360/65 Computer to the PDP-15 Computer

Good PDP-15 Vertex 74131	Bad ADC 0	Randoms 11341	Reals 62790
# Elastic 13791	# ppγ Real 507	# ppγ Rand 75	# Net ppγ 432
# D_2 Real 1588	# D_2 Rand 284	# Ambig 0	# Deut Net 1304

KL = 1.041 KR = 0.996

No. of times slopes adjusted = 59

Length of Run	3.5 hours
Beam intensity	1 na

KL and KR give the ratio of the p-p elastic pulse heights to their desired values. The "D_2" events are D(p,2p)n events.

VI.3.3 Results of PDP-15 Analysis

In this section some operating characteristics of the wire chambers are discussed. The rejection efficiency for neutron-proton and neutron-neutron coincidences is considered and possible systematic errors due to events being misinterpreted by the PDP-15 computer are estimated.

In Table 9, a run summary from the VRTX program for p-p elastic events at 3 na beam intensity is presented. Some explanation of the table is necessary. In principle, with three planes it is possible to resolve any number of particle tracks. However, because of the software complexity involved, events with more than two particle tracks were rejected. In the VRTX program all combinations of spark coordinates in the horizontal, vertical and diagonal planes were tested to see if they intersected at a common point (such a combination was called a set of consistent coordinates and is abbreviated by COORD in the table). Depending on the number of tracks detected in a chamber (0, 1 or 2), and information lost due to wire chamber inefficiencies, there could be 0, 1 or 2 consistent coordinates. Very rarely, when two tracks passed very close to each other, there could appear to be more than 2 coordinates. Events of this type were labelled as "too ambiguous" and

Table 9

Summary of PDP-15 Analysis for p-p Elastic Events

Chamber		Accept - Process next Chamber	Reject - Not enough Information	Reject - All Planes Empty	Reject - Too many Tracks (>2)
Front	Left	980	0	2	18
	Right	944	10	1	6
Back	Left	924	1	1	2
	Right	913	0	1	6

Chamber		Reject - 1 track 0 co-ord	1 track 1 co-ord	Reject - 2 tracks 0 co-ord	2 tracks 1 co-ord	2 tracks 2 co-ords	Reject - Too Ambiguous
Front	Left	0	763	6	116	82	13
	Right	3	825	3	73	30	10
Back	Left	0	825	0	61	34	4
	Right	0	826	1	35	47	4

Too Complex For Analysis	No Vertex	Outside Target Region	Acceptable Vertex Errors	# Triggers
1	52	7	848	1000

Beam intensity	3.0 na
# prompt coincidences	1000
# random coincidences	17
Vertex efficiency	86 %

rejected. When the total number of consistent coordinates in the four wire chambers was greater than six the event was too complex for analysis. The Y and Z vertex errors determined from the reconstructed tracks were restricted to be less than 2.5 cm and 5 cm respectively. In Table 9, the chambers were not triggered on the random coincidences. A similar number are presumed to have occurred in the prompt coincidences. These (17 ± 4) events are assumed not to make a vertex when calculating vertex efficiencies. (In Table 10, which follows later, the wire chambers were sparked on these random coincidences.) The effects of chamber inefficiencies are determined by observation of the "Reject" columns, while the presence of multiple sparks is indicated by the columns with "2 tracks" or "$>$2 tracks". The number of complete misses in any chamber is small. The events that do not make a vertex have several origins. They result

(a) from random events with uncorrelated particle tracks;

(b) when a spark due to a δ-ray or a second proton robs the track of interest in one or more chambers;

(c) when one of the elastic protons hits a tungsten wire in the front chambers and is badly scattered. (For the example shown this occurs only $\sim$1% of the time.)

As can be seen from Table 9, the overall vertex efficiency for this particular run at 3 na was ~86% after correction for random triggers. About 5% of the time, the elastic proton track has been robbed by an extra spark in at least one of the chambers and the system was unable to make an acceptable vertex. Events of this nature are similar to random events so far as the vertex criteria is concerned, except that they are probably less likely to make a good vertex because relatively few of the δ-rays and extra protons come from the same region of the target volume as p-p elastic events.

A typical ppγ run summary is given in Table 10. The complete misses were due primarily to events where one or both of the triggering particles was a neutron. The fraction of events with multiple tracks (ratio of events in the "2 tracks" columns to the events processed in each chamber) was about 10% in the front chambers and ~5% in the rear chambers. This also represents an estimate of the fraction of neutral particles that are accompanied by a charged particle, resulting in a detectable track. In the total of 29204 events that pass the coarse PDP-15 vertex constraints in this data run, an approximate breakdown (similar to that in Table 8) would indicate that 14000 were

Table 10

Summary of PDP-15 Analysis of a PPγ Data Run

Chamber		Accept - Process next Chamber	Reject - Not enough Information	Reject - All Planes Empty	Reject - Too many Tracks (>2)
Front	Left	170 115	883	60 955	1297
	Right	118 513	4761	40 520	204
Back	Left	100 444	1532	12 320	69
	Right	87 781	568	11 796	181

Chamber		Reject - 1 track 0 co-ord	1 track 1 co-ord	Reject - 2 tracks 0 co-ord	2 tracks 1 co-ord	2 tracks 2 co-ords	Reject - Too Ambiguous
Front	Left	1188	141 754	4328	16 338	5907	600
	Right	1182	104 698	2769	7436	2232	196
Back	Left	16	96 890	29	2811	625	73
	Right	461	81 543	1292	3073	1281	131

Too Complex For Analysis	No Vertex	Outside Target Region	Acceptable Vertex Errors	# Triggers
8	47 931	8754	29 204	233 244

Beam Intensity	2.5 na
# prompt coincidences	138 372
# random coincidences	94 872
Vertex efficiency (from a previous run)	82 %

due to calibration and other p-p elastic events, 15000 were due to (C_P and C_R) random events, 150 were ppγ events and 300 were D(p,2p)n events. At 3 na beam intensity, typical sparking rates were 50/sec. Of these, 10 triggers were caused by p-p elastic events and 40 by random coincidences. A data buffer of 45 events was usually filled about every 5 - 7 seconds.

The fractions of pp, np and nn coincidences during ppγ runs were discussed earlier. Some events were misinterpreted by the PDP-15 because of extra proton or δ-ray tracks and passed the coarse vertex cuts. Coincidences where a neutron was one of the triggering particles present the greatest problem. The number of misinterpreted events is probably comparable to the total number of ppγ events. Vertex criteria reject about 90% of these events. A conservative estimate of the resulting background in the ppγ data is $\sim$3.5% after all background rejection criteria have been applied. This is summarized in Table 11.

Table 11

Effect of Multiple Tracks

Below is a tally of net prompt events that are misinterpreted because spurious tracks rob the track of interest or provide a spark when a neutral particle passes through the chamber.

	Fraction	Ratio to ppγ after vertex*
pp events affected	5%	0.5
np and pn events affected	5%	0.2
nn events affected	1%	0.06
calibration elastics affected	5%	0.2

		Net Ratio to ppγ
Rejection of events on an energy basis		
pp events	99%	0.003
np + nn + pn events	90%	0.03
calibration elastics	99%	0.002
Net background in ppγ regions		3.5%

* **Refer to column titled "Net:Ratio to ppγ" in Table 7. Assume 90% of affected events are rejected by vertex criteria.**

CHAPTER VII

DATA REDUCTION

The ppγ data accumulated included ppγ events, D(p,2p)n events on the natural deuterium contaminant in H_2 gas, (p,2p) and similar reactions on other impurities in the target gas, calibration p-p elastic and other p-p elastic events that had undergone differing amounts of multiple-scattering and were detected in spite of the geometrical obstructions intended to eliminate them. In addition, random events from different beam bursts were collected simultaneously with the prompt events in order to provide accurate random background estimates.

The computer analysis of this data corresponded to imposing constraints equivalent to those provided by hardware in previous experiments. For example, vertex error and position restrictions had the same effect as collimators, baffles or target containers that define the reaction volume; energy constraints were like discriminator cut-offs; and, angular binning took the place of defining slits or counters used in other experiments. Computer cuts had a distinct advantage in that they produced no multiple-scattering or energy degraded protons and the energy and angle cut-offs were sharp and known precisely.

In this sense computer applied constraints were better than physical constraints. The statistical (X^2) analysis* performed to reject background and choose the ppγ events was a useful analysis tool. The rejection or acceptance of events by a well-defined statistical method was preferable to the somewhat arbitrary procedure of only counting events in some region of an E_L-E_R plot.

The hardware constraints imposed on the present data were necessarily loose because of the large kinematical range observed. The possibility of undetected systematic errors causing rejection of ppγ events was therefore reduced when compared to other experiments. Furthermore, the extra information calculated for each event allowed problems to be traced back to their origin, understood and, in many cases, eliminated.

There are three basic methods by which backgrounds were separated from the ppγ events. Vertex errors were used to eliminate 95% of all random events and most multiple-scattered p-p elastic events as well. Vertex

---

* In the experiment, six variables (E_L, E_R, θ_L, θ_R, Φ_L and Φ_R) were measured. Only five variables were necessary to completely describe each event since there are four energy-momentum conservation relations. This extra variable allowed a goodness-of-fit parameter (X^2) to be calculated for each event, which was used to reject background. This is described later in this Chapter.

positions were used to eliminate some random events since there are concentrations of these events in regions near the upstream and downstream baffles. Undesired p-p elastic events could also be rejected since they came from a very restricted region of the gas target. Finally, large fractions of both random and prompt background events were eliminated by using a χ^2 analysis which also allowed good estimates of unrejected prompt backgrounds to be made. The data reduction procedures are now discussed in more detail.

VII.1 VERTEX CONSIDERATIONS

VII.1.1 Vertex Error Adjustments

The widths of the vertex error distributions depended on the particle energies, polar angles and origin in the target (See Sec. III.2.9 and Appendix D). It was desirable to accept events according to a statistically well-defined prescription. For example, events with vertex errors greater than 3 standard deviations from their expected values could be rejected. This would require variable limits to be applied on the allowed vertex errors. In practice, it would have been much easier to apply constant vertex cuts for all the data independent of the geometric and kinematic parameters, but this would have resulted in a systematic variation in the fraction of events rejected, depending on these parameters. To eliminate this problem, the values of the vertex errors were adjusted (DVZ and DVY) so that all events had the same statistical distribution as the calibration p-p elastic events. The correction factors used are derived in Appendix D. The effect of the vertex error adjustment is demonstrated in Fig. 23 where the HWHM's of the original and adjusted vertex errors for D(p,2p)n events are shown as a function of the opening angle between the protons. Similar results

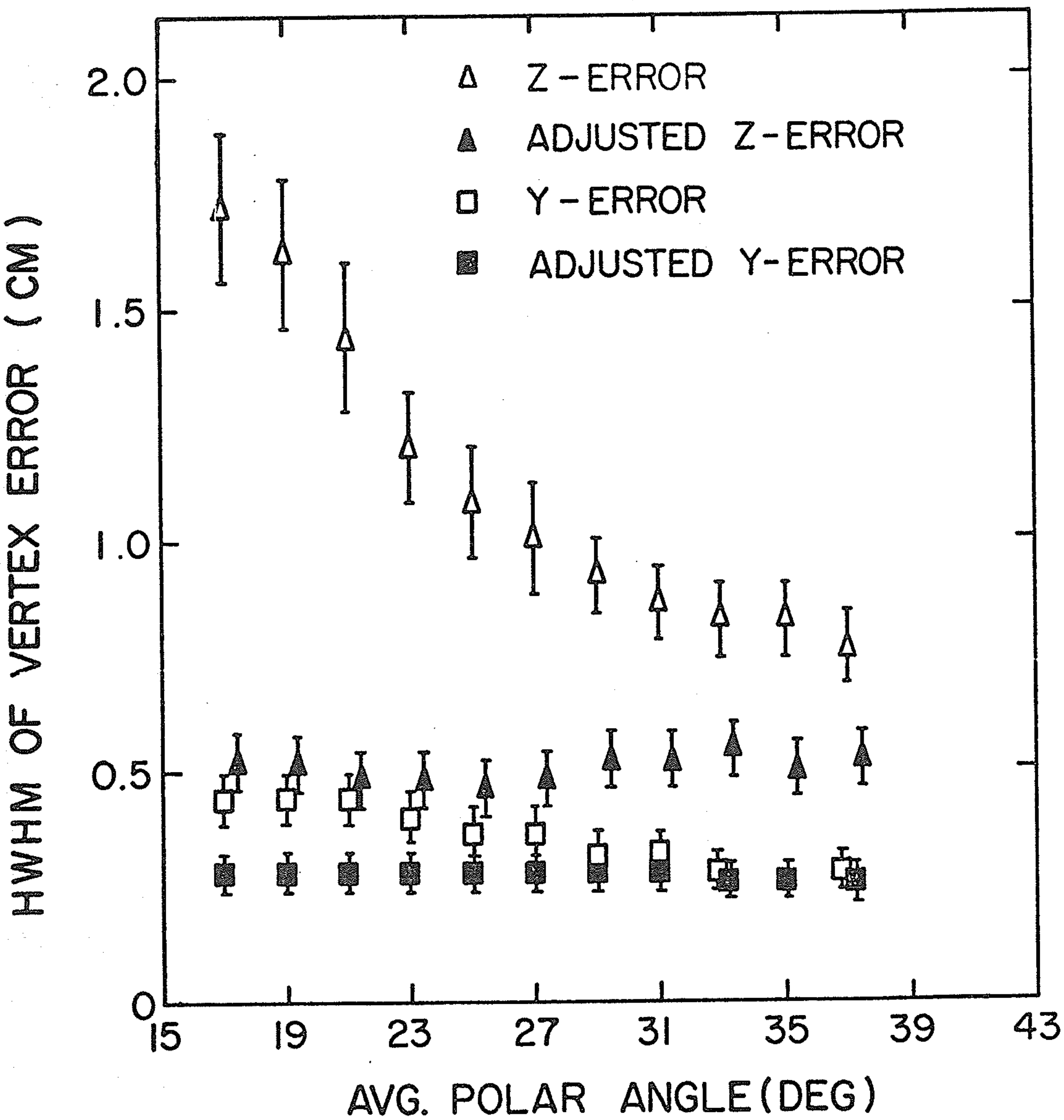

Figure 23

Distributions of the adjusted and unadjusted vertex errors for D(p,2p)n events as a function of $(\theta_L+\theta_R)/2$. The unadjusted Z-vertex error is dominated by geometrical effects depending on the polar angles of the two protons.

were obtained for the ppγ data (but with larger uncertainties since the number of events was smaller).

VII.1.2 Vertex Error Limits

The choice of the vertex error limits represented a trade-off between maximum rejection of random events and minimum loss of good ppγ events. The Z-vertex error limits were chosen so that the increase in lost ppγ events for a 1 mm shift in the beam was $< 2\%$. The 1 mm beam shift corresponded to a 0.3 standard deviation shift in the Z-vertex error. Consideration was also made for those events where one of the protons hit a wire in a front chamber. The limits chosen were $\pm$ 7.5 mm and $\pm$ 12 mm for the Y and Z adjusted vertex errors respectively. These corresponded to approximately 4σ for events not hitting any wires and $\sim 1\sigma$ for events where one proton passed through a tungsten wire.

VII.1.3 Vertex Acceptance

In spite of the adjustment of vertex errors, systematic errors due to vertex cuts were not completely eliminated. The vertex limits used at the PDP-15 (on the unadjusted vertex errors) were sufficiently wide that all events which would have been accepted in the subsequent

360/65 analysis were retained. Reference to the vertex error distribution shown in Fig. 15 shows that the only events rejected by the vertex cuts hit tungsten wires in the front chambers. However, some ppγ events also hit these wires and are still accepted by all rejection criteria. Since the adjustment of the vertex errors in the KIN program only partially compensated for multiple-scattering in the tungsten wires, there was a variation in the fraction of ppγ events detected depending on the particle energies. In order to evaluate these systematic errors, sets of $He^4(p,2p)T^3$, $N^{14}(p,2p)C^{13}$ and D(p,2p)n data as well as the ppγ data were analyzed and the total fraction of events eliminated by vertex cuts estimated.

The systematic error due to variation in the vertex error acceptance for ppγ events was determined relative to 42 MeV p-p elastic events at 45° to the beam, since the ppγ cross sections were normalized to these events. The total fraction of events lost was obtained by compounding the effects of the Y and Z vertex errors. Calculations of this error from the equations used in the vertex error adjustments and the multiple-scattering in tungsten wires indicate that it varied from $\sim$7% for $18^\circ - 18^\circ$ ppγ events to $\sim$5% for $38^\circ - 34^\circ$ events. This was verified by observation of the ppγ events except that statistical fluctuations (typically $\pm$ 4%) were larger than the variation with polar angles. For this reason an average value of 6 $\pm$ 1% is used to compensate for lost ppγ events. The 1% error was based on the estimated variation over the polar angle range observed.

VII.1.4 Vertex Position

The two baffles along the beam were possible sources of prompt and random backgrounds. The ppγ data has been restricted to a region which excludes the baffles at B2 in the downstream portion of the scattering chamber. The B1 baffles were included in the allowed reaction volume since analysis of vertex distributions indicated that a tolerable increase in random backgrounds resulted.

VII.2 STATISTICAL ANALYSIS

VII.2.1 Definition of X^2

Each ppγ event detected was once over-determined since five physically significant variables were measured (E_L, E_R, θ_L, θ_R, Φ_r). This allowed a goodness-of-fit parameter (X^2) with one degree of freedom to be used to reject background. The quantity that was chosen for comparison to a known value was the total energy of the system in the final state as calculated from momentum conservation. The definition of X^2 given by

$$X^2 = \frac{(E_F - E_I)^2}{\Delta E_F{}^2} \qquad \text{VII-1}$$

is at best a first order approximation to the rigorous X^2 for one degree of freedom, and has been discussed in detail elsewhere[47,76]. The uncertainty (ΔE_F) in the final state energy E_F was determined by compounding the expected errors* of all the measured parameters[47]. An error in E_I of $\pm$600 keV was included to allow for beam energy changes and detector calibration errors.

VII.2.2 Systematic Errors Due to X^2 Cuts

The X^2 determined was only an approximation as were the estimates of the uncertainties in the measured parameters. The X^2 cut in the ppγ data was chosen to be

---

* The error estimates used in the X^2 analysis were HWHM values (HWHM = 1.17σ). This allowed for uncertainties in estimating resolutions and reduced the danger of rejecting good ppγ events.

5.412. For a rigorous X^2 parameter, this would correspond to rejection of 2% of all events. The fraction of events rejected by the X^2 cut was investigated in several ways. The X^2 distributions for 42 and 24 MeV p-p elastic events, D(p,2p)n events and for ppγ events with random backgrounds subtracted are shown in Fig. 24.

In parts (a) and (b), for the p-p elastic events, the vertex error limits were not comparable. The allowed vertex errors in (a) were the same as in the ppγ data analysis, while in (b) they were somewhat smaller and a larger fraction of events was rejected (mainly events hitting the tungsten wires). This indicates the effect of eliminating events that hit the wires. The X^2 distributions for 42 and 24 MeV p-p elastic events, unrestricted on their vertex errors, are very similar to each other.

The bar histogram in (d) represents all net prompt events in the ppγ data with $X^2 \leqslant 50$. The surplus of events in the tail of the X^2 distribution is obvious and is mainly due to D(p,2p)n events and (p,2p) reactions on other contaminants in the H_2 gas. The dots represent the X^2 distribution for ppγ events with the estimated background subtracted.

The procedure used to subtract this background

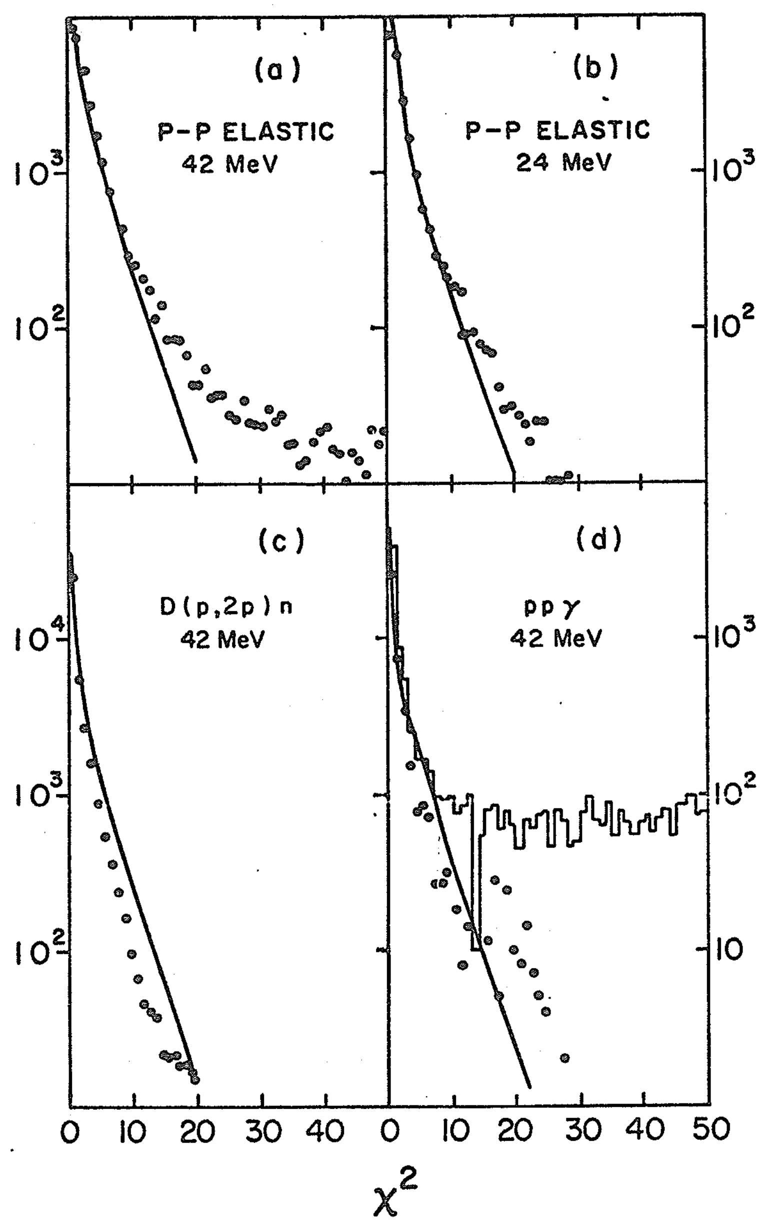

Figure 24

X^2 distribution of events for several different reactions.
(a) P-P elastic events at 42 MeV beam energy.
(b) P-P elastic events at 24 MeV beam energy.
(c) D(p,2p)n events at 42 MeV beam energy.
(d) PPγ events at 42 MeV beam energy.

Random backgrounds are subtracted. In (d) the bar histogram includes the effects of all prompt contaminants. The dots show the distribution with the estimated backgrounds subtracted. The smooth curve in each part is the expected X^2 distribution for one degree of freedom normalized to the total number of events with $X^2 \leqslant 5$.

was quite straightforward. Using the set of D(p,2p)n data in (c) the distribution in X^2 when analyzed as ppγ was determined. This distribution was scaled according to the number of D(p,2p)n events, which are easily identified on the basis of their energies, in the ppγ data, and subtracted from the bar histogram in (d). This left all prompt background not due to D(p,2p)n events. It was then assumed that no ppγ events would have $X^2 \geqslant 40$. All events in the region $40 \leqslant X^2 \leqslant 50$ were assumed to be due to (p,2p) reactions on N^{14}. The X^2 distribution for a set of data taken with N_2 gas in the gas cell, and analyzed as ppγ, was then scaled and subtracted in a similar manner as for the D(p,2p)n events. This yielded an estimated background of 14 $\pm$ 3% in the ppγ data with $X^2 \leqslant 5.412$. It is estimated that 4 $\pm$ 2% of the ppγ events have $X^2 \geqslant 5.412$. The error is due mainly to uncertainty in the background subtraction. Points in (d) are not shown for $X^2 \geqslant 30$ because of large statistical errors in the individual points.

VII.3 PPγ EVENT VERIFICATION

VII.3.1 Kinematic Considerations

The kinematics of ppγ events is such that for a given non-coplanarity the events must lie on an elliptical closed curve in the $E_L - E_R$ plane. This "ellipse" shrinks to a point in the limit as the maximum possible non-coplanarity is reached. A number of representative ppγ loci and kinematic loci for some contaminant (p,2p) reactions are shown in Appendix B. Because of finite energy and angular resolution, the events do not lie precisely on the expected loci. The X^2 statistical test was used to select those events that are sufficiently close to their proper loci.

VII.3.2 Detected Events

$E_L - E_R$ scatter plots of the ppγ data provide striking visual verification of the existence of ppγ events. The ppγ data have been separated into a number of polar angle bins (described earlier in Chapter IV). Three representative polar angle bins are shown, 34^o-26^o, 22^o-22^o and 30^o-30^o in Figs. 25, 26, and 27 respectively. In part (a) of each figure, the data were constrained only on good vertex, and random events have been subtracted. In (b) the

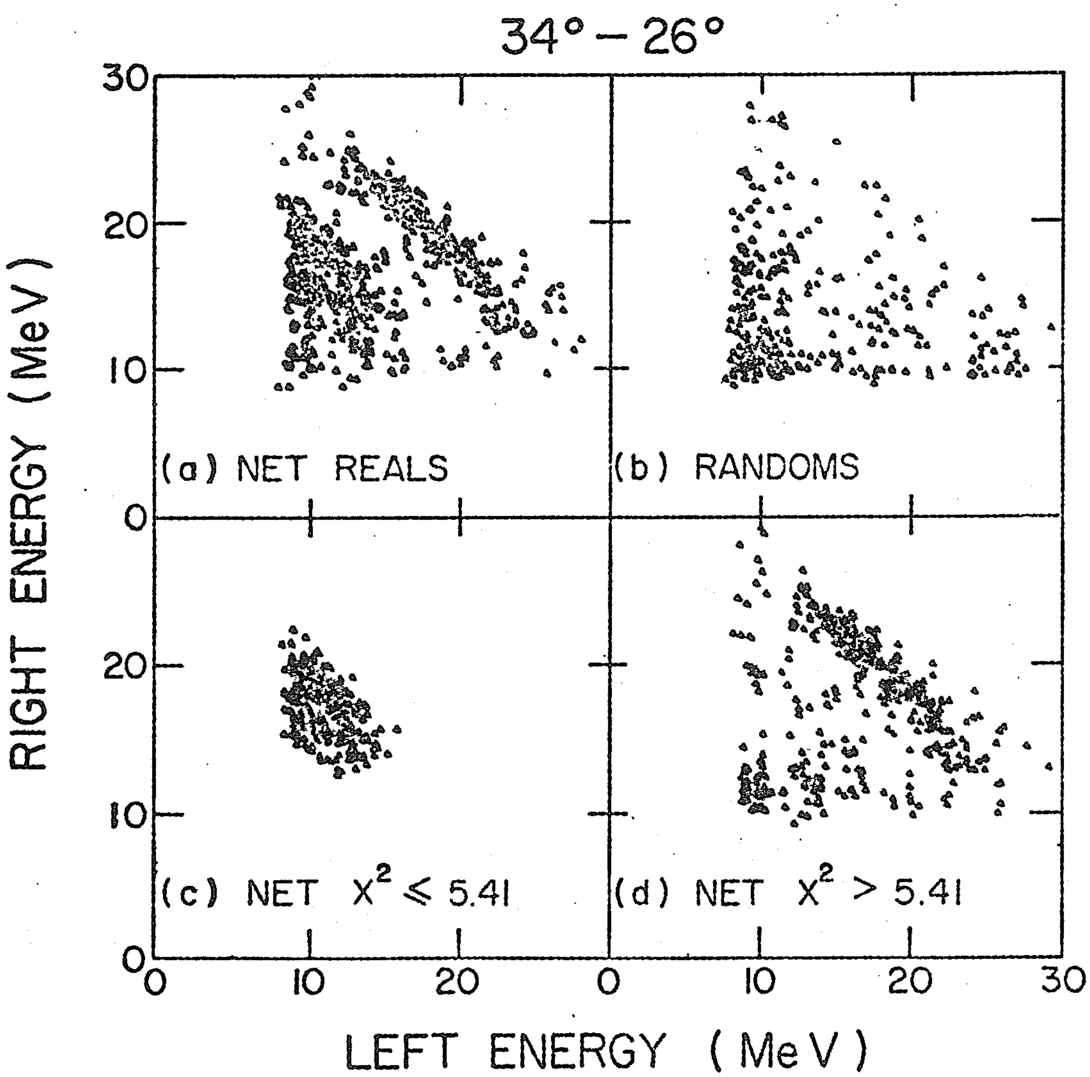

Figure 25

Distribution of events in the ppγ data in the 34°-26° polar angle bin limited on vertex errors.

(a) All events with random background subtracted.
(b) Random events.
(c) Events with $X^2 \leq 5.412$ with randoms subtracted.
(d) Events with $X^2 \geq 5.412$ with randoms subtracted.

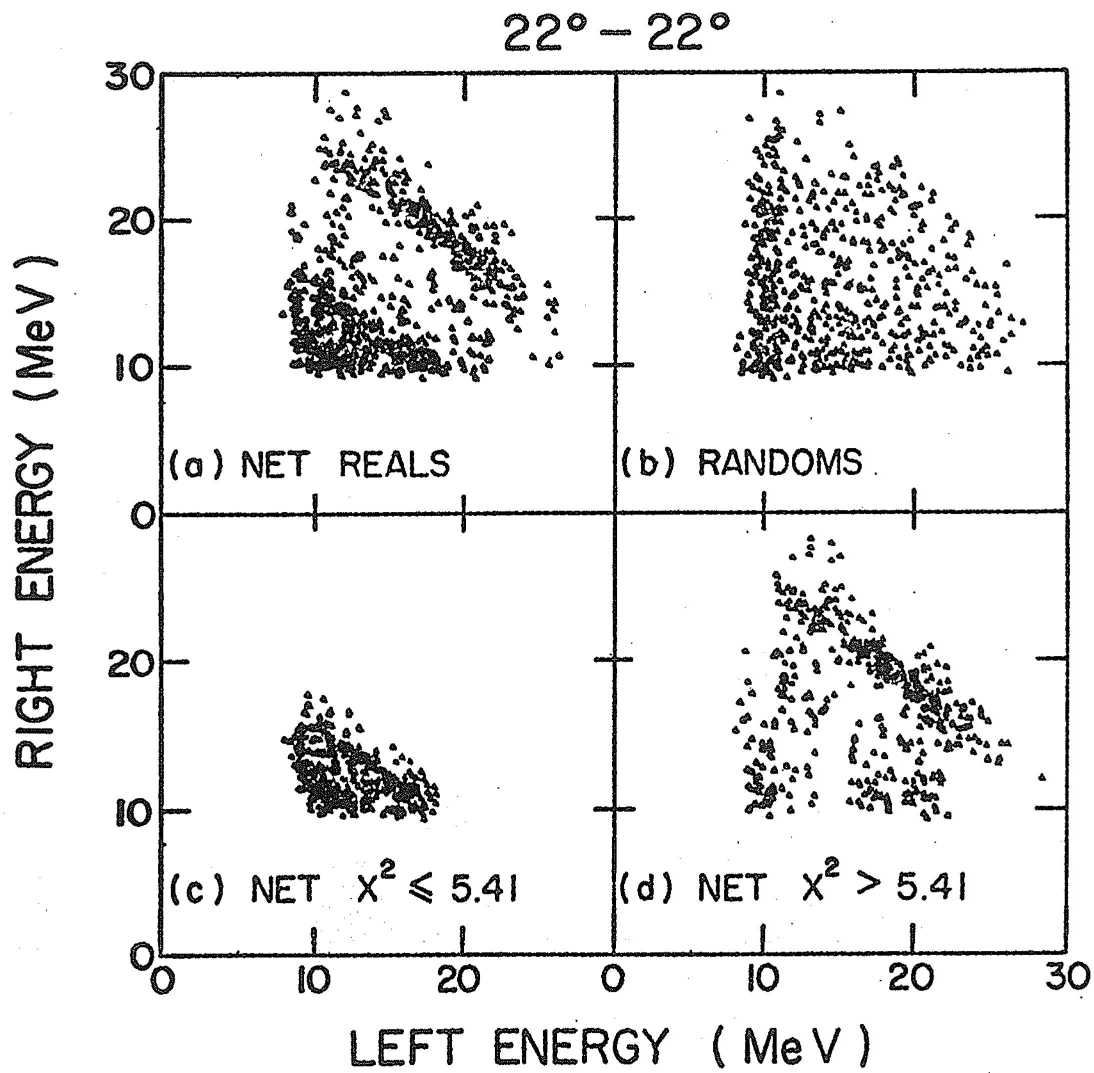

Figure 26

Distribution of events in the ppγ data in the 22°-22° polar angle bin limited on vertex errors.

(a) All events with random background subtracted.
(b) Random events.
(c) Events with $X^2 \leqslant 5.412$ with randoms subtracted.
(d) Events with $X^2 \geqslant 5.412$ with randoms subtracted.

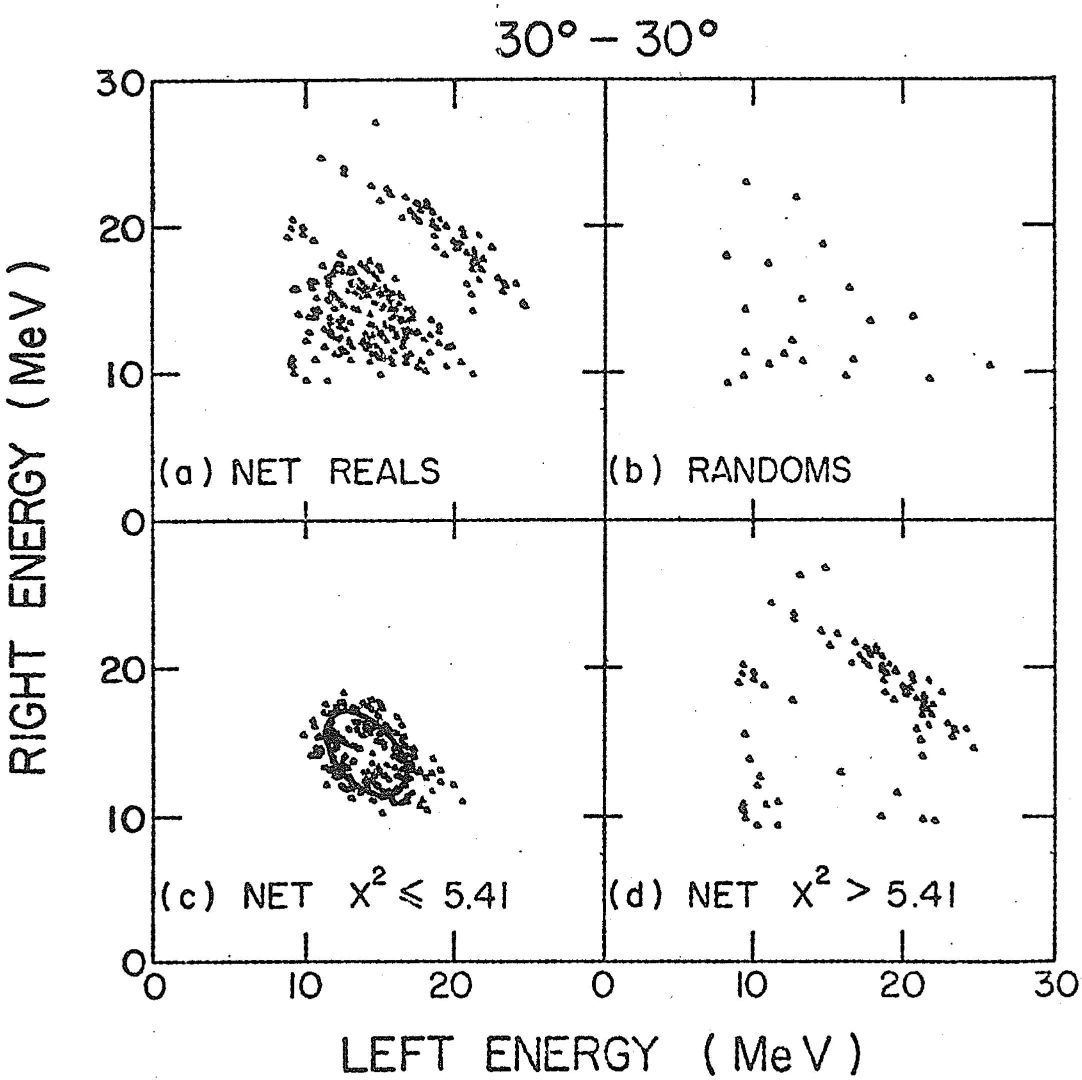

Figure 27

Distribution of events in the ppγ data for the 30°-30° polar angle bin limited on the vertex errors and $\Phi_r \leqslant 0.5$

(a) All events with random background subtracted.
(b) Random events.
(c) Events with $\chi^2 \leqslant 5.412$ with randoms subtracted.
(d) Events with $\chi^2 \geqslant 5.412$ with randoms subtracted.

The closed curve in (c) is the allowed kinematic locus for proton polar angles of 30°-30°. The lower density in the center of the cluster of points is apparent.

random contribution subtracted from (a) is shown. The clustering of events in part (a) of each figure is near the appropriate ppγ locus for the polar angles considered. The net events, after the χ^2 cut was applied, are shown in (c), while the rejected prompt events are shown in part (d). The band due to D(p,2p)n events from the D_2 contamination in the H_2 gas is prominent. The kinematic loci for D(p,2p)n events are nearly independent of the polar angles and do not appear to move in the figures shown. The increase in the number of random events at small angles is indicated by the difference in the densities of points in part (b) of each figure. The effect of the energy cut-offs is seen in all of the figures. For the $30^\circ - 30^\circ$ angular bin, the events have been restricted to have non-coplanarities ≤ 0.5 of the maximum allowed kinematically. The decreased density in the center of the cluster of events is evident. These plots, coupled with the striking χ^2 peak in Fig. 24(d), leave little doubt as to the nature of the events detected.

VII.4 BACKGROUND CORRECTIONS

VII.4.1 Random Events

While random events presented the largest background in the ppγ experiment, it was the easiest one to correct for. During data-taking, random events with particles from two successive beam bursts were recorded at the same time as prompt events (See Fig. 4 and Sec. III.1.3). Thus the random data and ppγ data were collected and analyzed under nearly identical experimental conditions. The contribution due to random events in the angular bins considered is summarized in Table 13.

VII.4.2 Prompt Backgrounds

Possible prompt background sources included

(a) p-d elastic scattering;

(b) p-p elastic events that underwent large angle scattering in the front wire chambers or 50 μm Mylar foil parallel to the beam;

(c) (p,2p), (p,pd), (p,pt) or breakup reactions on contaminants in the hydrogen gas;

(d) prompt events due to p-p elastic, np or nn coincidences that were misinterpreted at the PDP-15 level due to spurious tracks (See Sec. VI.3.3).

In order to investigate the origin of the prompt background in the ppγ data, events that had

$X^2 \geqslant 5.412$ have been examined. An example of a scatter plot and a single histogram of the missing energy are given in Fig. 28(a & b). Very restrictive vertex errors ($\leqslant 1$ standard deviation) have been used in these particular plots to eliminate multiple-scattered events and make identification of gas contaminants possible. PPγ events with X^2 values less than 2 were also eliminated. The dominant band is due to the D(p,2p)n reaction. The structure of the events in the missing energy plot is similar to one obtained during investigations with N_2 gas or air as the target. Some of the prompt events could be (p,2p) reactions on O^{16} of He^4.

The correction for all prompt backgrounds has been done by analyzing, as ppγ events, sets of data taken with D_2 or N_2 gas in the scattering chamber. It was found that consideration of only these two contaminants represented the possible backgrounds very well. Elastic p-d scattering cannot be seen because of the energy thresholds of the system and multiple-scattered elastic events are similar to deuterium breakup events. The correction procedure is now explained.

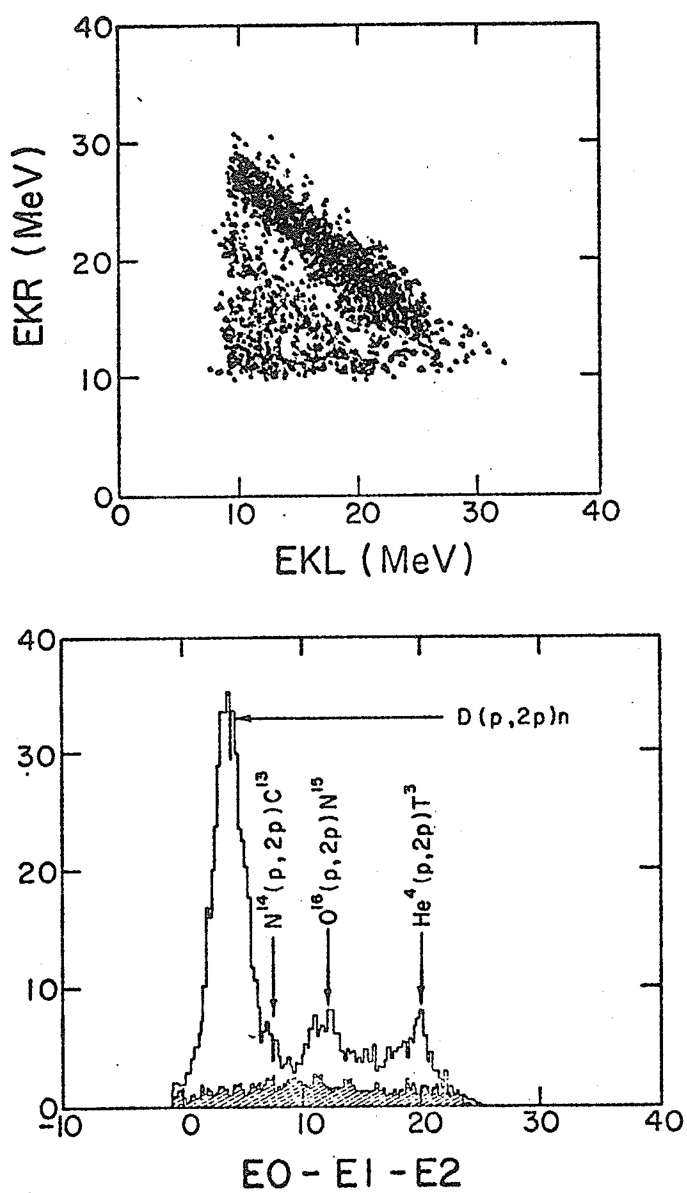

Figure 28

(a) E_L-E_R scatter plot of events that have very tight vertex limits ($\lesssim$1 standard deviation) and have $X^2 > 2$ for ppγ. Random backgrounds have been subtracted.

(b) Histogram of the missing energy for events in (a). The contribution due to random events is given by the shaded portion of the histogram. The four lines indicate the positions where (p,2p) reactions on (1) D^2, (2) N^{14}, (3) O^{16} and (4) He^4 would yield contributions.

VII.4.3 <u>Correction Procedure</u>

The ppγ data was taken using commercial grade H_2 gas which contained an estimated impurity of $\sim$400 - 500 ppm of air. This resulted in an average prompt background of $\sim$15% in the ppγ data. The X^2 analysis procedure was used to estimate this background. Sets of data with D_2, N_2, Air or H_2 gas targets and the Monte Carlo ppγ data were processed off-line on the 360/65 computer and a X^2 value calculated for each of the following reaction hypotheses

(a)	$p + p \rightarrow p + p + \gamma$		$Q = 0$
(b)	$p + D^2 \rightarrow p + p + n$		$Q = -2.226$ MeV
(c)	$p + N^{14} \rightarrow p + p + C^{13}$		$Q = -7.54$ MeV
(d)	$p + O^{16} \rightarrow p + p + N^{15}$		$Q = -12.17$ MeV
(e)	$p + C^{12} \rightarrow p + p + B^{11}$		$Q = -15.94$ MeV
(f)	$p + He^4 \rightarrow p + p + T^3$		$Q = -19.86$ MeV

Reactions (b) - (f) span the full energy range for ppγ events. The more negative Q values correspond to ppγ events with smaller polar angles. The six X^2 values calculated were summarized in a table (matrix) for each set of data mentioned above. The summaries for the Monte Carlo "fake" ppγ data, the actual ppγ data and the data with an N_2 gas target are contained in Tables 12(a), 12(b) and 12(c) respectively.

Table 12

Distribution of Net Real Events According to Hypothesis

(a) Monte Carlo ppγ events   Total = 22788 events

		(1)	(2)	(3)	(4)	(5)	(6)
ppγ	(1)	10	1	716	5364	9153	2467
D(p,2p)n	(2)	1	0	0	0	0	0
N^{14}(p,2p)C^{13}	(3)	716	0	4	3	0	0
O^{16}(p,2p)N^{15}	(4)	5364	0	3	29	16	0
C^{12}(p,2p)B^{11}	(5)	9153	0	0	16	36	8
He^{4}(p,2p)T^{3}	(6)	2467	0	0	0	8	13

χ^2 for reactions	(1,2,3)	(1,3,4)	(1,4,5)	(1,5,6)	5.412
	2	488	3351	1126	

(b) ppγ data   Total = 14314 events

		(1)	(2)	(3)	(4)	(5)	(6)
ppγ	(1)	4	4	255	1273	1548	618
D(p,2p)n	(2)	4	5693	1742	-1	0	0
N^{14}(p,2p)C^{13}	(3)	255	1742	316	78	0	0
O^{16}(p,2p)N^{15}	(4)	1273	-1	78	639	149	0
C^{12}(p,2p)B^{11}	(5)	1548	0	0	149	302	55
He^{4}(p,2p)T^{3}	(6)	618	0	0	0	55	438

χ^2 for reactions	(1,2,3)	(1,3,4)	(1,4,5)	(1,5,6)	5.412
	8	136	775	287	

(c) N_2 gas data   Total = 15586 events

		(1)	(2)	(3)	(4)	(5)	(6)
ppγ	(1)	0	0	55	329	1241	500
D(p,2p)n	(2)	0	42	1861	0	0	0
N^{14}(p,2p)C^{13}	(3)	55	1861	3115	434	0	0
O^{16}(p,2p)N^{15}	(4)	329	0	434	1772	1267	0
C^{12}(p,2p)B^{11}	(5)	1241	0	0	1267	2593	289
He^{4}(p,2p)T^{3}	(6)	500	0	0	0	289	1156

χ^2 for reactions	(1,2,3)	(1,3,4)	(1,4,5)	(1,5,6)	5.412
	0	23	562	347	

The rows and columns of each table correspond to the reaction hypothesis indicated. The number of events that have $X^2 \leqslant 5.412$ for one reaction only appear along the diagonal of the tables. Off-diagonal elements contain tallies of events that have $X^2 \leqslant 5.412$ for the two corresponding reactions. Events that were ambiguous between three reactions (three of the six X^2 values were $\leqslant 5.412$) were counted separately.

Table 12(a) for the Monte Carlo events shows that almost all $pp\gamma$ events were ambiguous with at least one of the other reactions. Only a few events ($\sim$0.5%) did not have $X^2 \leqslant 5.412$ for the $pp\gamma$ hypothesis because of the effects of angular and energy resolutions. The expected fraction of $pp\gamma$ events of this type in the actual $pp\gamma$ data was about 4%. Table 12(b), for the distribution of X^2 values for the actual $pp\gamma$ data, indicates that a significant number of events were not due to the $pp\gamma$ reaction, but probably arose from reactions on contaminants in the H_2 gas. Table 12(c) shows the results for the N_2 gas data which allowed the fraction of contaminant events that appear similar to $pp\gamma$ to be estimated. (A similar table for the D_2 data was used.) The events distinguished from $pp\gamma$ in Table 12(b) could then be used to estimate the the background in the $pp\gamma$ data.

The procedure adopted for correction of prompt backgrounds in the $pp\gamma$ data (which were separated into the angular bins described in Chapter IV) was based on the following:

(a) Observation of prompt events in the $pp\gamma$ data that were not $pp\gamma$ events showed that deuterium break-up was the major contaminant and that the remaining events could be reasonably assumed to have arisen from reactions on nitrogen contaminants in the H_2 gas.

(b) The D_2 and N_2 gas data allowed the fractions of possible contaminant events that appeared similar to $pp\gamma$ ($X^2 \leqslant 5.412$) to be determined. Since the events in these data sets were very similar to the background in the $pp\gamma$ data, the same fractions of the contaminant events in the $pp\gamma$ data should have had $X^2 \leqslant 5.412$ for the $pp\gamma$ reaction hypothesis.

(c) The number of events in the three data sets (N_2 gas, D_2 gas and H_2 gas targets) that were statistically distinguished from $pp\gamma$ ($X^2 > 10$) provided the proper normalization for estimation of the background. Very few true $pp\gamma$ events had $X^2 > 10$ and therefore did not affect the background normalization (See Fig. 24(d)). Since the $pp\gamma$ data provided the estimate of the total number of contaminant events that occurred and the other data sets only indicated the fractions of these events that had $\chi^2 \leqslant 5.412$, the corrections obtained were relatively insensitive to minor ($\pm$ 20%) differences between the distributions of events in the three sets of data.

The number of prompt background events for each angular bin was estimated using the following equation.

$$N_B = \frac{A_{pp\gamma}}{A_{non-pp\gamma}} \cdot N_{non-pp\gamma} \qquad \text{VII-2}$$

where $N_{non-pp\gamma}$ and $A_{non-pp\gamma}$ were the numbers of events with $\chi^2 > 10$ in the ppγ and background data (D_2 or N_2 gas targets) respectively. $A_{pp\gamma}$ was the number of contaminant events that appeared similar to ppγ events ($\chi^2 \leqslant 5.412$) in the D_2 or N_2 gas data. The ratio $N_{non-pp\gamma}/A_{non-pp\gamma}$ determines what proportion of $A_{pp\gamma}$ corresponded to the actual background.

The correction due to contamination by D(p,2p)n events was small in all angular regions. When both polar angles were $\geqslant 30^\circ$ it was typically $\sim 2\%$. Background corrections not due to deuterium were about 15%. Background corrections determined using data sets with N_2 gas or air targets were very similar and no systematic difference could be detected. Since the N_2 data had better statistics, it was used for the corrections.

The statistical uncertainties in these corrections were large ($\pm$ 25%). Systematic errors due to the procedure adopted are believed to be small compared to the statistical uncertainty. The results of all background corrections are summarized in Table 13.

VII.4.4 Determination of $N_{pp\gamma}$

The cross sections to be calculated are proportional to the number of ppγ events corrected for random and prompt backgrounds.

Let P denote prompt events and R random events. Then

$$A_{pp\gamma} = \begin{cases} P_D - R_D & \text{for } D_2 \text{ gas data} \\ P_N - R_N & \text{for } N_2 \text{ gas data} \end{cases} \qquad \text{VII-3}$$

$$A_{non-pp\gamma} = \begin{cases} P_{Dnon} - R_{Dnon} & \text{for } D_2 \text{ data} \\ P_{Nnon} - R_{Nnon} & \text{for } N_2 \text{ data} \end{cases} \qquad \text{VII-4}$$

$$N_{non-pp\gamma} = P_{non\gamma} - R_{non\gamma} \qquad \text{VII-5}$$

$P_{non\gamma}$ and $R_{non\gamma}$ are prompt and random events in the ppγ

Table 13

Summary of PPγ Data

θ_L-θ_R	# Real Events	# Random Events	% Contam	# Contam Events	Net Events
18-18	306	97	13 ± 7	28	181
22-18	298	68	30 ± 7	69	161
18-22	310	93	11 ± 6	29	194
22-22	444	103	21 ± 5	71	270
26-18	161	45	20 ± 7	23	93
18-26	118	30	19 ± 6	17	71
30-18	73	12	11 ± 5	7	54
18-30	20	1	21 ± 10	4	15
26-22	385	85	18 ± 5	53	247
22-26	298	51	15 ± 4	38	209
26-26	391	60	21 ± 5	70	261
34-18	13	2	22 ± 14	2	9
18-34	0	0		0	0
30-22	264	49	9 ± 3	19	196
22-30	95	7	10 ± 4	9	79
34-22	81	9	21 ± 5	15	57
22-34	19	1	17 ± 8	3	15
30-26	337	22	13 ± 3	41	274
26-30	190	8	9 ± 3	15	167
30-30	262	12	7 ± 2	18	232
34-26	213	15	13 ± 3	26	172
26-34	77	1	9 ± 4	7	69
34-30	226	6	11 ± 2	25	195
30-34	112	0	9 ± 4	10	102
34-34	137	0	4 ± 2	5	132
38-18	0	1		0	-1
38-22	30	0	13 ± 4	4	26
38-26	126	3	4 ± 2	5	118
38-30	182	1	7 ± 3	13	168
38-34	149	0	3 ± 2	5	144
Other *	798	346	15 ± 2	72	380
Totals	6115	1108	14 ± 3	705	4303

* Includes events in the ranges $14^\circ \leqslant \theta_L \leqslant 42^\circ$, $14^\circ \leqslant \theta_R \leqslant 38^\circ$ not counted in the other polar angle bins. About 10% of all ppγ events, eliminated by cuts on the wire chamber coordinates, are not counted in the table.

data with $X^2 > 10$. $N_{pp\gamma}$ is defined by

$$N_{pp\gamma} = (P_{pp\gamma} - R_{pp\gamma}) - (P_D - R_D) f_D - (P_N - R_N) f_N \qquad \text{VII-6}$$

The quantities f_D and f_N are given by

$$f = N_{non-pp\gamma} / A_{non-pp\gamma} \qquad \text{VII-7}$$

for the D_2 and N_2 data sets respectively.

The uncertainty in $N_{pp\gamma}$ is obtained by compounding in quadrature all the statistical errors in equations VII-3 to VII-7.

$$\delta^2 N_{pp\gamma} = (P_{pp\gamma} + R_{pp\gamma}) + f_D^2 (P_D + R_D) + f_N^2 (P_N + R_N)$$

$$+ (P_D - R_D)^2 \delta^2 f_D + (P_N - R_N)^2 \delta^2 f_N \qquad \text{VII-8}$$

$\delta^2 f$ is given by the expression

$$\delta^2 f = \delta^2 \frac{(N_{non-pp\gamma})}{(A_{non-pp\gamma})}$$

$$\delta^2 f = \frac{(P_{non\gamma} + R_{non\gamma})}{A^2_{non-pp\gamma}} + \frac{N_{non-pp\gamma}}{A^4_{non-pp\gamma}} (P_{non} + R_{non}) \qquad \text{VII-9}$$

where $P_{non} = P_{Dnon}$ or P_{Nnon} depending on $f = f_D$ or f_N. Similarly $R_{non} = R_{Dnon}$ or R_{Nnon}.

VII.5 PPγ CROSS SECTION NORMALIZATION

VII.5.1 Identification of Calibration p-p Elastic Events

The extraction of the p-p elastic events was the easiest part of the analysis, since they came from a well-defined part of the reaction volume and passed through an isolated part of the back right wire chamber. Since the reason for detecting p-p elastic events was to provide proper charge normalization, the computer constraints used in their identification had to match as closely as possible the conditions under which calibration runs were taken (See Chapter V). The analysis of the ppγ events also involved application of X^2 and vertex constraints which eliminated a certain fraction of good events. Systematic error in the ratio $N_{pp\gamma}/N_{el}$ due to vertex cuts was partially eliminated by applying the same vertex acceptance conditions for the calibration p-p elastic events as for ppγ events.

It was not possible to apply X^2 cuts to the p-p elastic events without introducing sizeable corrections to $N_{pp\gamma}/N_{el}$. The r.m.s. multiple-scattering in the tungsten wires was about 2.4^o, which was about six times worse than for the rest of the spectrometer. Since 24% of the events hit the tungsten wires, the X^2 distribution was seriously affected.

The X^2 distribution for p-p elastic events was more seriously affected than for ppγ events. The correlation between angle and energy is much weaker for ppγ events and multiple-scattering of as much as 5^o in the polar angles sometimes has almost no effect on the X^2 value[47)]. This is due to the extended size of the kinematic loci for ppγ events. The X^2 distribution for p-p elastic events was also more sensitive to minor errors in the PHT-energy calibration constants which occurred at the beginning of each run. The number of p-p elastic events with $X^2 \geqslant 5.412$ was about 15%, mainly due to events hitting the tungsten wires. The corresponding figure for ppγ events was about 4 ± 2%. In calculating the charge normalization, the fraction of ppγ events eliminated by the X^2 cut was compensated for. Vertex cuts were applied to the p-p elastic events since the adjusted vertex error distributions were nearly the same for all events. The 6 ± 1% correction to $N_{pp\gamma}/N_{el}$ for ppγ events that are eliminated was discussed in Sec. VII.1.3. A summary of the elastic events detected is given in Table 14, in Section VII.5.2

VII.5.2 Corrections for Undetected P-P Elastic Events

The spectrometer introduces a few systematic errors that result in some p-p elastic events passing through the system undetected. These are outlined below.

(a) During the experiment there was a dead wire in the calibration p-p elastic region of the back right wire chamber. This resulted in an inefficiency for one plane ($\sim$6%) that did not occur for most ppγ events. Since there was some redundancy for track detection inefficiencies, less than 6% of p-p elastic events were lost. The correction was determined by observation of the spark distribution on the plane where the dead wire occurred, and was estimated as $3 \pm 1\%$. The error is due to statistical fluctuations in the spark distribution near the dead wire.

(b) Electronic drifts and the poor energy resolution of the counters sometimes resulted in some p-p elastic events being rejected by the upper (ΔE) discriminator thresholds. The number of lost p-p elastic events was determined for each run from observation of the elastic pulse heights and the discriminator cut-offs. The correction to N_{el} for these lost events is $4 \pm 1\%$.

The corrections in (a) and (b) as well as the corrections for lost ppγ events are combined into the factor β in equation V-1. Other effects such as wire chamber detection uniformity ($\epsilon_{we}/\epsilon_{w\gamma}$) result in negligible corrections and are not considered. A summary of the charge normalization factor C_N from equation V-2 is given in Table 14.

Table 14

Summary of Cross Section Normalization

# of calibration p-p elastic events	
Prompt	189 193
Random	250
Net (N_{el})	188 943 ± 0.23%
Corrections to N_{el}	
Effect of dead wire	1.03 ± 1%
Multiple-Scattering	1.03 ± 1%
Effect of ΔE cut-offs	1.04 ± 1%
Vertex error acceptance (relative to ppγ)	0.943 ± 1%
X^2 cut-off (relative to ppγ)	0.962 ± 2%
Net Correction factor (β)	1.00 ± 2.8%
$\left.\frac{d\sigma}{d\Omega}\right)_{el}$ mb/sr	30.15 ± 3.6%
Solid Angle ($\Delta\Omega$) msr	0.296 ± 1.7%
Target Length (L_{el}) mm	4.206 ± 1.5%
Vertex efficiency correction ($\epsilon_{we}/\epsilon_{w\gamma}$)	1.00
C_N (Equation V-2) mb-cm	1.984×10^{-35} ± 3.9%

CHAPTER VIII

RESULTS

VIII.1 CONVENTIONAL ANALYSIS

The ppγ events detected had polar angle ranges from 14° to 46° on the left and 14° to 40° on the right. In the conventional analysis, the events were separated into a large number of bins depending on the variables θ_L, θ_R, Φ_r and Ψ_γ. These were described in Chapter IV. There were a total of 30 polar angle bins, but since the protons are identical particles, it was possible to combine bins corresponding to similar polar angle pairs* (i.e. 18°-22° and 22°-18°). This reduced the number of independent polar angle combinations to 18, and the differential cross sections have been obtained for each.

In some cases, cross sections were averaged or summed over certain ranges of the angular variables. For calculation of simple averages (or sums) the following procedure was used.

$$c \pm \delta c = \frac{1}{N}\sum_{i=1}^{N} a_i \pm \frac{1}{N}\left\{\sum_{i=1}^{N} \delta^2 a_i\right\}^{1/2} \qquad \text{VIII-1}$$

The calculation of weighted averages, used when similar

---

* By combining polar angle bins, the distinction between left and right is lost. The subscripts used from this point on will be (1) and (2) rather than (L) and (R).

polar angle bins were combined, was as follows: for $a \pm \delta a$ and $b \pm \delta b$

$$c \pm \delta c = \frac{\dfrac{a}{\delta^2 a} + \dfrac{b}{\delta^2 b}}{\left(\dfrac{1}{\delta^2 a} + \dfrac{1}{\delta^2 b}\right)} \pm \sqrt{\frac{\delta^2 a \; \delta^2 b}{\delta^2 a + \delta^2 b}} \qquad \text{VIII-2}$$

VIII.1.1 $\frac{d\sigma}{d\Omega_1 d\Omega_2 d\Psi_\gamma}$ Cross Sections*

The $d\sigma/d\Omega_1 d\Omega_2 d\Psi_\gamma$ cross sections are defined in equation IV-16. $N_{pp\gamma}$ is given by equation VII-6. Uncertainties in the cross sections are due to $N_{pp\gamma}$ (eqn. VII-8), ϵ_0 and ϵ_1 (eqn. IV-13). The events were integrated over Φ_r from 0.0 to 0.7 in order to improve statistics. The cross section varies slowly as a function of Φ_r up to this point so the results are very similar to those for coplanar events. This can be seen from the example of the theoretical cross sections given in Appendix F, Fig. F-1(a).

The polar angle combinations with the best statistics are shown in Fig. 29. These are for polar angles of 22°-22°, 26°-26°, 30°-30°, 22°-26°, 26°-30° and 30°-34°. For symmetric polar angle pairs (e.g. 22°-22°) the Ψ_γ distributions are symmetric about $\Psi_\gamma = 180°$. The data for $180° \leq \Psi_\gamma \leq 360°$ have been combined with those in the

---

* Strictly speaking $\Delta\Omega_1 = \Delta\cos\theta_L \; \Delta\phi_L$
and $\Delta\Omega_2 = \Delta\cos\theta_R \; 2\Delta\phi_m \; \Delta\Phi_r$

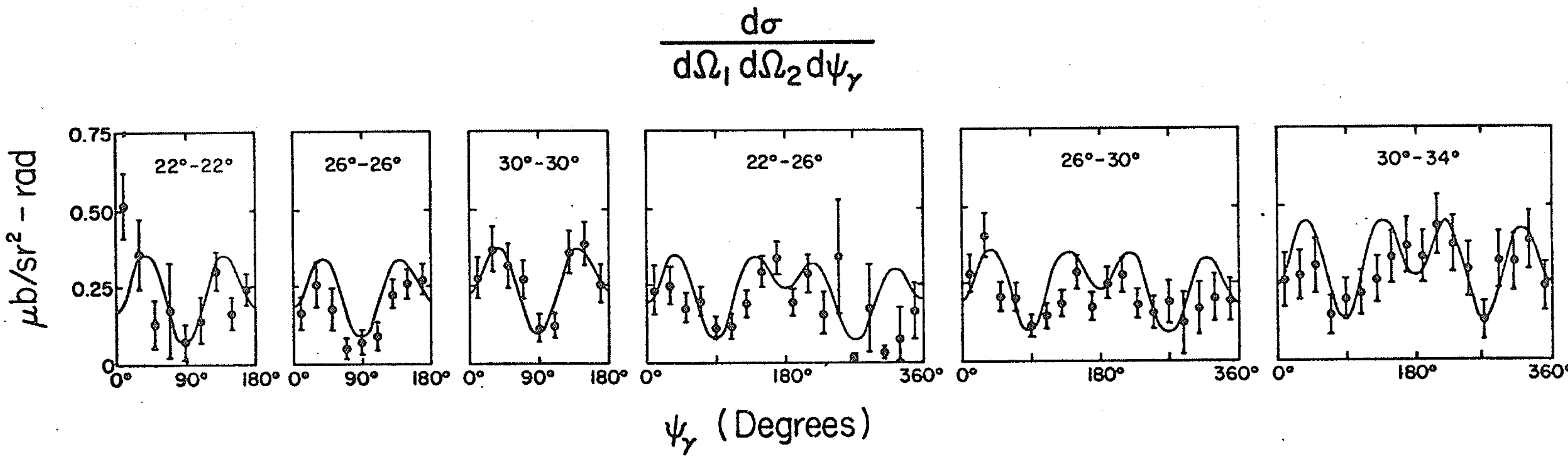

Figure 29

The $d\sigma/d\Omega_1 d\Omega_2 d\Psi_\gamma$ cross sections for polar angle pairs of 22°-22°, 26°-26°, 30°-30°, 22°-26°, 26°-30° and 30°-34°. The data have been integrated over the range $0 \leq \Phi_r \leq 0.7$. The smooth curves are the theoretical predictions of the Hamada-Johnston potential for $\Phi_r \approx 0.4$.

other half-range by calculating the weighted averages of corresponding points. This was done to improve statistics. The smooth curves show Liou's Hamada-Johnston theoretical predictions as a function of Ψ_γ for $\Phi_r \approx 0.4$. In general, the shapes of the distributions are reproduced well by the theoretical results. Because of poor statistics, comparison to theory is not very meaningful. Two other polar angle combinations are shown in Fig. 30. For 38°-30° the resolution in Ψ_γ is very poor and the structure in the cross sections is smoothed out. The Ψ_γ resolutions are better for smaller polar angles because the kinematic loci are larger and the absolute energy resolutions better. For 26°-26° the Ψ_γ resolution is about $\pm 15^\circ$ while for 38°-30° it is about $\pm 30^\circ$. The results for 18°-26° show what happens when the detection efficiency $\epsilon_1 \rightarrow 0$ for part of the Ψ_γ range. The numerical results of all the measured $d\sigma/d\Omega_1 d\Omega_2 d\Psi_\gamma$ cross sections are summarized in Appendix G.

VIII.1.2 $\frac{d\sigma}{d\Omega_1 d\Omega_2}$ Cross Sections

The $d\sigma/d\Omega_1 d\Omega_2$ cross sections are defined in equation IV-18. The events in each polar angle bin were integrated over Ψ_γ and the net $pp\gamma$ events and cross section uncertainties determined in a similar manner as for the

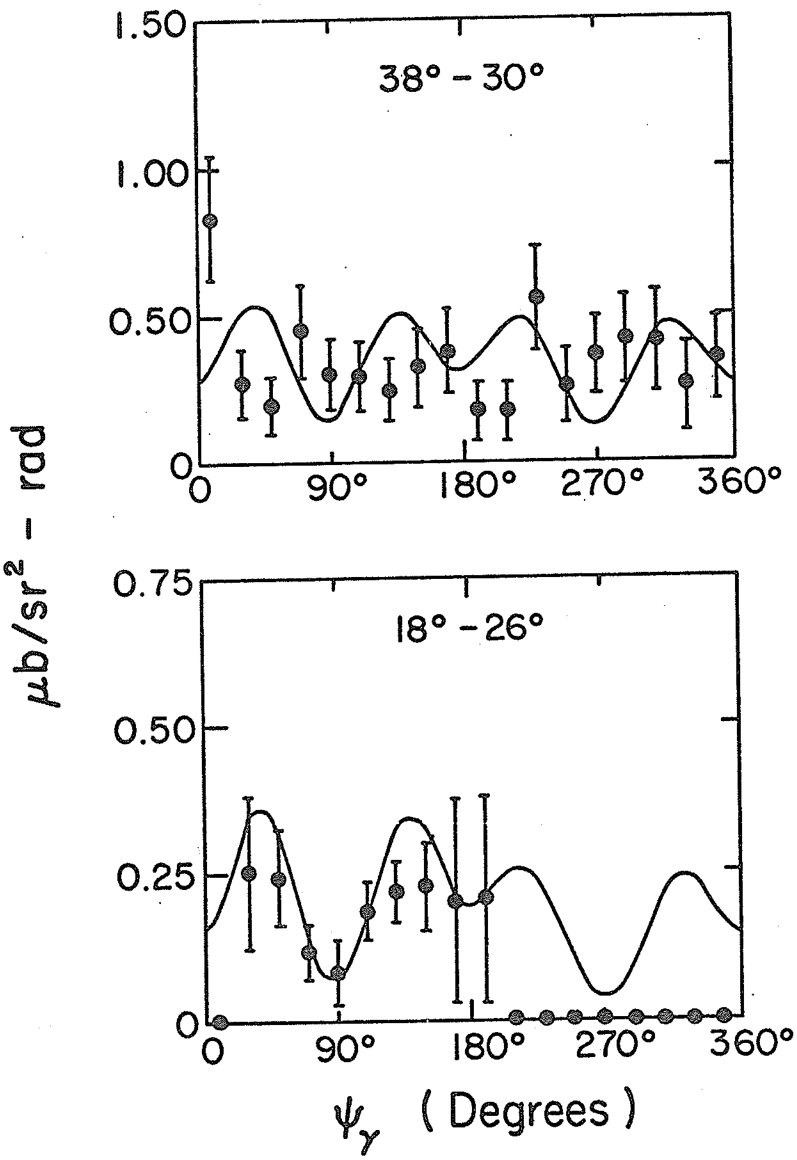

Figure 30

The $d\sigma/d\Omega_1 d\Omega_2 d\Psi_\gamma$ cross sections for polar angle pairs of 38°-30° and 18°-26°. The results for 38°-30° are smoothed out because of poor resolution in Ψ_γ. Results for 18°-26° show the effects of the detection efficiency $\epsilon_1 \rightarrow 0$ for part of the Ψ_γ range. The error bars are statistical only.

$d\sigma/d\Omega_1 d\Omega_2 d\psi_\gamma$ cross sections. The events were initially separated into bins in Φ_r that were 0.1 wide. To improve statistics, the cross sections for adjacent bins were combined by taking the simple average of the two results. The errors were added in quadrature.

The $d\sigma/d\Omega_1 d\Omega_2$ cross sections as a function of Φ_r are shown in Fig. 31. Only statistical errors in the evaluation of $N_{pp\gamma}$, ϵ_o and ϵ_1 are included in the error bars. The smooth curve shown for each polar angle combination represents the theoretical prediction of the Hamada-Johnston potential adjusted for the resolution in Φ_r. The shape of the theoretical predictions and the experimental results are in excellent agreement.

The coplanar cross sections, obtained by averaging the first two data points ($\Phi_r \leq 0.4$) for each polar angle pair are summarized in Table 15. This was permissible because the variation of the cross section with Φ_r is small in the range $0 \leq \Phi_r \leq 0.4$. Liou's Hamada-Johnston theoretical predictions for coplanar events are also included in this table. These predictions have been corrected for the effects of finite resolutions ($\delta\Phi_r$) in the event non-coplanarity. The measured $d\sigma/d\Omega_1 d\Omega_2$ cross sections are summarized in Appendix G.

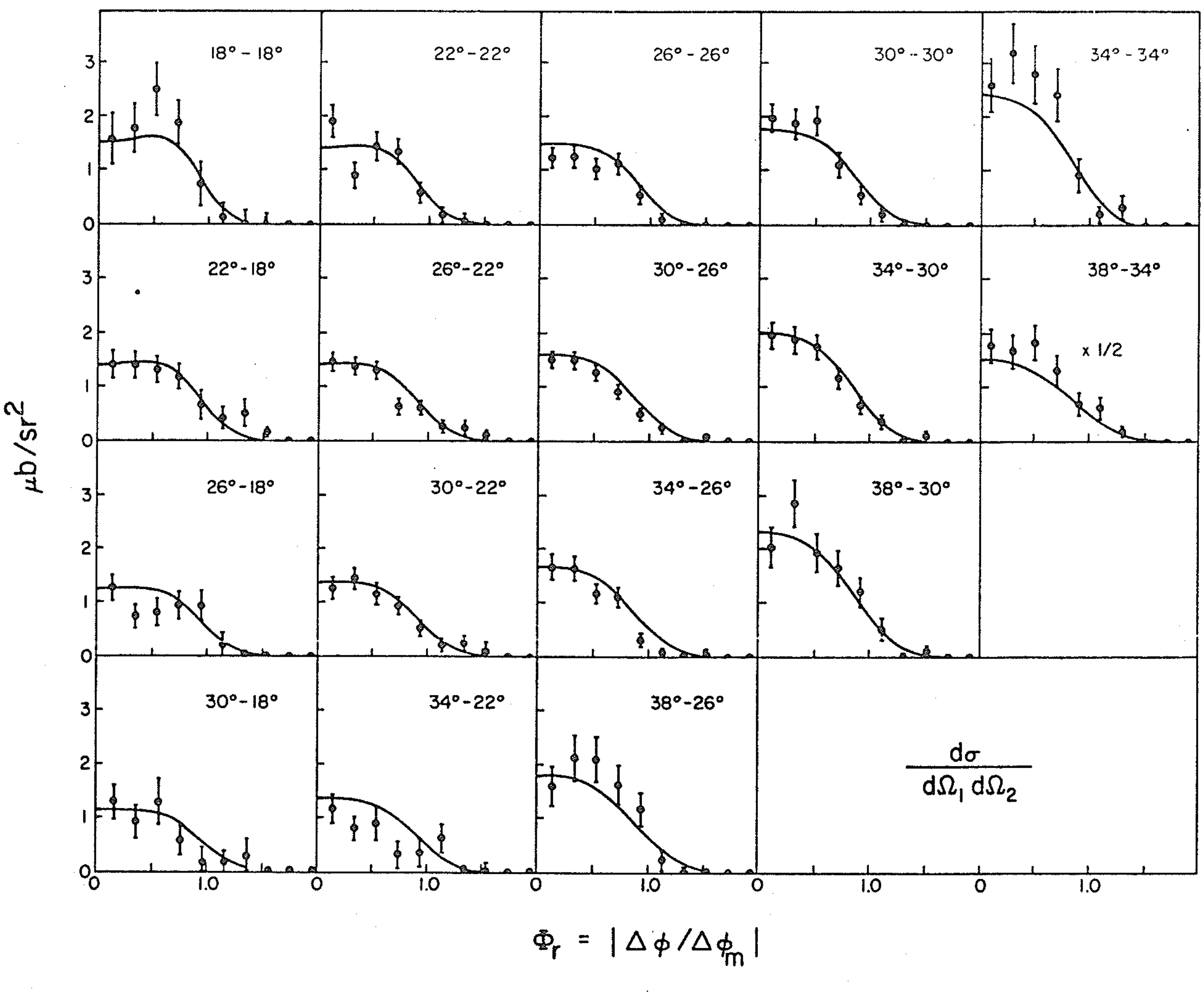

Figure 31

The $d\sigma/d\Omega_1 d\Omega_2$ cross sections for the 17 polar angle pairs indicated showing the dependence of cross sections on Φ_r. The smooth curves are the theoretical predictions for the Hamada-Johnston potential adjusted to include effects of angular resolutions. The error bars are due to statistical uncertainties only. There is an uncertainty in the vertical scale of 3.9%.

Table 15

Summary of Coplanar $\frac{d\sigma}{d\Omega_1 d\Omega_2}$ Cross Sections

θ_1-θ_2 deg.	Experiment $\mu b/sr^2$	Theory $\mu b/sr^2$	Ratio - 1	$\delta\Phi_r$
18-18	1.73 ± 0.33	1.62	0.07 ± 0.20	0.216
18-22	1.42 ± 0.29	1.45	-0.02 ± 0.20	0.217
22-22	1.44 ± 0.19	1.46	-0.01 ± 0.13	0.212
18-26	1.01 ± 0.16	1.27	-0.16 ± 0.13	0.226
18-30	0.93 ± 0.22	1.14	-0.18 ± 0.19	0.241
22-26	1.48 ± 0.12	1.42	0.04 ± 0.08	0.216
26-26	1.27 ± 0.14	1.50	-0.15 ± 0.09	0.216
22-30	1.05 ± 0.14	1.37	-0.23 ± 0.10	0.226
22-34	1.15 ± 0.18	1.35	-0.15 ± 0.13	0.243
26-30	1.44 ± 0.18	1.57	-0.08 ± 0.11	0.224
30-30	1.95 ± 0.19	1.76	0.11 ± 0.11	0.230
26-34	1.66 ± 0.17	1.65	0.01 ± 0.10	0.239
30-34	1.93 ± 0.17	1.97	-0.02 ± 0.09	0.246
34-34	2.91 ± 0.38	2.38	0.22 ± 0.16	0.266
38-22	1.07 ± 0.33	1.35	-0.21 ± 0.24	0.267
38-26	1.86 ± 0.28	1.76	0.06 ± 0.16	0.263
38-30	2.46 ± 0.29	2.26	0.09 ± 0.13	0.273
38-34	3.47 ± 0.45	2.94	0.18 ± 0.15	0.301

VIII.1.3 $\frac{d\sigma}{d\theta_1 d\theta_2}$ Cross Sections

The $d\sigma/d\theta_1 d\theta_2$ cross sections were obtained from the cross sections described in Sec. VIII.1.2, by integrating over Φ_r. Equation IV-19 was used in the calculation. Since these cross sections have the best statistics they are a better test of the theoretical predictions than those described previously. In addition, the effects of experimental biases, due to energy and Φ_r angular resolutions and the energy cut-offs, are minimized (but not eliminated). Fig. 32 shows the ratio of experiment to theory for each angular bin. The results are summarized in Table 16.

In calculating the ratio of experiment to theory, an uncertainty of $\pm$ 3% in the theoretical results has been included. This uncertainty is due to possible errors in interpolating between the calculated $d\sigma/d\Omega_1 d\Omega_2$ cross sections because the shape of the cross section was not accurately known in the range $\Phi_r \geqslant 0.7$. The value of the theoretical cross section, used to calculate the ratio in Table 16, was obtained by averaging the theoretical results over the polar angle bin. This is probably a more reliable procedure than simply taking the value for the central point. Typical differences between the average of the theoretical cross sections and that for the central point were $\sim 1 - 2\%$.

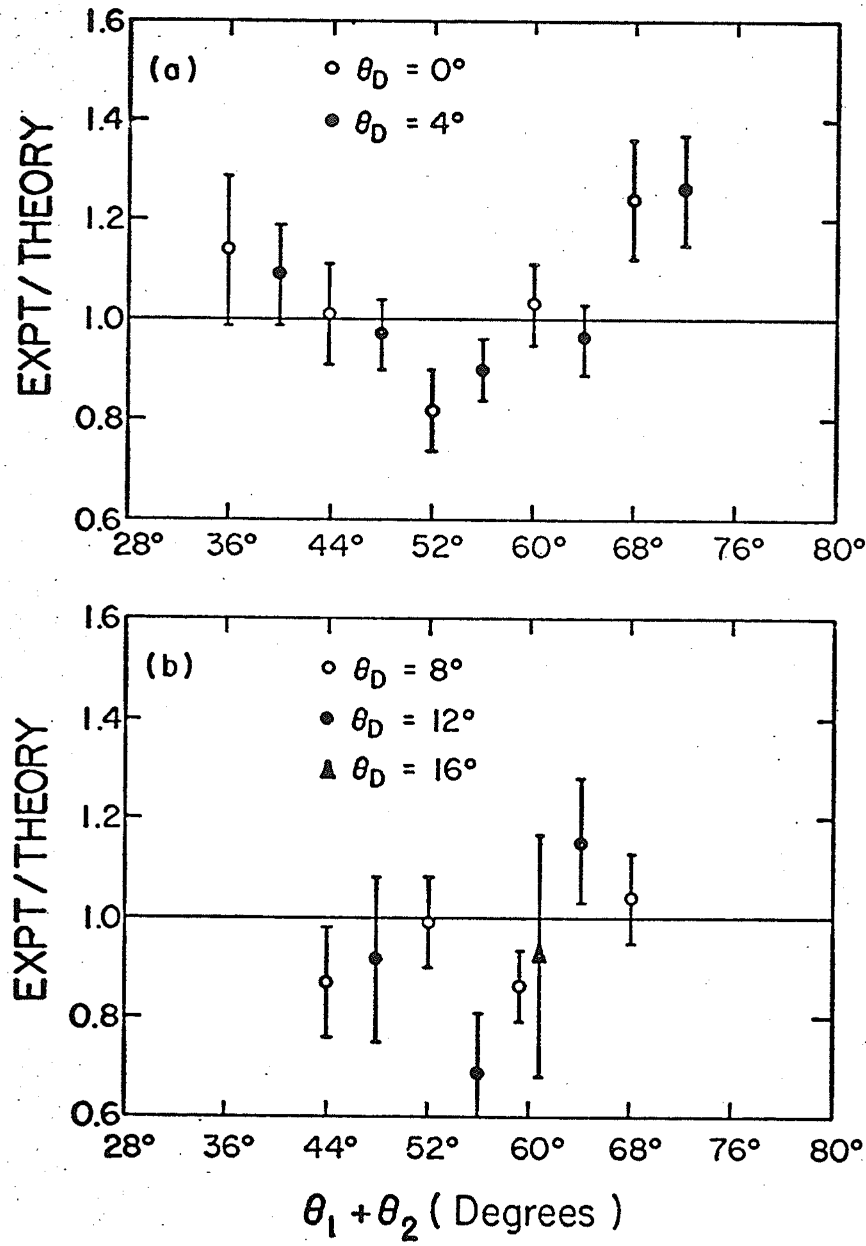

Figure 32

(a) Ratio of Experiment/Theory for the $d\sigma/d\theta_1 d\theta_2$ cross sections for polar angle combinations with $|\theta_1-\theta_2| = 0°$ and $4°$. The error bars contain statistical uncertainties in the measured results and a 3% uncertainty in theoretical results. There is an uncertainty in the vertical scale of 3.9%.

(b) Similar to (a) for $|\theta_1-\theta_2| = 8°$, $12°$ and $16°$.

Table 16

Summary of $\frac{d\sigma}{d\theta_1 d\theta_2}$ Cross Sections

θ_1-θ_2 deg.	Experiment $\mu b/rad^2$	Theory* $\mu b/rad^2$	Ratio - 1	% Error from Eng. Cut-offs#
18-18	0.421 ± 0.055	0.368	0.14 ± 0.15	± 8
18-22	0.371 ± 0.034	0.340	0.09 ± 0.10	± 6
22-22	0.354 ± 0.033	0.350	0.01 ± 0.10	± 5
18-26	0.262 ± 0.032	0.300	-0.13 ± 0.11	± 10
18-30	0.243 ± 0.044	0.263	-0.08 ± 0.17	± 20
22-26	0.333 ± 0.023	0.342	-0.03 ± 0.07	± 4
26-26	0.298 ± 0.026	0.363	-0.18 ± 0.08	± 3
22-30	0.323 ± 0.027	0.325	-0.01 ± 0.09	± 8
22-34	0.213 ± 0.036	0.308	-0.31 ± 0.12	± 15
26-30	0.332 ± 0.019	0.370	-0.10 ± 0.06	± 3
30-30	0.415 ± 0.030	0.401	0.03 ± 0.08	± 2
26-34	0.318 ± 0.025	0.370	-0.14 ± 0.07	± 7
30-34	0.405 ± 0.026	0.424	-0.04 ± 0.07	± 1
34-34	0.588 ± 0.053	0.474	0.24 ± 0.12	0
38-22	0.275 ± 0.072	0.295	-0.07 ± 0.25	± 30
38-26	0.428 ± 0.043	0.372	0.15 ± 0.12	± 12
38-30	0.476 ± 0.039	0.460	0.04 ± 0.09	± 1
38-34	0.669 ± 0.054	0.532	0.26 ± 0.11	0

Weighted Average Value of (Ratio-1) = -0.033 ± 0.023**

* A 3% error has been added in quadrature to the uncertainty in (RATIO - 1) for numerical errors in calculating the theoretical cross section.

** The $d\sigma/d\Omega)_{el}$ value, measured with Collimator II (Table 4), was used in the cross section normalization. If the average of the $d\sigma/d\Omega)_{el}$ measurements had been used, the value of (Ratio - 1) would have been -0.057 ± 0.023.

\# These uncertainties are not included in the quoted experimental errors. Most cross sections will tend to change in the same direction if the energy thresholds are in error.

The weighted mean value of expt/theory is 0.967 ± 0.023. The distribution of the ratios is close to the one expected for random statistical errors only. When compared to theory, ten measurements differ by less than one standard deviation, five differ by less than two standard deviations, and the remaining three by less than three standard deviations. The expected frequencies were 12 ± 3, 5 ± 2 and 1 ± 1 respectively. The points in Fig. 32 indicate that for larger opening angles $(\theta_1 + \theta_2)$ between the two protons, the experimental results are too high. The 18^o-18^o and 18^o-22^o points which also tend to indicate an upward trend in the ratio, are sensitive to the choice of the energy cut-offs. However, some other more asymmetric polar angle combinations are even more seriously affected and do not show the same trend. The upward variation in the ratio at small nearly symmetric angles is probably a statistical fluctuation.

One possible reason for the shape of the distribution in Fig. 32(a) for nearly symmetric events is that the choice for the theoretical prediction in the extreme cases is a poor one due to the effects of the baffles at B1 and B2. For example, the B2 baffles preferentially stop protons with smaller polar angles on the right side. Thus detected events may have an average opening angle somewhat larger than that used for the theoretical value. Since the cross sections are increasing rapidly at this point, this would have the effect of raising the expt/theory ratio. A similar effect could occur at smaller polar angles due to the B1 baffles and the wire chamber cut-off near the beam. Events with $44^{\circ} \leqslant \theta_1 + \theta_2 \leqslant 60^{\circ}$ are not seriously affected by these considerations and results in this range are the most reliable.

VIII.2 GLOBAL ANALYSIS

In this part of the analysis, an attempt was made to use all of the ppγ data collected rather than just the part in the 30 polar angle regions previously considered. For this reason, the set of ppγ data was integrated over the proton polar angle ranges up to 38° on the right and 42° on the left. At polar angles larger than this the contamination due to multiple-scattered p-p elastic events became large and the data unreliable. At polar angles $\lesssim 14^{\circ}$ the random background became very large and so a lower limit at 14° was also placed on the proton polar angle ranges. Since the only theoretical predictions attempted to date have been for the $d\sigma/d\Omega_1 d\Omega_2 d\Psi_\gamma$ and $d\sigma/d\Omega_1 d\Omega_2$ cross sections, there were no results to compare directly with the experimental measurements. A comparison to the theoretical predictions of the Hamada-Johnston potential was made indirectly by using the "fake" set of ppγ events discussed in Section IV.1. The events in this set of data have distributions that include the effects of the biases introduced by the experimental apparatus (See Sec. IV.3.4).

The corrections for prompt and random backgrounds were made in a manner similar to that described previously. (See Sec. VII.4.3 and VII.4.4) Histograms of the desired variables (Φ_r, Ψ_γ, $\theta_L + \theta_R$ and $\theta_L - \theta_R$) were made for the Monte Carlo data and the ppγ data and compared. A scaling factor for the Monte Carlo data was obtained from the ratio of the net number of "fake" ppγ events (weighted) to net measured ppγ events for the polar angle ranges discussed above.*

VIII.2.1 Φ_r Distribution

Fig. 33(a) shows the Φ_r distribution of events integrated over the proton polar angles and Ψ_γ. The points and error bars represent the measured data and the solid histogram an expected distribution for the Hamada-Johnston potential. This allows the Φ_r shape to be examined with good statistics. As can be seen, the shapes of the two histograms are in excellent agreement. Events extend past $\Phi_r = 1$ because of the resolutions in the azimuthal angles. Fig. 33(b) shows the ratio of the two histograms (Expt/Theory) with the error bars indicating only statistical errors. This provides conclusive evidence for the

---

* The Monte Carlo data was checked for systematic errors by examining the normalization factor required to yield the theoretical $d\sigma/d\theta_1 d\theta_2$ cross section for each of the 30 polar angle bins. All of these factors were nearly the same except for small statistical errors ($\sim 5\%$).

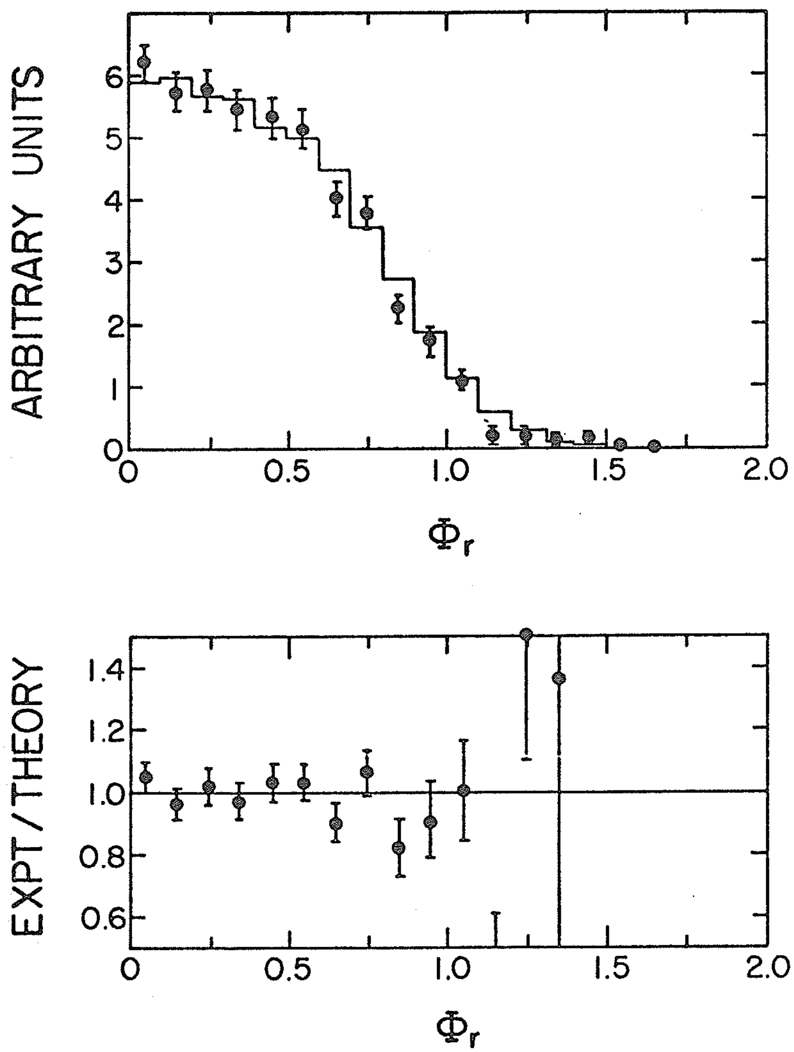

Figure 33

(a) The observed distribution of event non-coplanarity Φ_r integrated over the proton polar angles. The bar histogram gives the distribution for the Monte Carlo events.

(b) The ratio of expt/theory for histograms in (a). The theory corresponds to the prediction of the Hamada-Johnston potential. The error bars are statistical uncertainties only.

validity of **obtaining** coplanar cross sections from previous experimental $pp\gamma$ results by using the theoretical Φ_r distributions.

VIII.2.2 Ψ_γ Distributions

The Ψ_γ distributions were integrated over the polar angles and examined as a function of Φ_r. Fig. 34 shows Ψ_γ distributions for five values of the relative non-coplanarity ($\Phi_r \leq 0.2$, $0.2 \leq \Phi_r \leq 0.4$, $0.4 \leq \Phi_r \leq 0.6$, $0.6 \leq \Phi_r \leq 0.8$ and $\Phi_r \geq 0.8$). The shape, which theoretically has a quadrupole form is badly distorted by the energy cut-offs of the spectrometer. The dotted histograms give the Monte Carlo results for the Hamada-Johnston potential. The theoretical distributions show qualitative agreement with the measured results but the value of the comparison is reduced because of the poor resolution in Ψ_γ and the huge distortion caused by experimental biases.

In an effort to reduce the effect of the energy cut-offs, the polar angle ranges were changed so that

(a) $24^\circ \leq \theta_L \leq 42^\circ$

(b) $24^\circ \leq \theta_R \leq 38^\circ$

(c) $|\theta_L - \theta_R| \leq 6^\circ$

and the same Ψ_γ histograms were made. These events were not so seriously affected by the energy cut-offs. The

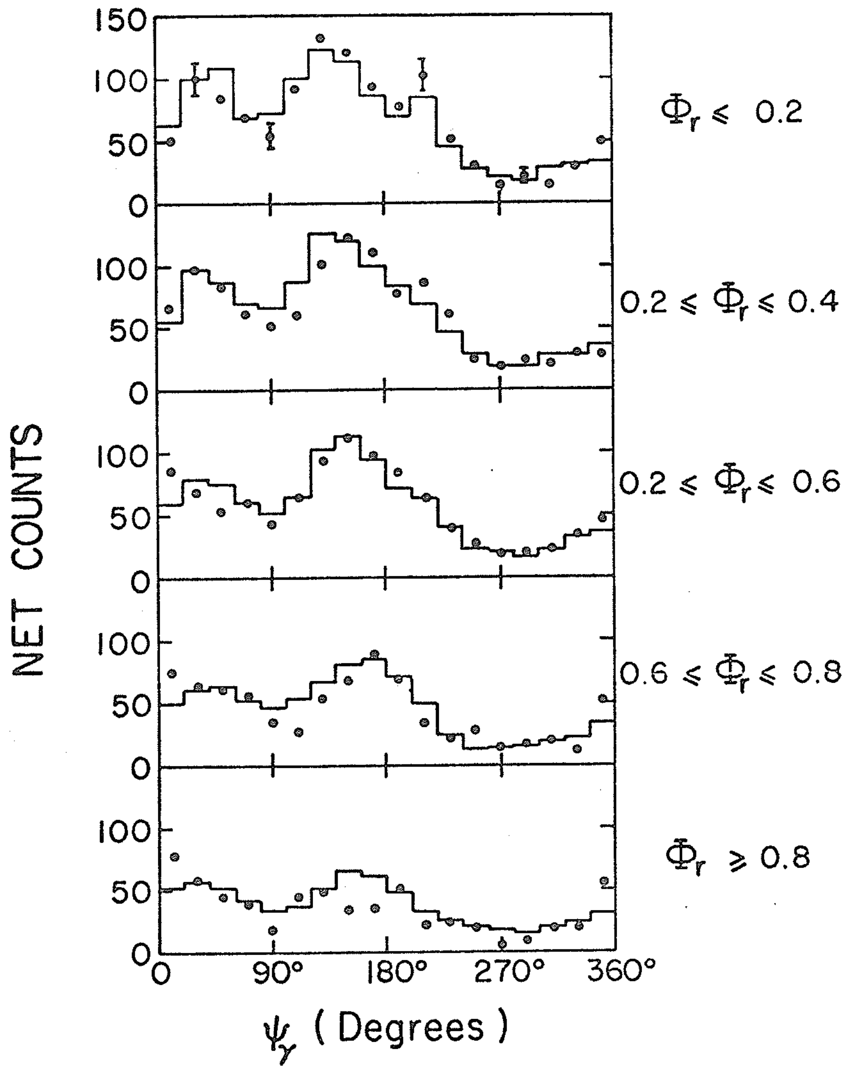

Figure 34

The Ψ_γ distributions integrated over ranges of Φ_r

(a) $0 \leqslant \Phi_r \leqslant 0.2$ (b) $0.2 \leqslant \Phi_r \leqslant 0.4$

(c) $0.4 \leqslant \Phi_r \leqslant 0.6$ (d) $0.6 \leqslant \Phi_r \leqslant 0.8$

(e) $\Phi_r \geqslant 0.8$

The solid histograms give the Monte Carlo results for the Hamada-Johnston potential. Only a few typical error bars are shown for the experimental results.

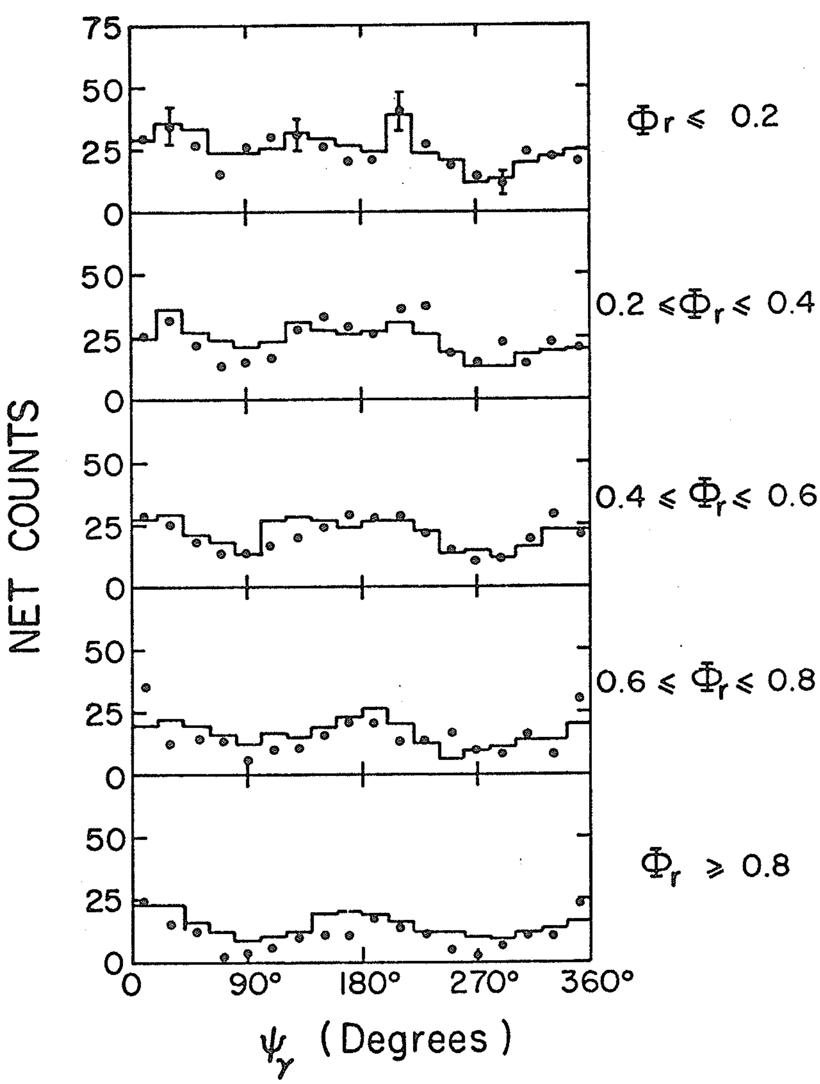

Figure 35

The Ψ_γ distributions for the same ranges of Φ_r as in Fig. 34. The events are limited on the polar angles to avoid the energy cut-offs.

results are shown in Fig. 35. The expected quadrupole shape is more clearly indicated, but again the Ψ_γ resolutions are poor and the statistical accuracy is limited. Only a few typical error bars are shown on the histograms. The shapes of the distributions can also be compared visually to the example given in Figure F-2(a).

VIII.2.3 Polar Angle Distributions

Fig. 36(a) shows the dependence of the ppγ events on the sum of the proton polar angles. Both Φ_r and Ψ_γ have been integrated over. The distribution of the Monte Carlo events (solid histogram) is very similar to the measured results. The ratio of the experimental and theoretical results is given in Fig. 36(b). The error bars are statistical only. This indicates that the experimental results are too high at large polar angles. This may be caused by p-p elastic events that have been multiple-scattered and also had their energies degraded. The Φ_r angular resolutions for p-p elastic events hitting tungsten wires would be very similar to ppγ events for polar angles $\gtrsim 35^\circ$ and make these events hard to identify or make accurate corrections for.

Fig. 37 shows similar results for the distribution of events as a function of the asymmetry in the proton polar angles. The HJ theoretical predictions are in good agreement with the measured results.

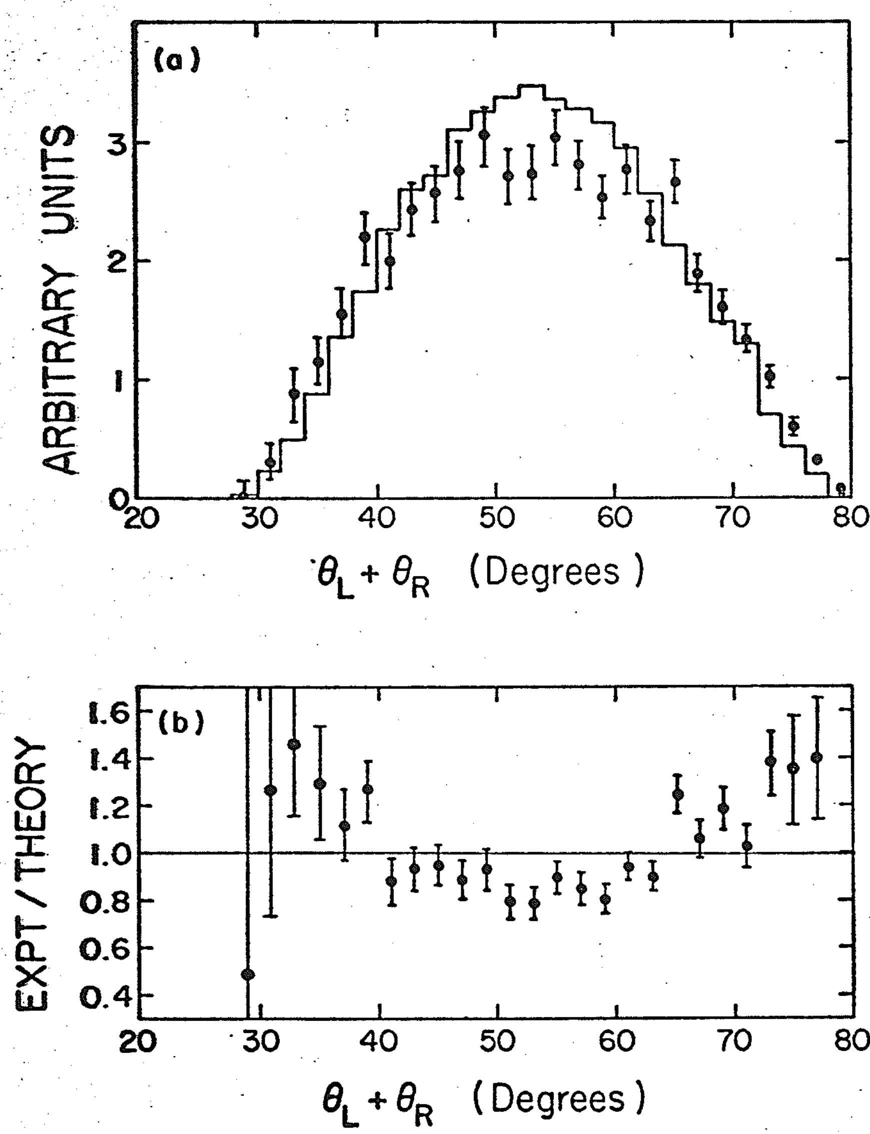

Figure 36

(a) The distribution of measured ppγ events (points and error bars) and Monte Carlo HJ ppγ events (solid histogram) as a function of the opening angle.

(b) The ratio of expt/theory for the histograms in (a). The error bars contain statistical errors only.

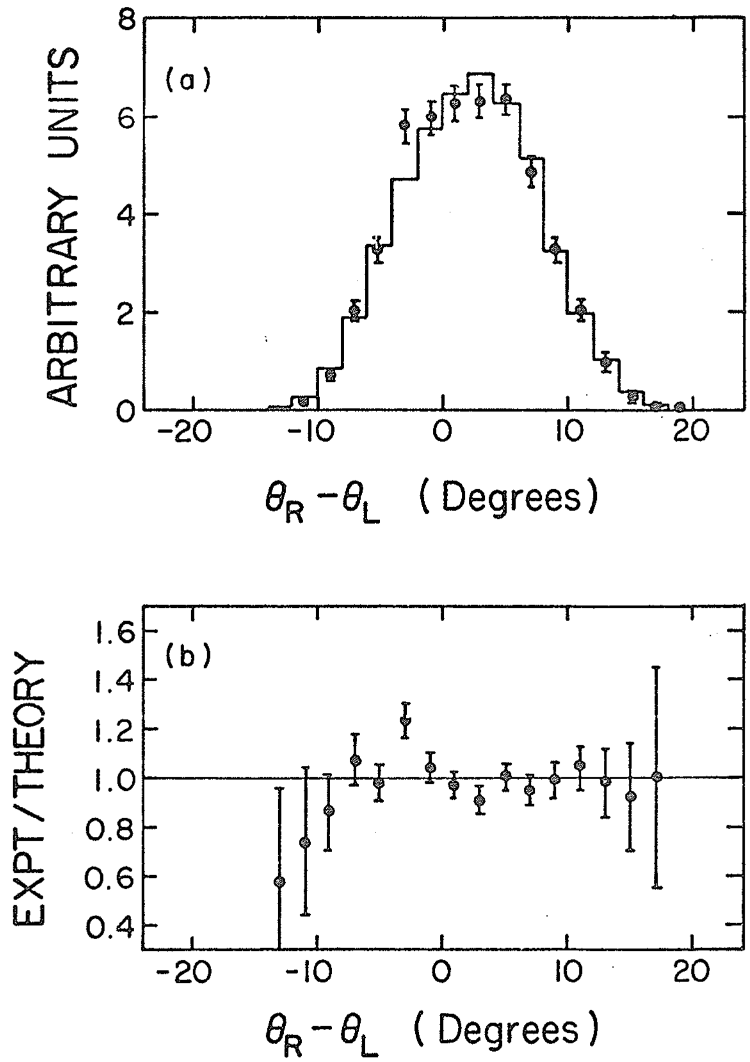

Figure 37

(a) The distribution of measured ppγ events (points and error bars) and Monte Carlo HJ ppγ events (solid histogram) as a function of $\Theta_R - \Theta_L$.

(b) The ratio of expt/theory for the histograms in (a). The error bars contain statistical errors only.

CHAPTER IX

CONCLUSIONS

$PP\gamma$ cross sections have been measured at an incident proton energy of 42 MeV and compared to the predictions of the Hamada-Johnston potential. Comparison to theory has been possible over a wide polar angle range and the relatively large number of events has permitted a stringent test to be made on the form of the non-coplanarity (Φ_r) distribution. Ψ_γ distributions have been found to agree qualitatively with the HJ predictions. The average of all integrated cross sections does not indicate any statistically significant deviation from Liou's predictions for the Hamada-Johnston potential. The overall ratio of experiment to theory for the integrated $d\sigma/d\theta_1 d\theta_2$ cross sections was found to be $0.967 \pm 4.6\,\%$.* The normalization uncertainty of 3.9% is included in the error. Liou's calculations, however, do not include Coulomb effects, which it is believed will lower the theoretical predictions by 6 - 10%. Thus the measured results would probably be consistent with revised theoretical predictions as well.

---

* Using a slightly different normalization procedure, a value of $0.943 \pm 4.6\%$ is obtained. The normalization error included is 3.8%.

The results of this experiment confirm that theoretical ppγ calculations can give a reasonable representation of measured data in a relatively model independent region. The minor discrepancies observed for certain angular combinations are not statistically significant. They occur in regions where experimental conditions pose the greatest problems and the stated uncertainties are large. Since experimental biases introduce large uncertainties in some of the measured results, it would be desirable to repeat the experiment with improved experimental conditions and better statistics in the number of events to obtain more reliable data at small angles.

Since experiment and theory appear to agree in a model-independent region, it would be a worthwhile endeavour to investigate regions where model-splitting is expected to be larger, for example at small polar angles in the 5 - 15^{o} range, or at energies of 100 MeV or above. A small angle experiment would be a most difficult proposition at any energy.

If an experiment similar to the present one at higher incident proton energies was to be attempted, a number of improvements could be made. In this experiment, charged particle fluxes in the front wire chambers, and not the number of random events, limited the data-taking rates. This problem could be reduced considerably by the use of proportional wire chambers in place of the present front wire chambers. Not only would this reduce the effects of spurious sparks due to δ-rays and additional protons entering the hodoscopes, but would also provide a means to prevent triggers where a neutral particle was detected in the counters. This would reduce the computer dead-time which also is a serious problem as far as data-taking rates are concerned. Elimination of the tungsten wires in the front wire chambers, or modification of the geometry to improve vertex resolution, would probably eliminate any remaining background in the ppγ regions from prompt p-p elastic events. The reduced multiple-scattering, improved energy resolution, lower p-p elastic cross sections and higher ppγ cross sections also make such an experiment easier to perform. These more favorable conditions might allow the present experimental geometry to be modified to observe polar angles as low as 10°.

The study of inelastic nuclear reactions, other than NNγ, for determining the nuclear potential is beset by serious theoretical difficulties. Thus, the possibility of relatively precise measurements at higher incident proton energies practically assures continued interest in ppγ as a useful tool for investigating the nucleon-nucleon interaction.

REFERENCES

1. T. Hamada and I. D. Johnston, Nucl. Phys. 34 : 352 (1962)
2. K. E. Lassila, M. H. Hull, Jr., H. M. Rupple, F. A. MacDonald and G. Breit, Phys. Rev. 126 : 881 (1962)
3. R. V. Reid, Jr., Ann. Phys. 50 : 411 (1968)
4. C. B. Bressel and A. K. Kerman, quoted in Bhargava and Sprung, Ann. Phys. (N. Y.) 42 : 222 (1967)
5. E. L. Lomon and H. Feshbach, Ann. Phys. (N. Y.)
6. F. Tabakin, Ann. Phys. (N. Y.) 30 : 51 (1964)
7. G. A. Baker, Jr., Phys. Rev. 128 : 1485 (1962)
   R. A. Bryan and B. L. Scott, Phys. Rev. 164 : 1215 (1967)
8. N. Hoshizaki, S. Otsuku, W. Watari and M. Yonezawa, Progr. Theoret. Phys. (Kyoto) 27 : 1199 (1962); S. Sawada, T. Ueda, W. Watari and M. Yonezawa, Progr. Theoret. Phys. (Kyoto) 28 : 991 (1962)
9. P. Signell, The Nuclear Potential, Chapter 4 in Advances in Nuclear Physics, Vol. 2. Edited by M. Baranger and E. Vogt, Plenem Press (1969)
10. J. Ashkin and R. E. Marshak, Phys. Rev. 76 : 989 (1949)
11. M. Sobel and A. Cromer, Phys. Rev. 132 : 2698 (1963)
12. W. A. Pearce and I. M. Duck, Phys. Letters 21 : 669 (1966)
13. M. I. Sobel, Ph.D. Thesis, unpublished
14. M. I. Sobel, Phys. Rev. 152 : 1385 (1966)
15. P. Signell and D. Marker, Proc. Williamsburg Conf. on Interm. Energy Physics, published by the College of William and Mary, Williamsburg, Va. (1966)
16. W. A. Pearce, W. A. Gale and I. M. Duck, Nucl. Phys. B3 : 241 (1967)
17. A. H. Cromer and M. I. Sobel, Phys. Rev. 152 : 1351 (1966); Erratum : Phys. Rev. 162 : 1174 (1967)

18. P. Signell, in Proceedings of the International Conference On Light Nuclei, Few Body Problems and Nuclear Forces, Brela, Yugoslavia, 1967; Gordon and Breach Science Publishers, Inc., New York, 1969

19. F. E. Low, Phys. Rev. 110 : 974 (1958)

20. E. M. Nyman, Phys. Rev. 170 : 1628 (1968); also Phys. Letters 25B : 135 (1967)

21. G. Felsner, Phys. Letters 25B : 290 (1967)

22. J. H. McGuire and W. A. Pearce, Nucl. Phys. A162 : 561 (1971)

23. J. H. McGuire, Ph.D. Thesis, unpublished

24. J. H. McGuire, preprint

25. P. Signell and D. Marker, Phys. Letters 26B : 559 (1968)

26. D. Marker and P. Signell, Phys. Rev. 185 : 1286 (1969)

27. V. R. Brown, Phys. Rev. 177 : 1498 (1969)

28. R. Baier, H. Kuhnelt and P. Urban, Nucl. Phys. B11 : 675 (1969)

29. D. Drechsel and L. C. Maximon, Ann. Phys. 49 : 403 (1968)

30. L. Heller, Phys. Rev. 174 : 1580 (1968); also Phys. Rev. 180 : 1616 (1969)

31. M. K. Liou, Phys. Rev. C2 : 131 (1970); also M. K. Liou and M. I. Sobel, Phys. Rev. C3 : 1430 (1971)

32. A. H. Cromer, preprint

33. M. K. Liou and K. S. Cho, Nucl, Phys. A160 : 417 (1971)

34. M. K. Liou and M. I. Sobel, preprint

35. E. M. Nyman, Nucl. Phys. A160 : 517 (1971)

36. M. K. Liou, Ph.D. Thesis, unpublished

37. L. I. Schiff, Quantum Mechanics, Third Edition, McGraw-Hill, Inc., 1968

38. J. H. McGuire, A. B. Cromer and M. I. Sobel, Phys. Rev. 179 : 948 (1969)

39. J. McKeown, L. G. Greeniaus, J. V. Jovanovich, W. F. Prickett, K. F. Suen and J. C. Thompson, to be published

40. J. McKeown, to be published

41. D. Reimer, L. G. Greeniaus, J. V. Jovanovich, J. McKeown and J. C. Thompson, to be published

42. D. G. Peterson, to be published

43. T. W. Millar and J. V. Jovanovich, to be published

44. D. Reimer, J. V. Jovanovich, J. McKeown and J. C. Thompson, Proc. DECUS Spring Symposium 1968

45. L. W. Funk, J. V. Jovanovich, R. Kawchuk, R. King, J. McKeown, C. A. Miller, D. Peterson, D. Reimer, K. G. Standing and J. C. Thompson, Proc. DECUS Fall Symposium, 1967

46. L. G. Greeniaus, J. V. Jovanovich, J. McKeown, T. Millar, D. G. Peterson and J. C. Thompson, Proc. of the International Sympos. on Nucl. Electronics, Versailles 1968, Vol. III, P. 53 - 1

47. J. McKeown, Ph.D. Thesis, unpublished

48. D. G. Peterson, M.Sc. Thesis, unpublished

49. T. W. Millar, M.Sc. Thesis, unpublished

50. Univ. of Man. Cyclotron Reports, 1970-06, 1970-07

51. B. Gottschalk, W. Schlaer and K. Wang, Phys. Letters 16 : 294 (1965)

52. B. Gottschalk, W. Schlaer and K. Wang, Nucl. Phys. 75 : 549 (1966)

53. B. Gottschalk, W. Schlaer and K. Wang, Nucl. Phys. A94 : 491 (1967)

54. K. W. Rothe, P. F. M. Koehler and E. H. Thorndike, Phys. Rev. Letters 16 : 1118 (1966)

55. K. W. Rothe, P. F. M. Koehler and E. H. Thorndike, Phys. Rev. 157 : 1247 (1967)

56. P. F. M. Koehler, K. W. Rothe and E. H. Thorndike, Phys. Rev. Letters 18 : 933 (1967)

57. R. E. Warner, Can. J. Phys. 44 : 1225 (1966); also Phys. Letters 18 : 289 (1965)

58. J. C. Thompson, S. I. H. Naqvi and R. Warner, Phys. Rev. 156 : 1156 (1967)

59. D. Drechsel, L. C. Maximon and R. E. Warner, Phys. Rev. 181 : 1720 (1969)

60. I. Slaus, J. W. Verba, J. R. Richardson, R. F. Carlson, W. T. H. Van Oers and L. S. August, Phys. Rev. Letters 18 : 536 (1966)

61. M. L. Halbert, D. L. Mason and L. C. Northcliffe, Phys. Rev. 168 : 1130 (1968)

62. D. L. Mason, M. L. Halbert and L. C. Northcliffe, Phys. Rev. 176 : 1159 (1968)

63. A. Bahnsen and R. L. Burman, Phys. Letters 26B : 585 (1968)

64. G. M. Crawley, D. L. Powell and B. V. Narasimha Rao, Phys. Letters 26B : 576 (1968)

65. E. A. Silverstein and K. G. Kibler, Phys. Rev. Letters 21 : 922 (1968)

66. F. Sannes, J. Trischuk and D. G. Stairs, Nucl. Phys. A146 : 438 (1970); also Phys. Rev. Letters 21 : 1474 (1968)

67. D. L. Mason, M. L. Halbert, A. van der Woude and L. C. Northcliffe, Phys. Rev. 179 : 940 (1969)

68. A. Niiler, C. Joseph, V. Valkovic, R. Spiger, T. Canada, S. T. Emerson, J. Sandler and G. D. Phillips, Phys. Rev. 178 : 1621 (1969)

69. D. O. Galde, M. L. Halbert, C. A. Ludemann and A. van der Woude, Phys. Rev. Letters 25 : 1581 (1970)

70. J. V. Jovanovich, L. G. Greeniaus, J. McKeown, T. W. Millar, D. G. Peterson, W. F. Prickett, K. F. Suen and J. C. Thompson, Phys. Rev. Letters 26 : 277 (1971)

71. D. W. Storm and R. Heffner, preprint

72. M. L. Halbert, Gull Lake Symposium on the Two-Body Force in Nuclei

73. J. Sanada, M. Yamanouchi, Y. Tagishi, Y. Nojiri, K. Kondo, S. Kobayashi, K. Nagamine, N. Ryu, H. Hasai, M. Nishi, M. Seki and D. C. Worth, Progr. Theoret. Phys. 39 : 853 (1968)

74. U. E. Kruse, J. M. Teem and N. F. Ramsey, Phys. Rev. 101 : 1079 (1956)

75. L. H. Johnston and D. A. Swanson, Phys. Rev. 111 : 212 (1958)

76. W. F. Prickett, PPb Note 70-01

77. C. A. Miller and F. Wilson, Univ. of Manitoba, private communication

78. A. M. Hanna, R. J. Griffiths, N. M. Clarke and G. T. A. Squier, Phys. Letters 37B : 361 (1971)

79. L. Welch, C. Chang, H. Forster, C. Kim, D. Devins and P. Deutchman, Nucl. Phys. A158 : 644 (1970)

80. R. M. Eisberg, D. Ingham, M. Makino, C. C. Kim and C. N. Waddell, Nucl. Phys. A175 : 58 (1971)

81. L. G. Greeniaus, PPB-Note 71-15

82. F. James, CERN 68-15 (1968)

83. K. F. Suen, Private Communication

84. L. Wolfenstein and J. Ashkin, Phys. Rev. 85 : 947 (1952)

APPENDIX A - DEFINITION OF VARIABLES

The variables used in the text are defined in alphabetical order. If a particular symbol has been used for two different meanings, the intended use is obvious when considered in its proper context. The section numbers where important variables are discussed are also given.

A	- Wolfenstein coefficient; abbreviated symbol for the V_{em} matrix element. (Appendix F)
α	- Square of the proton charge = 1/137 in the units used ($\hbar = c = 1$); angular resolution in polar angle. (Appendix C)
$A_{non-pp\gamma}$	- Number of events with $X^2 > 10$ in $pp\gamma$ background data. (Sec. VII.4.3)
$A_{pp\gamma}$	- Similar to $A_{non-pp\gamma}$ except events appear to simulate $pp\gamma$ conditions ($X^2 \leq 5.412$) (Sec. VII.4.3)
A_o	- Loschmidt's number = $2.687 \times 10^{19}/cm^3$.
B	- Wolfenstein coefficient. (Appendix F)
β	- Correction to number of detected p-p elastic calibration events. (Sec. VII.5.2)
C	- Wolfenstein coefficient; constant factor.
C_C	- Correction for coincidence circuit efficiency in $\left.\frac{d\sigma}{d\Omega}\right)_{el}$ measurement. (Sec. V.2.1)
C_{DT}	- Dead-time correction in $\left.\frac{d\sigma}{d\Omega}\right)_{el}$ measurement.
C_ϵ	- Factor including effects of spectrometer bias.
X^2	- Goodness of fit parameter in the statistical analysis. (Sec. VII.2.1)
C_I	- Correction for charge integrator in $\left.\frac{d\sigma}{d\Omega}\right)_{el}$ measurement. (Sec. V.2.2)

A - 2

C_N	- Normalization Constant. (Sec. V.1)
C_P	- Counts in prompt coincidence circuit.
C_{FC}	- Correction for charge collection efficiency of the Faraday Cup. (Sec. V.2.2)
C_{MS}	- Multiple-scattering correction in $\left.\frac{d\sigma}{d\Omega}\right)_{el}$ measurement. (Sec. V.2.7)
C_Q	- Charge calibration constant - number of calibration p-p elastic events/nc. (Sec. V.2.2)
C_R	- Counts in random coincidence circuit.
C_{TP}	- Correction of gas density to STP conditions. (Sec. V.2.6)
d_1	- Distance from beam to the elastic collimator.
d_2	- Distance from beam to slit in B2 baffles in Fig. 2.
δE	- Resolution of proton energy. (Sec. III.2.6)
ΔE_F	- Uncertainty in total energy of the final state as calculated from momentum conservation. (Sec. VII.2.1)
ΔE_x	- Energy denominator in relativistic form as calculated from $G_o(E')$. (Appendix F)
$d\Omega_L, \Delta\Omega_L$	- Solid angle for left proton.
$d\Omega_R, \Delta\Omega_R$	- Solid angle for right proton.
$d\Omega$, $\Delta\Omega$	- p-p elastic solid angle.
$\Delta\phi$	- Non-coplanarity in spherical polar coordinates - equal to $\phi_R - \phi_L - 180°$.
$d\phi_L, \Delta\phi_L$	- Azimuthal angle range for left proton.
$\Delta\phi_m$	- Maximum kinematically allowed value for $\Delta\phi$
$\delta\phi_D$	- Resolution in $\Delta\phi$

$d\phi_R, \Delta\phi_R$	- Azimuthal angle range for right proton.
$\delta\Phi_r$	- Resolution in relative non-coplanarity.
$\Delta\Phi_r$	- Range of relative non-coplanarity (see Φ_r).
$\Delta\psi_\gamma$, $d\psi_\gamma$	- Angular range of photon for Harvard coordinate system.
$d\theta_\gamma$, $\Delta\theta_\gamma$	- Range of polar angle of gamma ray.
$\langle \Delta Y \rangle$ $\langle \Delta Z \rangle$	-)) Vertex errors - standard deviations. (Sec. III.2.9) -)
$\langle \Delta Y_o \rangle$ $\langle \Delta Z_o \rangle$	-)) P-P Elastic vertex errors - standard deviations (Sec. III.2.9) -)
ΔV_Y, $\langle \Delta V_Y \rangle$ ΔV_Z, $\langle \Delta V_Z \rangle$	-))Vertex errors, values and mean value. (Sec. III.2.9) -)
DVY DVZ	-)) Adjusted vertex errors. (Appendix D) -)
δz, $\langle \delta z \rangle$	- Average observed target lengths (Sec. II.3).
$d\sigma$	- Cross section probability for $pp\gamma$.
$\left.\frac{d\sigma}{d\Omega}\right)_{el}$	- p-p elastic cross section.
$\hat{e}$	- Polarization vector of the gamma ray.
E	- Wolfenstein coefficient.
E, E'	- Initial and final state kinetic energies.
E_D	- Detected proton energy.
E_F	- Total energy of final state from momentum conservation.
E_L, E_l	- Kinetic energy of the left proton.

A - 4

E_{Lmin}	- Left energy cutoff = 9.25 MeV.
E_1'	- Final state total energy of left proton.
E_I	- Total energy of the initial state.
E_o	- Incident proton kinetic energy.
E_R, E_2	- Kinetic energy of the right proton.
E_{Rmin}	- Right energy cutoff = 10.25 MeV.
E_2'	- Total final state energy of right proton.
ϵ	- Total detection efficiency of the spectrometer. (Sec. II.3)
ϵ_o	- Detection efficiency due to geometrical effects. (Sec. IV.2.1)
ϵ_1	- Detection efficiency due to kinematic effects. (Sec. IV.2.2)
ϵ_{we}	- Wire chamber vertex efficiency for p-p elastic events. (Sec. V.1)
$\epsilon_{w\gamma}$	- Wire chamber vertex efficiency for ppγ events. (Sec. V.1)
f	- Function of polar angles used for vertex error adjustment. (Appendix D)
f_D	- Fraction of D_2 events appearing as contaminants in ppγ. (Sec. VII.4.4)
f_N	- Fraction of N_2 events appearing as contaminants in ppγ. (Sec. VII.4.4)
$\vert f\rangle$	- Denotes final plane wave state.
F	- Wolfenstein coefficient, non-relativistic phase space factor (Sec. IV.1.2); distribution function of beam profile (Sec. II.3).
F'	- Non-relativistic phase space factor (Sec. IV.1.2)

g	- Function of vertex position for vertex error adjustment. (Appendix D)
G	- Wolfenstein coefficient.
G_N, G_o	- Green's function operators for H_N and H_o respectively. (Appendix F)
h	- Function of energies for vertex error adjustment. (Appendix D)
H_N	- Hamiltonian for nucleon-nucleon interaction. (Appendix F)
H_o	- Free particle Hamiltonian. (Appendix F)
i	- $\sqrt{-1}$
$\vert i\rangle$	- Denotes initial plane wave state.
I	- Beam current in na.
$\hat{I}$	- Unit vector used in Wolfenstein expansion.
I_o	- Number of protons in 1 nc of charge.
K, $\underline{K}$, K_μ	- Energy, vector momentum and 4-momentum component of gamma ray.
K_1, K_2	- Kinetic energy operator for protons.
K_γ	- Kinetic energy operator for gamma ray.
$\underline{k}_1$, $\underline{k}_2$	- Proton momenta.
$\underline{k}$, $\underline{k}'$	- Relative proton momenta in initial and final states.
$\underline{k}_i$, $\underline{k}_f$	- Same as $\underline{k}$, $\underline{k}'$.
L	- Length of gas target for ppγ case.
L_{el}	- Length of gas target for p-p elastic events.
m, m_i	- Particle masses, usually proton mass.
M	- Center of mass scattering matrix. (Appendix F)

A - 6

M_o	- Geometrical correction factor $M_o = 1/\epsilon_o = N_{go}/N_{do}$. (Sec. IV.2.3)
M_1	- Monte Carlo correction factor $M_1 = 1/\epsilon_1 = \sum N_{g1}/\sum N_{d1}$. (Sec. IV.2.3)
M_X	- Center of mass scattering matrix for a single pole term. (Appendix F)
$\mathcal{M}, \mathcal{M}^\dagger$	- Evaluated center of mass scattering matrix. (Appendix F)
$\hat{m}$	- Unit vector used in Wolfenstein expansion.
μ_p	- Proton mganetic moment.
$\hat{n}$	- Unit vector used in Wolfenstein expansion.
N_B	- Number of prompt background events in $pp\gamma$ data. (Sec. VII.4.3)
N_{el}, N'_{el}	- Number of elastic events.
N_{do}	- Number of detected trajectories in evaluation of ϵ_o. (Sec. IV.2.1)
N_{go}	- Number of generated trajectories in evaluation of ϵ_o. (Sec. IV.2.1)
N_{uo}	- Number of undetected trajectories in evaluation of ϵ_o. (Sec. IV.2.1)
N_{d1}	- Number of detected Monte Carlo events in evaluation of ϵ_1. (Sec. IV.2.2)
N_{g1}	- Number of generated Monte Carlo events in evaluation of ϵ_1. (Sec. IV.2.2)
N_{u1}	- Number of undetected Monte Carlo events in evaluation of ϵ_1. (Sec. IV.2.2)
n_L	- Count rate in left counter.
$N_{non-pp\gamma}$	- Net number of events with $X^2 > 10$ in $pp\gamma$ data. (Sec. VII.4.4)
$N_{pp\gamma}, dN_{pp\gamma}$	- Net number of $pp\gamma$ events.

n_R	- Count rate in right counter.
η	- Pole indicator in the Green's functions.
O_i	- Sixteen independent bilinear operators formed from $\underline{\sigma}_1$, $\underline{\sigma}_2$, $\hat{I}$, $\hat{m}$, $\hat{n}$, 1 (Appendix F)
p	- Geometrical function used in angular resolution calculations. (Sec. III.2.4)
P_D	- Prompt events in D_2 data that have $X^2 \leqslant 5.412$. — See Sec. VII.4.4 for details
P_N	- Prompt events in N_2 data that have $X^2 \leqslant 5.412$. — See Sec. VII.4.4 for details
P_{non}	- Prompt events in D_2 or N_2 data that have $X^2 > 10$. — See Sec. VII.4.4 for details
P_f	- Final state 4-momentum. (Sec. IV.1.2)
P_i	- Initial state 4-momentum. (Sec. IV.1.2)
$\underline{p}_1$, $\underline{p}_1'$ / $\underline{p}_2$, $\underline{p}_2'$	- Initial and final proton momenta.
P_1	- Lab momentum of incident proton.
Φ	- Plane wave state, eigenstates of H_0.
$\bar{\Phi}$	- Harvard geometry non-coplanarity angle. (Appendix B)
Φ_{eff}	- Effective azimuthal range for left hodoscope. (Sec. III.2.3)
Φ_1, Φ_L	- Left hodoscope azimuthal angle.
Φ_2, Φ_R	- Right hodoscope azimuthal angle.
Φ_3, Φ_γ	- Azimuthal angle of gamma ray.
$\bar{\Phi}_r$, $\Delta\bar{\Phi}_r$	- Relative non-coplanarity and its range.
$\psi^{\pm}$	- Distorted plane wave state, eigenstates of H_N. (Appendix F)

Ψ_γ	- Photon angle in Harvard coordinate system. (Appendix B)
q	- Function used in angular resolution calculations. (Appendix C)
Q	- Charge in nanocoulombs.
$\bar{q}_1$, $\bar{q}_2$	- Proton momenta for intermediate scattering states.
R, R'	- Random event rates in ppγ experiment. (Sec. II.1.2)
R_D	- Random events in D_2 data that have $X^2 \leqslant 5.412$. See Sec. VII.4.4 for details
R_N	- Random events in N_2 data that have $X^2 \leqslant 5.412$. See Sec. VII.4.4 for details
R_{non}	- Random events in D_2 or N_2 data that have $X^2 > 10$. See Sec. VII.4.4 for details
R_3	- Lorentz invariant 3-body phase space factor. (Sec. IV.1.2)
ρ	- Energy dependent factor used for vertex error adjustment. (Sec. III.2.9)
$\underline{\sigma}$	- Pauli spin matrices.
T, t_x	- T-matrix and T-matrix elements.
2τ	- Resolving time of coincidence circuits.
θ_γ	- Laboratory polar angle of the gamma ray.
θ_1, θ_L	- Laboratory polar angle of left-side proton.
θ_2, θ_R	- Laboratory polar angle of right-side proton.
θ_S	- Sum of left and right proton polar angles.
U_o, U_1	- Unit step functions. (Sec. II.3)
U_N	- Operator relating scattered and plane wave states. (Appendix F)

V_{em}	- Operator representing the electromagnetic interaction. (Appendix F)
V_N	- Operator for the nucleon-nucleon interaction. (Appendix F)
W	- Width of slit in B2 baffles defining calibration p-p elastic region. (Sec. V.2.4)
Wt	- Weight for Monte Carlo event proportional to the cross section. (Sec. IV.1.2)
$\langle X_B \rangle$	- Lateral position of proton beam. (Sec. III.2.9)
X_i	-) Functions of the Wolfenstein coefficient) used in cross section calculations.
Y_i	-) (Appendix F)
Y_{min}	- Lowest vertical extent of the beam profile (Sec. II.3).
Y_{max}	- Maximum vertical extent of the beam profile (Sec. II.3).
Z	- Vertex position of $pp\gamma$ event.
Z_{el}	- Vertex position along beam direction of p-p elastic calibration events.
Z_{min}	- Lower Z-vertex position cut-off. (Sec. II.3)
Z_{max}	- Upper Z-vertex position cut-off. (Sec. II.3)

APPENDIX B - PPγ KINEMATICS

The definition of the variables associated with the three particles is given in Fig. B-1 for the spherical polar coordinate system (SPCS). The Z-axis is defined to be along the beam direction. The momenta for the left proton, right proton and photon are labelled as $\underline{P}_L$, $\underline{P}_R$ and $\underline{K}$ respectively. The polar angles are defined by the angles these momenta make with the beam direction. The azimuthal angles are measured from the X-axis in a counter-clockwise direction. The non-coplanarity of the protons is given by the azimuthal angles as follows

$$\Delta\phi = \phi_R - \phi_L - \pi \qquad \text{B-1}$$

The variables for the Harvard coordinate system (HCS) are given in Fig. B-2 for the same event shown in Fig. B-1. The vector $\underline{K}_o$ is the momentum vector for the limiting kinematic case for the polar angles of two protons. The Harvard polar angles $\bar{\theta}_L$ and $\bar{\theta}_R$ are defined by the angle between the projections of $\underline{P}_L$ and $\underline{P}_R$ in the X-Z plane and the Z-axis. The $\bar{\phi}$ angles are defined by the angles made by $\underline{P}_L$ and $\underline{P}_R$ with their projections in the X-Z plane. The orientation of the X-Z plane is chosen so that $\bar{\phi}_L = \bar{\phi}_R$. The event non-coplanarity is defined

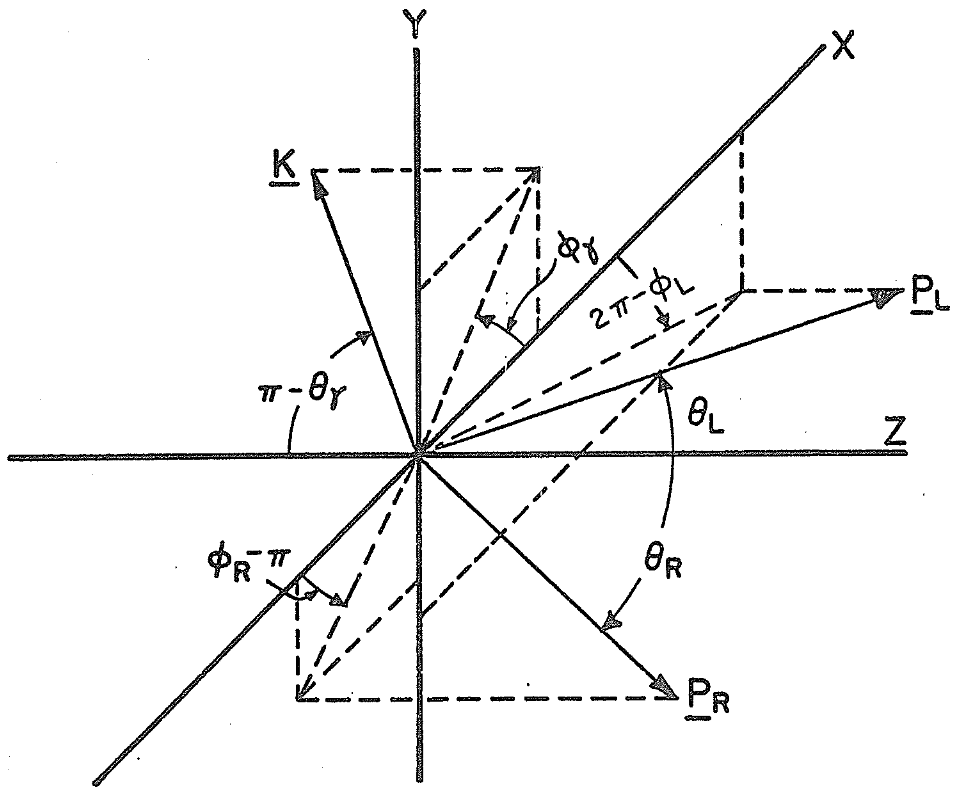

Figure B-1

Schematic diagram of a ppγ event in the Spherical Polar Co-ordinate System (SPCS). $\underline{P_L}$ and $\underline{P_R}$ are the left and right proton momentum vectors and $\underline{K}$ is the γ-ray momentum.

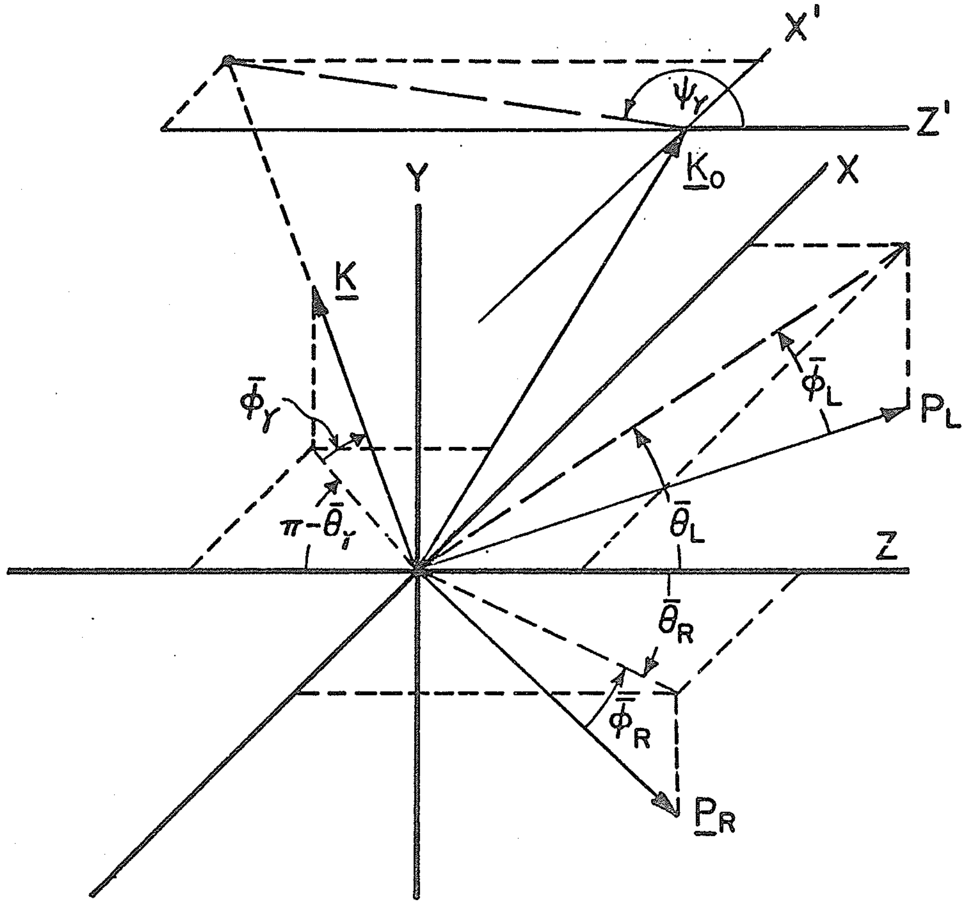

Figure B-2

Schematic diagram of a ppγ event in the Harvard Coordinate System. $\underline{P}_L$, $\underline{P}_R$ and $\underline{K}$ are the momenta for the left proton, right proton and γ-ray respectively. $\underline{K}_o$ is the momentum of the γ-ray for the limiting kinematic case.

by $\bar{\Phi} = \bar{\Phi}_L = \bar{\Phi}_R$.

The photon angular variable used is Ψ_γ and is defined relative to the limiting photon momentum. A plane X'Z' is drawn parallel to the XZ plane passing through the point of the $\underline{K}_o$ vector. The photon momentum $\underline{K}$ is multiplied by a constant α so that the point of $\alpha\underline{K}$ meets the X'Z' plane. Ψ_γ is defined as the angle between the beam direction and the vector $\underline{q} = \alpha\underline{K} - \underline{K}_o$. The constant α is determined by setting $q_y = 0$. Let θ_o and Φ_o ($\theta_o \approx 75^o$ and $\Phi_o \approx 90^o$ or 270^o) be the polar and azimuthal angles of $\underline{K}_o$ in the SPCS. Then

$$\alpha = \frac{K_{oy}}{K_y} = \frac{K_o \sin\theta_o \sin\Phi_o}{K \sin\theta_\gamma \sin\Phi_\gamma} \qquad \text{B-2}$$

Then Ψ_γ is defined as

$$= \tan^{-1} (q_x/q_z)$$

$$= \tan^{-1} \left(\frac{\alpha K \sin\theta_\gamma \cos\Phi_\gamma - K_o \sin\theta_o \cos\Phi_o}{\alpha K \cos\theta_\gamma - K_o \cos\theta_o}\right) \qquad \text{B-3}$$

Substituting for α and simplifying, we get

$$= \tan^{-1} \left(\frac{\sin\theta_\gamma \cos\Phi_\gamma - \sin\theta_\gamma \cot\Phi_o \sin\Phi_\gamma}{\cos\theta_\gamma - \sin\theta_\gamma \sin\Phi_\gamma \cot\theta_o \csc\Phi_o}\right) \qquad \text{B-4}$$

The variables θ_γ and Φ_γ are defined in SPCS.

The geometrical construction showing the definition of Ψ_γ also indicates that the experimental resolution for this quantity will deteriorate as the non-coplanarity increases. Note that for coplanar events ($\Phi_\gamma = 0^\circ$ or 180°) Ψ_γ becomes equal to θ_γ.

The small momentum carried away by the photon results in three prominent features of the ppγ kinematics. The opening angle ($\theta_L + \theta_R$) between the two protons must always be less than 90°. Thus in principle, ppγ events can be unambiguously separated from p-p elastic events. Second, for all proton polar angle combinations there is a maximum value of the event non-coplanarity. In this experiment the maximum non-coplanarity varies from $\Delta\Phi_m = 23.67^\circ$ for $18^\circ - 18^\circ$ events to $\Delta\Phi_m = 5.27^\circ$ for $38^\circ - 34^\circ$. Finally, for given values of the proton polar angles and non-coplanarity, the allowed proton energies form an elliptical closed curve on an $E_L - E_R$ plot. Some representative curves, of interest to this experiment, are shown in Fig. B-3. The photon direction changes for different points on the allowed kinematic locus. The size of the ring is maximum for coplanar events and shrinks to a point as the maximum non-coplanarity is reached. The shaded vertical lines indicate the low energy cut-offs of the spectrometer. The photon energy does not increase

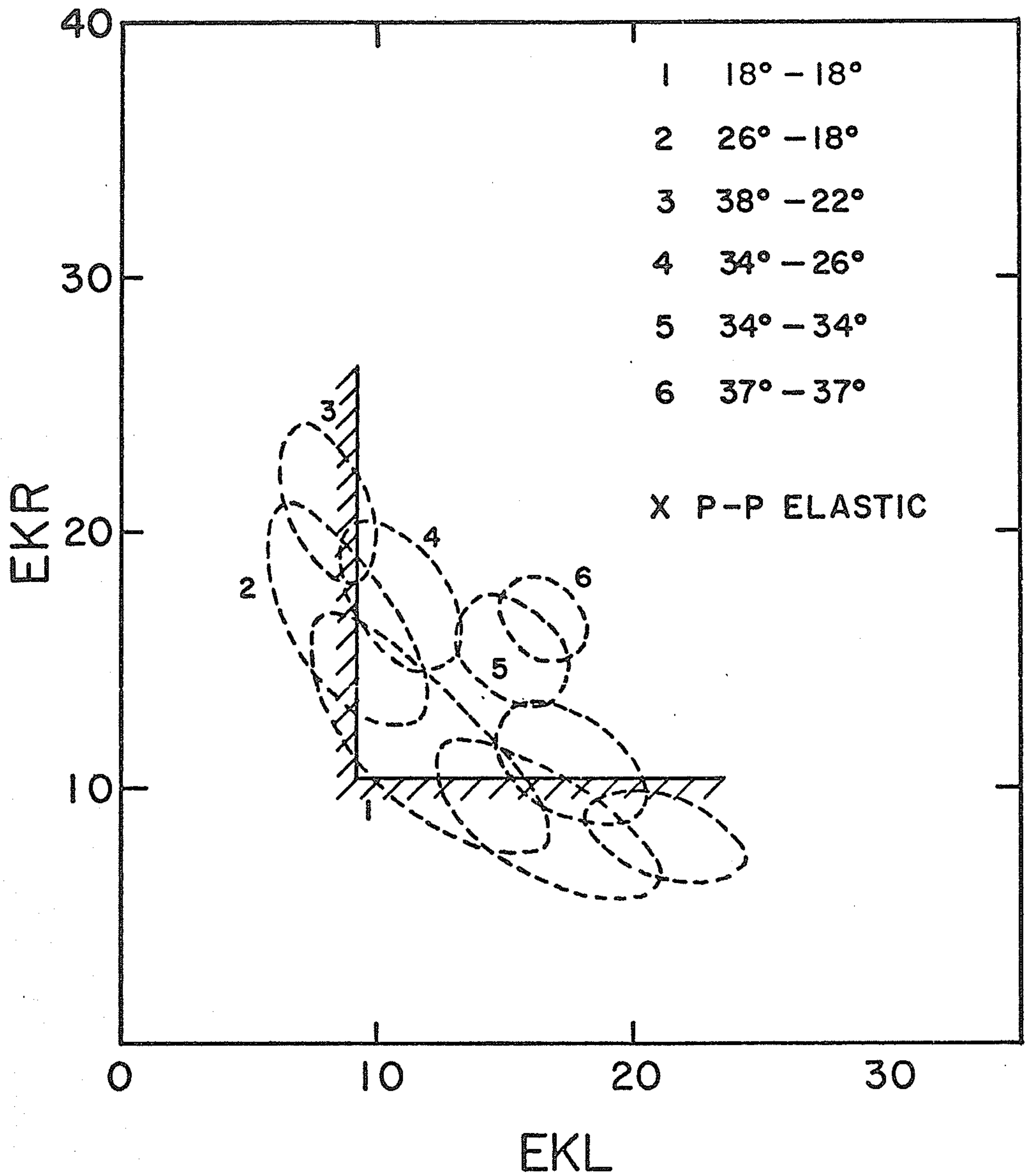

Figure B-3

Some representative kinematic loci for coplanar ppγ events at 42 MeV incident beam energy. The shaded areas represent the energy cut-offs of the spectrometer. These were 9.25 MeV for the left proton and 10.25 MeV for the right proton.

very much beyond the lower cut-off point. Since momentum must be conserved, even if the protons are both along the beam direction, they must have ~ 130 MeV/c momentum. This corresponds to a 25 MeV photon also parallel to the beam.

When the SPCS is used for theoretical cross section calculations, kinematic singularities result in the cross sections for non-coplanar events because the photon polar angle is not continuous in the range from 0 to π. The HCS was defined in order to define variables that are continuous over their allowed range for all events.

Fig. B-4 shows the kinematic loci for (p,2p) reactions on possible contaminants in the H_2 gas. Events for these reactions do not have maximum limits for the non-coplanarity. The allowed loci for the D(p,2p)n reaction show some spread as the polar angles change. For the other reactions the spread in loci is so small that for our purposes they can be assumed to lie on a straight line defined by their respective Q-values. When the kinematics for the contaminants and for ppγ are compared, it is seen that the D(p,2p)n reaction and $N^{14}(p,2p)C^{13}$ reaction (to the C^{13} ground state) do not seriously overlap with ppγ kinematic regions, so they do not present serious problems. Reactions on C^{12}, O^{16}, He^4 and to excited states of C^{13} do yield background in the ppγ region and therefore must be reduced as much as possible.

B - 8

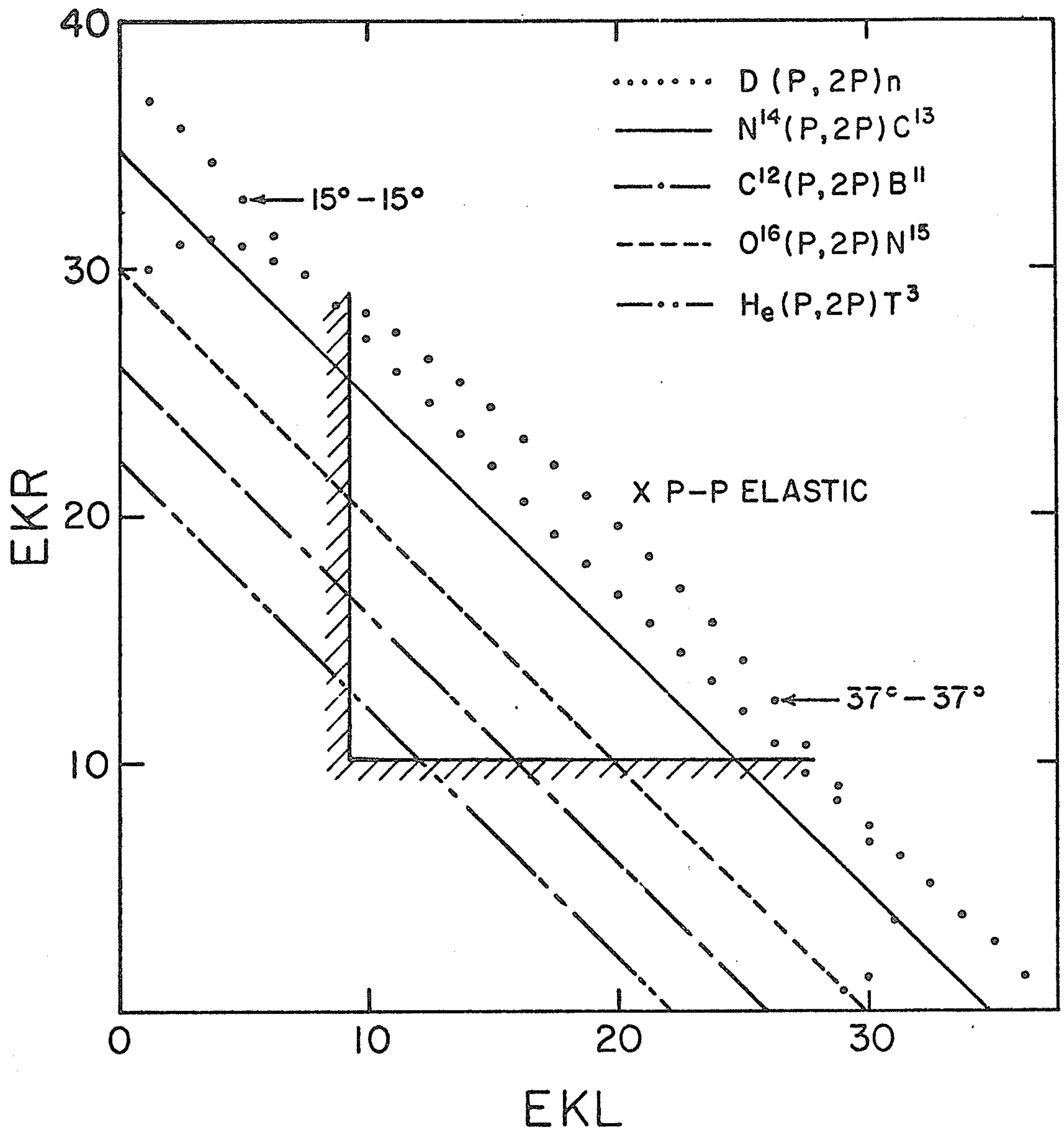

Figure B-4

Kinematic loci for (p,2p) reactions on some of the possible contaminants in the ppγ experiment. For the D(p,2p)n reaction the position of the kinematic band depends on the proton polar angles. Two extreme cases are shown. The kinematic loci for the other reactions are nearly independent of the proton polar angles and depend only on the Q-value of the reaction. The energy cut-offs of the spectrometer are shown by the shaded areas.

APPENDIX C - ANGULAR RESOLUTIONS

In this appendix the various factors contributing to the angular resolutions are combined and the dependence of the angular resolutions on energy and angles is derived.

The various quantities used are defined in Fig. C-1. The maximum azimuthal angle range seen in either hodoscope is about $\pm 40^\circ$ and the average value closer to $\sim 15^\circ$. The range of polar angles is from 15° to 45°. Thus, particle trajectories make average angles with the normal to the wire chambers of $\sim 15^\circ$. To a first approximation the path length of a particle, D_2, can be replaced by R, the separation between the wire chambers. Then approximately

$$X \approx R \sin\theta \cos\phi \qquad \text{C-1}$$

$$Y \approx R \tan\beta \qquad \text{C-2}$$

$$\tan\phi = \frac{Y}{X} \approx \frac{\tan\beta}{\sin\theta \cos\phi} \qquad \text{C-3}$$

If δX and δY are the uncertainties in X and Y due to wire spacing and multiple-scattering, then we have

$$\delta(\tan\phi) = \left\{ \frac{\delta Y^2}{X^2} + \frac{Y^2}{X^4} \delta X^2 \right\}^{\frac{1}{2}} = \sec^2\phi \, \delta\phi \qquad \text{C-4}$$

If α is the r.m.s. angular uncertainty in the particle direction, $\delta X \approx \delta Y \approx \alpha R$

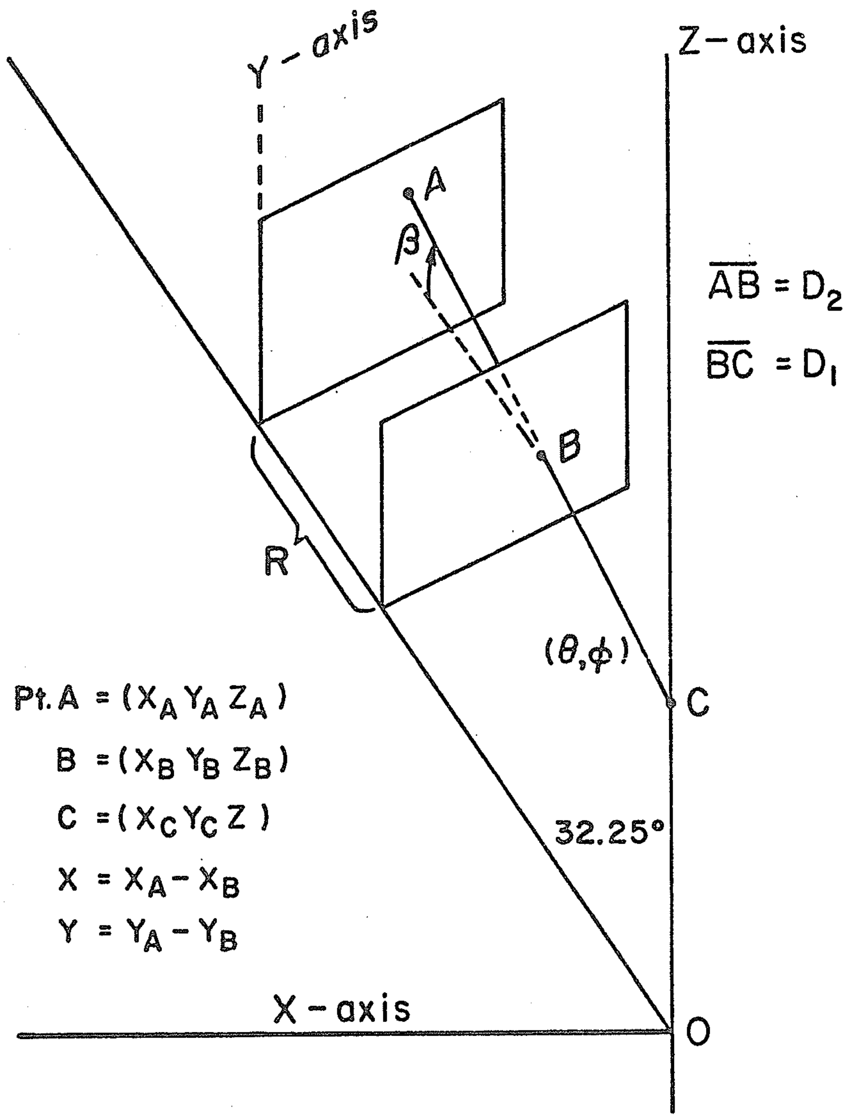

Figure C-1

Schematic diagram of a proton trajectory passing through a hodoscope. The observer is directly over the beam plane looking down the beam direction. β is defined by the angle between line $\overline{AB}$ and its projection parallel to the XZ plane. (θ, ϕ) indicates the polar and azimuthal angles of the trajectory in the SPCS.

Substituting in equation C-4

$$(\delta\phi) = \alpha \frac{\cos\phi}{\sin\theta} \left\{ 1 + \frac{\tan^2\beta}{\sin^2\theta \cos^2\phi} \right\}^{\frac{1}{2}}$$

$$= \frac{\alpha}{\sin\theta} \qquad \text{C-5}$$

The origin of the uncertainty is contained in α. The rest of the expression C-5 is strictly a geometrical factor.

Using a similar analysis for θ we obtain

$$\delta\theta = \alpha \cos\theta \left\{ 1 + (\sin^2\theta \cos^2\phi + \sin^2\theta \tan^2\phi) \tan^2\theta \right\}^{\frac{1}{2}} \qquad \text{C-6}$$

The angular uncertainty α arises from the chamber wire spacing and multiple-scattering in the material between the beam and the rear wire chamber. The latter can be separated into two parts — the 50 μm Mylar foil parallel to the beam, and everything else. The distance of Mylar traversed depends approximately as $1/\sin\theta$ while the distance traversed through all other media is nearly independent of the direction and vertex position. Multiple-scattering has the following dependence on particle energy (E) and thickness (t) of material traversed.

$$\alpha' = \frac{C\sqrt{t}}{E} \qquad \text{C-7}$$

The contribution of wire spacing to α is nearly constant.

If the contributions of wire spacing, the material from the Mylar foil to the rear chamber and the 50 µm Mylar foil are added in quadrature, then

$$\alpha = \left\{ a^2 + \frac{b^2}{E^2} + \frac{c^2}{E^2 \sin\theta} \right\}^{\frac{1}{2}} \qquad \text{C-8}$$

The dependence on ϕ in equation C-6 is so small it can be neglected. Then

$$\delta\theta = \alpha \cos\theta \left\{ 1 + \sin^2\theta \tan^2\theta \right\}^{\frac{1}{2}} \qquad \text{C-9}$$

The ratio of $\delta\phi / \delta\theta$ is then

$$\frac{\delta\phi}{\delta\theta} = \frac{2}{\sin 2\theta \left\{ 1 + \sin^2\theta \tan^2\theta \right\}^{\frac{1}{2}}} \qquad \text{C-10}$$

The polar and azimuthal angle resolutions for p-p elastic events at $\theta = 45^\circ$ have been measured under the following conditions

(a) 42 MeV incident beam with no Mylar foil present;

(b) 42 MeV incident beam with Mylar foil present;

(c) 24 MeV incident beam with Mylar foil present.

The measured polar angle resolutions were $\pm\, 0.30^\circ$, $\pm\, 0.385^\circ$ and $\pm\, 0.58^\circ$ respectively. The azimuthal angle resolutions were almost exactly a factor of 2 larger. Evaluation of C-10 at $\theta = 45^\circ$ yields an expected ratio of 1.63. The reason for this discrepancy is only partially understood.

C - 5

Thus the observed ratio of resolutions is used when evaluating $\delta\phi$ as a function of angles and energies. If α_o is the angular resolution for 42 MeV p-p elastic events at $\theta = 45°$, then evaluation of the constants in equation C-8 yields

$$\delta\theta = \alpha_o \sqrt{\tfrac{4}{3}} \cos\theta \left\{1 + \sin^2\theta \tan^2\theta\right\}^{\frac{1}{2}} \qquad \text{C-11}$$

$$\delta\phi = \frac{2\alpha_o}{\sin\theta} \qquad \text{C-12}$$

$$\alpha_o = \left\{(0.23°)^2 + \frac{(0.19°)^2}{E_r^{\,2}} + \frac{(0.25°)^2}{\sqrt{2}\,E_r^{\,2}\sin\theta}\right\}^{\frac{1}{2}} \qquad \text{C-13}$$

$$E_r = E(\text{MeV})/21 \qquad \text{C-14}$$

The resolutions are normalized to polar angles of 45° and particle energies of 21 MeV. The results of equations C-11 and C-12 yield one standard deviation resolutions.

APPENDIX D - VERTEX ERROR RESOLUTION

The vertex errors have two primary origins. These are the finite wire spacing in the spark chambers and multiple-scattering in the front chambers. The contributions from other sources can be neglected[1].

The geometric variables used are defined in Fig. C-1. The vertical vertex error is considered first. The vertex error along the beam direction is simply related to this provided the horizontal and vertical spatial resolutions of the wire chambers are the same. If the contribution $\langle \Delta V_Y \rangle$ of each particle to the Y-vertex error is considered separately, then

$$\langle \Delta V_Y \rangle^2 = (\delta Y)^2 \left\{ \frac{(D_1 + D_2)^2}{D_2^2} + \frac{D_1^2}{D_2^2} \right\} + \alpha^2 D_1^2 \qquad \text{D-1}$$

α is the angular resolution due to multiple-scattering in the front chamber and δY is the uncertainty in the spark position. D_1 is the distance from the origin to the front chamber and D_2 is the distance between the chambers, both along the particle path. Equation D-1 is obtained using simple lever arm effects. The effects of multiple-scattering in the front wire chamber, and wire spacing in each chamber are added in quadrature. The results for the two particles must also be compounded together.

APPENDIX D - VERTEX ERROR RESOLUTION

The vertex errors have two primary origins. These are the finite wire spacing in the spark chambers and multiple-scattering in the front chambers. The contributions from other sources can be neglected[1].

The geometric variables used are defined in Fig. C-1. The vertical vertex error is considered first. The vertex error along the beam direction is simply related to this provided the horizontal and vertical spatial resolutions of the wire chambers are the same. If the contribution $\langle \Delta V_Y \rangle$ of each particle to the Y-vertex error is considered separately, then

$$\langle \Delta V_Y \rangle^2 = (\delta Y)^2 \left\{ \frac{(D_1 + D_2)^2}{D_2^2} + \frac{D_1^2}{D_2^2} \right\} + \alpha^2 D_1^2 \qquad \text{D-1}$$

α is the angular resolution due to multiple-scattering in the front chamber and δY is the uncertainty in the spark position. D_1 is the distance from the origin to the rear chamber and D_2 is the distance between the chambers, both along the particle path. Equation D-1 is obtained using simple lever arm effects. The effects of multiple-scattering in the front wire chamber, and wire spacing in each chamber are added in quadrature. The results for the two particles must also be compounded together.

D - 2

In principle, $\langle \Delta V_Y \rangle$ in equation D-1 could be evaluated for each particle detected in the spectrometer. In practice, it is a relatively complicated function of the measured quantities (wire chamber coordinates) and it is a time consuming quantity to evaluate on an event-by-event basis. Since the purpose of deriving the functional dependence is to obtain a means of adjusting the measured vertex errors, a number of simplifying approximations are made. It has been found empirically that a good approximation to the dependence of $\langle \Delta V_Y \rangle$ on the vertex position ($\lesssim 10\%$ error) is obtained by evaluating the extreme values of D-1 and assuming a linear change with vertex position along the beam direction. The value of $\langle \Delta V_Y \rangle$ increases by a factor of 1.7 going from the B2 baffles (p-p elastic position) to the B1 baffles (See Fig. 2 in Chapter III).

The multiple-scattering factor α also has a 1/E dependence. The effect on the vertex error of wire spacing (independent of energy) and multiple-scattering has been included by use of a term of the form $(a^2 + b^2/E_r^2)^{\frac{1}{2}}$. In this approximation, the dependence on the particle direction in 'a' (due to wire spacing) has been neglected. Similarly, the multiple-scattering in the front wire chambers is assumed to be independent of direction. The constants 'a' and 'b' have been adjusted empirically to give the desired Y-vertex error distribution.

If $\langle \Delta Y \rangle$ is the quadrature sum of the effects of the two particles and $\langle \Delta Y_o \rangle$ the Y-vertex error for p-p elastic events at 42 MeV and 45^o polar angles, then

$$\langle \Delta Y \rangle = \langle \Delta Y_o \rangle \left(1.7 - \frac{0.7Z}{Z_{el}}\right) \left(0.34\,\rho^2 + 0.66\right)^{\frac{1}{2}} \qquad \text{D-2}$$

$$\rho^2 = \frac{21}{2} \; \frac{E_L^2 + E_R^2}{E_L^2 \; E_R^2} \qquad \text{D-3}$$

where Z is the vertex position and Z_{el} the average vertex position for p-p elastic events defining $\langle \Delta Y_o \rangle$. The Z-vertex error contribution $\langle \Delta Z \rangle$ is related to $\langle \Delta Y \rangle$ by

$$\langle \Delta Z \rangle = \frac{\langle \Delta Y \rangle}{\sin\theta} \qquad \text{D-4}$$

Thus

$$\langle \Delta Z \rangle = \frac{\langle \Delta Y \rangle}{\sqrt{2}} \left(\csc^2\theta_L + \csc^2\theta_R\right)^{\frac{1}{2}} \qquad \text{D-5}$$

Writing

$$g(Z) = \left(1.7 - \frac{0.7Z}{Z_{el}}\right)^{-1} \qquad \text{D-6}$$

$$h(E_L, E_R) = \left(0.34\,\rho^2 + 0.66\right)^{-\frac{1}{2}} \qquad \text{D-7}$$

$$f(\theta_L, \theta_R) = 2\left(\csc^2\theta_L + \csc^2\theta_R\right)^{-\frac{1}{2}} \qquad \text{D-8}$$

Then the adjusted vertex errors, defined on an event by event basis, are

$$DVZ = \Delta V_Z \; f(\theta_L, \theta_R) \; g(Z) \; h(E_L, E_R) \qquad \text{D-9}$$

$$DVY = \Delta V_Y \; g(Z) \; h(E_L, E_R) \qquad \text{D-10}$$

Reference to Fig. 23 in Sec. VII.1.1 shows that the correction procedure used is adequate. This has also been verified by observation of the ppγ data, but the number of events is smaller and the statistical error larger.

Reference:

1. J. McKeown, Ph.D. Thesis 1970, unpublished.

APPENDIX E - THEORETICAL CROSS SECTIONS

The cross sections calculated using M. K. Liou's computer code are summarized here. The integrated cross sections only are given. The calculations as a function of Ψ_γ can be obtained in Ref. 1.

$\bar{\Phi}_m$ is the maximum Harvard geometry non-coplanarity.
$\Delta\phi_m$ is the maximum spherical geometry non-coplanarity.
Φ_r is the relative non-coplanarity.

The angles specified at the top of each table are the Harvard geometry $\bar{\Theta}$ angles (not the polar angles with the beam direction).

References:

1. M. K. Liou, L. G. Greeniaus and K. F. Suen, PPB-Note 71-16.

14° - 18°

$\bar{\Phi}_m = 3.71^\circ$ $\Delta\phi_m = 27.61^\circ$

Φ_r	$d\sigma/d\Omega_1 d\Omega_2$ $\mu b/sr^2$
0.03	1.5690
0.24	1.7142
0.49	1.9795
0.75	1.8001
0.97	0.6465

$d\sigma/d\theta_1 d\theta_2 = 0.3788\ \mu b/rad^2$

14° - 22°

$\bar{\Phi}_m = 3.46^\circ$ $\Delta\phi_m = 23.71^\circ$

Φ_r	$d\sigma/d\Omega_1 d\Omega_2$ $\mu b/sr^2$
0.03	1.2680
0.26	1.3486
0.49	1.4651
0.75	1.2731
0.98	0.3944

$d\sigma/d\theta_1 d\theta_2 = 0.3173\ \mu b/rad^2$

14° - 26°

$\bar{\Phi}_m = 3.18^\circ$ $\Delta\phi_m = 20.50^\circ$

Φ_r	$d\sigma/d\Omega_1 d\Omega_2$ $\mu b/sr^2$
0.03	1.0143
0.25	1.0587
0.50	1.1183
0.75	0.9417
0.97	0.3204

$d\sigma/d\theta_1 d\theta_2 = 0.2291\ \mu b/rad^2$

14° - 30°

$\phi_m = 2.89^\circ$ $\Delta\phi_m = 17.80^\circ$

Φ_r	$d\sigma/d\Omega_1 d\Omega_2$ $\mu b/sr^2$
0.03	0.8465
0.24	0.8718
0.52	0.9040
0.76	0.7455
0.97	0.3102

$d\sigma/d\theta_1 d\theta_2 = 0.1844\ \mu b/rad^2$

18° - 18°

$\bar{\Phi}_m = 3.63^\circ$ $\Delta\phi_m = 23.67^\circ$

Φ_r	$d\sigma/d\Omega_1 d\Omega_2$ $\mu b/sr^2$
0.03	1.4925
0.14	1.5364
0.43	1.7944
0.69	1.7950
0.99	0.4157

$d\sigma/d\theta_1 d\theta_2 = 0.3816\ \mu b/rad^2$

18° - 22°

$\bar{\Phi}_m = 3.45^\circ$ $\Delta\phi_m = 20.45^\circ$

Φ_r	$d\sigma/d\Omega_1 d\Omega_2$ $\mu b/sr^2$
0.03	1.3733
0.29	1.4892
0.58	1.5895
0.84	1.1193
0.96	0.4768

$d\sigma/d\theta_1 d\theta_2 = 0.3509\ \mu b/rad^2$

18° - 26°

$\bar{\Phi}_m = 3.20°$ $\Delta\phi_m = 17.75°$

Φ_r	$d\sigma/d\Omega_1 d\Omega_2$ $\mu b/sr^2$
0.03	1.2314
0.25	1.2883
0.50	1.3518
0.75	1.1427
0.97	0.4340

$d\sigma/d\theta_1 d\theta_2 = 0.3043\ \mu b/rad^2$

18° - 30°

$\bar{\Phi}_m = 2.94°$ $\Delta\phi_m = 15.42°$

Φ_r	$d\sigma/d\Omega_1 d\Omega_2$ $\mu b/sr^2$
0.03	1.1169
0.24	1.1479
0.51	1.1756
0.75	0.9776
0.95	0.4358

$d\sigma/d\theta_1 d\theta_2 = 0.2654\ \mu b/rad^2$

18° - 34°

$\bar{\Phi}_m = 2.65°$ $\Delta\phi_m = 13.36°$

Φ_r	$d\sigma/d\Omega_1 d\Omega_2$ $\mu b/sr^2$
0.04	1.0406
0.26	1.0628
0.53	1.0585
0.79	0.8048
0.98	0.3126

$d\sigma/d\theta_1 d\theta_2 = 0.2367\ \mu b/rad^2$

18° - 38°

$\bar{\Phi}_m = 2.37°$ $\Delta\phi_m = 11.53°$

Φ_r	$d\sigma/d\Omega_1 d\Omega_2$ $\mu b/sr^2$
0.04	0.9995
0.25	1.0166
0.51	1.0060
0.76	0.8022
0.97	0.3349

$d\sigma/d\theta_1 d\theta_2 = 0.2126\ \mu b/rad^2$

22° - 22°

$\bar{\Phi}_m = 3.31°$ $\Delta\phi_m = 17.73°$

Φ_r	$d\sigma/d\Omega_1 d\Omega_2$ $\mu b/sr^2$
0.03	1.3952
0.15	1.4225
0.45	1.5563
0.75	1.3149
1.00	0.3988

$d\sigma/d\theta_1 d\theta_2 = 0.3612\ \mu b/rad^2$

22° - 26°

$\bar{\Phi}_m = 3.10°$ $\Delta\phi_m = 15.39°$

Φ_r	$d\sigma/d\Omega_1 d\Omega_2$ $\mu b/sr^2$
0.03	1.3762
0.26	1.4297
0.52	1.4705
0.77	1.1679
0.94	0.5350

$d\sigma/d\theta_1 d\theta_2 = 0.3480\ \mu b/rad^2$

E - 4

$22^\circ - 30^\circ$

$\bar{\Phi}_m = 2.85^\circ$ $\Delta\phi_m = 13.34^\circ$

Φ_r	$d\sigma/d\Omega_1 d\Omega_2$ $\mu b/sr^2$
0.04	1.3533
0.25	1.3856
0.49	1.3969
0.77	1.0879
0.98	0.4452

$d\sigma/d\theta_1 d\theta_2 = 0.3311\ \mu b/rad^2$

$22^\circ - 34^\circ$

$\bar{\Phi}_m = 2.58^\circ$ $\Delta\phi_m = 11.50^\circ$

Φ_r	$d\sigma/d\Omega_1 d\Omega_2$ $\mu b/sr^2$
0.04	1.3484
0.23	1.3677
0.50	1.3549
0.74	1.1057
0.93	0.4940

$d\sigma/d\theta_1 d\theta_2 = 0.3092\ \mu b/rad^2$

$22^\circ - 38^\circ$

$\bar{\Phi}_m = 2.29^\circ$ $\Delta\phi_m = 9.83^\circ$

Φ_r	$d\sigma/d\Omega_1 d\Omega_2$ $\mu b/sr^2$
0.04	1.3748
0.26	1.3894
0.52	1.3361
0.79	1.0414
0.96	0.4612

$d\sigma/d\theta_1 d\theta_2 = 0.2977\ \mu b/rad^2$

$22^\circ - 42^\circ$

$\bar{\Phi}_m = 1.99^\circ$ $\Delta\phi_m = 8.29^\circ$

Φ_r	$d\sigma/d\Omega_1 d\Omega_2$ $\mu b/sr^2$
0.05	1.4471
0.25	1.4571
0.50	1.4031
0.75	1.1026
0.95	0.4504

$d\sigma/d\theta_1 d\theta_2 = 0.2792\ \mu b/rad^2$

$26^\circ - 26^\circ$

$\bar{\Phi}_m = 2.92^\circ$ $\Delta\phi_m = 13.33^\circ$

Φ_r	$d\sigma/d\Omega_1 d\Omega_2$ $\mu b/sr^2$
0.03	1.4777
0.17	1.4969
0.51	1.5230
0.86	0.9347
0.99	0.3230

$d\sigma/d\theta_1 d\theta_2 = 0.3738\ \mu b/rad^2$

$26^\circ - 30^\circ$

$\bar{\Phi}_m = 2.68^\circ$ $\Delta\phi_m = 11.49^\circ$

Φ_r	$d\sigma/d\Omega_1 d\Omega_2$ $\mu b/sr^2$
0.04	1.5659
0.22	1.5860
0.49	1.5814
0.71	1.3337
0.97	0.4604

$d\sigma/d\theta_1 d\theta_2 = 0.3726\ \mu b/rad^2$

$26^\circ - 34^\circ$

$\bar{\Phi}_m = 2.41^\circ$ $\Delta\phi_m = 9.82^\circ$

I_r	$d\sigma/d\Omega_1 d\Omega_2$ ub/sr^2
0.21	1.6787
0.41	1.6675
0.62	1.5114
0.83	1.0527
0.95	0.5596

$d\sigma/dO_1dO_2 = 0.3728\ \mu b/rad^2$

$26^\circ - 38^\circ$

$\bar{\Phi}_m = 2.12^\circ$ $\Delta\phi_m = 8.27^\circ$

Φ_r	$d\sigma/d\Omega_1 d\Omega_2$ $\mu b/sr^2$
0.05	1.8109
0.24	1.8154
0.47	1.7564
0.71	1.3910
0.94	0.6488

$d\sigma/d\theta_1 d\theta_2 = 0.3685\ \mu b/rad^2$

$26^\circ - 42^\circ$

$\bar{\Phi}_m = 1.81^\circ$ $\Delta\phi_m = 6.83^\circ$

I_r	$d\sigma/d\Omega_1 d\Omega_2$ $\mu b/sr^2$
0.06	2.0374
0.22	2.0384
0.50	1.9351
0.72	1.5772
0.99	0.6242

$d\sigma/dO_1dO_2 = 0.3777\ \mu b/rad^2$

$30^\circ - 30^\circ$

$\bar{\Phi}_m = 2.45^\circ$ $\Delta\phi_m = 9.81^\circ$

Φ_r	$d\sigma/d\Omega_1 d\Omega_2$ $\mu b/sr^2$
0.04	1.7783
0.21	1.7877
0.61	1.6201
0.82	1.1570
0.98	0.4505

$d\sigma/d\theta_1 d\theta_2 = 0.4059\ \mu b/rad^2$

$30^\circ - 34^\circ$

$\bar{\Phi}_m = 2.18^\circ$ $\Delta\phi_m = 8.27^\circ$

I_r	$d\sigma/d\Omega_1 d\Omega_2$ $\mu b/sr^2$
0.05	2.0233
0.23	2.0247
0.46	1.9601
0.73	1.5267
0.92	0.8314

$d\sigma/dO_1dO_2 = 0.4265\ \mu b/rad^2$

$30^\circ - 38^\circ$

$\bar{\Phi}_m = 1.88^\circ$ $\Delta\phi_m = 6.82^\circ$

Φ_r	$d\sigma/d\Omega_1 d\Omega_2$ $\mu b/sr^2$
0.05	2.3539
0.27	2.3421
0.53	2.1717
0.74	1.6980
0.96	0.7156

$d\sigma/d\theta_1 d\theta_2 = 0.4452\ \mu b/rad^2$

E - 6

$30^\circ - 42^\circ$

$\bar{\Phi}_m = 1.56^\circ$ $\Delta\phi_m = 5.46^\circ$

Φ_r	$d\sigma/d\Omega_1 d\Omega_2$ $\mu b/sr^2$
0.06	2.8748
0.26	2.8569
0.51	2.6614
0.77	1.9473
0.96	0.8550

$d\sigma/d\theta_1 d\theta_2 = 0.4707\ \mu b/rad^2$

$34^\circ - 34^\circ$

$\bar{\Phi}_m = 1.91^\circ$ $\Delta\phi_m = 6.82^\circ$

Φ_r	$d\sigma/d\Omega_1 d\Omega_2$ $\mu b/sr^2$
0.05	2.4695
0.26	2.4576
0.58	2.2038
0.79	1.6177
0.94	0.6576

$d\sigma/d\theta_1 d\theta_2 = 0.4718\ \mu b/rad^2$

$34^\circ - 38^\circ$

$\bar{\Phi}_m = 1.60^\circ$ $\Delta\phi_m = 5.46^\circ$

Φ_r	$d\sigma/d\Omega_1 d\Omega_2$ $\mu b/sr^2$
0.06	3.1211
0.25	3.0949
0.50	2.8817
0.75	2.1423
0.94	1.0120

$d\sigma/d\theta_1 d\theta_2 = 0.5222\ \mu b/rad^2$

$34^\circ - 42^\circ$

$\bar{\Phi}_m = 1.26^\circ$ $\Delta\phi_m = 4.15^\circ$

Φ_r	$d\sigma/d\Omega_1 d\Omega_2$ $\mu b/sr^2$
0.08	4.2828
0.24	4.2497
0.56	3.7937
0.79	2.6329
0.95	1.2480

$d\sigma/d\theta_1 d\theta_2 = 0.5886\ \mu b/rad^2$

$38^\circ - 38^\circ$

$\bar{\Phi}_m = 1.28^\circ$ $\Delta\phi_m = 4.15^\circ$

Φ_r	$d\sigma/d\Omega_1 d\Omega_2$ $\mu b/sr^2$
0.08	4.4331
0.23	4.3865
0.55	3.9179
0.78	2.7321
0.94	0.9645

$d\sigma/d\theta_1 d\theta_2 = 0.6053\ \mu b/rad^2$

$38^\circ - 42^\circ$

$\bar{\Phi}_m = 0.92^\circ$ $\Delta\phi_m = 2.88^\circ$

Φ_r	$d\sigma/d\Omega_1 d\Omega_2$ $\mu b/sr^2$
0.11	7.4328
0.33	7.2681
0.54	6.5842
0.76	4.8074
0.98	2.0373

$d\sigma/d\theta_1 d\theta_2 = 0.7790\ \mu b/rad^2$

APPENDIX F - BASIC THEORY

The basic DWBA theory, first developed by Sobel and Cromer[11,17], is presented. Places where serious errors have occurred are noted and refinements in the procedures indicated.

The total Hamiltonian of the system in its various useful forms can be given by

$$\begin{aligned} H &= K_1 + K_2 + K_\gamma + V_N + V_{em} \\ &= H_N + K_\gamma + V_{em} \\ &= H_o + V_N + V_{em} \end{aligned} \qquad \text{F-1}$$

K_1, K_2 and K_γ are kinetic energy operators, V_N is the nuclear potential and V_{em} is the electromagnetic interaction due to the coupling of the proton currents to the electromagnetic field. The Hamiltonian for free nucleon-nucleon scattering is given by H_N and the free particle Hamiltonian by H_o. In the following analysis we regard H_N as the unperturbed Hamiltonian and $(V_{em} + K_\gamma)$ as the perturbation. The perturbation V_{em} is given by

$$\langle \underline{k}_1 \underline{k}_2 \underline{K} \,|\, V_{em} \,|\, \underline{q}_1 \underline{q}_2 \underline{0} \rangle = \langle f \,|\, V_{em} \,|\, i \rangle$$

$$= \frac{\sqrt{\alpha}}{2\pi m \sqrt{K}} \Big\{ A(\underline{q}_1)\, \delta^3(\underline{q}_2 - \underline{k}_2)\, \delta^3(\underline{q}_1 - \underline{K} - \underline{k}_1) + A(\underline{q}_2)\, \delta^3(\underline{q}_1 - \underline{k}_1)\, \delta^3(\underline{q}_2 - \underline{K} - \underline{k}_2) \Big\} \qquad \text{F-2}$$

Where

$$A(\underline{q}) = \underline{q}\cdot\hat{e} + \frac{i}{2}\mu_p\hat{e}\cdot(\underline{K} \times \underline{\sigma}) \qquad \text{F-3}$$

m is the proton mass, $\mu_p = 2.79$ is the proton magnetic moment, and $\sqrt{\alpha}$ is the proton charge.

Liou and Cho[33] have obtained the relativistic spin correction by applying the Foldy-Wouthuysen (F-W) transformation to the Dirac electromagnetic interaction Hamiltonian. Keeping terms to order m^{-2}, the form of $A(\underline{q})$ is modified

$$A(\underline{q}) = \underline{q}\cdot\hat{e} + \frac{i}{2}\mu_p\hat{e}\cdot \left\{(\underline{K}-\frac{\bar{q}}{m}K+\frac{K}{2\mu_p m}\bar{q}) \times \underline{\sigma}\right\} \qquad \text{F-4}$$

Let Φ be an eigenstate of H_o and Ψ an eigenstate of H_N for the same energy E. Then

$$(E - H_N)\Psi = 0 = (E - H_o)\Phi \qquad \text{F-5}$$

The state Φ represents a plane wave state. The total scattering states with either incoming or outgoing spherical waves (ψ^+ and ψ^-) are obtained by introduction of a pole indicator η which is assumed to approach zero from the positive direction. Then

$$\psi^{\pm} = \Phi + \frac{1}{E - H_N \pm i\eta} V_N\Phi \qquad \text{F-6}$$

Two Green's function operators are defined by

$$G_N(E) = (E - H_N + i\eta)^{-1}$$

$$G_o(E) = (E - H_o + i\eta)^{-1} \qquad \text{F-7}$$

Also we define

$$U_N(E) = 1 + G_N(E)V_N \qquad \text{F-8}$$

It is then easy to obtain

$$\psi^+ = U_N(E)\,\Phi$$

$$\psi^- = \Phi^\dagger U_N^\dagger \qquad \text{F-9}$$

where $\dagger$ denotes Hermitian conjugation.

The T-matrix is defined such that

$$T_N\Phi = V_N\,\psi^+ = V_N U_N\,\Phi \qquad \text{F-10}$$

A more convenient relation between U_N and T_N can be obtained through the use of operator identities

$$U_N = 1 + G_o(E)T_N \qquad \text{F-11}$$

where $G_o(E)$ is the zeroth order Green's function.

For ease of notation we shall denote plane waves states by $|i\rangle$ for the initial state, $|f\rangle$ for the final state and $|m\rangle$ for the intermediate states. Following Schiff[37)] we write for the DWBA approximation

$$\langle f|T|i\rangle = \langle f|T_N|i\rangle + \langle \Psi_f^-|K_\gamma + V_{em}|\Psi_i^+\rangle \qquad \text{F-12}$$

The energy of the unperturbed initial state is $E(\underline{p}_1,\underline{p}_2)$ and of the final state $E'(\underline{p}_1',\underline{p}_2')$. The distorted waves Ψ_i^+ and Ψ_f^- are those of the two-nucleon system. From F-9 and F-11 we obtain

$$\langle f|T|i\rangle = \langle f|T_N|i\rangle + \langle f|U_N^\dagger(K_\gamma+V_{em})U_N|i\rangle$$
$$= \langle f|T_N + [1+T_N(E')G_o(E')][K_\gamma+V_{em}]\cdot[1+G_o(E)T_N(E)]|i\rangle \qquad \text{F-13}$$

On the assumption that V_N (and therefore T_N) is diagonal in the photon states, then we can write

$$\begin{aligned}\langle f|T|i\rangle = \langle f|\, & T_N + V_{em} + V_{em}G_o(E)T_N(E) \\ & + T_N(E')G_o(E')V_{em} \qquad \text{F-14} \\ & + T_N(E')G_o(E')V_{em}G_o(E)T_N(E)\,|i\rangle\end{aligned}$$

The first term describes normal nucleon-nucleon elastic scattering without photon emission. The second term describes photon emission without nuclear scattering and is not kinematically allowed. The third and fourth terms are the pole or single scattering terms and represent photon emission after and before the nuclear scattering respectively. The final expression is the double or rescattering term and describes photon emission between two nuclear interactions. These last three are the ppγ terms. Standard procedure has been to neglect rescattering. To obtain ppγ cross sections, the other relevant parts of the expressions are evaluated.

$$\langle f|T|i\rangle = \sum_m \langle f|T_N|m\rangle G_o(E_m) \langle m|V_{em}|i\rangle + \sum_n \langle f|V_{em}|n\rangle G_o(E_n) \langle n|T_N|i\rangle \qquad \text{F-15}$$

The δ-functions introduced in the evaluation of $\langle m|V_{em}|i\rangle$ and $\langle f|V_{em}|n\rangle$ result in 4 terms that correspond to photon emission by one or the other of the two protons before or after nuclear interaction. The possibilities are described by the following four expressions.

$$\begin{aligned}
&(a) \quad t_a = \langle \underline{p}_1', \underline{p}_2' | T_N | \underline{p}_1 - \underline{K}, \underline{p}_2 \rangle \\
&(b) \quad t_b = \langle \underline{p}_1', \underline{p}_2' | T_N | \underline{p}_1, \underline{p}_2 - \underline{K} \rangle \\
&(c) \quad t_c = \langle \underline{p}_1' + \underline{K}, \underline{p}_2' | T_N | \underline{p}_1, \underline{p}_2 \rangle \\
&(d) \quad t_d = \langle \underline{p}_1', \underline{p}_2' + \underline{K} | T_N | \underline{p}_1, \underline{p}_2 \rangle
\end{aligned} \qquad \text{F-16}$$

The energy denominators that result from G_o in these four different cases are non-relativistic. For example,

(a) yields

$$G_o(E_a) = \Delta E_a = e(\underline{p}_1-\underline{K}) + e(\underline{p}_2) - (E-K)$$

$$= \frac{1}{2m}(p_1^2-2\underline{p}_1\cdot\underline{K}+K^2+p_2^2) - E + K$$

$$= K - \frac{\underline{p}_1\cdot\underline{K}}{m} + \frac{K^2}{2m} \qquad \text{F-17}$$

The term $K^2/2m$ is very much smaller than K. Then the expression F-17 is very close to the relativistic form

$$\Delta E_a = \frac{1}{m}K_\mu p_{1\mu}$$

For all four terms together we have

$$\begin{aligned} \Delta E_a &= \frac{1}{m}K_\mu p_{1\mu} \\ \Delta E_b &= \frac{1}{m}K_\mu p_{2\mu} \\ \Delta E_c &= -\frac{1}{m}K_\mu p'_{1\mu} \\ \Delta E_d &= -\frac{1}{m}K_\mu p'_{2\mu} \end{aligned} \qquad \text{F-18}$$

Use of these factors in relativistic form reduces the non-covariance of the calculations. Thus we have for the total T-matrix element

$$\langle f|T|i\rangle = \frac{\sqrt{\alpha}}{2\pi m\sqrt{K}}\Big\{t_a\Delta E_a A(\underline{p}_1) + t_b\Delta E_b A(\underline{p}_2) + A(\underline{p}'_1)t_c\Delta E_c + A(\underline{p}'_2)t_d\Delta E_d \qquad \text{F-19}$$

The matrix elements t_x (x = a, b, c, d) can be written in terms of the off-energy-shell center-of-mass scattering matrix $M_x(\underline{k},\underline{k}')$. (Actually the t_x are matrices in spin space.) The quantities $\underline{k} \equiv \underline{k}_i$ and $\underline{k}' \equiv \underline{k}_f$ are the relative momenta between the two nucleons in the initial and final nuclear scattering states. The relation between t_x and M_x is given by

$$t_x = -\frac{M_x(\underline{k}_x,\underline{k}_x')}{2\pi^2 m}\,\delta^3(\underline{p}_1'+\underline{p}_2'+\underline{K}-\underline{p}_1-\underline{p}_2) \qquad \text{F-20}$$

where x = a, b, c, d. Substituting in equation F-19, we get

$$\langle f|T|i\rangle = \frac{\sqrt{\alpha}}{4\pi^3 m^2\sqrt{K}}\,\mathcal{M}\,\delta^3(\underline{p}_1'+\underline{p}_2'+\underline{K}-\underline{p}_1-\underline{p}_2) \qquad \text{F-21}$$

The cross section is obtained from $|\langle f|T|i\rangle|^2$ averaged over the initial proton spins, summed over the final proton spins and summed over the photon polarizations since these are not measured. It is then given by

$$d\sigma = \frac{\alpha}{\pi^2 m^3 P_1 K}\left\langle \tfrac{1}{4}\mathrm{tr}\,\mathcal{M}^\dagger\mathcal{M}\right\rangle \delta^3(\underline{p}_1'+\underline{p}_2'+\underline{K}-\underline{p}_1-\underline{p}_2) \times \delta(E_f-E_i)\,d^3p_1'\,d^3p_2'\,d^3K \qquad \text{F-22}$$

The laboratory incident proton momentum P_1 arises from the incident proton flux and is valid in the non-relativistic limit for both the laboratory and center-of-mass frames of reference.

F - 8

In evaluating (F-19), SC used laboratory momenta. This resulted in the wrong cross section values being obtained. Omission of the double scattering terms results in a non-gauge invariant theory. The reader is referred to Signell[18)] for a detailed discussion of this error.

On the energy-shell the scattering matrix M_x has a well known expansion in terms of the Pauli spin operators and the Wolfenstein parameters[84)]. This can be generalized to include off-energy-shell situations. PGD[16)] define the three perpendicular unit vectors in the center of mass as

$$\hat{n} = \frac{\hat{k}_i \times \hat{k}_f}{|\hat{k}_i \times \hat{k}_f|}, \quad \hat{m} = \frac{\hat{k}_i - \hat{k}_f}{|\hat{k}_i - \hat{k}_f|}, \quad \hat{I} = \frac{\hat{k}_i + \hat{k}_f}{|\hat{k}_i + \hat{k}_f|} \qquad \text{F-23}$$

In some applications, coplanar scattering in particular, a more convenient choice of $\hat{m}$ and $\hat{I}$ can be found. The off-energy-shell M-matrix is not time-reversal invariant and an additional term which changes sign under time reversal must be added to the Wolfenstein expansion. The Wolfenstein parameters A, B, C, E, F, G are scalar functions of the kinematic invariants k_i^2, k_f^2 and $\underline{k}_i \cdot \underline{k}_f$. We have

$$\begin{aligned} M_x = {} & A_x + B_x(\underline{\sigma}_1 \cdot \hat{n})(\underline{\sigma}_2 \cdot \hat{n}) + C_x(\underline{\sigma}_1 \hat{n} + \underline{\sigma}_2 \cdot \hat{n}) \\ & + E_x(\underline{\sigma}_1 \cdot \hat{m})(\underline{\sigma}_2 \cdot \hat{m}) + F_x(\underline{\sigma}_1 \cdot \hat{I})(\underline{\sigma}_2 \cdot \hat{I}) \\ & \pm G_x \ (\underline{\sigma}_1 \cdot \hat{m})(\underline{\sigma}_2 \cdot \hat{I}) + (\underline{\sigma}_1 \cdot \hat{I})(\underline{\sigma}_2 \cdot \hat{m}) \end{aligned} \qquad \text{F-24}$$

The plus sign is used for $x = a$, b and the minus sign for $x = c$, d. The six amplitudes can be expressed in terms of the singlet-triplet elements of M_x. The reader is referred to the papers by SC[17] and PGD[16] for a more detailed discussion of this part of the analysis and the actual evaluation of the coefficients.

In SC[17] it is shown that for coplanar scattering and choice of $\hat{m}$ along the photon direction ($\hat{I}$ is also redefined)

$$\hat{e} = \hat{n}\cos\phi + \hat{I}\sin\phi$$

$$(\underline{K} \times \hat{e}) = K(\hat{I}\cos\phi - \hat{n}\sin\phi) \qquad \text{F-25}$$

We then have in equation (F-3)

$$A(\underline{p}_x) = \underline{p}_x\cdot\hat{n}\cos\phi - \tfrac{i}{2}K\mu_p(\underline{\sigma}_x\cdot\hat{n}\cos\phi - \underline{\sigma}_x\cdot\hat{I}\sin\phi) \qquad \text{F-26}$$

Using equations (F-24), (F-26) and (F-20) in equation (F-19), we can easily group terms and find

$$\sin\phi\sum_{i=1}^{16} X_i O_i + \cos\phi\sum_{i=1}^{16} Y_i O_i = \langle f|T|i\rangle \qquad \text{F-27}$$

The O_i are the 16 independent bilinear operators formed from 1, $\underline{\sigma}_1\cdot\hat{n}$, $\underline{\sigma}_2\cdot\hat{n}$, $\underline{\sigma}_1\cdot\hat{m}$, $\underline{\sigma}_2\cdot\hat{m}$, $\underline{\sigma}_1\cdot\hat{I}$, $\underline{\sigma}_2\cdot\hat{I}$. It can be shown that the O_i satisfy the relation

$$\mathrm{tr}(O_i O_j) = 4\delta_{ij} \qquad \text{F-28}$$

The coefficients are linear combinations of the Wolfenstein amplitudes divided by their appropriate energy denominator. It turns out conveniently that either X_i or Y_i is zero. The sum over photon polarization is performed

$$\langle \tfrac{1}{4}\mathrm{tr}\,\mathcal{M}^{\dagger}\mathcal{M} \rangle = \frac{1}{\pi}\int_0^{2\pi} d\phi \; \tfrac{1}{4}\mathrm{tr}\,\mathcal{M}^{\dagger}\mathcal{M} \qquad \text{F-29}$$

From equations (F-27) and (F-28) we obtain in (F-22)

$$d\sigma = \frac{\alpha}{\pi^2 m^3 P_1 K} \sum_{i=1}^{16} |X_i|^2 + |Y_i|^2 \, \delta^4(P_f - P_i) \; d^3p_1' d^3p_2' d^3K \qquad \text{F-30}$$

The desired form of the differential cross section can be obtained by a transformation to the desired variables and integration over the unobserved parameters. In this thesis we use Liou's predictions for the Hamada-Johnston Potential. His result is calculated in the form

$$\frac{d^3\sigma}{d\Omega_1 d\Omega_2 d\Psi_\gamma} = \frac{\alpha}{\pi^2 m^3 P_1 K} \langle \tfrac{1}{4}\mathrm{tr}\,\mathcal{M}^{\dagger}\mathcal{M} \rangle F \qquad \text{F-31}$$

The phase space factor F has been derived in Liou's Ph.D. thesis[36].

An excellent summary of the theoretical procedures used is contained in a preprint by Liou and Sobel[34].

F - 11

RESULTS

A typical example of the $\frac{d\sigma}{d\Omega_1 d\Omega_2 d\psi_\gamma}$ cross section is given in Fig. F-1(a) for several values of the non-coplanarity Φ_r of the protons. The cross sections have a quadrupole form for the nearly coplanar cases ($\Phi_r \approx 0$). A typical example of the $d\sigma/d\Omega_1 d\Omega_2$ cross section obtained by integrating Equation F-31 over ψ_γ is shown in Fig. F-1(b) by the dotted curve (See equation II-13 in Chapter II). The smooth curve extending past $\Phi_r = 1$ shows the effects of experimental angular resolutions on the observed cross section.

The $d\sigma/d\theta_1 d\theta_2$ cross sections obtained by a further integration of Φ_r are shown in Fig. F-2 as a function of the opening angle between the two protons. The various curves are for different values of proton polar angle asymmetry.

A few comments here are pertinent. Occasionally, due to numerical errors in the computer code, the points near $\psi_\gamma = 0^\circ$, 180° and 360° could not be calculated. This was due to minor inaccuracies in determination of the kinematic parameters of the limiting gamma ray. These points have been extrapolated from the shape of the distribution and may be in error by as much as 5 - 10%. Since the cross

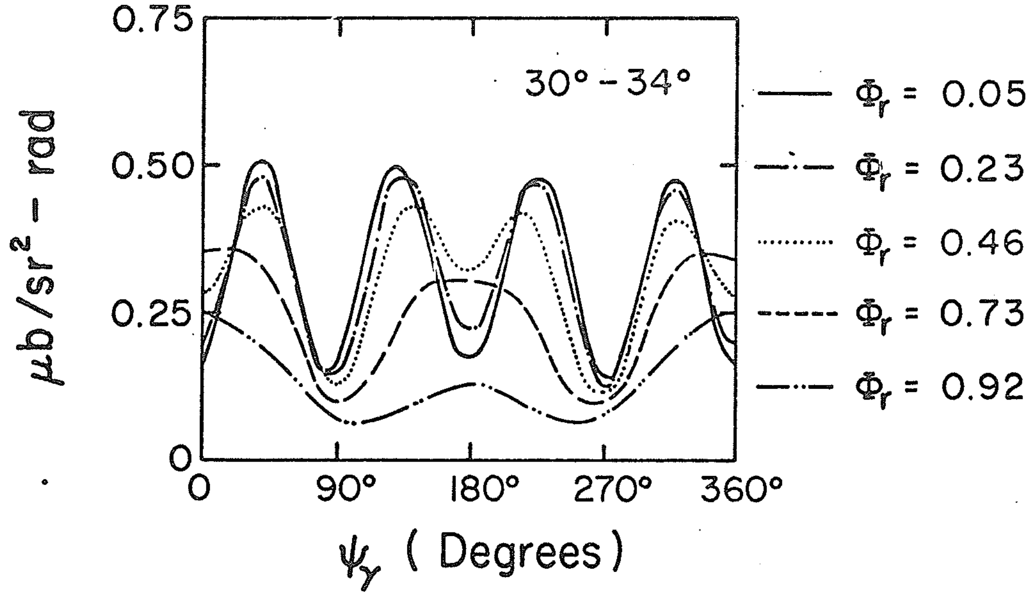

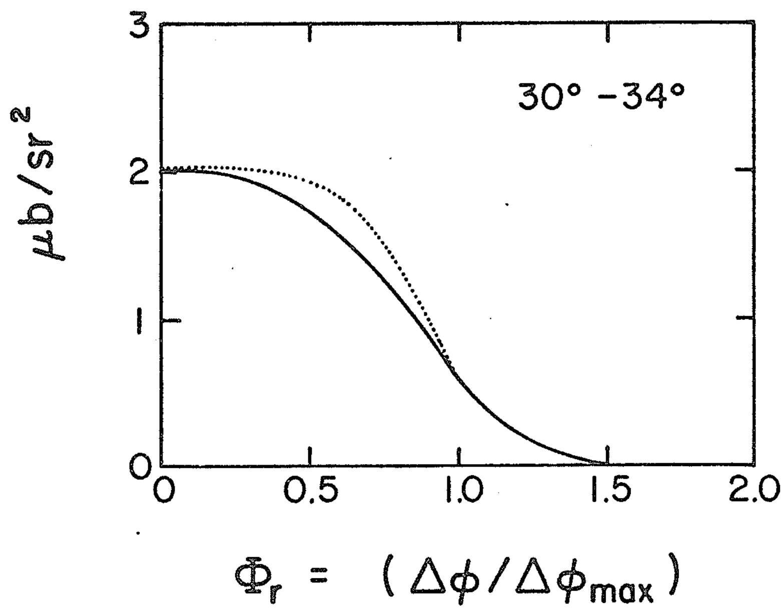

Figure F-1

(a) Diagram showing the dependence of the ppγ $d\sigma/d\Omega_1 d\Omega_2 d\Psi_\gamma$ cross section on Ψ_γ for several values of non-coplanarity Φ_r. The shape of the curves is typical for proton polar angles other than 30°-34°.

(b) The dotted line gives the theoretical dependence of the ppγ $d\sigma/d\Omega_1 d\Omega_2$ cross section on the non-coplanarity Φ_r. The solid line extending past Φ_r = 1.0 shows the effect of experimental angular resolutions on the observed distribution. In this case $\delta\Phi_r$ = 0.246.

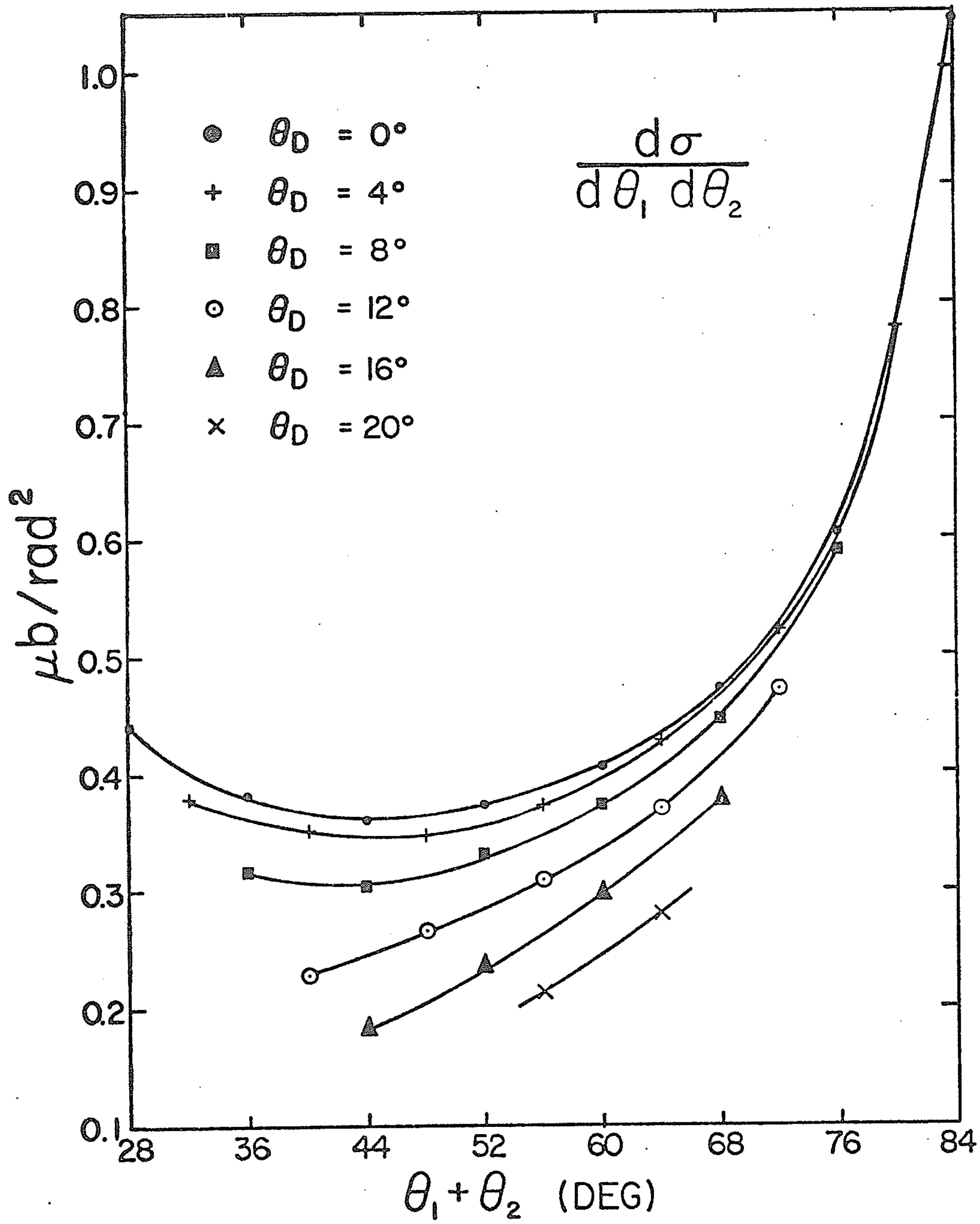

Figure F-2

The integrated ppγ cross section $d\sigma/d\theta_1 d\theta_2$ as a function of the opening angle $(\theta_1+\theta_2)$ between the protons. The various curves are for different asymmetries $|\theta_1-\theta_2|$ in the proton polar angles. The solid lines are to guide the eye only.

sections are small at these points, negligible error ($\lesssim 1\%$) is introduced into the integrated cross sections. The coplanar cross sections quoted in the summary were calculated for $\bar{\Phi} = 0.1^{\circ}$. The ppγ cross section is nearly flat near zero coplanarity so again errors are negligible. The value of $\bar{\Phi} = 0.1^{\circ}$ typically corresponds to a relative non-coplanarity $\Phi_r \approx 0.05$.

References:

See List of References after Chapter IX.

APPENDIX G

SUMMARY OF CROSS SECTION MEASUREMENTS

The numerical values of the $d\sigma/d\Omega_1 d\Omega_2 d\Psi_\gamma$ and the $d\sigma/d\Omega_1 d\Omega_2$ cross sections, presented graphically in Chapter VIII, are given in this Appendix.

Table G-1 gives the $d\sigma/d\Omega_1 d\Omega_2 d\Psi_\gamma$ results as a function of Ψ_γ. Polar angle bins have been combined where possible to improve statistics and the cross sections for symmetric polar angle bins in the half-range $180^\circ \leq \Psi_\gamma \leq 360^\circ$ have been combined statistically (weighted averages) with the corresponding points in the other half-range, $0 \leq \Psi_\gamma \leq 180^\circ$. The cross sections are defined by equation IV-16 with $\Phi_r \leq 0.7$.

Table G-2 gives the $d\sigma/d\Omega_1 d\Omega_2$ cross sections as a function of Φ_r, defined in equation IV-18. Again polar angle bins have been combined where possible. The uncertainty in the net number of $pp\gamma$ events in both tables is purely statistical.

The uncertainty in the cross sections has been obtained by compounding statistical uncertainties in $N_{pp\gamma}$, ϵ_0 and ϵ_1 in quadrature. There is an additional normalization uncertainty of $\pm$ 3.9% common to all points, which is not included in either Table G-1 or Table G-2.

Table G-1

Summary of $\frac{d\sigma}{d\Omega_1 d\Omega_2 d\psi_\gamma}$ Cross Sections

Table G-1

$\theta_1 = 18^o$ $\theta_2 = 18^o$

ψ_γ	CROSS SECTION ± UNCERTAINTY MICROBARNS PER SR**2-RAD				NET EVENTS
10.00	0.730	±	0.245	(34.%)	25.7
30.00	0.248	±	0.136	(55.%)	14.7
50.00	0.017	±	0.016	(94.%)	5.0
70.00	0.017	±	0.017	(100.%)	-0.3
90.00	0.073	±	0.124	(170.%)	1.8
110.00	0.202	±	0.105	(52.%)	9.9
130.00	0.354	±	0.118	(33.%)	20.9
150.00	0.366	±	0.081	(22.%)	40.0
170.00	0.256	±	0.069	(27.%)	34.0

TOTAL NET EVENTS= 151.5 ± 11.3%

$\theta_1 = 22^o$ $\theta_2 = 22^o$

ψ_γ	CROSS SECTION ± UNCERTAINTY MICROBARNS PER SR**2-RAD				NET EVENTS
10.00	0.517	±	0.106	(21.%)	45.4
30.00	0.359	±	0.116	(32.%)	26.0
50.00	0.129	±	0.078	(61.%)	5.1
70.00	0.175	±	0.155	(89.%)	3.6
90.00	0.072	±	0.058	(81.%)	4.8
110.00	0.141	±	0.075	(53.%)	11.2
130.00	0.300	±	0.063	(21.%)	40.4
150.00	0.163	±	0.051	(31.%)	30.3
170.00	0.243	±	0.051	(21.%)	40.2

TOTAL NET EVENTS= 207.1 ± 9.1%

$\theta_1 = 26^o$ $\theta_2 = 26^o$

ψ_γ	CROSS SECTION ± UNCERTAINTY MICROBARNS PER SR**2-RAD				NET EVENTS
10.00	0.167	±	0.054	(32.%)	24.7
30.00	0.258	±	0.072	(28.%)	27.6
50.00	0.178	±	0.069	(39.%)	14.4
70.00	0.051	±	0.033	(64.%)	5.9
90.00	0.071	±	0.040	(57.%)	8.6
110.00	0.091	±	0.048	(53.%)	12.3
130.00	0.227	±	0.048	(21.%)	34.8
150.00	0.260	±	0.046	(18.%)	36.7
170.00	0.274	±	0.049	(18.%)	38.2

TOTAL NET EVENTS= 203.2 ± 7.0%

Table G-1
(continued)

$\theta_1 = 30^\circ$ $\theta_2 = 30^\circ$

ψ_γ	CROSS SECTION ± UNCERTAINTY MICROBARNS PER SR**2-RAD				NET EVENTS
10.00	0.283	±	0.067	(24.%)	21.6
30.00	0.374	±	0.075	(20.%)	30.0
50.00	0.321	±	0.074	(23.%)	22.4
70.00	0.275	±	0.064	(23.%)	20.3
90.00	0.117	±	0.046	(39.%)	8.9
110.00	0.125	±	0.042	(34.%)	10.3
130.00	0.364	±	0.071	(19.%)	29.5
150.00	0.390	±	0.072	(19.%)	30.3
170.00	0.259	±	0.062	(24.%)	20.5

TOTAL NET EVENTS= 193.8 ± 5.5%

$\theta_1 = 34^\circ$ $\theta_2 = 34^\circ$

ψ_γ	CROSS SECTION ± UNCERTAINTY MICROBARNS PER SR**2-RAD				NET EVENTS
10.00	0.359	±	0.128	(36.%)	10.8
30.00	0.419	±	0.127	(30.%)	11.0
50.00	0.386	±	0.129	(34.%)	11.1
70.00	0.297	±	0.111	(37.%)	8.7
90.00	0.085	±	0.063	(74.%)	2.4
110.00	0.564	±	0.149	(26.%)	15.7
130.00	0.447	±	0.131	(29.%)	12.0
150.00	0.452	±	0.135	(30.%)	12.4
170.00	0.608	±	0.153	(25.%)	16.0

TOTAL NET EVENTS= 100.1 ± 7.5%

Table G-1
(continued)

$\theta_1 = 18^o$ $\theta_2 = 22^o$

ψ_γ	CROSS SECTION ± UNCERTAINTY MICROBARNS PER SR**2-RAD				NET EVENTS
10.00	0.365	±	0.208	(57.%)	14.7
30.00	0.430	±	0.123	(29.%)	27.6
50.00	0.433	±	0.133	(31.%)	25.7
70.00	0.173	±	0.076	(44.%)	22.0
90.00	0.141	±	0.089	(63.%)	8.9
110.00	0.143	±	0.052	(36.%)	16.8
130.00	0.261	±	0.057	(22.%)	35.3
150.00	0.289	±	0.065	(23.%)	40.2
170.00	0.312	±	0.069	(22.%)	39.6
190.00	0.203	±	0.095	(47.%)	18.9
210.00	0.279	±	0.101	(36.%)	16.2
230.00	-0.011	±	-0.011	(100.%)	0.0
250.00	0.063	±	0.075	(119.%)	1.0
270.00	-0.002	±	-0.002	(100.%)	-0.3
290.00	0.015	±	0.015	(100.%)	1.0
310.00	0.0	±	0.0	(0.%)	0.0
330.00	-0.040	±	-0.040	(100.%)	-1.3
350.00	0.005	±	0.005	(100.%)	-0.3

TOTAL NET EVENTS= 266.0 ± 11.9%

$\theta_1 = 18^o$ $\theta_2 = 26^o$

ψ_γ	CROSS SECTION ± UNCERTAINTY MICROBARNS PER SR**2-RAD				NET EVENTS
10.00	-0.001	±	-0.001	(100.%)	-0.2
30.00	0.253	±	0.130	(51.%)	8.5
50.00	0.245	±	0.082	(34.%)	19.9
70.00	0.118	±	0.048	(41.%)	12.6
90.00	0.083	±	0.056	(67.%)	5.9
110.00	0.186	±	0.050	(27.%)	22.2
130.00	0.219	±	0.051	(23.%)	23.7
150.00	0.228	±	0.075	(33.%)	21.5
170.00	0.202	±	0.173	(86.%)	6.7
190.00	0.204	±	0.176	(86.%)	6.1
210.00	-0.008	±	-0.008	(100.%)	-1.0
230.00	0.0	±	0.0	(0.%)	0.0
250.00	0.0	±	0.0	(0.%)	0.0
270.00	0.0	±	0.0	(0.%)	0.0
290.00	0.0	±	0.0	(0.%)	0.0
310.00	0.0	±	0.0	(0.%)	0.0
330.00	0.0	±	0.0	(0.%)	0.0
350.00	0.0	±	0.0	(0.%)	0.0

TOTAL NET EVENTS= 125.9 ± 18.3%

Table G-1
(continued)

$\theta_1 = 18^o$ $\theta_2 = 30^o$

ψ_γ	CROSS SECTION MICROBARNS PER SR**2-RAD	± UNCERTAINTY		NET EVENTS
10.00	0.0	± 0.0	(0.%)	0.0
30.00	0.046	± 0.046	(100.%)	0.7
50.00	0.090	± 0.048	(53.%)	6.2
70.00	0.132	± 0.093	(70.%)	11.2
90.00	0.129	± 0.076	(59.%)	6.4
110.00	0.087	± 0.081	(93.%)	4.7
130.00	0.308	± 0.099	(32.%)	13.9
150.00	0.184	± 0.109	(59.%)	9.0
170.00	0.075	± 0.055	(73.%)	10.4
190.00	0.0	± 0.0	(0.%)	0.0
210.00	0.0	± 0.0	(0.%)	0.0
230.00	0.0	± 0.0	(0.%)	0.0
250.00	0.0	± 0.0	(0.%)	0.0
270.00	0.0	± 0.0	(0.%)	0.0
290.00	0.0	± 0.0	(0.%)	0.0
310.00	0.0	± 0.0	(0.%)	0.0
330.00	0.0	± 0.0	(0.%)	0.0
350.00	0.0	± 0.0	(0.%)	0.0
		TOTAL NET EVENTS=		62.6 ± 21.3%

$\theta_1 = 22^o$ $\theta_2 = 26^o$

ψ_γ	CROSS SECTION MICROBARNS PER SR**2-RAD	± UNCERTAINTY		NET EVENTS
10.00	0.236	± 0.081	(34.%)	22.6
30.00	0.251	± 0.059	(24.%)	34.9
50.00	0.177	± 0.049	(28.%)	23.8
70.00	0.198	± 0.047	(24.%)	28.0
90.00	0.112	± 0.036	(33.%)	14.9
110.00	0.117	± 0.040	(34.%)	18.0
130.00	0.190	± 0.045	(24.%)	28.9
150.00	0.293	± 0.051	(17.%)	49.5
170.00	0.338	± 0.054	(16.%)	50.3
190.00	0.194	± 0.044	(23.%)	29.4
210.00	0.287	± 0.062	(22.%)	36.3
230.00	0.157	± 0.067	(43.%)	14.1
250.00	0.342	± 0.186	(54.%)	6.7
270.00	0.014	± 0.014	(100.%)	1.8
290.00	0.173	± 0.141	(82.%)	2.8
310.00	0.029	± 0.020	(71.%)	2.0
330.00	0.075	± 0.103	(138.%)	0.6
350.00	0.164	± 0.092	(56.%)	14.8
		TOTAL NET EVENTS=		379.4 ± 9.9%

Table G-1
(continued)

$\theta_1 = 22^{\circ}$ $\theta_2 = 30^{\circ}$

ψ_γ	CROSS SECTION MICROBARNS	±	UNCERTAINTY PER SR**2-RAD		NET EVENTS
10.00	0.026	±	0.024	(91.%)	4.9
30.00	0.278	±	0.079	(28.%)	21.6
50.00	0.202	±	0.050	(25.%)	21.3
70.00	0.133	±	0.044	(33.%)	13.6
90.00	0.080	±	0.030	(38.%)	17.3
110.00	0.168	±	0.045	(27.%)	21.0
130.00	0.185	±	0.048	(26.%)	21.5
150.00	0.267	±	0.058	(22.%)	29.7
170.00	0.311	±	0.066	(21.%)	29.4
190.00	0.242	±	0.074	(31.%)	22.2
210.00	0.404	±	0.225	(56.%)	10.4
230.00	0.102	±	0.093	(91.%)	1.7
250.00	0.0	±	0.0	(0.%)	0.0
270.00	0.0	±	0.0	(0.%)	0.0
290.00	0.0	±	0.0	(0.%)	0.0
310.00	-0.001	±	-0.001	(100.%)	0.0
330.00	0.0	±	0.0	(0.%)	0.0
350.00	-0.036	±	-0.036	(100.%)	-1.0
			TOTAL NET EVENTS=		213.6 ± 12.7%

$\theta_1 = 22^{\circ}$ $\theta_2 = 34^{\circ}$

ψ_γ	CROSS SECTION MICROBARNS	±	UNCERTAINTY PER SR**2 -RAD		NET EVENTS
10.00	0.042	±	0.034	(81.%)	1.8
30.00	0.114	±	0.079	(69.%)	3.3
50.00	0.087	±	0.077	(88.%)	4.2
70.00	0.164	±	0.076	(47.%)	9.3
90.00	0.135	±	0.080	(59.%)	5.5
110.00	0.120	±	0.060	(50.%)	4.5
130.00	0.110	±	0.054	(49.%)	6.7
150.00	0.250	±	0.068	(27.%)	14.4
170.00	0.056	±	0.128	(229.%)	5.0
190.00	0.083	±	0.053	(64.%)	3.3
210.00	0.023	±	0.023	(100.%)	1.0
230.00	0.0	±	0.0	(0.%)	0.0
250.00	0.0	±	0.0	(0.%)	0.0
270.00	0.C	±	0.0	(0.%)	0.0
290.00	0.0	±	0.0	(0.%)	0.0
310.00	0.0	±	0.0	(0.%)	0.0
330.00	0.0	±	0.0	(0.%)	0.0
350.00	0.0	±	0.0	(0.%)	0.0
			TOTAL NET EVENTS=		58.8 ± 20.1%

Table G-1
(continued)

$\theta_1 = 26^o$ $\theta_2 = 30^o$

ψ_γ	CROSS SECTION MICROBARNS	±	UNCERTAINTY PER SR**2-RAD		NET EVENTS
10.00	0.287	±	0.061	(21.%)	27.9
30.00	0.410	±	0.073	(18.%)	42.7
50.00	0.209	±	0.049	(24.%)	22.4
70.00	0.207	±	0.049	(23.%)	21.4
90.00	0.114	±	0.036	(32.%)	12.9
110.00	0.146	±	0.041	(28.%)	17.2
130.00	0.186	±	0.044	(23.%)	24.0
150.00	0.289	±	0.056	(19.%)	30.7
170.00	0.176	±	0.046	(26.%)	18.4
190.00	0.250	±	0.051	(20.%)	26.2
210.00	0.278	±	0.056	(20.%)	31.6
230.00	0.182	±	0.047	(26.%)	22.3
250.00	0.156	±	0.054	(35.%)	12.4
270.00	0.191	±	0.070	(36.%)	10.1
290.00	0.120	±	0.102	(85.%)	2.3
310.00	0.168	±	0.085	(51.%)	7.0
330.00	0.202	±	0.078	(39.%)	11.6
350.00	0.194	±	0.071	(36.%)	15.0

TOTAL NET EVENTS= 356.1 ± 6.9%

$\theta_1 = 26^o$ $\theta_2 = 34^o$

ψ_γ	CROSS SECTION MICROBARNS	±	UNCERTAINTY PER SR**2-RAD		NET EVENTS
10.00	0.122	±	0.064	(52.%)	7.1
30.00	0.320	±	0.081	(25.%)	19.9
50.00	0.151	±	0.062	(41.%)	10.7
70.00	0.195	±	0.064	(33.%)	11.4
90.00	0.201	±	0.060	(30.%)	12.2
110.00	0.314	±	0.075	(24.%)	18.9
130.00	0.174	±	0.066	(38.%)	8.1
150.00	0.217	±	0.062	(29.%)	15.4
170.00	0.137	±	0.054	(39.%)	13.8
190.00	0.243	±	0.071	(29.%)	16.4
210.00	0.331	±	0.085	(26.%)	21.7
230.00	0.269	±	0.078	(29.%)	13.7
250.00	0.243	±	0.109	(45.%)	7.4
270.00	0.110	±	0.064	(58.%)	7.0
290.00	0.160	±	0.137	(85.%)	3.4
310.00	0.071	±	0.071	(100.%)	1.4
330.00	0.085	±	0.057	(67.%)	4.0
350.00	0.266	±	0.197	(74.%)	4.2

TOTAL NET EVENTS= 196.8 ± 10.3%

Table G-1
(continued)

$\theta_1 = 30^o$ $\theta_2 = 34^o$

Ψ_γ	CROSS SECTION MICROBARNS	±	UNCERTAINTY PER SR**2-RAD		NET EVENTS
10.00	0.261	±	0.090	(34.%)	12.2
30.00	0.277	±	0.082	(29.%)	12.9
50.00	0.307	±	0.090	(29.%)	14.6
70.00	0.145	±	0.062	(43.%)	6.9
90.00	0.198	±	0.067	(34.%)	9.5
110.00	0.217	±	0.073	(33.%)	10.1
130.00	0.262	±	0.077	(29.%)	14.7
150.00	0.334	±	0.087	(26.%)	15.7
170.00	0.372	±	0.092	(25.%)	17.4
190.00	0.335	±	0.086	(26.%)	15.7
210.00	0.438	±	0.098	(22.%)	20.8
230.00	0.377	±	0.094	(25.%)	17.8
250.00	0.293	±	0.090	(31.%)	13.9
270.00	0.125	±	0.063	(50.%)	4.8
290.00	0.322	±	0.092	(29.%)	14.9
310.00	0.316	±	0.094	(30.%)	13.1
330.00	0.386	±	0.096	(25.%)	19.1
350.00	0.239	±	0.080	(34.%)	11.0
			TOTAL NET EVENTS=		244.9 ± 6.9%

$\theta_1 = 38^o$ $\theta_2 = 22^o$

Ψ_γ	CROSS SECTION MICROBARNS	±	UNCERTAINTY PER SR**2-RAD		NET EVENTS
10.00	0.0	±	0.0	(0.%)	0.0
30.00	0.249	±	0.286	(115.%)	2.0
50.00	0.215	±	0.188	(88.%)	2.3
70.00	0.105	±	0.109	(104.%)	2.0
90.00	0.050	±	0.063	(126.%)	1.3
110.00	0.208	±	0.128	(62.%)	3.0
130.00	0.262	±	0.163	(62.%)	3.8
150.00	0.174	±	0.136	(78.%)	2.5
170.00	0.239	±	0.175	(73.%)	3.0
190.00	0.175	±	0.205	(117.%)	1.0
210.00	0.0	±	0.0	(0.%)	0.0
230.00	0.0	±	0.0	(0.%)	0.0
250.00	0.0	±	0.0	(0.%)	0.0
270.00	0.0	±	0.0	(0.%)	0.0
290.00	0.0	±	0.0	(0.%)	0.0
310.00	0.0	±	0.0	(0.%)	0.0
330.00	0.0	±	0.0	(0.%)	0.0
350.00	0.0	±	0.0	(0.%)	0.0
			TOTAL NET EVENTS=		20.9 ± 30.8%

Table G-1
(continued)

$\theta_1 = 38^o$ $\theta_2 = 26^o$

ψ_γ	CROSS SECTION MICROBARNS	±	UNCERTAINTY PER SR**2-RAD		NET EVENTS
10.00	0.643	±	0.320	(50.%)	10.7
30.00	0.356	±	0.124	(35.%)	8.7
50.00	0.494	±	0.145	(29.%)	11.8
70.00	0.285	±	0.111	(39.%)	6.8
90.00	0.331	±	0.131	(40.%)	8.0
110.00	0.239	±	0.104	(44.%)	5.7
130.00	0.212	±	0.095	(45.%)	5.0
150.00	0.184	±	0.097	(53.%)	4.0
170.00	0.021	±	0.043	(208.%)	0.5
190.00	0.225	±	0.103	(46.%)	5.0
210.00	0.577	±	0.250	(43.%)	8.5
230.00	0.165	±	0.166	(100.%)	2.0
250.00	0.359	±	0.252	(70.%)	5.0
270.00	0.084	±	0.101	(121.%)	0.8
290.00	0.407	±	0.316	(78.%)	5.0
310.00	0.0	±	0.0	(0.%)	0.0
330.00	-0.007	±	0.007	(107.%)	-0.2
350.00	0.118	±	0.073	(62.%)	2.8
			TOTAL NET EVENTS=		90.2 ± 14.7%

$\theta_1 = 38^o$ $\theta_2 = 30^o$

ψ_γ	CROSS SECTION MICROBARNS	±	UNCERTAINTY PER SR**2-RAD		NET EVENTS
10.00	0.835	±	0.208	(25.%)	16.6
30.00	0.278	±	0.123	(44.%)	5.6
50.00	0.200	±	0.100	(50.%)	4.0
70.00	0.456	±	0.159	(35.%)	9.2
90.00	0.300	±	0.123	(41.%)	6.0
110.00	0.299	±	0.122	(41.%)	6.0
130.00	0.249	±	0.112	(45.%)	5.0
150.00	0.328	±	0.133	(41.%)	6.6
170.00	0.384	±	0.144	(37.%)	7.6
190.00	0.178	±	0.101	(57.%)	3.6
210.00	0.178	±	0.101	(57.%)	3.6
230.00	0.560	±	0.175	(31.%)	11.2
250.00	0.263	±	0.127	(48.%)	5.2
270.00	0.369	±	0.134	(36.%)	7.4
290.00	0.423	±	0.152	(36.%)	8.0
310.00	0.417	±	0.170	(41.%)	7.0
330.00	0.263	±	0.152	(58.%)	5.2
350.00	0.356	±	0.143	(40.%)	7.2
			TOTAL NET EVENTS=		125.0 ± 9.4%

Table G-1
(continued)

$\theta_1 = 38^o$ $\theta_2 = 34^o$

ψ_γ	CROSS SECTION ± UNCERTAINTY MICROBARNS PER SR**2-RAD				NET EVENTS
10.00	0.878	±	0.290	(33.%)	9.7
30.00	0.679	±	0.265	(39.%)	7.3
50.00	0.535	±	0.218	(41.%)	6.0
70.00	0.094	±	0.094	(100.%)	1.0
90.00	0.361	±	0.180	(50.%)	4.0
110.00	0.519	±	0.226	(44.%)	5.7
130.00	0.407	±	0.208	(51.%)	4.5
150.00	0.369	±	0.185	(50.%)	4.0
170.00	0.425	±	0.205	(48.%)	4.7
190.00	0.361	±	0.181	(50.%)	4.0
210.00	0.876	±	0.288	(33.%)	9.7
230.00	0.094	±	0.094	(100.%)	1.0
250.00	0.609	±	0.245	(40.%)	6.7
270.00	0.546	±	0.223	(41.%)	6.0
290.00	0.279	±	0.161	(58.%)	3.0
310.00	0.456	±	0.204	(45.%)	5.0
330.00	0.812	±	0.271	(33.%)	9.0
350.00	1.489	±	0.378	(25.%)	16.3
			TOTAL NET EVENTS=		107.5 ± 9.9%

Table G-2

Summary of $\frac{d\sigma}{d\Omega_1 d\Omega_2}$ Cross Sections

Table G-2

$\theta_1 = 18^\circ \qquad \theta_2 = 18^\circ$

Φ_r	CROSS SECTION MICROBARNS PER SR**2	±	UNCERTAINTY		NET EVENTS
0.10	1.634	±	0.475	(29.%)	29.6
0.30	1.830	±	0.458	(25.%)	40.6
0.50	2.552	±	0.493	(19.%)	55.4
0.70	1.925	±	0.406	(21.%)	42.8
0.90	0.776	±	0.411	(53.%)	13.7
1.10	0.160	±	0.256	(160.%)	3.2
1.30	-0.088	±	0.294	(335.%)	-1.1
1.50	-0.295	±	0.218	(74.%)	-3.1
1.70	0.0	±	0.0	(0.%)	0.0
1.90	0.0	±	0.0	(0.%)	0.0

TOTAL NET EVENTS= 181.1 ± 13.0%

$\theta_1 = 18^\circ \qquad \theta_2 = 22^\circ$

Φ_r	CROSS SECTION MICROBARNS PER SR**2	±	UNCERTAINTY		NET EVENTS
0.10	1.429	±	0.256	(18.%)	83.5
0.30	1.421	±	0.248	(17.%)	78.9
0.50	1.324	±	0.239	(18.%)	71.9
0.70	1.194	±	0.235	(20.%)	62.4
0.90	0.670	±	0.278	(42.%)	24.9
1.10	0.427	±	0.203	(48.%)	15.2
1.30	0.518	±	0.253	(49.%)	12.6
1.50	0.156	±	0.098	(63.%)	4.9
1.70	0.0	±	0.0	(0.%)	0.0
1.90	0.0	±	0.0	(0.%)	0.0

TOTAL NET EVENTS= 354.3 ± 9.2%

$\theta_1 = 22^\circ \qquad \theta_2 = 22^\circ$

Φ_r	CROSS SECTION MICROBARNS PER SR**2	±	UNCERTAINTY		NET EVENTS
0.10	1.946	±	0.299	(15.%)	74.9
0.30	0.935	±	0.244	(26.%)	39.0
0.50	1.472	±	0.277	(19.%)	62.7
0.70	1.374	±	0.239	(17.%)	58.9
0.90	0.607	±	0.189	(31.%)	25.3
1.10	0.193	±	0.147	(76.%)	8.3
1.30	0.099	±	0.123	(124.%)	4.2
1.50	-0.078	±	0.047	(61.%)	-3.2
1.70	0.0	±	0.0	(0.%)	0.0
1.90	0.0	±	0.0	(0.%)	0.0

TOTAL NET EVENTS= 270.2 ± 9.1%

Table G-2
(continued)

$\theta_1 = 18^\circ \qquad \theta_2 = 26^\circ$

Φ_r	CROSS SECTION MICROBARNS	± UNCERTAINTY PER SR**2		NET EVENTS
0.10	1.282	± 0.240	(19.%)	52.7
0.30	0.741	± 0.222	(30.%)	30.0
0.50	0.818	± 0.259	(32.%)	28.1
0.70	0.953	± 0.258	(27.%)	28.9
0.90	0.934	± 0.283	(30.%)	24.5
1.10	0.203	± 0.236	(116.%)	0.5
1.30	0.043	± 0.043	(100.%)	0.6
1.50	-0.013	± -0.013	(100.%)	-0.5
1.70	0.0	± 0.0	(0.%)	0.0
1.90	0.0	± 0.0	(0.%)	0.0

TOTAL NET EVENTS= 164.7 ± 12.4%

$\theta_1 = 18^\circ \qquad \theta_2 = 30^\circ$

Φ_r	CROSS SECTION MICROBARNS	± UNCERTAINTY PER SR**2		NET EVENTS
0.10	1.301	± 0.318	(24.%)	22.2
0.30	0.931	± 0.307	(33.%)	16.4
0.50	1.299	± 0.431	(33.%)	17.9
0.70	0.577	± 0.281	(49.%)	8.4
0.90	0.148	± 0.303	(204.%)	1.8
1.10	0.154	± 0.217	(142.%)	0.9
1.30	0.261	± 0.336	(129.%)	1.7
1.50	-0.011	± -0.011	(100.%)	-0.1
1.70	0.0	± 0.0	(0.%)	0.0
1.90	0.0	± 0.0	(0.%)	0.0

TOTAL NET EVENTS= 69.2 ± 18.1%

$\theta_1 = 22^\circ \qquad \theta_2 = 26^\circ$

Φ_r	CROSS SECTION MICROBARNS	± UNCERTAINTY PER SR**2		NET EVENTS
0.10	1.475	± 0.176	(12.%)	118.8
0.30	1.387	± 0.164	(12.%)	119.5
0.50	1.304	± 0.162	(12.%)	105.1
0.70	0.631	± 0.153	(24.%)	47.7
0.90	0.608	± 0.129	(21.%)	46.1
1.10	0.260	± 0.119	(46.%)	14.7
1.30	0.235	± 0.138	(59.%)	0.8
1.50	0.103	± 0.096	(93.%)	3.7
1.70	0.C	± 0.0	(0.%)	0.0
1.90	0.0	± 0.0	(0.%)	0.0

TOTAL NET EVENTS= 456.5 ± 6.8%

Table G-2
(continued)

$\theta_1 = 26^o$ $\theta_2 = 26^o$

Φ_r	CROSS SECTION MICROBARNS	±	UNCERTAINTY PER SR**2		NET EVENTS
0.10	1.267	±	0.198	(16.%)	63.4
0.30	1.282	±	0.210	(16.%)	65.0
0.50	1.056	±	0.191	(18.%)	52.6
0.70	1.152	±	0.194	(17.%)	55.5
0.90	0.573	±	0.171	(30.%)	26.4
1.10	0.112	±	0.132	(117.%)	4.7
1.30	-0.156	±	0.086	(55.%)	-6.7
1.50	0.013	±	0.048	(356.%)	0.6
1.70	0.0	±	0.0	(0.%)	0.0
1.90	0.0	±	0.0	(0.%)	0.0

TOTAL NET EVENTS= 261.4 ± 8.7%

$\theta_1 = 22^o$ $\theta_2 = 30^o$

Φ_r	CROSS SECTION MICROBARNS	±	UNCERTAINTY PER SR**2		NET EVENTS
0.10	1.279	±	0.206	(16.%)	64.1
0.30	1.450	±	0.203	(14.%)	77.3
0.50	1.162	±	0.203	(18.%)	52.5
0.70	0.947	±	0.165	(17.%)	43.5
0.90	0.522	±	0.153	(29.%)	21.4
1.10	0.213	±	0.126	(59.%)	9.3
1.30	0.254	±	0.144	(57.%)	6.9
1.50	0.100	±	0.179	(180.%)	1.2
1.70	-0.035	±	-0.035	(100.%)	-1.0
1.90	0.C	±	0.0	(0.%)	0.0

TOTAL NET EVENTS= 275.3 ± 8.4%

$\theta_1 = 22^o$ $\theta_2 = 34^o$

Φ_r	CROSS SECTION MICROBARNS	±	UNCERTAINTY PER SR**2		NET EVENTS
0.10	1.165	±	0.279	(24.%)	23.5
0.30	0.801	±	0.224	(28.%)	19.5
0.50	0.897	±	0.314	(35.%)	16.3
0.70	0.312	±	0.248.	(79.%)	5.1
0.90	0.348	±	0.269	(77.%)	3.8
1.10	0.622	±	0.273	(44.%)	6.8
1.30	0.052	±	0.052	(100.%)	-0.7
1.50	-0.170	±	-0.170	(100.%)	-2.0
1.70	0.0	±	0.0	(0.%)	0.0
1.90	0.0	±	0.0	(0.%)	0.0

TOTAL NET EVENTS= 72.3 ± 17.0%

Table G-2
(continued)

$\theta_1 = 26^\circ$ $\theta_2 = 30^\circ$

Φ_r	CROSS SECTION MICROBARNS	±	UNCERTAINTY PER SR**2		NET EVENTS
0.10	1.514	±	0.158	(10.%)	117.6
0.30	1.502	±	0.159	(11.%)	115.2
0.50	1.270	±	0.149	(12.%)	91.0
0.70	0.917	±	0.130	(14.%)	65.1
0.90	0.496	±	0.114	(23.%)	33.7
1.10	0.235	±	0.096	(41.%)	14.7
1.30	-0.009	±	-0.009	(100.%)	-1.2
1.50	0.079	±	0.038	(48.%)	5.2
1.70	0.0	±	0.0	(0.%)	0.0
1.90	0.0	±	0.0	(0.%)	0.0

TOTAL NET EVENTS= 441.3 ± 5.6%

$\theta_1 = 30^\circ$ $\theta_2 = 30^\circ$

Φ_r	CROSS SECTION MICROBARNS	±	UNCERTAINTY PER SR**2		NET EVENTS
0.10	1.998	±	0.263	(13.%)	62.1
0.30	1.895	±	0.271	(14.%)	60.1
0.50	1.946	±	0.265	(14.%)	57.9
0.70	1.129	±	0.228	(20.%)	31.9
0.90	0.569	±	0.174	(31.%)	15.6
1.10	0.195	±	0.128	(65.%)	5.2
1.30	-0.015	±	0.058	(395.%)	-0.4
1.50	-0.008	±	0.008	(103.%)	-0.2
1.70	0.0	±	0.0	(0.%)	0.0
1.90	0.0	±	0.0	(0.%)	0.0

TOTAL NET EVENTS= 232.2 ± 7.3%

$\theta_1 = 26^\circ$ $\theta_2 = 34^\circ$

Φ_r	CROSS SECTION MICROBARNS	±	UNCERTAINTY PER SR**2		NET EVENTS
0.10	1.676	±	0.240	(14.%)	66.7
0.30	1.649	±	0.232	(14.%)	61.6
0.50	1.172	±	0.185	(16.%)	52.6
0.70	1.110	±	0.189	(17.%)	40.7
0.90	0.307	±	0.129	(42.%)	14.8
1.10	0.062	±	0.107	(171.%)	2.4
1.30	0.001	±	0.001	(100.%)	0.5
1.50	0.037	±	0.103	(280.%)	0.9
1.70	0.0	±	0.0	(0.%)	0.0
1.90	0.0	±	0.0	(0.%)	0.0

TOTAL NET EVENTS= 240.1 ± 7.8%

Table G-2
(continued)

$\theta_1 = 30^\circ$ $\theta_2 = 34^\circ$

Φ_r	CROSS SECTION MICROBARNS PER SR**2	±	UNCERTAINTY		NET EVENTS
0.10	1.971	±	0.247	(13.%)	75.3
0.30	1.898	±	0.244	(13.%)	72.0
0.50	1.760	±	0.229	(13.%)	65.9
0.70	1.180	±	0.190	(16.%)	44.3
0.90	0.676	±	0.160	(24.%)	26.0
1.10	0.374	±	0.130	(35.%)	13.0
1.30	0.016	±	0.016	(100.%)	0.4
1.50	0.105	±	0.105	(100.%)	0.0
1.70	0.0	±	0.0	(0.%)	0.0
1.90	0.0	±	0.0	(0.%)	0.0

TOTAL NET EVENTS= 296.9 ± 6.4%

$\theta_1 = 34^\circ$ $\theta_2 = 34^\circ$

Φ_r	CROSS SECTION MICROBARNS PER SR**2	±	UNCERTAINTY		NET EVENTS
0.10	2.614	±	0.507	(19.%)	28.5
0.30	3.217	±	0.555	(17.%)	34.4
0.50	2.820	±	0.537	(19.%)	29.5
0.70	2.438	±	0.491	(20.%)	25.4
0.90	0.935	±	0.312	(33.%)	9.0
1.10	0.207	±	0.146	(71.%)	2.0
1.30	0.339	±	0.227	(67.%)	3.1
1.50	0.0	±	0.0	(0.%)	0.0
1.70	0.0	±	0.0	(0.%)	0.0
1.90	0.0	±	0.0	(0.%)	0.0

TOTAL NET EVENTS= 131.9 ± 8.9%

$\theta_1 = 38^\circ$ $\theta_2 = 22^\circ$

Φ_r	CROSS SECTION MICROBARNS PER SR**2	±	UNCERTAINTY		NET EVENTS
0.10	1.119	±	0.502	(45.%)	6.3
0.30	1.020	±	0.424	(42.%)	7.3
0.50	0.859	±	0.609	(71.%)	3.0
0.70	1.879	±	0.873	(46.%)	7.3
0.90	0.303	±	0.319	(105.%)	1.0
1.10	-0.077	±	0.086	(112.%)	-0.2
1.30	0.507	±	0.638	(126.%)	1.8
1.50	0.0	±	0.0	(0.%)	0.0
1.70	-0.081	±	0.115	(141.%)	-0.2
1.90	0.0	±	0.0	(0.%)	0.0

TOTAL NET EVENTS= 26.1 ± 26.2%

Table G-2
(continued)

$\theta_1 = 38^o$ $\theta_2 = 26^o$

Φ_r	CROSS SECTION MICROBARNS	± UNCERTAINTY PER SR**2		NET EVENTS
0.10	1.595	± 0.373	(23.%)	21.7
0.30	2.121	± 0.429	(20.%)	28.2
0.50	2.090	± 0.417	(20.%)	29.4
0.70	1.615	± 0.369	(23.%)	21.3
0.90	1.163	± 0.311	(27.%)	15.5
1.10	0.215	± 0.196	(91.%)	2.5
1.30	-0.043	± 0.096	(226.%)	-0.7
1.50	-0.012	± 0.013	(110.%)	-0.2
1.70	0.0	± 0.0	(0.%)	0.0
1.90	0.0	± 0.0	(0.%)	0.0

TOTAL NET EVENTS= 117.7 ± 10.1%

$\theta_1 = 38^o$ $\theta_2 = 30^o$

Φ_r	CROSS SECTION MICROBARNS	± UNCERTAINTY PER SR**2		NET EVENTS
0.10	2.047	± 0.381	(19.%)	34.2
0.30	2.873	± 0.442	(15.%)	46.2
0.50	1.946	± 0.364	(19.%)	31.6
0.70	1.659	± 0.332	(20.%)	26.2
0.90	1.211	± 0.277	(23.%)	20.2
1.10	0.509	± 0.210	(41.%)	8.0
1.30	-0.012	± 0.078	(642.%)	-0.2
1.50	0.111	± 0.103	(92.%)	1.6
1.70	0.0	± 0.0	(0.%)	0.0
1.90	0.0	± 0.0	(0.%)	0.0

TOTAL NET EVENTS= 167.8 ± 8.2%

$\theta_1 = 38^o$ $\theta_2 = 34^o$

Φ_r	CROSS SECTION MICROBARNS	± UNCERTAINTY PER SR**2		NET EVENTS
0.10	3.582	± 0.631	(18.%)	32.7
0.30	3.376	± 0.633	(19.%)	29.3
0.50	3.700	± 0.645	(17.%)	34.7
0.70	2.656	± 0.575	(22.%)	22.9
0.90	1.400	± 0.417	(30.%)	11.7
1.10	1.254	± 0.415	(33.%)	10.2
1.30	0.368	± 0.213	(58.%)	3.0
1.50	-0.043	± 0.044	(101.%)	-0.3
1.70	-0.065	± 0.065	(100.%)	-0.5
1.90	0.0	± 0.0	(0.%)	0.0

TOTAL NET EVENTS= 143.6 ± 8.6%

Table G-3

Summary of $\frac{d\sigma}{d\theta_1 d\theta_2}$ Cross Sections
From a Preliminary Analysis*

θ_1-θ_2 deg.	Experiment $\mu b/rad^2$	Theory $\mu b/rad^2$	Ratio - 1	Number of Events
18-18	0.296 ± 0.046	0.368	-0.20 ± 0.13	97
18-22	0.296 ± 0.030	0.340	-0.13 ± 0.09	213
22-22	0.314 ± 0.026	0.350	-0.10 ± 0.08	262
18-26	0.160 ± 0.029	0.300	-0.47 ± 0.10	93
18-30	0.217 ± 0.064	0.263	-0.17 ± 0.25	22
22-26	0.348 ± 0.022	0.342	0.02 ± 0.07	525
26-26	0.331 ± 0.024	0.363	-0.09 ± 0.07	314
22-30	0.301 ± 0.026	0.325	-0.07 ± 0.09	234
22-34	0.175 ± 0.032	0.308	-0.43 ± 0.11	47
26-30	0.317 ± 0.020	0.370	-0.14 ± 0.06	465
30-30	0.434 ± 0.032	0.401	0.08 ± 0.09	253
26-34	0.354 ± 0.026	0.370	-0.04 ± 0.08	267
30-34	0.387 ± 0.028	0.424	-0.09 ± 0.07	316
34-34	0.473 ± 0.053	0.474	-0.00 ± 0.13	116
38-22	0.238 ± 0.079	0.295	-0.19 ± 0.27	12
38-26	0.404 ± 0.049	0.372	0.09 ± 0.14	96
38-30	0.429 ± 0.042	0.460	-0.07 ± 0.10	157
38-34	0.618 ± 0.065	0.532	0.16 ± 0.15	144

Weighted Average Value of (Ratio-1) = -0.097 ± 0.022

* These are results published in Ref. 70. The analysis procedure used was completely different from that described in the thesis, and only part of the events in each angular bin were retained. Uncertainty in normalization was ± 10%. Error for uncertainty in the energy thresholds is not included (See Table 16). In the analysis presented earlier in the thesis, one data tape containing ~7% of all PPγ events was damaged and could not be processed and limits placed on wire chamber coordinates eliminated an additional 5 - 10% of all events.